
**What Do Magnetic Shieldings Tell Us About
Bonding, Aromaticity and Antiaromaticity in
Mono-, Bi- and Tricyclic Molecules?**

Muntadar Abd Al-Barri Hussain Al-Yassiri - *MSc*

PhD Thesis

Chemistry

University of York

August 2019

To My Family...

Abstract

Some chemical concepts such as aromaticity, antiaromaticity, and chemical bonding have been evaluated for some molecules based on isotropic magnetic shielding calculations. This includes utilising points as local shielding probes which have been used as a single point or multiple points aligned in one-, two-, or three-dimensional grids. Each of the grids was placed at a specific location around/at the molecular space of the studied molecules.

Nuclear and off-nucleus NMR shielding calculations were performed at different levels of theory using different quantum chemical methods of HF, MP2, and CASSCF with a variety of basis sets. The calculations were performed on some organic and inorganic mono-, bi-, and tricyclic molecules in their ground and, in some cases, low-lying excited states. These molecules are borazine, borazanaphthalene, deltate, squarate, croconate, rhodizonate, disulfur dinitride, naphthalene, anthracene and phenanthrene.

Based on analysing and scanning the changes in the magnetic shielding data of values, 1D curves, 2D contour maps and 3D isosurfaces, the targeted molecular features for the above molecules have been obtained.

The chemical bonding, aromaticity, and antiaromaticity of the molecules are assessed based on the above evaluations. The results show that both borazine and the borazanaphthalene are moderately aromatic. The oxocarbon dianions vary from aromatic deltate, moderately aromatic squarate to antiaromatic croconate and rhodizonate. Also, the vertical excitation of the moderately aromatic ground state disulfur dinitride leads to strongly antiaromatic S_1 and moderate antiaromatic T_1 states. Naphthalene shows obvious magnetic variations among its different electronic states. In terms of decreasing aromaticity, the naphthalene states follow this order: S_2 (strongly aromatic) > S_0 (aromatic) > T_1 (antiaromatic) > S_1 (strongly antiaromatic). Both anthracene and phenanthrene display a strong magnetic behaviour. The central ring of anthracene is more magnetically shielded than the two terminal rings, whereas a contrast shielding profile is found in phenanthrene rings. For all the above molecules, the magnetic shieldings around bonds help in understanding the overall magnetic behaviour and the aromaticity level.

List of Contents

ABSTRACT	3
LIST OF CONTENTS	4
LIST OF TABLES	7
LIST OF FIGURES	8
PREFACE	13
ACKNOWLEDGEMENTS	14
DECLARATION	15
1 INTRODUCTION	16
1-1 Aromaticity	17
1-2 Magnetic Criterion	20
1-2-1 Electron Delocalisation and Ring Current	20
1-2-2 NMR Chemical Shift	22
1-2-3 Diamagnetic Anisotropy and Diamagnetic Susceptibility Exaltation as Global (Bulk) Magnetic Evaluations.....	23
1-2-4 Off-Nucleus Chemical Shift as a (Local) Through-Space Magnetic Probe.....	25
1-2-5 Lithium Ion Magnetic Probe Model	25
1-2-6 Nucleus Independent Chemical Shift (NICS) Model	26
1-2-7 Other Types of NICS-based Indices	28
1-2-8 Isochemical Shielding Surface (ICSS)	28
1-2-9 Finer ICSS and 2D Isotropic Shielding Maps.....	29
1-2-10 Usefulness of the 2D Isotropic Shielding Maps in Assessing Aromaticity and Antiaromaticity	30
2 METHODS AND PROCEDURE	31
2-1 Methods	32
2-1-1 Hartree-Fock Self-Consistent Field Method (HF-SCF).....	32

LIST OF CONTENTS

2-1-2 Møller-Plesset Second Order Perturbation Theory (MP2).....	35
2-1-3 Complete Active Space Self-Consistent Field (CASSCF) Method.....	36
2-1-4 Density Functional Theory (DFT)	37
2-1-5 Some Notes on the Isotropic Shielding Calculations and Keywords Used with the Gaussian Program Package.....	39
2-2 Procedures	40
2-2-1 One-Dimensional (1D) Grids	40
2-2-2 Two-Dimensional (2D) Grids	42
2-2-2-1 Horizontal 2D Grids	42
2-2-2-2 Use of Horizontal 2D Grids to Investigate the Shielding Tensor Component Perpendicular to the Molecular Plane	43
2-2-2-3 Vertical 2D Grids	44
2-2-2-4 A Specialized Script for Setting Up Vertical 2D Grids	45
2-2-3 Three-Dimensional Grids	46
2-2-3-1 Standard Three-Dimensional Grids	46
2-2-3-2 A New Computationally Efficient Technique for Performing 3D Shielding Calculations	48
2-2-3-3 Improving the Resolution of Isotropic Shielding Isosurfaces ..	51
3 BORAZINE AND BORAZANAPHTHALENE.....	54
3-1 Introduction	55
3-2 Borazine	58
3-3 Borazanaphthalene	65
3-4 Conclusions	73
4 CYCLIC OXOCARBON DIANIONS	75
4-1 Introduction	76
4-2 Deltate	78
4-2 Squarate	85

LIST OF CONTENTS

4-3 Croconate	92
4-4 Rhodizonate	99
4-5 Conclusions	106
5 DISULFUR DINITRIDE	108
5-1 Introduction	109
5-2 Ground State of S_2N_2	111
5-3 First Singlet (S_1) Excited State of S_2N_2	118
5-4 First Triplet (T_1) Excited State of S_2N_2	124
5-5 Conclusions.....	130
6 NAPHTHALENE	132
6-1 Introduction	133
6-2 Ground State (S_0) of Naphthalene	136
6-3 The First Singlet State (S_1) of Naphthalene	145
6-4 The Second Singlet State (S_2) of Naphthalene	153
6-5 The First Triplet State (T_1) of Naphthalene.....	162
6-6 Conclusions.....	170
7 ANTHRACENE AND PHENANTHRENE	171
7-1 Introduction	172
7-2 Anthracene.....	175
7-3 Phenanthrene	186
7-4 Conclusions.....	197
8 CONCLUSIONS	199
8-1 Conclusions.....	200
ABBREVIATIONS	205
REFERENCES	206

List of Tables

3-1 Isotropic Shielding Data of Borazine	58
3-2 Isotropic Shielding Data of Borazanaphthalene (1)	65
3-3 Isotropic Shielding Data of Borazanaphthalene (2)	65
4-1 Isotropic Shielding Data of Deltate	78
4-2 Isotropic Shielding Data of Squarate	85
4-3 Isotropic Shielding Data of Croconate	92
4-4 Isotropic Shielding Data of Rhodizonate	99
5-1 Isotropic Shielding Data of S_0 S_2N_2	111
5-2 Isotropic Shielding Data of S_1 S_2N_2	118
5-3 Isotropic Shielding Data of T_1 S_2N_2	124
6-1 Isotropic Shielding Data of S_0 Naphthalene.....	136
6-2 Isotropic Shielding Data of S_1 Naphthalene.....	145
6-3 Isotropic Shielding Data of S_2 Naphthalene.....	153
6-4 Isotropic Shielding Data of T_1 Naphthalene	162
7-1 Isotropic Shielding Data of Anthracene (1)	175
7-2 Isotropic Shielding Data of Anthracene (2)	176
7-3 Isotropic Shielding Data of Phenanthrene (1).....	186
7-4 Isotropic Shielding Data of Phenanthrene (2).....	187

List of Figures

1-1 Some Formulae of Benzene.....	18
1-2 Ring Current Models	21
1-3 Chemical Shifts of [18]Annulene and Dianionic [18]Annulene.....	23
1-4 Naphthalene Magnetic Susceptibility Tensor Elements	24
1-5 Lithium Ion Magnetic Probe Model	26
1-6 NICS Magnetic Probe Model.....	27
1-7 2D Isotropic Shielding Maps of Benzene and Cyclobutadiene	30
2-1 CASSCF(6,6) Orbitals.....	37
2-2 One-Dimensional Grids.....	41
2-3 Five Horizontal 2D Layers	43
2-4 Differences Between Isotropic Shielding Components	44
2-5 Standard Vertical 2D Grids.....	44
2-6 Implementations of a Specialised Script for Setting up 2D Grids.....	45
2-7 Flowchart of Standard 2D and 3D Isotropic Shielding Calculations	47
2-8 Replications of Isotropic Shielding Results	48
2-9 Comparison Between Standard and New Technique Calculations.....	50
2-10 Flowchart of New Technique for 3D Isotropic Shielding Calculations..	52
2-11 Improving Isotropic Shielding Isosurfaces	53
3-1 Borazine: Five Layer Magnetic Shielding Maps	59
3-2 Borazine: $\sigma_{\text{iso}(zz)}$ Shielding Map at 1 Å.....	60
3-3 Borazine: Vertical Cross-Section Shielding Maps	61
3-4 Borazine: Shielding Variation at Ring Centre	62
3-5 Borazine: Shielding Variation Along and Above N-B Bond	63

LIST OF FIGURES

3-6 Borazine: 3D Isotropic Shielding Isosurfaces	64
3-7 Borazanaphthalene: Five Layer Magnetic Shielding Maps	66
3-8 Borazanaphthalene: $\sigma_{\text{iso}(zz)}$ Shielding Map at 1 Å	67
3-9 Borazanaphthalene: Cross-Section Shielding Maps of N-B Bonds(1) ...	68
3-10 Borazanaphthalene: Cross-Section Shielding Maps of N-B Bonds(2) .	69
3-11 Borazanaphthalene: Shielding Variation at Ring Centre	69
3-12 Borazanaphthalene: Shielding Variation Along/Above N-B Bonds	70
3-13 Borazanaphthalene: 3D Isotropic Shielding Isosurfaces	72
4-1 Deltate: Five Layer Magnetic Shielding Maps	79
4-2 Deltate: $\sigma_{\text{iso}(zz)}$ Shielding Map at 1 Å	80
4-3 Deltate: Shielding Variation at Ring Centre	81
4-4 Deltate: Vertical Cross-Section Shielding Maps	81
4-5 Deltate: Shielding Variation Along and Above C-C/C-O Bonds	82
4-6 Deltate: 3D Isotropic Shielding Isosurfaces	83
4-7 Squarate: Five Layer Magnetic Shielding Maps	86
4-8 Squarate: $\sigma_{\text{iso}(zz)}$ Shielding Map at 1 Å	87
4-9 Squarate: Vertical Cross-Section Shielding Maps	88
4-10 Squarate: Shielding Variation at Ring Centre	89
4-11 Squarate: Shielding Variation Along and Above C-C/C-O Bonds	90
4-12 Squarate: 3D Isotropic Shielding Isosurfaces	91
4-13 Croconate: Five Layer Magnetic Shielding Maps	93
4-14 Croconate: Vertical Cross-Section Shielding Maps	94
4-15 Croconate: $\sigma_{\text{iso}(zz)}$ Shielding Map at 1 Å	95
4-16 Croconate: Shielding Variation at Ring Centre	96
4-17 Croconate: Shielding Variation Along and Above C-C/C-O Bonds	97
4-18 Croconate: 3D Isotropic Shielding Isosurfaces	98

LIST OF FIGURES

4-19 Rhodizonate: Five Layer Magnetic Shielding Maps	100
4-20 Rhodizonate: $\sigma_{\text{iso}(zz)}$ Shielding Map at 1 Å	101
4-21 Rhodizonate: Shielding Variation at Ring Centre	101
4-22 Rhodizonate: Vertical Cross-Section Shielding Maps	102
4-23 Rhodizonate: Shielding Variation Along/Above C-C/C-O Bonds.....	103
4-24 Resonance Structures of rhodizonate & Mulliken Charge Distributions of cyclic oxocarbon dianions.....	103
4-25 Rhodizonate: 3D Isotropic Shielding Isosurfaces	105
5-1 S ₂ N ₂ : Most Common Electronic Structures	109
5-2 S ₂ N ₂ – S ₀ : Five Layer Magnetic Shielding Maps	112
5-3 S ₂ N ₂ – S ₀ : $\sigma_{\text{iso}(zz)}$ Shielding Map at 1 Å	113
5-4 S ₂ N ₂ – S ₀ : Shielding Variation at Ring Centre	114
5-5 S ₂ N ₂ – S ₀ : Vertical Cross-Section Shielding Maps.....	115
5-6 S ₂ N ₂ – S ₀ : Vertical Cross-Section Shielding Maps of S-N Bond	116
5-7 S ₂ N ₂ – S ₀ : Shielding Variation Along and Above S-N Bond.....	116
5-8 S ₂ N ₂ – S ₀ : 3D Isotropic Shielding Isosurfaces.....	117
5-9 S ₂ N ₂ – S ₁ : Five Layer Magnetic Shielding Maps	119
5-10 S ₂ N ₂ – S ₁ : Sulfur Shielded-Sphere & $\sigma_{\text{iso}(zz)}$ Shielding Maps	120
5-11 S ₂ N ₂ – S ₁ : Vertical Cross-Section Shielding Maps	121
5-12 S ₂ N ₂ – S ₁ : Vertical Cross-Section Shielding Maps of S-N Bond	121
5-13 S ₂ N ₂ – S ₁ : Shielding Variation at Ring Centre	122
5-14 S ₂ N ₂ – S ₁ : Shielding Variation Along and Above S-N Bond.....	123
5-15 S ₂ N ₂ – S ₁ : 3D Isotropic Shielding Isosurfaces.....	123
5-16 S ₂ N ₂ – T ₁ : Five Layer Magnetic Shielding Maps	125
5-17 S ₂ N ₂ – T ₁ : $\sigma_{\text{iso}(zz)}$ Shielding Map at 1 Å	126
5-18 S ₂ N ₂ – T ₁ : Shielding Variation at Ring Centre	126

LIST OF FIGURES

5-19 S ₂ N ₂ – T ₁ : Vertical Cross-Section Shielding Maps.....	127
5-20 S ₂ N ₂ – T ₁ : Vertical Cross-Section Shielding Maps of S-N Bond.....	128
5-21 S ₂ N ₂ – T ₁ : Shielding Variation Along and Above S-N Bond.....	128
5-22 S ₂ N ₂ – T ₁ : 3D Isotropic Shielding Isosurfaces.....	129
6-1 Naphthalene – S ₀ : Five Layer Magnetic Shielding Maps	137
6-2 Naphthalene – S ₀ : $\sigma_{\text{iso}(zz)}$ Shielding Map at 1 Å	138
6-3 Naphthalene – S ₀ : Vertical Cross-Section Shielding Maps.....	139
6-4 Naphthalene – S ₀ : Cross-Section Shielding Maps of C-C Bonds (1)...	140
6-5 Naphthalene – S ₀ : Cross-Section Shielding Maps of C-C Bonds (2)...	142
6-6 Naphthalene – S ₀ : Shielding Variation at Ring Centre	142
6-7 Naphthalene – S ₀ : Shielding Variation Along and Above C-C Bonds..	143
6-8 Naphthalene – S ₀ : 3D Isotropic Shielding Isosurfaces	144
6-9 Naphthalene – S ₁ : Five Layer Magnetic Shielding Maps	146
6-10 Naphthalene – S ₁ : $\sigma_{\text{iso}(zz)}$ Shielding Map at 1 Å	147
6-11 Naphthalene – S ₁ : Vertical Cross-Section Shielding Maps.....	147
6-12 Naphthalene – S ₁ : Cross-Section Shielding Maps of C-C Bonds (1).	148
6-13 Naphthalene – S ₁ : Cross-Section Shielding Maps of C-C Bonds (2).	149
6-14 Naphthalene – S ₁ : Shielding Variation at Ring Centre	149
6-15 Naphthalene – S ₁ : Shielding Variation Along and Above C-C Bonds	150
6-16 Naphthalene – S ₁ : 3D Isotropic Shielding Isosurfaces	152
6-17 Naphthalene – S ₂ : Five Layer Magnetic Shielding Maps	154
6-18 Naphthalene – S ₂ : $\sigma_{\text{iso}(zz)}$ Shielding Map at 1 Å	155
6-19 Naphthalene – S ₂ : Vertical Cross-Section Shielding Maps.....	156
6-20 Naphthalene – S ₂ : Cross-Section Shielding Maps of C-C Bonds (1).	156
6-21 Naphthalene – S ₂ : Cross-Section Shielding Maps of C-C Bonds (2).	158
6-22 Naphthalene – S ₂ : Shielding Variation at Ring Centre	158

LIST OF FIGURES

6-23 Naphthalene – S ₂ : Shielding Variation Along and Above C-C Bonds	159
6-24 Naphthalene – S ₂ : 3D Isotropic Shielding Isosurfaces	161
6-25 Naphthalene – T ₁ : Five Layer Magnetic Shielding Maps	163
6-26 Naphthalene – T ₁ : $\sigma_{\text{iso}(zz)}$ Shielding Map at 1 Å	164
6-27 Naphthalene – T ₁ : Vertical Cross-Section Shielding Maps	165
6-28 Naphthalene – T ₁ : Cross-Section Shielding Maps of C-C Bonds (1).	165
6-29 Naphthalene – T ₁ : Cross-Section Shielding Maps of C-C Bonds (2).	167
6-30 Naphthalene – T ₁ : Shielding Variation at Ring Centre	167
6-31 Naphthalene – T ₁ : Shielding Variation Along and Above C-C Bonds	168
6-32 Naphthalene – T ₁ : 3D Isotropic Shielding Isosurfaces	169
7-1 Anthracene: Five Layer Magnetic Shielding Maps.....	177
7-2 Anthracene: $\sigma_{\text{iso}(zz)}$ Shielding Map at 1 Å	178
7-3 Anthracene: Shielding Variation at Ring Centres	178
7-4 Anthracene: Vertical Cross-Section Shielding Maps	179
7-5 Anthracene: Cross-Section Shielding Maps of C-C Bonds (1)	180
7-6 Anthracene: Cross-Section Shielding Maps of C-C Bonds (2)	181
7-7 Anthracene: Shielding Variation Along and Above C-C Bonds	182
7-8 Anthracene: 3D Isotropic Shielding Isosurfaces.....	185
7-9 Phenanthrene: Five Layer Magnetic Shielding Maps	188
7-10 Phenanthrene: $\sigma_{\text{iso}(zz)}$ Shielding Map at 1 Å	189
7-11 Phenanthrene: Shielding Variation at Ring Centres	189
7-12 Phenanthrene: Vertical Cross-Section Shielding Maps.....	190
7-13 Phenanthrene: Cross-Section Shielding Maps of C-C Bonds (1).....	191
7-14 Phenanthrene: Cross-Section Shielding Maps of C-C Bonds (2).....	192
7-15 Phenanthrene: Shielding Variation Along and Above C-C Bonds.....	193
7-16 Phenanthrene: 3D Isotropic Shielding Isosurfaces.....	196

Preface

It's a long story, started as a dream directly after completing my MSc degree at the University of Baghdad and got the HCED-Iraq scholarship in the early days of 2012. The dream has started to become more real in 2015 when I stepped the first step in my PhD journey. The journey filled with hopes, enthusiasm, pains, difficulties and lots of unexpected events.

During around four years, I found that the way to success and creativity is based on firmness in facing difficulties and the insistence to think even in simple or impossible thoughts.

This thesis is not an article of a number of pages, it is a life story. Every word, molecule, figure, page or chapter reminds me of a specific time-period on the timeline of the PhD journey.

Struggling with ideas, turning the ideas into scripts, performing calculations, finding explanations, discussing the results and visualising the dreams, all these were some of the stations of the PhD journey, with much more hidden stations.

Like binary codes, there are only two expressions: either 0 or 1. I have been influenced by this logic when I did this project, but in a different way. Namely, either to do my project in a best form or to not do it at all. This decision was uneasy, making the required time of completing this project longer. The fingerprint of a huge number of trial and error to make imaginative ideas to become real scripts and applicable techniques are hidden here, but only their fruitful results are represented through this project.

At the end of my study, my conclusion is that, the PhD degree is associated with and based on the idea of how to think out of the box and how to do new, effective and unusual project. I found, for any idea, there is always a door, even for a hardest idea. I encourage every student, who may read my words, to think in a new idea and to seek the way to its door.

Acknowledgements

Firstly, I would like to thank my supervisor Dr Peter Karadakov for his supervision, supports, advices and for kindness over around four years, and special thanks for his feedback and efforts during writing up this thesis.

Also, I grateful to the Higher Committee for Education Development in Iraq (HCED Iraq) for sponsoring my PhD scholarship at the University of York.

Thanks to Department of Chemistry and the Library at the University of York for offering a wide range of courses and scientific material.

Finally, special thanks to my family for supporting, patience and for sharing me all happy and sad moments during my scholarship in the UK.

Declaration

I declare that this thesis is a presentation of original work and I am the sole author. The research contained within this thesis was carried out between October 2015 and August 2019 in the Department of Chemistry at the University of York. This work has not previously been presented for an award at this, or any other, University. All sources are acknowledged as References.

The work on disulfur dinitride has been published in the Journal of **Chemistry A European Journal**.

Muntadar Abd Al-Barri Hussain Al-Yassiri

CHAPTER ONE

INTRODUCTION

1 introduction

1-1 Aromaticity

Aromaticity is a term which has a long history filled with researchers' efforts. In 1825, Michael Faraday^[1] discovered benzene. This can be considered as the first important turning point in the history of aromaticity. Forty years later, in 1865, a suggestion was made by Kekulé^[2] for the benzene structure, in which its hexagonal form is nowadays known as Kekulé structure. The Kekulé's structural suggestion had preceded Thomson's discovery of the electron by around 30 years.

Due to the odour properties of benzene and its derivatives, Kekulé termed these molecules as "aromatic compounds" thinking about the existence of benzene in such compounds.^[3] The word "aromatic", however, was known since the beginning of the nineteenth century in reference to volatile odour compounds isolated from vegetable oils,^[4] as well as to distinguish these compounds from fatty compounds,^[5] since the aromatic and the aliphatic (non-aromatic) compounds were known, at that time, as sub-groups of the carbon compounds.^[6] Between the mid-nineteenth to mid-twentieth centuries, the "aromatic" term was used to define benzenoid compounds.^[5] Whereas, due to their less-defined aromatic characters, non-benzenoids and heterocyclic aromatics were excluded from being described as "aromatic".^[7]

Benzene, therefore, was considered as the most important member of the aromatic family and the term "aromatic character" is related to its properties.^[3] Thus, in terms of proposing a hypothetical structure to fit its unusual properties^[3,8], benzene had attracted significant interest between the time of Kekulé's suggestion till the end of the nineteenth century, see figure (1-1). However, most of these structures were not able to reliably express the chemistry of benzene.^[5]

Nevertheless, until the twenties of the twentieth century, namely, the birth of quantum mechanics, no significant accurate descriptions for the nature of the electronic structure of benzene were available. Maybe the most notable events at that time were the "aromatic sextet", by Armit and Robinson^[9] in 1925, and the well-known Hückel theory with the $(4n+2)$ π -electron rule of aromaticity in 1931. Despite the success of the $(4n+2)$ rule in dealing with the aromaticity of some planar monocyclic molecules as well as some polycyclic

hydrocarbons by extending this rule^[8], the rule, however, was strongly discouraged for polycyclic benzenoid compounds.^[10] Also, it cannot be utilised to evaluate the degree of aromaticity.

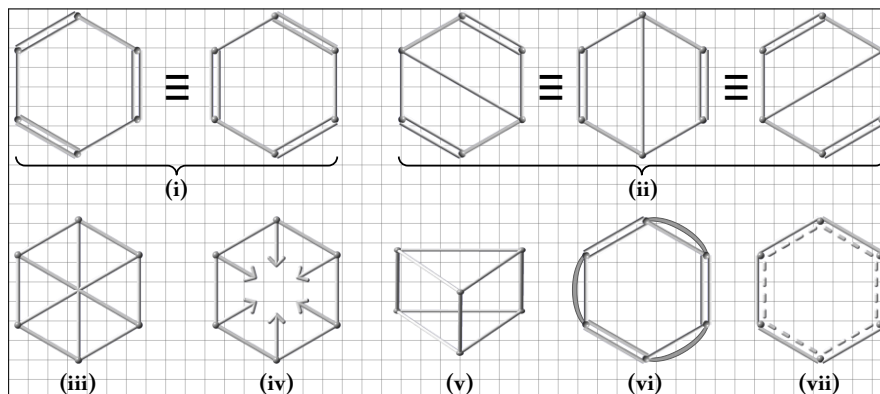


Figure 1-1: Some benzene formulae proposed between (1865) and (1899) (i-vi). by (i) Kekule, (ii) Stadelers-Wichelhaus (or Dewar), (iii) Claus, (iv) Armstrong-Baeyer, (v) Ladenburg, (vi) Thiele and (vii) the real structure.

It can be said that, in chemistry, aromaticity and antiaromaticity can be considered as fundamental concepts.^[11] The concept “aromaticity” has significant importance in organic chemistry.^[4,12] Moreover, the “aromaticity” comes at first as the most controversial and hard to define concept,^[12] and, since the benzene discovery, the concept has been roughly defined.^[13] Perhaps the most common and the simplest description used by chemists to define aromaticity is “like benzene”^[4,6] Even so, very few compounds have high likeness degree with benzene.^[3]

In more detail, benzene is chemically described as stable; inert toward Diels-Alder reactions; resists oxidation; and does not follow addition reactions but rather electrophilic substitutions.^[5] Even so, cyclooctatetraene or cyclobutadiene, homologues which come after and before benzene as (C₈H₈) and (C₄H₄), respectively, show contrasting chemical behaviours just because they do not have the exact benzene ring.^[5] On the other hand, azulene, which structurally has no benzene ring, shares with aromatic compounds their chemical and physical features. However, some benzene derivatives, polycyclic benzenoids, non-benzenoids and heterocyclic compounds behave differently from benzene’s chemical reactivity.^[3] Thus, “aromatic” does not specify the overall behaviour of a given aromatic compound owing to its structural or chemical features,^[5] but it rather means possessing an electron organisation acting as benzene.^[6] Between factors of chemical reactivity,

stability and electronic structure, the aromaticity is the only function of the last factor.^[3]

Experimentally, the properties of aromaticity cannot be measured directly since it has no straightforward physical definition.^[13] However, in the classical theme of thermodynamics, aromaticity can be defined as a molecule exhibits lower total energy and more stability than an identical compound constructed from simple two-electron bonds.^[6] In other words, classically, the definition of the aromaticity relied on features of chemical reactivity; cyclic character; and stability,^[3] whereas π -electron delocalisation is the cause of the destabilisation features of the antiaromaticity.^[6]

One definition of an aromatic compound is a compound in which an induced ring current is sustained.^[7] Another definition is that a compound with a cyclic form with a diamagnetic ring current and all atoms of its cyclic-skeleton contribute and form a single system of conjugation.^[8] According to a more recent definition,^[14] a compound is considered as aromatic if it shows a remarkable diamagnetic susceptibility besides the existence of electron circulation where the bonds are showing equalisation in their length, unusual magnetic anisotropy and chemical shift, as well as energetic stabilisation which is reflected on the physical and chemical properties of that compound. Whereas the antiaromatic compound may be distinguished by its paramagnetic susceptibility exaltation.^[14]

Thus, the indirect means of measuring the degree of aromaticity can be obtained via inspecting one or more of three criteria: energetic, structural, and magnetic.^[12] However, among the criteria which indirectly measure aromaticity, no one of the criteria has an absolute ability to measure the aromaticity, and each criterion has an extent of limitation.^[15] In addition, there are many aromaticity indices involved as tools to examine corresponding criteria. All aromaticity indices are no more than experimental or theoretical approximations which become quantitatively valid only if a comparison is made with a reliable reference.^[16] However, since the electron delocalisation, and its consequent ring currents, induce the magnetic properties, these last are then the properties most closely associated with the term aromaticity.^[17] Thus, this project is based on the magnetic criterion, and this chapter is restricted to deal with this criterion. The other two criteria, the energetic and the structural criteria, are out of the scope of this project.

1-2 Magnetic Criterion

As a consequence of what was said above about the relation between aromaticity and magnetic properties, the magnetic criterion can then be considered as an effective means of representing aromaticity.^[14,18-21] Since the magnetic criterion includes several magnetic concepts and indices, the following sections will cover the main ones in detail whenever the concept is relevantly linked to the aims of this thesis.

1-2-1 Electron Delocalisation and Ring Current

The π -electron delocalisation and the ring current are two fundamental and explanatory concepts in terms of the aromaticity phenomenon. Therefore, some basics of these concepts will be explained as an introduction to other sections of this chapter.

The idea of electron delocalisation and ring current comes from the free electron model suggested by Pauling^[22] who calculated the diamagnetic anisotropy and the ring current of some aromatic molecules. Accordingly, when applying an external magnetic field perpendicular to an aromatic system, only one p_z -electron per aromatic carbon atom is able to move to the adjacent carbon, the induced current from the electron movement has a similar feature of mobility from atom to atom. The benzene six π -electrons are distributed according to their wavefunction probability as two circular-domains, one above and one below the hexagonal ring. For aromatic molecules, the diamagnetic moment was attributed to such currents.

Likewise, Pople^[23] in 1956 pointed out that, for a hexagonal skeleton of an aromatic system, the precession of the movement of electrons from carbon to the neighbouring carbon forms a current moving along the hexagon within a circle of a radius equivalent to C-C distance.^[23] In addition, Pople also denoted that when benzene is exposed to an external magnetic field, the “formed” magnetic dipole at the ring centre is antiparallel to the external magnetic field and exhibits a diamagnetic moment.^[23]

In 1957, supportive experimental evidence to Pople’s assumption was reported by Waugh and Fessenden,^[24] but with some disagreements. According to their π -electron current model, the current is divided into two current loops, one above and one below the benzene plane, with separation

distance of 0.9 Å. Unlike the Pople magnetic dipole, the current loops of electron movement form a circular magnetic field (shell) which can be sensed by the nearby nuclei.^[24]

In this context, Johnson and Bovey^[25] denoted a similar model to the Waugh and Fessenden's two loops current model. According to their findings, the π -electron current shares the benzene ring radius. In addition, the separating distance between the two loops is 1.28 Å, not 0.9 Å.

The above current models are represented in figure (1-2) which shows the Pople model, (a), and the Waugh-Fessenden and Johnson-Bovey two loops current model (b).

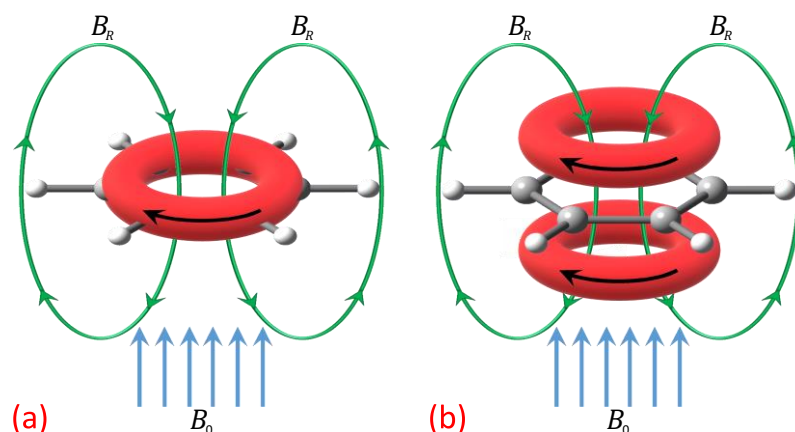


Figure 1-2: Pople ring current model, (a), Waugh-Fessenden and Johnson-Bovey two loops current model, (b). In both models, B_0 represents the applied (external) field which induces π -electron delocalisation and ring current. B_R demonstrates the induced magnetic shell or the residual magnetic field formed by the ring current.

π -Electron delocalisation directly affects energy and stabilisation. For example, the π -electron energy for ethylene is 2β (β is resonance integral). Whereas the energy for the three double-bond Kekulé benzene is 8, not 6β .^[10] Note that increasing β means increasing the stability of a molecule.

Studying the ring current has high importance in explaining aromaticity. This is because π -electron delocalisation can be inferred from the magnitude of the ring current and then can be used for aromaticity measuring.^[7] Diamagnetism and paramagnetism are two features of the ring current.^[6,20] The former results electron circulation around the ring, whereas the latter from distorting the clouds of electrons by the applied field.^[6] Also, the former is associated with $(4n+2)$, while the latter with $(4n)$ molecules.^[20]

1-2-2 NMR Chemical Shift

Utilising a H-NMR spectroscopy can be considered as an informative tool for measuring proton shielding/deshielding of cyclic molecules which is relevant to the diatropic/paratropic nature of $(4n+2)/(4n)$ systems^[5] and to the degree of aromaticity depending on induced ring currents.^[7] In other words, the shielding of aromatic protons is affected by π -electron delocalisation and current flow in aromatic molecules.^[23,25] Moreover, the H-NMR signals are observed in a different range than the expectation in the case of nonexistence of the ring current.^[6] Thus, for benzene and similar molecules, protons resonate at a lower applied field than nonaromatic protons.^[6]

As an advantage, in terms of quantitatively characterising aromatic character, utilising NMR chemical shifts is more convenient in comparison to the resonance energy since the former can be used to assess the aromatic extent for all kinds of cyclic systems.^[7]

The total magnetic field felt by a nucleus in a molecule of interest equals the sum of the applied magnetic field, (B_0), and any other magnetic fields existing in that molecule or created by the applied field, B_R ,^[6] see figure (1-2). The magnetic field felt by a nucleus, B_R , can be defined as:^[26]

$$B_R = (1 - \sigma_R)B_0 \quad \dots (1.1)$$

where B_0 is the applied field; σ_R is the shielding tensor, which is expressed as a 3×3 matrix and it can be used to obtain the isotropic shielding, σ_{iso} , as will be shown in chapter two. The tendency of B_R to be greater or smaller than B_0 plays a key role in distinguishing the paramagnetic and the diamagnetic shieldings.^[26]

It is useful here to point out some experimental observations of a chemical phenomenon which support the idea of ring current and its magnetic consequences for aromatic molecules. The contrast between chemical shift values of the outer (positive) and inner (negative) protons of the aromatic $(4n+2)$ annulenes supports the diamagnetic ring current in these compounds. Whereas the protons of the analogues antiaromatic $(4n)$ annulenes show a reversed behaviour.^[4] Perhaps the best example for both cases is annulene^[18]. The chemical shifts data for this example are shown in figure (1-3), see the tables in page (285) in reference [4] and the references therein.

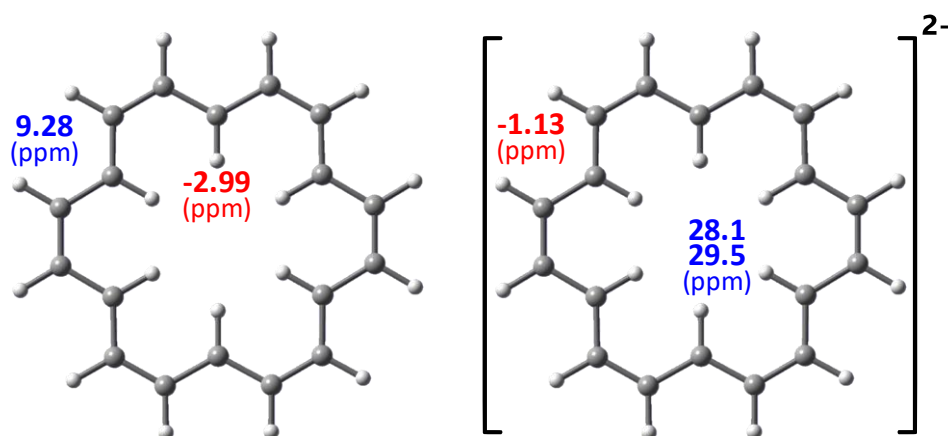


Figure 1-3: Chemical shift values (in ppm) of the inner and outer protons of the aromatic neutral [18]annulene, on the left, and antiaromatic dianionic [18]annulene, on the right.

1-2-3 Diamagnetic Anisotropy and Diamagnetic Susceptibility Exaltation as Global (Bulk) Magnetic Evaluations

Two magnetic parameters, the diamagnetic anisotropy and the diamagnetic susceptibility exaltation, serve in the magnetic evaluation of molecules. In terms of the diamagnetic anisotropy, if the magnetic susceptibility tensor is evenly formed by the contributions of the benzene electrons along the three orthogonal components of the tensor, the ring current only contributes to the component which is perpendicular to the benzene plane.^[27] Therefore, the existence of π -electron delocalisation and ring current cause significant diamagnetic anisotropies in aromatic molecules.^[22] Subsequently, the diamagnetic anisotropy, $\Delta\chi$, depends on the ring current and can be written^[27,28] as the difference between the out-of-plane (perpendicular) component and the average of the other (in-plane) components (which are almost equal in aromatic molecules^[6]), equation (1.2). See figure (1-4) for the susceptibility component orientations.

$$\Delta\chi = \chi_{zz} - \frac{1}{2}(\chi_{xx} + \chi_{yy}) \quad \dots (1.2)$$

The diamagnetic susceptibility exaltation, Λ , can be obtained by finding the difference in total molar magnetic susceptibility for a system showing electron delocalisation, (χ_M), and for its isomer without electron delocalisation (χ'_M)^[29], equation (1.3).

$$\Delta = \chi_M - \chi'_M \quad \dots (1.3)$$

The χ_M or χ'_M expressions are the molar susceptibility, which are given as:^[29]

$$\chi_M = \frac{1}{3}(\chi_{xx} + \chi_{yy} + \chi_{zz}) \quad \dots (1.4)$$

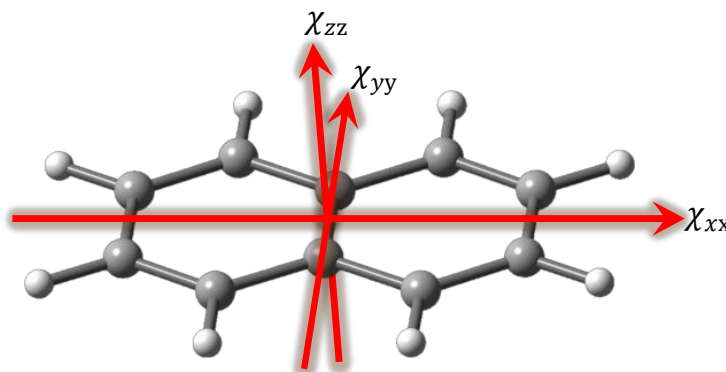


Figure 1-4: Directions of the magnetic susceptibility tensor elements along the Cartesian coordinates of the naphthalene molecule. The perpendicular (out of plane) magnetic susceptibility component, χ_{zz} , is normally greater than the other two (in-plane) susceptibility components, χ_{xx} and χ_{yy} , in an aromatic molecule.

The diamagnetic susceptibility exaltation can be utilised in aromaticity evaluations as its value can be used as an indicator for the presence or absence of electron delocalisation.^[28] Moreover, negative and positive values of the Δ represent the diamagnetic and paramagnetic behaviour, which, in turn, reflect the aromatic and antiaromatic features of a system, respectively.^[11] Among several aromaticity evaluations performed under different aromaticity criteria, the magnetic susceptibility exaltation showed a unique ability as a tool for aromaticity assessment.^[14]

Experimentally,^[8] evaluation of the diamagnetic anisotropy is difficult because single crystal is required in which its molecular axes have to be aligned with the magnetic axes. Diamagnetic susceptibility exaltation measurements do not have such requirements, but rather, they require calculating the exaltation of a hypothetical reference.

Also, when the number of rings of a polycyclic compound increases, the diamagnetic anisotropy increases as well.^[26] The exaltation also relies on the area of the ring^[30] making the comparison of the magnetic properties between compounds with different sizes unreliable. In other words, the anisotropy and

exaltation are a size-depended properties.^[16]

Since the magnetic susceptibility can be considered as a global (bulk) magnetic feature of a molecule,^[31] this, in addition to observations that both diamagnetic anisotropy and diamagnetic susceptibility exaltation seem to be crude quantitative measures of aromaticity,^[8] increases the need to use more specific approaches which indicate the local magnetic behaviour for the molecule. Some approaches of this type are discussed below.

1-2-4 Off-Nucleus Chemical Shift as a (Local) Through-Space Magnetic Probe

So far, in contrast to the quantum-chemical methods, no experimental technique able to measure off-nucleus shieldings.^[32] As noted earlier in section (1-2-1), Johnson and Bovey^[25], in 1958, were the first chemists who succeeded in calculating the diamagnetic and paramagnetic chemical shift in the space around benzene. In addition, they visualised their results as a 2D “isoshielding” contour plot. Since that work, there have been several attempts to use off-nucleus shielding evaluations for finding explanations for some chemical phenomenon, such as for instance, aromaticity. In the following, the most important developments in the off-nucleus shielding implementations and techniques will be pointed out.

1-2-5 Lithium Ion Magnetic Probe Model

Depending on the Li^+ chemical shift, aromaticity and antiaromaticity were assessed using a suitably placed lithium ion.^[11,33] Basically, Li^+ can be utilised as a (local) magnetic probe for the ring of interest. The technique depends on comparing the theoretical^[33] or experimental chemical shift of isolated Li^+ with its chemical shift when it is involved in a complex. Normally, Li^+ is placed over the π -face domains of a ring under study,^[11] see figure (1-5).

The change in the Li^+ chemical shift gives an idea about the effects of the ring current.^[33] Moreover, negative and positive values of the chemical shifts of Li^+ were found above aromatic and antiaromatic molecules, respectively.^[11] For instance, the diatropic effects of the aromatic dilithium silole (CH_4SiLi_2)^[34] and the paratropic effects of the antiaromatic 8π benzene dianion^[35] influence the change of the Li^+ chemical shift.

An advantage of calculating the Li^+ chemical shift over the rings is that, when possible, it can be compared with the experimental Li^+ chemical shift values of complexes, i.e., the Li^+ -compound under study.^[31]

However, in addition to the limited number of such lithium complexes, another factor affects the use of Li^+ as a magnetic probe, the separation height between Li^+ and the ring π -face affects the Li^+ ability to probe the ring current.^[31] This is because the separation height in such lithium complexes is around 2 Å (or more).^[31,36] In addition, using NICS (as explained in the next section) to evaluate the aromaticity of some four-membered rings of $\text{Li}_2\text{C}_4\text{R}_4$ (R=H, Me, t-Bu) showed these complexes as more aromatic than benzene.^[36] This is because Li^+ complexation takes part in above observation, and Li^+ serves as a stabiliser in such complexes via reducing the repulsion of the electrons, and thus enhancing aromaticity.^[36] Therefore, for these reasons, and since the NICS (see next section) was introduced as a better alternative model, a decrease in the use of Li^+ has been observed.

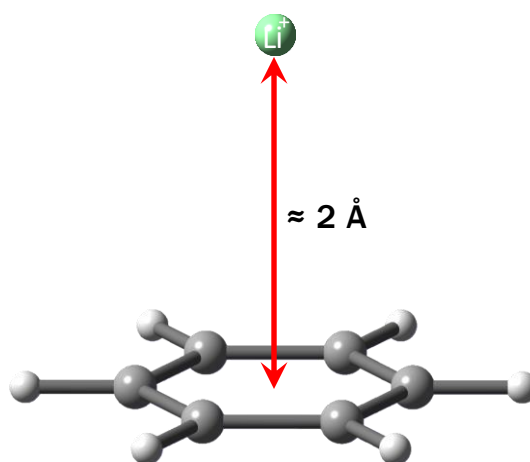


Figure 1-5: A demonstration of placing Li^+ above a ring (benzene) in order to evaluate the extent of the Li^+ chemical shift difference as a consequence of the diatropic/paratropic ring current effects in the ring.

1-2-6 Nucleus Independent Chemical Shift (NICS) Model

In 1996, around four decades after the Johnson and Bovey's approach, Schleyer et al.^[18] introduced the nucleus independent chemical shift (NICS) as a magnetic probe for aromatic/antiaromatic systems. Yet, NICS can be considered as the most important contribution in the off-nucleus approaches and one of the most famous and applicable aromaticity indices.

An advantage of NICS is that the magnetic profile can be probed (locally) for each individual ring of a polycyclic compound.^[11] Also, unlike the Li^+ technique, section (1-2-5), utilising the NICS model does not involve any interaction with the system in question. This is because Li^+ is replaced by a “ghost atom”^{*} which is placed at the ring centre where the applied and the enhanced magnetic fields are in a competition, see figure (1-6 (i)). However, the sign of the obtained isotropic shielding value from the ghost atom has to be reversed (multiplied it by (-1)). The reason for this is to keep the agreement with the negative upfield and positive downfield directions of the observed experimental chemical shifts.^[31,37] Negative NICS value means more diatropic ring current and higher aromaticity, whereas positive NICS indicates nonaromatic or antiaromatic features since the activity of the paratropic ring current.^[17,37]

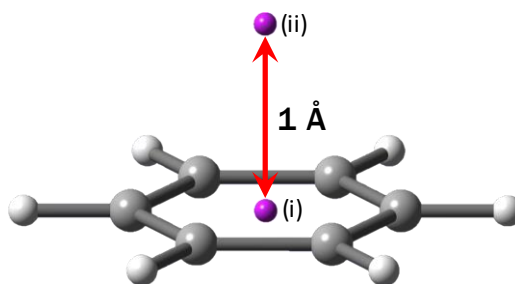


Figure 1-6: An illustration of placing the ghost atoms at and above the ring centre of benzene according to the nucleus-independent chemical shift (NICS). The reversed sign of the absolute shielding from the ghost atom (i) and (ii) represent $\text{NICS}(0)$ and $\text{NICS}(1)$; respectively.

NICS are often in good agreement with other aromaticity criteria-based indices, namely, the energetic, geometric or magnetic criteria.^[11,18,21] Moreover, unlike the other magnetic properties aforementioned in this chapter, namely, the magnetic anisotropy and magnetic susceptibility exaltation, NICS is less size-dependent^[11,18] and it does not need a model compound^[17]. However, the size of the ring has to be, to some extent, large to probe the shielding of the electron delocalisation without the interference of the local shieldings.^[37] For this reason, and to avoid several in-plane interferences, another type of NICS was also introduced, as will be shown in the next section.

* The ghost atom is a virtual atom with a symbol of “Bq” or “X” (under the Gaussian and Dalton packages, respectively). Unlike real atoms, the ghost atom has no electrons, basis functions or nuclear charge, but it can be used as a probe to feel some physical properties, such as the isotropic magnetic shieldings.

1-2-7 Other Types of NICS-based Indices

Several types of NICS have been employed either to enhance the probing quality or to make the evaluation more specific. One of these types is NICS(1) which was introduced by Schleyer and coworkers and recommended as a refined model of NICS.^[30,37] Basically, NICS(1) depends on probing the isotropic shielding at 1 Å above the ring centre of the ring of interest, see figure (1-6 (ii)). Thus, the ghost atom can avoid the in-plane magnetic interferences, as well as feel the magnetic activity which corresponds to the diatropic or paratropic activities at that height.

However, both NICS (often denoted as NICS(0)) and NICS(1) depend on the total (bulk) isotropic shielding value. Thus, a refinement was done^[17] by separating the paratropic and diatropic contributions of σ and π bonds of several cyclic hydrocarbon compounds. Accordingly, the magnetic parameters of NICS(π) and NICS(σ), or in more detail, NICS(π -C-C); NICS(σ -C-C) and NICS(C-H) were probed.^[17] A similar evaluation was also documented for benzene and some of its inorganic analogues.^[30]

In addition to the above reasons for separating σ and π contributions, it is known, as mentioned earlier, that the applied magnetic field is normal to the molecular plane. As a further refinement, Schleyer et al.^[17,38] introduced two other kinds of NICS, NICS_(zz) and NICS(π)_{zz}. The former index is based only on the vertical component of the isotropic shielding tensor. The latter is based on the separation of the π and σ components within the vertical component of the isotropic shielding tensor (only).

Finally, it is appropriate to mention here that the NICS model can be computed not only as a point at 0 or 1 Å height to the ring centre but also as a batch of points of ghost atoms lined-up as a simple line,^[39,40] or as a simple grid of ghost atoms around the molecular space.^[31,37] Moreover, in the following, some patterns of multi-point NICS evaluations will be represented.

1-2-8 Isochemical Shielding Surface (ICSS)

Based on the idea of setting a regular 3D grid of multiple points (ghost atoms), with 0.5 Å separation spacings between the points, several multidimensional shielding/deshielding evaluations round the molecular space has been utilised by Klod and Kleinpeter.^[41] The evaluation was aimed to study the effects of

the ring current of some arenes and the anisotropy of some acyclic multiple-bond molecules.^[41] The absolute magnetic shielding resulted from the 3D grid were then visualised as iso-chemical shielding surface (ICSS).^[41] This procedure is called through space NMR shieldings (TSNMRs).^[42,43]

TSNMRs was also used to investigate the aromaticity and antiaromaticity of some fulvalenes;^[44] some aromatic and antiaromatic molecules;^[42] as well as the antiaromaticity of some neutral and ionic molecules.^[43]

The structural influences on the magnetic properties have also been studied. such as, for instance, the C-C bond in methane and similarly the equivalent bonds of its mono S; O and N substituents;^[45] the intramolecular resonance-assisted hydrogen bonds of some cyclic and acyclic systems;^[46] and finally benzenium cation and some of its substituted analogues.^[47]

Although TSNMRs technique succeeded in its aim of probing the magnetic properties of the above investigations, it, however, focused on performing the 3D calculations on an extremely large volume about a molecule. Also, involving (large) step-width of 0.5 Å as a separator among the points of the 3D grids lowers the points density of in the 3D grid. These technical points of TSNMRs prevent this approach from inspecting some magnetic details closer to the molecular structure of a molecule of interest. Therefore, other research groups, (section 1-2-9), addressed such technical problems.

1-2-9 Finer ICSS and 2D Isotropic Shielding Maps

As a development of utilising ICSS, Karadakov and Horner^[32], by using 3D grids of denser ghost atoms of 0.05 Å spacings, evaluated the magnetic shieldings and aromaticity of benzene and cyclobutadiene. Additionally, they employed 2D grids of 0.05 Å spacings which were oriented not only at the molecular plane and 1 Å parallelly above the plane but also vertically to fit some 2D areas. Using such evaluations led to obtaining very informative 2D and 3D isotropic shielding pictures in which magnifying the molecular magnetic behaviour and helps in assessing aromaticity.

Several other works were published by Karadakov and co-workers to study the shielding behaviours and/or aromaticity of mono-^[48] and di-^[49] heteroatom-five-membered rings; acyclic conjugated systems^[50] and for ground and some excited-states of organic^[51] and inorganic^[52] rings.

1-2-10 Usefulness of the 2D Isotropic Shielding Maps in Assessing Aromaticity and Antiaromaticity

An advantage of employing the 2D ghost atom grids, and, subsequently, the 2D isotropic shielding contour maps, is their ability to assess the aromaticity and antiaromaticity of molecules.

For instance, the two shielding maps in figure (1-7) below, published by Karadakov and Horner^[32], show the isotropic shielding behaviour at the molecular plane level of benzene and cyclobutadiene. For the former molecule, the well-shielded C-C bonds as well as the shielded ring centre indicate the actions of ring current and electron delocalisation on the shielding of the ring centre and then the aromaticity of benzene, see figure (1-2).

In contrast, the cyclobutadiene ring centre is deshielded and the C-C bonds show less shieldings than those in benzene. This can be attributed to the antiaromaticity impact of cyclobutadiene, which affects the electron delocalisation and the magnetic shieldings.

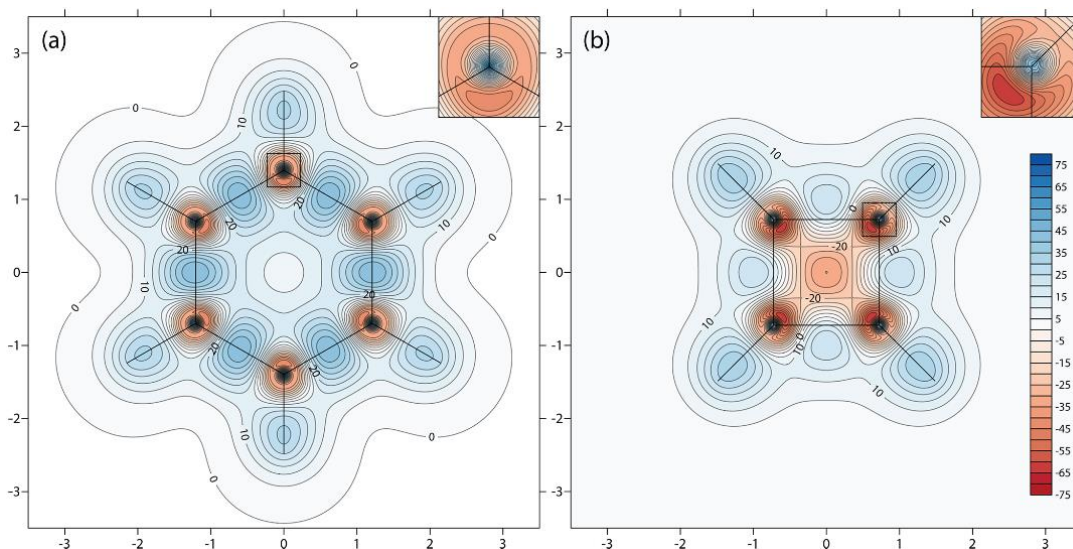


Figure 1-7: Examples^[32] of the 2D isotropic shielding maps for benzene (a) and cyclobutadiene (b) calculated at CASSCF(6,6)GIAO/6-311++G(d,p) and CASSCF(4,4)GIAO/6-311++G(d,p), respectively. (The above shielding contours are used here with permission).

CHAPTER TWO

METHODS AND PROCEDURE

2 Methods and procedure

2-1 Methods

During the work on this project, several quantum-chemical methods, defined as combinations between levels of theory and basis sets, were employed to calculate a wide range of molecular properties, such as energies, optimised geometries, harmonic frequencies, isotropic shielding tensors. This chapter provides short overviews of the quantum-chemical methods used in the project and discusses the practical problems associated with the applications of these methods in the context of the project.

2-1-1 Hartree-Fock Self-Consistent Field Method (HF-SCF)

The primary aim of any quantum chemical method is to solve the Schrödinger equation. However, for many-electron systems obtaining the exact solution of the Schrödinger equation can be very difficult or not possible at all, as this requires a high level of theory and huge computational effort. There is a number of theoretical approaches which provide approximate solutions to the Schrödinger equation subject to a trade-off between accuracy and computational effort and can be used to calculate various physical properties of chemical systems. One of these approaches is the Hartree-Fock (HF) method.

The Hartree-Fock (HF) method is an example of a self-consistent field (SCF) approach which was introduced by Hartree^[53] and Fock^[54] between 1928 and 1930. It is perhaps the most popular quantum-chemical approach and many *ab initio* (from first principles) calculations use HF theory with orbitals approximated as molecular orbital (MO) expansions in a suitable atomic basis set. The HF wavefunction is often used as a reference wavefunction in higher-level theoretical methods, which are referred to as post-Hartree-Fock methods.^[55] The HF method seeks a variational approximation to the wavefunction in the many-electron Schrödinger equation (equation 2.1) which minimizes its energy expectation value.

$$\hat{H}\Psi = E\Psi \quad \dots (2.1)$$

In this equation Ψ is the wavefunction; E is its energy and \hat{H} is the electronic Hamiltonian operator obtained after applying the Born-Oppenheimer approximation^[55] to the total Hamiltonian operator for all electrons and nuclei. \hat{H} is defined as:

$$\hat{H} = - \sum_{i=1}^N \frac{1}{2} \nabla_i^2 - \sum_{i=1}^N \sum_{A=1}^M \frac{Z_A}{r_{iA}} + \sum_{i=1}^N \sum_{i < j}^N \frac{1}{r_{ij}} \quad \dots (2.2)$$

∇_i^2 stands for the Laplacian operator ($\nabla_i^2 = \frac{\partial^2}{\partial x_i^2} + \frac{\partial^2}{\partial y_i^2} + \frac{\partial^2}{\partial z_i^2}$); N and M are the total numbers of electrons and nuclei, respectively; r_{iA} and r_{ij} denote the distances between electron i and nucleus A , and between electron i and electron j , respectively; Z_A is the atomic number of nucleus A .

The electronic wavefunction in HF method represents a single ($N \times N$) Slater determinant^[56], see equation (2.3), which is antisymmetric by design and includes N spin orbitals χ for the electrons in the system.

$$\Psi(x_1, x_2, \dots, x_N) = \frac{1}{\sqrt{N!}} \begin{vmatrix} \chi_1(x_1) & \chi_2(x_1) & \dots & \chi_N(x_1) \\ \chi_1(x_2) & \chi_2(x_2) & \dots & \chi_N(x_2) \\ \vdots & \vdots & \ddots & \vdots \\ \chi_1(x_N) & \chi_2(x_N) & \dots & \chi_N(x_N) \end{vmatrix} \quad \dots (2.3)$$

Each of these spin orbitals can be defined as:

$$\chi_i(x, y, z, \xi) = \phi_i(x, y, z) \omega(\xi) \quad \dots (2.4)$$

where ϕ_i is the molecular (spatial) orbital which depends on the Cartesian coordinates of the electron x, y and z ; ω is the spin function ($\xi = \pm 1/2$ for spin up or spin down).

Each of the molecular orbitals (ϕ_i) is expanded following the ideas of Roothaan^[57] and Hall^[58] as a MO construction, see equation (2.5), which uses a linear combination of atomic orbitals (LCAO) including all basis functions of the selected atomic basis set:

$$\phi_i = \sum_{k=1}^n c_{ki} \varphi_k \quad \dots (2.5)$$

In this equation, φ_k is an atomic orbital from the selected basis set; c_{ki} is the expansion coefficient for this atomic orbital in the MO ϕ_i .

The HF-SCF procedure solves iteratively the single-electron Fock equations, see equation (2.6). It starts with an initial guess for the MOs, which are then used to construct the Fock operator, see equation (2.7). The Fock equations provide new orbitals and the process is repeated until convergence (when the

differences between orbitals from two subsequent iterations become sufficiently small)

$$\hat{F}\phi_i = \varepsilon_i\phi_i \quad \dots (2.6)$$

$$\hat{F} = \hat{h} + \sum_{l=1}^n (2\hat{J}_l + \hat{K}_l) \quad \dots (2.7)$$

Here \hat{h} stands for the one-electron operator; \hat{J}_l and \hat{K}_l are the Coulomb and exchange operators, respectively.^[59] Using equations (2.5) and (2.6), the Fock equation can be written as:^[55]

$$\hat{F} \left(\sum_{k=1}^n c_{ki} \phi_k \right) = \varepsilon_i \left(\sum_{k=1}^n c_{ki} \phi_k \right) \quad \dots (2.8)$$

Multiplying both sides of equation (2.8) by the complex conjugate of an orbital, then integrating leads to:

$$\sum_{k=1}^n c_{ki} \int \phi_k^*(r) \hat{F} \phi_k(r) dr = \varepsilon_i \sum_{k=1}^n c_{ki} \int \phi_k^*(r) \phi_k(r) dr \quad \dots (2.9)$$

$$\sum_{k=1}^n c_{ki} F_{lk} = \varepsilon_i \sum_{k=1}^n c_{ki} S_{lk} \quad \dots (2.10)$$

$$\sum_{k=1}^n (F_{lk} - \varepsilon_i S_{lk}) c_{ki} = 0 \quad \text{or} \quad \mathbf{FC} = \mathbf{SCE} \quad \dots (2.11)$$

The last equations are known as Roothaan equations^[55]; equation (2.11) can be written down as a determinantal equation referred to as “the secular equation”^[56]. The SCF procedure iteratively tries to find the best MO expansion coefficients which lead to the lowest energy expectation value possible.^[60] The HF wavefunction is variational, i.e. it is obtained by optimizing a trial wavefunction. According to variational theory, the energy obtained using a variational method is greater than or equal the exact energy of the system under investigation,^[61,62] i.e., for the HF method $E \geq E_{exact}$.

HF does not account for individual pairwise electron-electron repulsions but rather averages the electron interactions; this can be considered as one of the HF limitations.^[63] As a result, the HF method does not take into account correlation energy (equation 2.12).

$$E_{correlation} = E_{exact} - E_{HF} \quad \dots (2.12)$$

2-1-2 Møller-Plesset Second Order Perturbation Theory (MP2)

As it was mentioned above, most post-HF approaches start with a HF wavefunction and try to improve it. One of these methods is Møller-Plesset (MP) perturbation theory which was introduced in 1934.^[64] It is a particular type of many-body perturbation theory (MBPT). MP theory adds perturbation corrections of consecutive orders to the HF wavefunction and energy. The HF energy is obtained with the *first-order* corrections (MP1). Improvements over HF are obtained with the *second-order* (MP2) corrections. *Third-order* (MP3) and *fourth-order* (MP4) correspond to adding the second and the third perturbation corrections to the HF energy, respectively.^[63] Some further details about MP perturbation theory are provided below.^[56,65]

The zeroth order (unperturbed) Hamiltonian is assumed to be the sum of the Fock operators (\hat{F}_i) for all n electrons:

$$\hat{H}_0 = \sum_{i=1}^n \hat{F}_i \quad \dots (2.13)$$

Also, zeroth order wavefunction (Ψ_0^0) is taken as the HF Slater determinant (see equation (2.3)). The Schrödinger equation in the zeroth order can be written as:

$$\hat{H}_0 \Psi_0^0 = E_0^0 \Psi_0^0 \quad \dots (2.14)$$

It is straightforward to show that the zeroth order MP energy is simply the sum of the HF orbital energies. Whereas the first-order correction to the energy can be obtained from the equation:

$$\hat{V} \Psi_0^0 = E_0^1 \Psi_0^0 \quad \dots (2.15)$$

where \hat{V} is the perturbation operator which accounts for the difference between the zeroth order Hamiltonian \hat{H}_0 and the many-electron Hamiltonian \hat{H} through the following equation:

$$\hat{H} = \hat{H}_0 + \lambda \hat{V} \quad \dots (2.16)$$

λ is a small “order” parameter. Solving equation (2.15) followed by adding together E_0^0 and E_0^1 gives the HF energy E_{HF} .

$$E_{MP1} = E_0^0 + E_0^1 = E_{HF} \quad \dots (2.17)$$

The energy correction for the second order perturbation can be calculated using the following expression:^[56]

$$E_0^2 = \sum_{i < j}^{Occ.} \sum_{a < b}^{Virt.} \frac{(\langle \Psi_i \Psi_j | \Psi_a \Psi_b \rangle - \langle \Psi_i \Psi_a | \Psi_j \Psi_b \rangle)^2}{\varepsilon_i + \varepsilon_j - \varepsilon_a - \varepsilon_b} \quad \dots (2.18)$$

$$E_{MP2} = \boxed{E_0^0 + E_0^1} + E_0^2 \quad \dots (2.19)$$

$$E_{MP2} = \boxed{E_{HF}} + E_0^2 \quad \dots (2.20)$$

Similarly, the third order (E_{MP3}) and fourth order (E_{MP4}) energies are given by the following equations:

$$E_{MP3} = \boxed{E_{HF}} + E_0^2 + E_0^3 \quad \dots (2.21)$$

$$E_{MP4} = \boxed{E_{HF}} + E_0^2 + E_0^3 + E_0^4 \quad \dots (2.22)$$

The MP2 method has been used in this project in order to evaluate the isotropic shieldings for several molecules.

2-1-3 Complete Active Space Self-Consistent Field (CASSCF) Method

The complete active space self-consistent field (CASSCF) method,^[66-69] which is also known as the full optimized reaction space (FORS)^[70] approach, is a type of multi-configurational self-consistent field (MCSCF) method. The MCSCF method produces reliable results for states of different spin multiplicities and for bond rearrangement processes during chemical reactions. CASSCF is a MCSCF method which includes all possible electron arrangements (configurations or configuration state functions, CSFs) for N electrons distributed among M orbitals, CASSCF(N,M).

The option of selecting active and inactive (or core) orbitals can be considered as the main advantage of this method. CASSCF uses the idea that the number of CSFs can be reduced by keeping a number of orbitals doubly-occupied in the inactive space and correlating the orbitals in the active space only. The selection of "active" and "inactive" orbitals is not always completely straightforward (see figure (2-1)). If the orbitals in these spaces are chosen incorrectly, in most cases the results are rendered unusable.

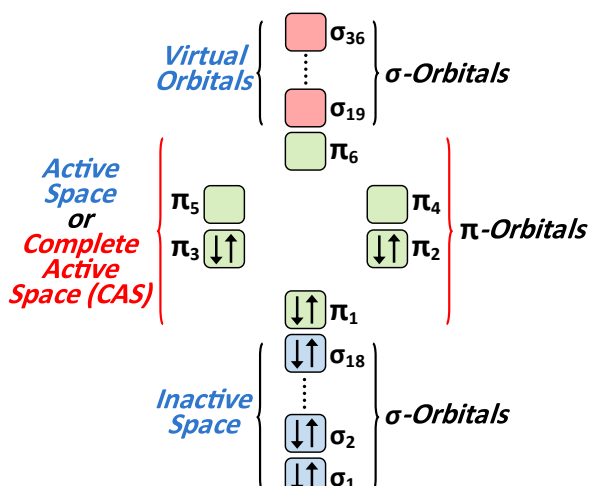


Figure 2-1: Illustration of the CASSCF active and inactive spaces in the case of a π -space CASSCF(6,6) wavefunction for benzene.

An example of a π -space CASSCF(6,6) wavefunction for benzene is shown in figure (2-1). Here, the 36 σ electrons populate 18 doubly-occupied σ orbitals which form the inactive space. These orbitals can be optimized or can be kept “frozen” during the CASSCF calculation. The 6 π electrons are included in the active space, and the starting guess for the 6 π orbitals in this space is provided by three occupied and three virtual π orbitals from a preliminary HF calculation. The CASSCF wavefunction can be written as a sum of CSFs:

$$\Psi_{\text{CASSCF}(N,M)} = \sum_{k=1}^L C_k \Psi_k \quad \dots (2.23)$$

The benzene ground state $\Psi_{\text{CASSCF}(6,6)}$ wavefunction includes 175 singlet CSFs, i.e., $L = 175$. In this project, the CASSCF method has been employed to calculate the isotropic shieldings for naphthalene and disulfur dinitride in their ground and low-lying excited states.

2-1-4 Density Functional Theory (DFT)

Density functional theory (DFT) was introduced by Hohenberg, Kohn and Sham during the 60s of the previous century.^[71] The idea is that the energy of a chemical system can be evaluated from its electron density, $\rho(r)$, rather than from its wavefunction.^[59,63] If the electron density is known, in addition to the ground state energy, one can also calculate all other ground state properties.^[72]

The first theorem of DFT, introduced by Hohenberg and Kohn, states that the

energy of the ground state in the Schrödinger equation is a unique functional of the electron density. [71] The electronic energy for a system which contains n electrons can be written according to DFT as:[59]

$$E = \underbrace{-\frac{1}{2} \sum_i \int \psi_i(r_1) \nabla_1^2 \psi_i(r_1) dr_1}_{\text{kinetic energy}} + \underbrace{\sum_A \int \frac{Z_A}{|r_1 - R_A|} \rho(r_1) dr_1}_{\text{potential energy}} + \underbrace{\frac{1}{2} \iint \frac{\rho(r_1)\rho(r_2)}{|r_1 - r_2|} dr_1 dr_2}_{\text{coulomb energy}} + \underbrace{E_{xc}}_{\text{exchange correlation energy}} \quad \dots (2.24)$$

The last term in the equation above, the exchange-correlation energy (E_{xc}), is an energy component which needs to be approximated.[59]

The second Hohenberg-Kohn theorem states that the functional that produces the ground state energy of the system gives the lowest energy if and only if the input density is the true ground state density.[71] Starting from this theorem, Kohn and Sham represented the total density as a sum of contributions from orbitals included in a Slater determinant and obtained one-electron equations for the orbitals, see equation (2.25), which can be solved using the SCF method:[59]

$$\left[\underbrace{-\frac{1}{2} \nabla_1^2 + \sum_A \frac{Z_A}{|r_1 - R_A|} + \int \frac{\rho(r_2)}{|r_1 - r_2|} dr_2 + V_{xc}}_{\text{effective one-electron Kohn-Sham operator}} \right] \psi_i(r_1) = \varepsilon_i \psi_i(r_1) \quad \dots (2.25)$$

V_{xc} denotes the exchange-correlation potential:

$$V_{xc}[\rho] = \frac{\delta E_{xc}[\rho]}{\delta \rho} \quad \dots (2.26)$$

In the local density approximation (LDA) $E_{xc}[\rho]$ is approximated as:

$$E_{xc}^{LDA}[\rho] = \int \rho(r) \varepsilon_{xc}(\rho) dr \quad \dots (2.27)$$

where ε_{xc} is the exchange-correlation energy per particle of a homogeneous electron gas of charge density ρ . Several other approximations for E_{xc} are in wide use. The most popular one is the Becke-3-parameters-Lee-Yang-Parr (B3LYP)[73-75], which can be expressed as:

$$E_{xc}^{B3LYP} = E_{xc}^{LDA} + a_0(E_x^{HF} - E_x^{LDA}) + a_x(E_x^{GGA} - E_x^{LDA}) + a_c(E_c^{GGA} - E_c^{LDA}) \quad \dots (2.28)$$

where the parameters are given by: $a_0 = 0.20$, $a_x = 0.72$, $a_c = 0.81$.

2-1-5 Some Notes on the Isotropic Shielding Calculations and Keywords Used with the Gaussian Program Package

- Going back to the notation used for isotropic shielding, σ_R , in equation (1.1) in the previous chapter, it is appropriate to provide some further details. The NMR isotropic shielding is defined as 1/3 of the trace of the shielding tensor σ_R for a nucleus R . The shielding tensor takes the form of a 3×3 matrix,

$$\sigma_R = \begin{pmatrix} \sigma_{xx} & \sigma_{xy} & \sigma_{xz} \\ \sigma_{yx} & \sigma_{yy} & \sigma_{yz} \\ \sigma_{zx} & \sigma_{zy} & \sigma_{zz} \end{pmatrix} \dots (2.29)$$

Then isotropic shielding can be calculated using the expression:

$$\sigma_{R,iso} = \frac{1}{3}(\sigma_{xx} + \sigma_{yy} + \sigma_{zz}) \dots (2.30)$$

- All NMR isotropic shielding calculations were carried out using gauge-including atomic orbitals (GIAOs). When the calculations were performed with the Gaussian^[76] package, the “CPHF(Separate)” keyword was included to improve accuracy in the presence of large numbers of ghost atoms.
- In practice, as it was briefly been mentioned in chapter one, and will be discussed in detail in the next section, each isotropic shielding calculation for a large grid of ghost atoms has to be performed in parts using multiple input files. This is due to limitations on the number of ghost atoms in a molecular system when carrying out NMR shielding calculations, imposed by the software packages. In a standard Gaussian input file, the maximum number of ghost atoms is around 100. If the maximum number is exceeded, the calculation fails with an error message saying: “*Maximum number of bonds=100 exceeded*” which is caused by the way in which the Gaussian input parser is trying to locate possible bonds involving the ghost atoms. There is an unobvious way of circumventing this type of processing discovered during the work on this project which allows the inclusion of more ghost atoms in a single calculation and reduces the number of separate calculations required for dealing with a large grid of ghost atoms. This can be achieved by using the keyword “Geom=connectivity” and specifying each ghost atom as an unbonded centre at the end of the input file. However, after several careful trials, it was found out that the number of ghost atoms in a single input file should not exceed 175 as otherwise the numerical errors in the shielding calculation become too large, even when use is made of the “CPHF(Separate)” keyword.

2-2 Procedure

Several types of grid of ghost atoms arranged within the space surrounding a molecule were used in this project. All grids were regular, with constant spacing between ghost atoms; the grids were one, two or three dimensional (1D, 2D or 3D), designed to span a region of space surrounding the whole molecule, or specific targeted parts of this space. The selection of the grid of ghost atoms is the first step in studying the variation of isotropic shielding around the molecule under investigation. Each ghost atom in a grid can be thought of as a local sensor which reports the isotropic shielding at its location.

This is followed by the preparation of multiple input files and running the corresponding calculations with either Gaussian^[76] or Dalton,^[77] depending on the required level of theory. After completing the calculations for all input files, the isotropic shielding values or shielding tensor components for all grid points (ghost atoms) are extracted from the output files. Then, these values are combined with the Cartesian coordinates of the ghost atoms. Depending on the presence of symmetry in the molecule and the grid of ghost atoms, the next step may include replication of the data for symmetry-unique grid points (to save time, in the presence of symmetry the calculations are carried out for symmetry-unique points only) through appropriate symmetry operations in order to obtain data for the whole grid. The last step includes processing and visualisation of the results. This approach has been found to work reliably and it provides a detailed picture of isotropic shielding variations within a molecular framework.

It is appropriate at this point to give detailed descriptions of all grids of ghost atoms which were used throughout this project.

2-2-1 One-Dimensional (1D) Grids

In order to trace the variations in isotropic shielding along a straight line in molecular space, a script was written and used for placing a set of 71 ghost atoms along a predefined vector. Applications of this script include:

- 1) Checking the variation in isotropic shielding along each symmetry unique bond of the molecules studied in this project. A linear grid of ghost atoms parallel to the bond was also set at a height of 1 Å above each of these bonds. These grids above bonds help examine the isotropic shielding behaviour close to π -bonding zones.

- 2) Checking the variation in isotropic shielding along a line perpendicular to the molecular plane, starting from the centre of each ring in a cyclic molecule and reaching a height of 2 Å. This allows monitoring changes in shielding with distance from the molecular plane in a similar manner to NICS(0), NICS(1) and NICS scans. The results can be used as a measure of aromaticity level in a cyclic planar molecule. However here, unlike NICS calculations, the signs of the isotropic shielding values are not reversed. The reason for this choice is to avoid confusion when comparing these shielding values to shielding results associated with other grids, such as the 2D and 3D shielding results discussed in subsequent chapters.

The arrangements of ghost atoms along and above bonds, and in a direction perpendicular to a ring centre are illustrated in figure (2-2), (a), (b) and (c), respectively. In all three cases, the first and the last ghost atoms are placed at the start and at the end of the respective line segment. When dealing with a bond, for example C1-C2, see (a) in figure (2-2), the coordinates of the first and the last ghost atoms coincide the coordinates of atoms C1 and C2, respectively. The remaining ghost atoms are spaced evenly between the end points along the C1-C2 bond. As the number of ghost atoms is kept constant (71), when dealing with bonds of different lengths, the spacings between consecutive ghost atoms will be different.

The results from these 1D analyses are represents as curves showing the variation of isotropic shielding with distance.

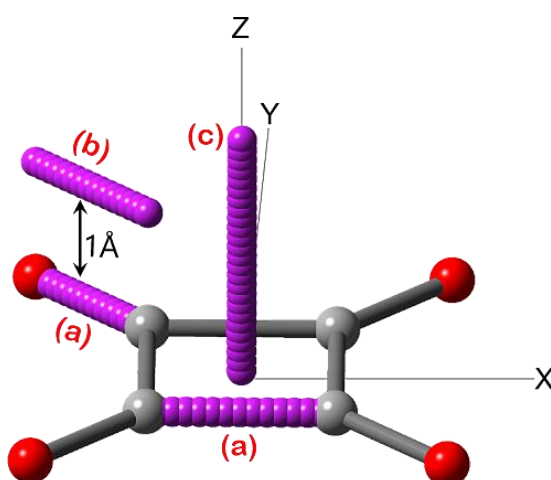


Figure 2-2: One-dimensional arrangements of ghost atoms used to examine variations in isotropic shielding. (a) along a bond; (b) at a height of 1 Å above a bond; (c) along a direction perpendicular to the ring centre up to a height of 2 Å.

2-2-2 Two-Dimensional (2D) Grids

The second type of ghost atom arrangement is a rectangular evenly spaced two-dimensional (2D) grid. The preferred spacing of ghost atoms in the 2D is 0.05 Å which provides the resolution required to see the fine detail of shielding changes in the vicinity of a nucleus and along a bond. The area of the 2D grid varies between molecules depending on molecular size or the feature targeted in the shielding analysis. The total number of the ghost atoms included in the 2D grid (N_{2D}) can be calculated from the following equation:

$$N_{2D} = \frac{\text{Grid_length (Å)} \times \text{Grid_width (Å)}}{(\text{Spacing (Å)})^2} \dots (2.31)$$

The N_{2D} ghost atoms are included in multiple input files each of which contains up to 175 ghost atoms per a gaussian input file, as it was explained earlier, or 25 per a Dalton input file.

The work on this project required use of several types of 2D grid.

2-2-2-1 Horizontal 2D Grids

This type of 2D grid either coincides with the molecular plane or is above and parallel to the molecular plane. It is often convenient to use a set of five 2D grids, the first of which is in the molecular plane, and the remaining four grids are at increasing heights above the molecular plane. Further details about the orientation and applications of these grids are given below.

- 1) The first 2D grid is in the molecular plane, see the height $z = 0.00$ in figure (2-3). This grid allows exploring magnetic shielding features around the nuclei, along sigma bonds, as well as inside and outside rings.
- 2) The other four grids are obtained by translating the first grid in a direction perpendicular to the molecular plane to heights of 0.25, 0.50, 0.75 and 1.00 Å (see figure 2-3). These additional grids help investigate vertical variations in isotropic shielding, moving from the molecular plane where the main contributions to shielding come from σ electrons, to a height of 1 Å where shielding effects are dominated by π electrons. In addition to the relative orientations of the five grids (see "Input"), Figure (2-3) shows examples of isotropic shielding contour plots obtained using such grids (see "Output").

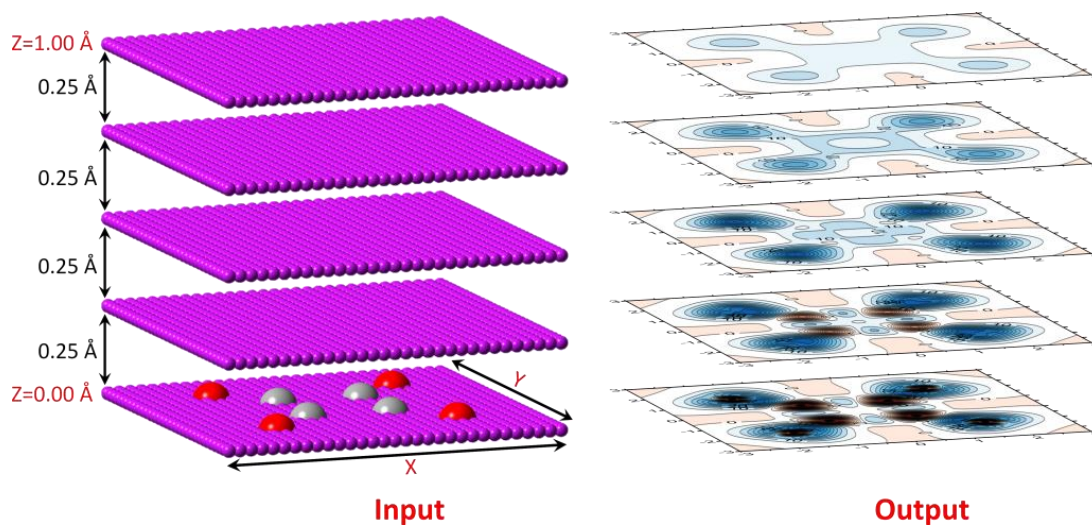


Figure 2-3: Five parallel 2D grids of ghost atoms (on the left), and corresponding isotropic shielding contour plots (on the right). The $z = 0.00 \text{ \AA}$ grid is in the molecular plane. The remaining grids are separated by 0.25 \AA and are placed at heights of 0.25 , 0.50 , 0.75 and 1 \AA above the molecular plane. Note that the vertical separation between grids is exaggerated.

2-2-2-2 Use of Horizontal 2D Grids to Investigate the Shielding Tensor Component Perpendicular to the Molecular Plane

As it was shown in equation (2.30), the total isotropic shielding is obtained by averaging the three diagonal components of the shielding tensor, σ_{xx} , σ_{yy} and σ_{zz} . During the work on this project, the component of the shielding tensor perpendicular to the molecular plane, σ_{zz} , was examined separately in order to find out the extent to which this component contributes to the isotropic shielding. In order to facilitate comparison between the values of σ_{zz} and σ_{iso} , σ_{zz} was scaled down to one third of its value; such scaled down σ_{zz} values are used throughout this thesis and denoted as $\sigma_{\text{iso}(zz)}$:

$$\sigma_{\text{iso}(zz)} = \frac{1}{3} \sigma_{zz} \dots (2.32)$$

σ_{zz} is used in two NICS indices, $\text{NICS}(0)_{zz}$ and $\text{NICS}(1)_{zz}$, and it is also related to ring currents. As $\text{NICS}(1)_{zz}$ is considered to be one of the most accurate NICS criteria, it is important to investigate the σ_{zz} variation in the π bonding region above the molecular plane. $\sigma_{\text{iso}(zz)}$ calculations for a grid of points identical to the fifth 2D grid at height of 1 \AA in figure (2-3) were carried out for all molecules studied in this project. The three contour plots in figure (2-4) illustrate the behaviour of the components of the isotropic shielding in the squarate dianion.

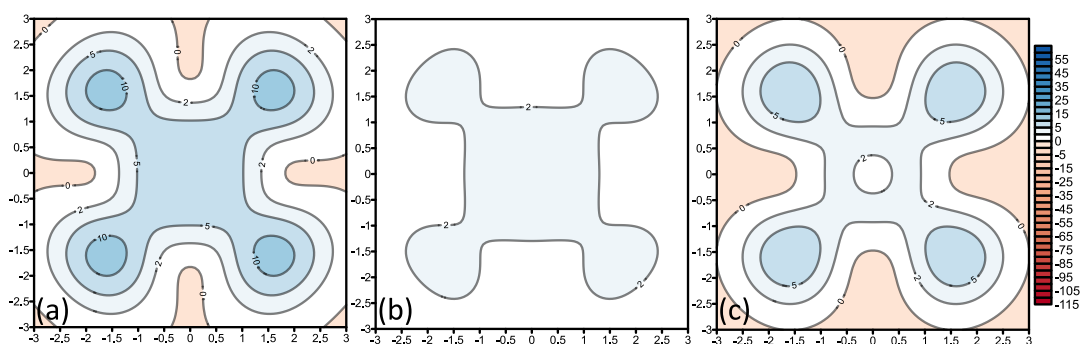


Figure 2-4: Shielding (in ppm) at 1 Å above the squarate dianion. (a) isotropic shieldings $\sigma_{iso} = 1/3(\sigma_{xx} + \sigma_{yy} + \sigma_{zz})$, (b) horizontal components as $1/3(\sigma_{xx} + \sigma_{yy})$, (c) vertical component as $1/3\sigma_{zz}$. Contour plots of types (a) and (c) were obtained for all molecules studied in this project; plots of type (b) are relatively uninformative and were not pursued.

2-2-2-3 Vertical 2D Grids

Vertical 2D grids are another type of ghost atom arrangement used in this project. These grids are perpendicular to the molecular plane (see figure (2-5)) and can pass either through atoms, or through bonds, see pictures (a) and (b), respectively, or in some cases through both atoms and bonds.

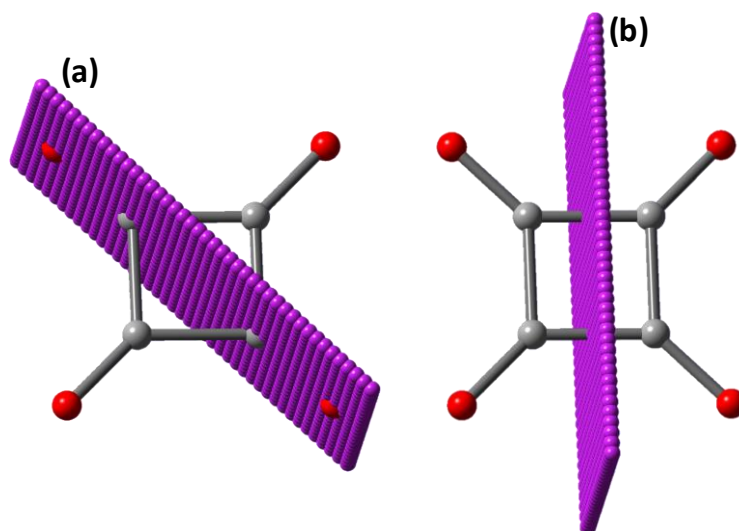


Figure 2-5: Vertical 2D grids of ghost atoms perpendicular to the molecular plane. Vertical 2D grids passing through atoms (a) and through bonds (b).

Vertical 2D grids can also be positioned along bonds. However, setting up a grid of this type is not straightforward and requires use of vector algebra. A specialised script has been written for generating different vertical 2D grids; details are explained in the next subsection.

2-2-2-4 A Specialised Script for Setting Up Vertical 2D Grids

This script uses vector algebra to generate a vertical 2D grid oriented along or perpendicularly to any chosen bond in a non-linear planar molecule.

The script offers two options for placing a 2D vertical grid. The first option places the vertical grid so that its plane is perpendicular to and passes through the midpoint of a selected bond. With the second option, the vertical grid is in a plane that contains the selected bond and the atoms involved in it. These two orientations are illustrated in figure (2-6), see (a) and (e), respectively.

The script has additional option related to the size and position of the vertical 2D grid, illustrated in figure (2-6). The 2D grid can be selected as a “full” grid centred on the bond (see (a) and (e)), a “top-half” grid (see (c) and (g)), a “side-half” grid (see (b) and (f)), or a “quarter” grid (see (d) and (h)). These options offering a range of choices for calculating all of a vertical 2D grid or just its symmetry unique areas (which can offer a time-saving opportunity if the environment of the selected bond is symmetric). After the calculation of shieldings for a partial vertical 2D grid, the results have to be replicated by symmetry in order to obtain a full 2D shielding map.

Finally, the script can also be used to generate grids in planes perpendicular to or passing through the line connecting any two selected points in the molecular plane.

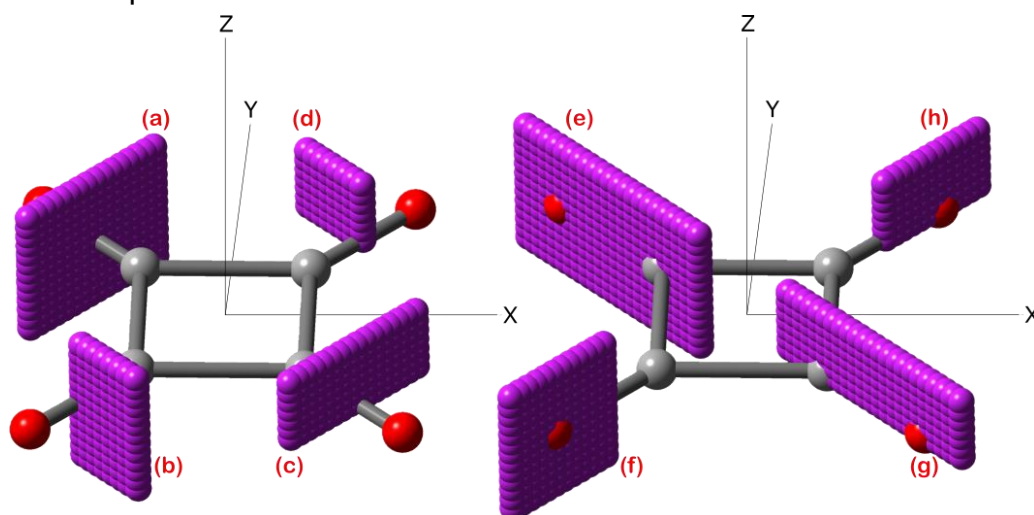


Figure 2-6: Vertical 2D grids of ghost atoms perpendicular to the midpoint of a bond (on the left), or along a bond (on the right) generated by a specialized script. In both cases, the script offers options to set a full 2D grid (a) and (e), a “side-half” grid (b) and (f), an “top-half” grid (c) and (g), or a “quarter” grid (d) and (h).

2-2-3 Three-Dimensional Grids

2-2-3-1 Standard Three-Dimensional Grids

Shielding calculations utilising 3D grids of ghost atoms offer the most detailed information about shielding variations in the space surrounding a molecule. The 3D grid can be viewed as an extension of a 2D grid in a third dimension. Whereas the points in a 2D grid occupy a rectangle, those in a 3D grid occupy a rectangular cuboid; the points remain evenly spaced. The visualisation of the results of shielding calculations on a 2D grid involves contour plots; for shielding calculations on a 3D grid use is made of shielding isosurfaces, or slices through these isosurfaces.

The consecutive steps associated with shielding calculations utilising 2D and 3D grids of ghost atoms are shown and explained in Figure (2-7).

As shielding calculations at a 3D grid of ghost atoms can be very time-consuming, it is important to use any molecular symmetry available and carry out calculations for the symmetry unique parts of the 3D grid only. As an example, figure (2-8) illustrates the symmetry unique section of the 3D grid for anthracene. This section corresponds to one-eighth of the total 3D grid. Shielding values for the whole 3D grid are obtained by replicating the results for the symmetry unique section seven times using appropriate reflections in symmetry planes. This symmetry replication is carried out using a script written for this purpose.

All isosurfaces reported in this project were generated using the VMD program^[78]. In all shielding calculations at 3D grids, the spacing between ghost atoms was chosen as 0.1 Å. The total number of ghost atoms in a regular 3D grid can be calculated using the equation:

$$N_{3D} = \frac{\text{Grid_length (Å)} \times \text{Grid_width (Å)} \times \text{Grid_height (Å)}}{(\text{Separation (Å)})^3} \dots (2.33)$$

As 3D isotropic shielding calculations remain very time-consuming, even when it is possible to use symmetry, a new technique has been developed to reduce the computational effort associated with these calculations.

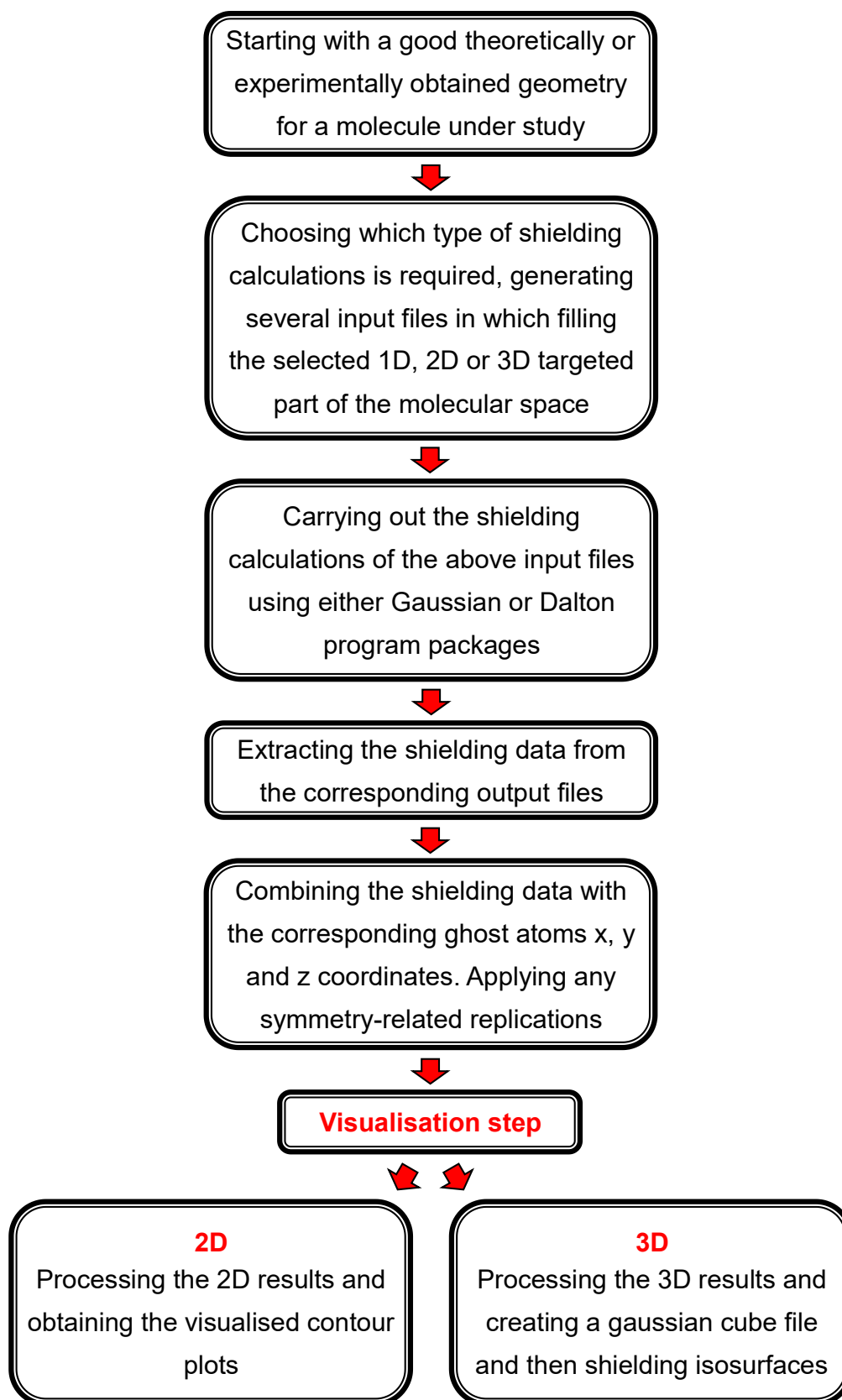


Figure 2-7: Flow chart for shielding calculations at 2D and 3D grids of ghost atoms.

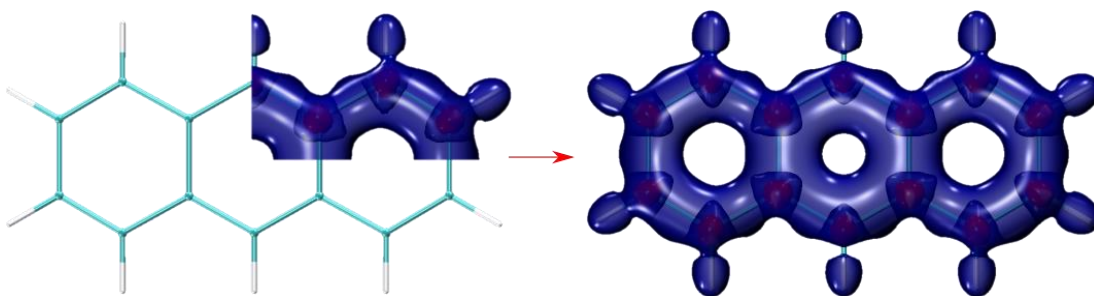


Figure 2-8: Shielding isosurfaces for the symmetry unique section of the 3D grid of ghost atoms and for the full 3D grid for anthracene. The results for the full 3D grid (on the right) are obtained by replicating the results for the symmetry-unique section (on the left) seven times using reflections in symmetry planes.

2-2-3-2 A New Computationally Efficient Technique for Performing 3D Shielding Calculations

Clearly, not all ghost atom positions within a 3D grid surrounding a molecule are equally important for the description of shielding behaviour throughout the region of space enclosed within the grid boundaries. Positions away from the nuclear framework can show very low levels of shielding or deshielding and excluding these positions from the shielding calculation has no detrimental effect on the final results.

Considering this observation, the volume of the 3D grid surrounding a molecule can be divided into two types of space, magnetically important space (MIS) and magnetically unimportant space (MUS). As a rule, the MIS surrounds the molecular framework and envelops atoms, bonds, σ and π bonding zones, lone pairs, etc. The isotropic shielding isosurfaces usually show the MIS as a cloud surrounding all these magnetically important regions around the molecule. When a ghost atom is within the MIS, shielding at this atom shows a high magnitude.

In contrast, the MUS contains ghost atoms which are far away from the molecular framework. The isotropic shielding magnitudes at MUS ghost atoms tend to be very low (close zero ppm). As a consequence, MUS ghost atoms can be ignored and omitted from a shielding calculation at a 3D grid.

However, the construction of shielding isosurfaces requires shielding values at MUS ghost atoms. Additionally, in order to identify MIS and MUS ghost atoms, it is required to have shielding values for both types of ghost atom.

During the work on the project, a new computational technique was developed which addresses this problem. The crucial point is to separate the MIS and MUS which can be done by running an initial 3D isotropic shielding calculation. This is followed by a higher level of 3D isotropic shielding calculation for the MIS ghost atoms only. Finally, MIS results from the higher-level calculation are combined with MUS results from the initial calculation to obtain data for the full 3D space. The details of the step by step implementation of this new technique are given below.

- 1) Experience suggest that for most molecules, the separation between the MIS and MUS is very much the same irrespective of the level of theory. This does not, however, mean that different levels of theory produce the same isotropic shielding values. Using this observation, the new technique starts by running a relatively fast shielding calculation for the whole grid volume using a lower level of theory. This calculation can be performed at the HF or some higher level of theory, with a small basis set.*
- 2) After the first step, the isotropic shielding values for all ghost atoms are extracted from the output files, combined with the corresponding x, y and z ghost atom coordinates and saved in a file.
- 3) The separation of shielding values and locations between the MIS and MUS can be achieved by applying adjustable numerical filtration to the data file from (2). Ghost atoms with shieldings within a preselected range of values are assigned to the MIS, and the remaining ghost atoms are assigned to the MUS. The coordinates of the MIS ghost atoms are saved in a '*MIS-coordinates-file*' (the corresponding shielding values are neglected). The coordinates and shieldings of all MUS ghost atoms are stored in a '*MUS-results-file*'.
- 4) The ghost atom positions from the '*MIS-coordinates-file*' are used to set up shielding calculations at a higher level of theory.
- 5) When these higher-level theory calculations have finished, the ghost atom shieldings are extracted, combined with coordinates as explained in (2), and stored in a '*MIS-results-file*'.
- 6) The two files, the '*MUS-results-file*', from step (3), and the '*MIS-results-file*',

* However, it is very important to check and choose a low level of theory which generally follows the shielding trends shown by the higher level of theory.

from step (5), are merged. The merged file includes isotropic shielding values and their coordinates for all points (ghost atoms) from the 3D grid. If any symmetry-related replication is required, it is done using the merged file. Then, the contents of the merged file are sorted with respect to ghost atom coordinates and saved for further processing in the next step.

- 7) The last step includes the creation of a Gaussian cube file which can be opened in VMD and used to obtain various shielding isosurfaces.

Each of these seven steps is carried out using a specialised script written during the work on the project. The new technique was applied to anthracene and phenanthrene as these molecules have large dimensions and require large 3D grids of ghost atoms. Figure (2-9) illustrates the reductions in the numbers of ghost atoms for the high-level theory shielding calculation achieved by applying the new technique to anthracene and phenanthrene.

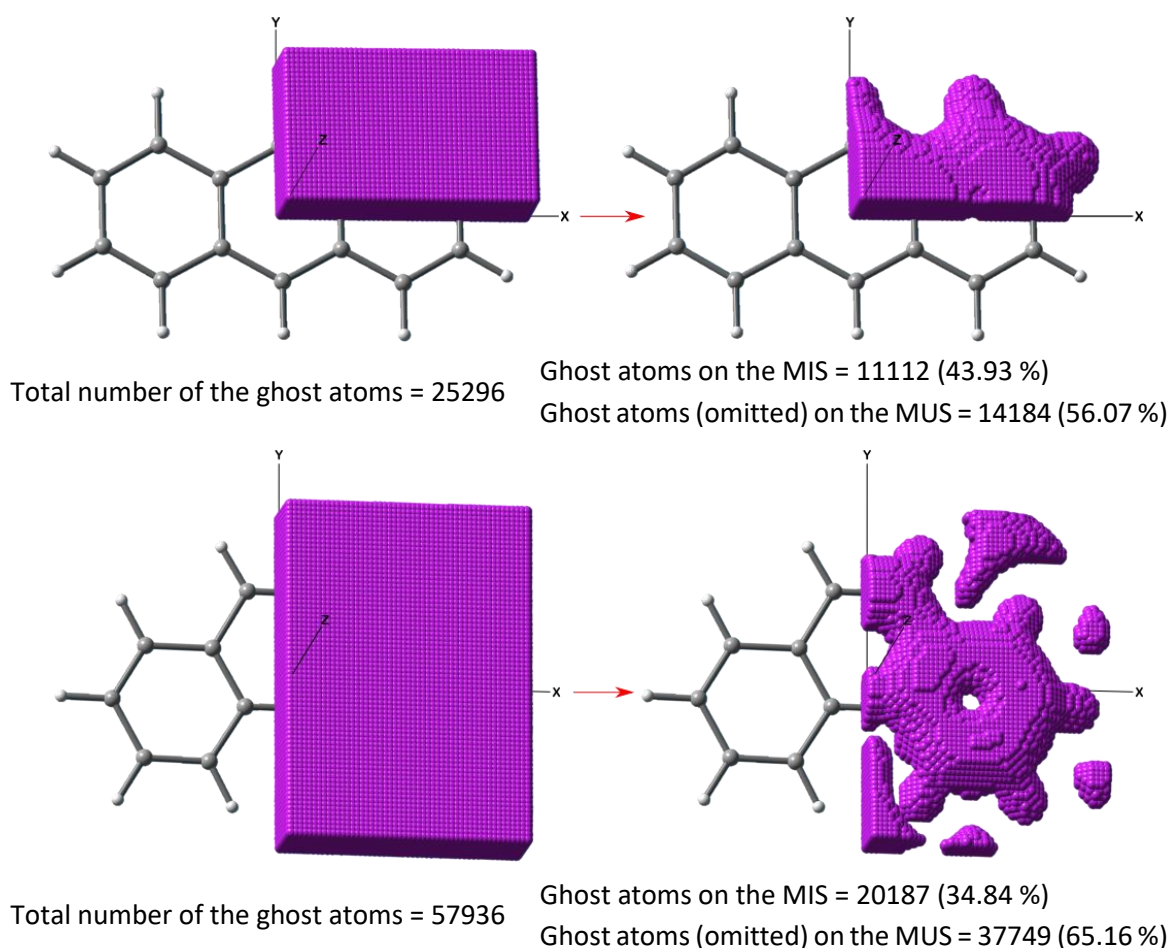


Figure 2-9: Difference in ghost atom numbers and their distributions for anthracene (top) and phenanthrene (bottom) when using the standard procedure (on the left), and the new technique (on the right).

For anthracene, more than a half of the total number of ghost atoms are included in the MUS. For phenanthrene, the MUS contains about two-thirds of the ghost atoms.

The numbers include in figure (2-9) suggest that computational time at the higher level of theory is reduced by the percentage of ghost atoms included in the MUS. This technique is particularly useful for large molecules, for which the 3D shielding calculations have very high computational demands. The computational savings are higher in molecules of lower symmetry, for which the numerical effort cannot be reduced by symmetry replication of the results for symmetry unique set of ghost atoms. The steps of the new technique are summarised in figure (2-10).

On a concluding note, it is very important to check the distribution of ghost in space before performing any 1D, 2D or 3D shielding calculations. This can be done conveniently by creating one input file including all ghost atoms which can then be examined with Gaussview.^[79]

2-2-3-3 Improving the Resolution of Isotropic Shielding Isosurfaces

Previous calculations of 3D shielding isosurfaces were performed using a separation of 0.05 Å between ghost atoms but, in this project, in order to reduce the computational effort associated with these calculations, the separation between ghost atoms was increased to 0.1 Å. The impact of this change is significant, as the number of ghost atoms in the 3D grid is decreased by a factor of 2 along each of its sides, or by $(1)^3 - (\frac{1}{2})^3 = 7/8$ overall. Clearly, the computational effort associated with a separation of 0.05 Å is about 7 times higher than that for a separation of 0.1 Å.

The comparison between isosurfaces obtained using grids with separations of 0.05 Å and 0.1 Å shows that the denser grids produce higher-resolution isosurfaces which are smoother and show additional detail in regions exhibiting large shielding changes, for example, around nuclei.

As shielding is a smooth function of position, an attempt was made to improve the resolution of isosurfaces generated using grids with a separation of 0.1 Å through interpolation.

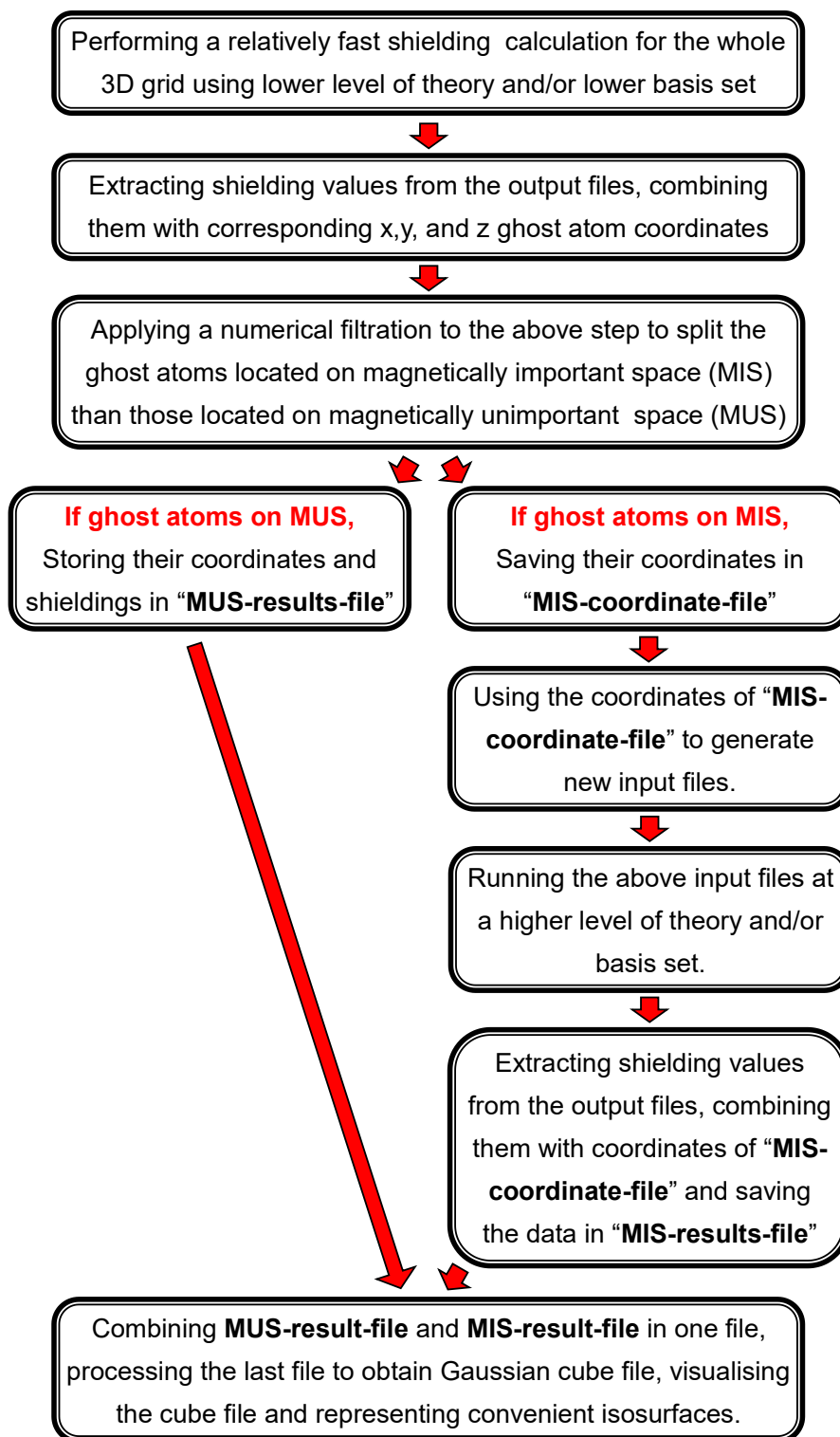


Figure 2-10: Flowchart illustrating the new technique for performing 3D isotropic shielding calculations. The technique depending on separating the grid of ghost atoms into two components, the magnetically important space (MIS) containing high shielding values, and the magnetically unimportant space (MUS) in which the shielding values are much lower.

For this purpose, the local polynomial method (LPM) can be applied to the shielding values for a grid with separation of 0.1 Å. The procedure creates a finer 3D grid which is populated with the original and interpolated shielding values. In this way, the density of the points from the 0.1 Å 3D grid can be increased to match that of the finer 0.05 Å grid, or even further. This process produces isosurfaces of visually higher resolution.

Figure (2-11) shows an example of a 0.1 Å isosurface (on the left) and an interpolated 0.025 Å isosurface (on the right). There is a noticeable improvement in resolution which shows that the interpolation procedure offers a reasonable alternative to the use of computationally-demanding finer grids.

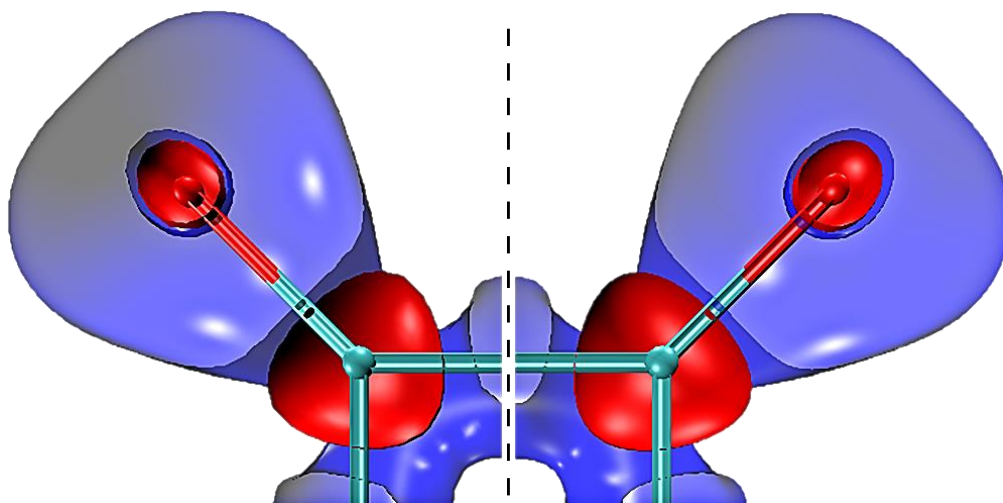


Figure 2-11: *Cross-sections of a standard and an interpolated isotropic shielding isosurfaces. The isosurface on the left corresponds to a calculation using a 3D grid with separation of 0.1 Å. The isosurface on the right is a mirror image of an interpolated version of the isosurface on the left obtained by means of the local polynomial treatment (LPN) with a separation of 0.025 Å.*

CHAPTER THREE

BORAZINE AND

BORAZANAPHTHALENE

3-1 Introduction

Borazine ($B_3N_3H_6$) and borazanaphthalene ($B_5N_5H_8$), two inorganic cyclic compounds, have received special attention. The importance of these B-N cyclic compounds comes from many points. Firstly, both are isoelectronic B-N analogues of benzene and naphthalene, respectively. Besides, the BN hexagonal ring is structurally important since its similarity to the building unit of white graphene or hexagonal boron nitride (h-BN) which can be prepared from borazine oligomers^[80]. Also, borazine is considered as a precursor of inorganic borazine-based polymers^[81,82] such as a polyborazylene polymer. This last is considered as a polymeric precursor of synthesising boron nitride coatings, which are used on ceramics and fibres.^[82]

Several synonym names for borazine are in circulation, such as triborine triamine; borazole or B-N inorganic benzene. Borazine was prepared in 1926 by Stock and Pohland^[83] as a volatile compound yielded from the thermal decomposition of the $B_2H_6(NH_3)_2$ at 200° . Structurally, electron diffraction indicated borazine as having D_{3h} symmetry with similar structure and bond lengths to the benzene.^[84] When gaseous borazine is thermally pyrolyzed at an elevated temperature between 340 and 440° , a mixture including volatile crystals of borazanaphthalene is yielded.^[85] Nonetheless, the irradiation of N-methylborazine^[86] or borazine^[87] at 1849 \AA photolytically produces impure borazanaphthalene. Also, borazanaphthalene can be isolated during the borazine dehydropolymerisation reactions.^[81] The formation of borazanaphthalene from borazine was suggested as a ring-opening reaction, followed by the formation of the final bicyclic structure.^[88]

The mass spectra for borazanaphthalene^[89] and for the decomposition process of liquid borazine into borazanaphthalene^[90] have been published. In addition, borazanaphthalene, as a sub-product oligomer during the polymerisation of borazine, has been identified.^[91]

Because of the similarity between these molecules and their cyclic hydrocarbon parents, a question can be raised. To what extent these analogues are similar in their bonding and aromatic content to their parent molecules? There have been several attempts to answer the question.

Scheiner et al.^[92] theoretically substituted the C-C bonds with B-N bonds in

benzene and naphthalene. They found, exchanging more C-C with B-N bonds causes lowering in molecular valency and increasing in hardness. A borazine Kekulé structure with three double bonds was assumed,^[93] which was attributed to donor-acceptor bonds formed by electron lone-pair donation from N to B.^[94] The contribution of the donor-acceptor double bond for boron was estimated through diamagnetic anisotropies as 24%.^[95]

The aromaticity of borazine has been argued about. Although borazine is geometrically similar to the benzene, Schleyer and Jiao^[14] found the magnetic susceptibility exaltations of both compounds as -1.7 and -13.4 (ppm cgs), respectively. Thus, they concluded that the aromaticity scaling is independent of the geometry criteria; and borazine is then not an aromatic compound and has its π -electrons localised on the nitrogens. Nevertheless, they^[30] obtained a similar conclusion by utilising NICS; some other magnetic criteria; and aromatic stabilization energies. Jemmis and Kiran^[96] investigated the borazine structural, magnetic, and energetic properties and decided that it is nonaromatic. Two studies, the first by Cooper et al.^[97] who found that the electron-density is localised on the N atoms which have two types of 2p orbitals, one is localised, whereas the other is delocalised over B atoms, thus, they considered the borazine as a non-aromatic. The second study was by Fowler and Steiner^[98] who employed the π -ring-current maps and observed that the current is localised around the N atoms. Both studies found negligible resonance energy. Fowler et al. ^[99] also noticed that, unlike the borons, the circulations of N-B and N-H σ -bonds are shifted toward the nitrogens, which form single-diamagnetic circulations around the nitrogens. Two opposite aromatic trends were observed by Islas et al.^[100]. The first, π -aromatic trend, due the total magnetic behaviour of borazine. While the second, non-aromatic trend, since electron localisation on nitrogens. They also noticed paratropic activity around the borons and at the ring centre.

According to valence bond theory, borazine is as aromatic as benzene depending on the delocalisation energy,^[101] or less aromatic than benzene because of its lower polarizability.^[102] Similar aromaticity level was stated in an *ab initio* study.^[103] Also, Jug^[104] identified borazine as moderately aromatic based on the 1.528 semiempirical N-B bond order. The N-B π -electron bond order is 0.45 according to π -electron molecular orbital calculations.^[95]

Homodesmotic reactions by Fink and Richards^[105] indicated that the reaction

energy ratio of benzene to borazine as 22.1 to 11.1 (kcal/mol). From estimated resonance energies, the aromaticity of benzene to borazine ratio was as 3:1.^[106] The same ratio was found using electron delocalisation^[107] and aromatic stabilisation energies^[30]. According to gas-phase methylation and protonation reactions^[108], borazine is aromatic and shares benzene behaviour in these reactions, but with lower reaction energies. In this context, borazine and borazanaphthalene follow addition reaction paths when they react with anhydrous hydrogen bromide or hydrogen chloride.^[109] Differently, the substitution reactions have been proved via the γ -radiolysis of gaseous borazine,^[110] in addition to the reaction of borazine with boron halides.^[111]

The impact of the electronegativity difference between N and B atoms on aromaticity has been reported. Generally, if the atoms of an inorganic benzene ring have the same electronegativity or show a small difference, the 6 π -electrons will be shared evenly.^[103] Increasing the difference causes an increase in bond polarity which decreases aromaticity^[105] as bonding becomes weaker.^[103] Another impact of electronegativity difference can be observed when comparing B-N compounds with their parent hydrocarbons. The B-N bonds have lower σ -content than C-C bonds, whereas less difference is found between C-C and B-N bonds in terms of π -contents.^[100]

The existence of charge transfer in borazine has been suggested. Armstrong and Clark^[112] and Hoffmann^[113] observed two different types of charge transfer. σ electron transfer from boron to nitrogen, and π electron transfer from nitrogen to boron. In both of transfers, nitrogen has a higher negative charge than boron^[113]. The B \rightarrow N charge-transfer and the delocalisation of the nitrogen lone-pair were schematically shown by Kalemos.^[114]

Relevantly, according to an *ab initio* study,^[115] the polarisation of σ -electrons is less than π -electrons, and the borons take π -electrons from the nitrogens.^[115] In addition to the relationship^[105] mentioned above between bond polarity electronegativity, increasing bond polarity leads to reducing the π -electron delocalisation.^[115] Therefore, the strong π -electron localisation on the nitrogen p-orbitals leaves boron with much less π -density. Thus, the B-H bond has higher localisation^[100] and more polarisation than the N-H bond.^[115]

This chapter aims to evaluate the aromaticity and chemical bonding of borazine and borazanaphthalene using their magnetic shieldings.

3-2 Borazine

The borazine geometry was first optimised under DFT using the B3LYP/cc-pVQZ method/basis set. The optimisation resulted in D_{3h} symmetry with no imaginary frequencies. The magnetic shielding evaluations were obtained using HF and MP2 level of theory with the 6-311++G(2d,2p) basis set. As can be seen from the isotropic shielding (σ_{iso}) data in table (3-1), there is a difference between the nuclear shielding values obtained from HF and MP2. Less shielding differences are observed between points vertically placed at 1 Å above nitrogen and boron nuclei. Remarkably, the ratio of the nuclear σ_{iso} of nitrogen to boron, according to MP2, is approximately 5:2. However, both nuclei are well shielded. A similar trend, but with much smaller σ_{iso} values, can be noticed for points at 1 Å. Also, σ_{iso} above the nitrogen nucleus is more than twice that above boron. In addition, according to both MP2 and HF, the absolute difference between nuclei of an N-B bond, $|\Delta\sigma_{\text{iso}(N-B)}^{0\text{Å}}|$, is significantly larger than the absolute difference between the points at 1 Å above the nuclei of the bond, $|\Delta\sigma_{\text{iso}(N-B)}^{1\text{Å}}|$.

Table 3-1: MP2/6-311++G(2d,2p) and HF/6-311++G(2d,2p) isotropic shielding data (σ_{iso}) (in ppm) for the borazine's nuclei and for points placed at 1 Å above the nuclei as well as the values of absolute shielding difference between N-B bond nuclei, $|\Delta\sigma_{\text{iso}(N-B)}^{0\text{Å}}|$, and between points 1 Å above them, $|\Delta\sigma_{\text{iso}(N-B)}^{1\text{Å}}|$.

	N		B		N-B	
	Nuclear σ_{iso} (ppm)	σ_{iso} 1Å above nuclei	Nuclear σ_{iso} (ppm)	σ_{iso} 1Å above nuclei	$ \Delta\sigma_{\text{iso}(N-B)}^{0\text{Å}} $	$ \Delta\sigma_{\text{iso}(N-B)}^{1\text{Å}} $
MP2	146.28	14.79	82.12	6.48	64.16	8.31
HF	151.10	14.91	84.72	5.61	66.38	9.30

Further insight into the magnetic shielding of borazine can be gained via five isotropic shielding maps shown in figure (3-1). Accordingly, the N-B bond regions, except near the borons in (a) and (b), have higher shieldings (the blue clouds) than more distant areas. Noticeably, the σ_{iso} clouds tend to be polarised towards the nitrogen atoms. Although the boron nuclei are shielded according to both table (3-1) and the circular-shielded areas at boron positions in figure (3-1 (a)), their shielded areas, however, are covered by a deshielded-spheres (the red zones) of less than 0.5 Å radius. Clearly, the deshielded-spheres disappear at heights 0.5 Å or more, see figure (3-1 (c-e)), and the shielding activities become predominant at these heights.

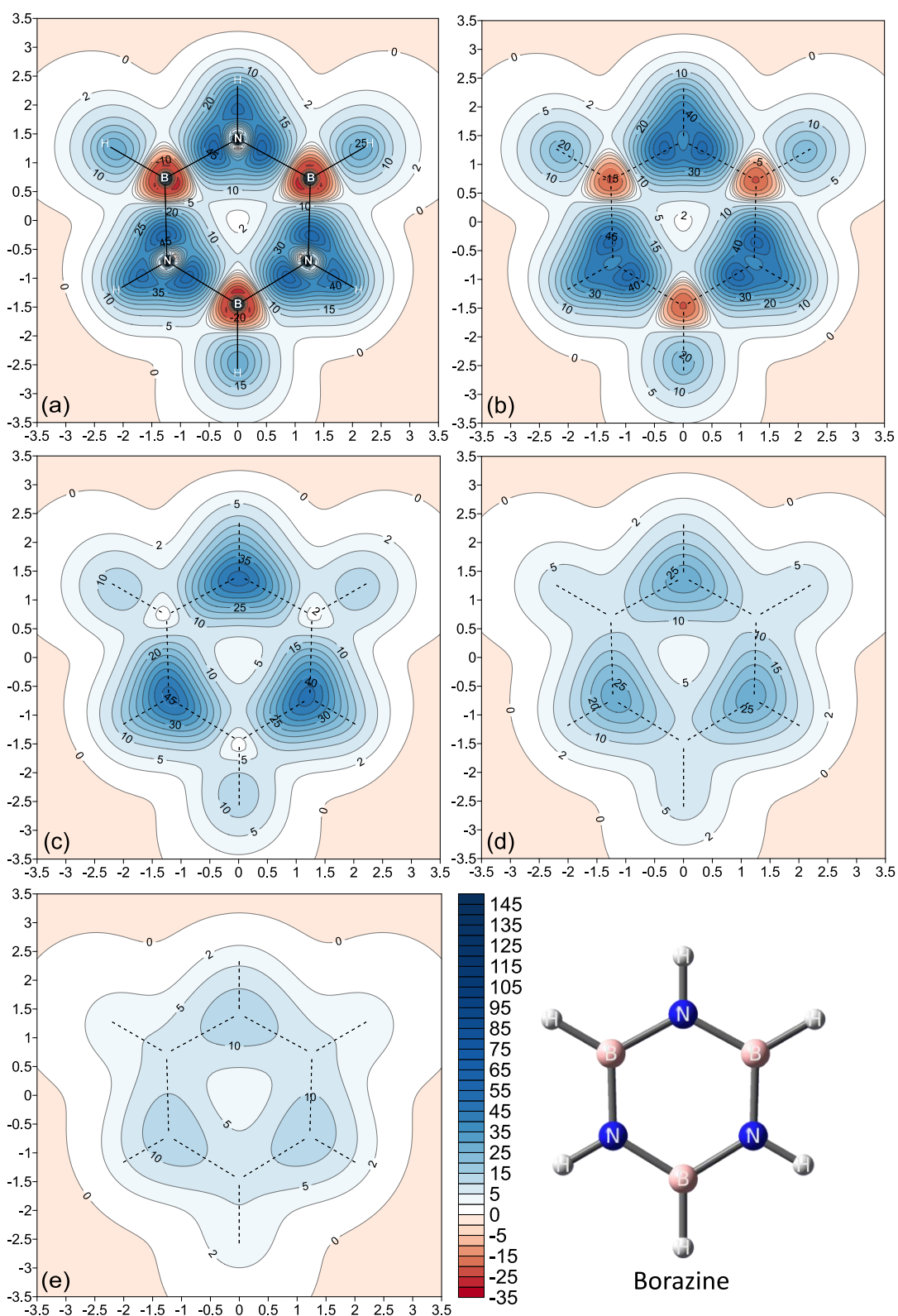


Figure 3-1: Five contour maps of the isotropic shieldings (σ_{iso}) (in ppm) obtained at the MP2/6-311++G(2d,2p) level of theory for borazine. (a-e): from grids parallelly placed at 0.00, 0.25, 0.50, 0.75 and 1.00 Å heights above the molecular plane, respectively.

Interestingly, the σ_{iso} at 1 Å height form a semi-triangular shielding cloud of 5 (ppm) above the borazine ring with three more-shielded islands of 10 (ppm) located vertically above the nitrogen atoms, see map (e) in figure (3-1). The semi-triangular cloud can be considered as a sign of existing π -electron delocalisation and ring current at 1 Å above the ring. The three islands represent the semi-localised lone pairs about the three nitrogens of borazine.

Comparing figure (1-7 (a)) with (3-1 (a)), one can notice likenesses/differences between benzene and borazine. Both have shielded ring centres but with remarkably lower shieldings for borazine. The deshielded sphere around boron is larger than that of carbon whereas the N-B bond shielding cloud shows a clear polarisation toward nitrogen. However, borazine possesses some degree of similarity to the overall shieldings of benzene.

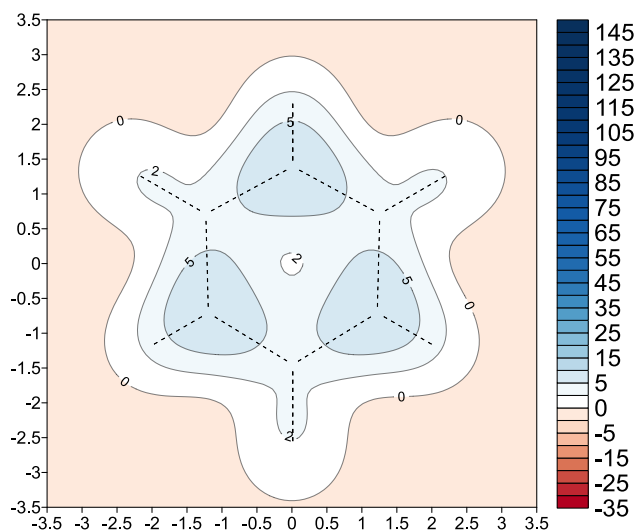


Figure 3-2: Contribution of the vertical-component of the isotropic shielding ($\sigma_{\text{iso}(zz)}$) (in ppm) to the total isotropic shielding σ_{iso} of the borazine, obtained at the MP2 6-311++G(2d,2p) level of theory for a grid placed parallelly at 1.00 Å above the molecular plane.

The vertical component of the isotropic shielding $\sigma_{\text{iso}(zz)}$ is shown in figure (3-2). $\sigma_{\text{iso}(zz)}$ illustrates the vertical magnetic activity formed by π -electron circulation and other π -contributions at 1 Å. We can compare the extents of shielding of the “partial” vertical component $\sigma_{\text{iso}(zz)}$ to the “total” isotropic magnetic shielding σ_{iso} in figures (3-2) and (3-1 (e)), respectively. Accordingly, $\sigma_{\text{iso}(zz)}$ turns not to be the main contributor to the isotropic shielding. From this observation, it can be said that borazine is moderately aromatic, due to its electron delocalisation. However, it is obvious that the shieldings of the lone pairs above the nitrogens indicate π -electron semi-localisation.

To obtain more shielding details of the borazine bonds, three 2D grids were placed perpendicularly to the borazine plane to probe the local σ_{iso} in different directions. The first grid diagonally bisects the borazine ring and includes H-N-ring-centre-B-H moieties, the second was set along an N-B bond, the last is right-angled and evenly bisects the N-B bond, see figures (3-3) (a) to (c) respectively. The shielding clouds of the N-B and N-H bonds, maps (a,b), seem to be localised around the nitrogen. Also, there is higher shielding around H rather than B atoms in the B-H bond. As mentioned earlier in the introduction to this chapter (section 3-1), the electronegativities of the N and B atoms are different, 3.04 and 2.04, respectively, which, as it has been suggested,^[108] cause lowering in π -electron delocalisation in borazine. This, in addition to the actions of the π -electron localisation and the lone pairs, induces the shieldings localisation about the nitrogens. However, the shielding cloud tends to be symmetric about the midpoint of the N-B bond with maximum shielding of around 35 (ppm), map (c).

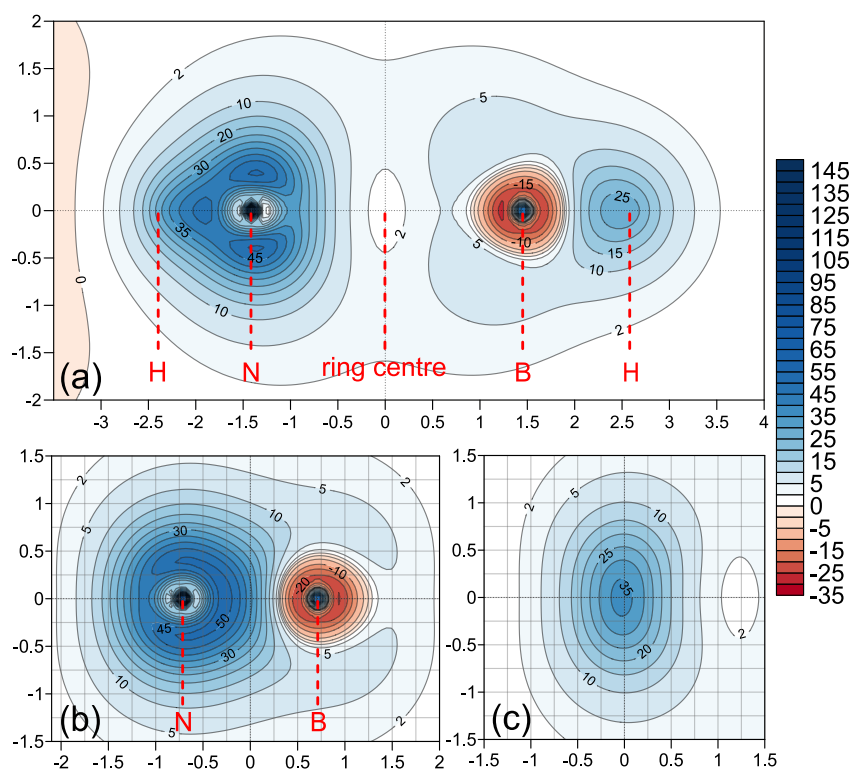


Figure 3-3: MP2/6-311++G(2d,2p) isotropic shielding vertical cross-sections set (a) perpendicular to the borazine H-N-ring-centre-B-H diagonal, (b) along the N-B bond and including the N and B nuclei, (c) passing through the N-B midpoint. Note that the right side of (c) is directed towards the ring centre, and the (0,0) (X,Y) corresponds to the N-B bond midpoint.

There are other observable details in the figure (3-3). Besides the σ_{iso} cloud around the nitrogen being larger around boron, there are two high-shielded spots above and below the nitrogen, map (a), which represent the partially localised lone pairs, see also figure (3-1 (c)). The extended cloud above and below the ring centre in figure (3-3 (a)) can be considered as a sign of the π -electron delocalisation in the π -region. There are two reasons making the shielding at the ring centre lower than nearby shieldings. The first is that the ring centre is located far from the π -region of delocalisation. The second is due to the in-plane σ -bonding contributions which lower the shielding of the ring centre. As a result, an egg-shaped less shielded core (LSC) is formed at the ring centre. The LSC can be seen as circular area centred in the ring in figure (3-1 (a,b)) or as an oval cross-section in figure (3-3 (a,c)).

Figures (3-4) and (3-5) confirm the above observations of LSC and the shieldings of the delocalised π -electron above the ring centre as well as the shieldings of the N-B bond. The fully positive shielding curve in figure (3-4) shows that the shielding value at the ring centre is 1.3 (ppm) which gradually increases to reach the maximum of 2.7 (ppm) at 0.94 Å above the centre. The initial value is located at the centre of LSC, whereas the maximum is on the extended shielding cloud.

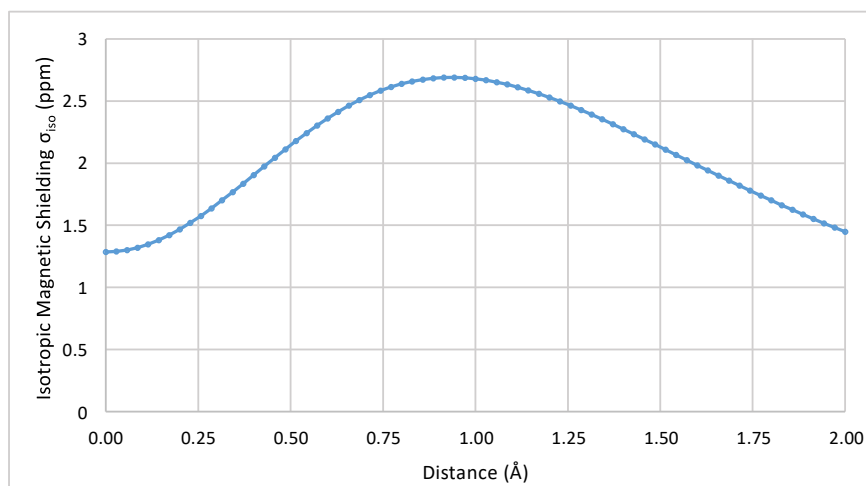


Figure 3-4: Variation in the MP2 6-311++G(2d,2p) isotropic shieldings σ_{iso} (in ppm) of the borazine ring obtained from 71 ghost-atom set placed perpendicularly from the ring centre to 2 Å height above it.

Figure (3-5 (a)) shows a high variation in σ_{iso} along the N-B bond since the shielding cloud, as mentioned earlier, is polarised towards nitrogen. It is useful

here to give the name AML (active middle bonding line) to the middle segment of a bond which can magnetically be recognised by eliminating the highly shielded/deshielded terminal segments (nuclei).

Noticeably, AML and the maximum shielding shift from the N-B bond midpoint towards the nitrogen, figure (3-5 (a)). Also, the deshielded-sphere surrounding boron is shown as deshielded points near the boron end.

On the other hand, the parallel line above the N-B bond is fully shielded with a higher shielding above nitrogen in comparison to boron, see figure (3-5 (b)). This agrees with the finding mentioned earlier about more shielding activity above nitrogen due to partial π -electron localisation. The shieldings of the remaining parts of the curve indicate partial π -electron delocalisation. Also, the variation in shielding between the two end points of the curve occurs gradually without abrupt changes.

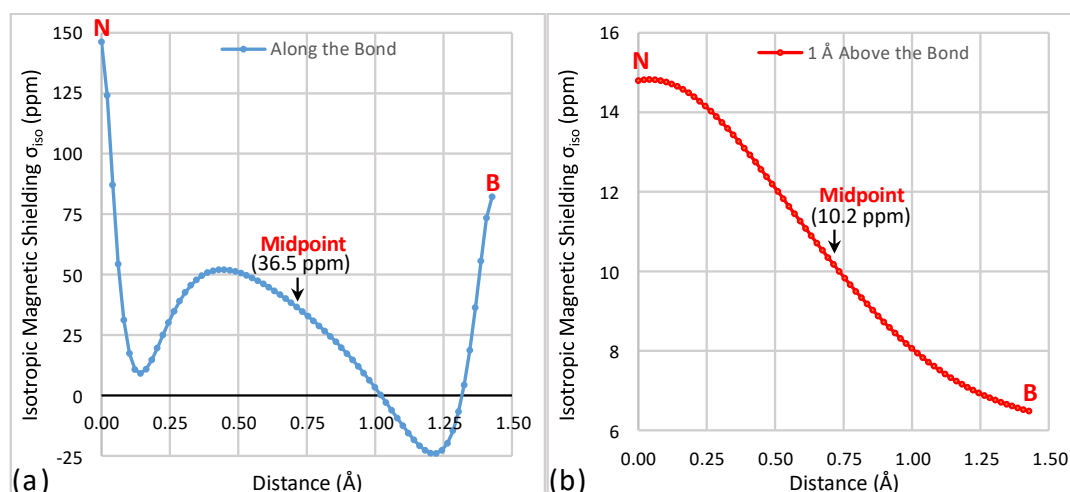


Figure 3-5: Variation in MP2/6-311++G(2d,2p) isotropic shielding (σ_{iso}) (in ppm) along the N-B bond in borazine obtained from 71 ghost-atom sets: (a) positioned along the N-B bond, and (b) placed 1 Å parallelly above the N-B bond.

To present the overall 3D isotropic shielding behaviour, two pairs of shielding isosurfaces were employed (figure (3-6)). The first visualises the +16/-16 (ppm) shielding values and is aimed to show the magnetic shielding similarity between borazine and strongly aromatic molecules such as benzene. These two values have also been used to visualise the 3D shielding isosurfaces of some aromatic^[32] and conjugated^[50] molecules.

The blue isosurface, which represents the value of +16 (ppm), indicates that the borazine atoms, except the borons, share the magnetic profile of aromatic and strongly bonded molecules. The red isosurface of -16 (ppm) shows that the borons share the deshielding behaviour observed in other aromatic molecules. The shielding behaviour in the blue isosurface indicates a clear semi-localisation of the shielding clouds of the lone pairs and π -electrons about the nitrogens which are more pronounced than the delocalisation of the π -electrons around the ring.

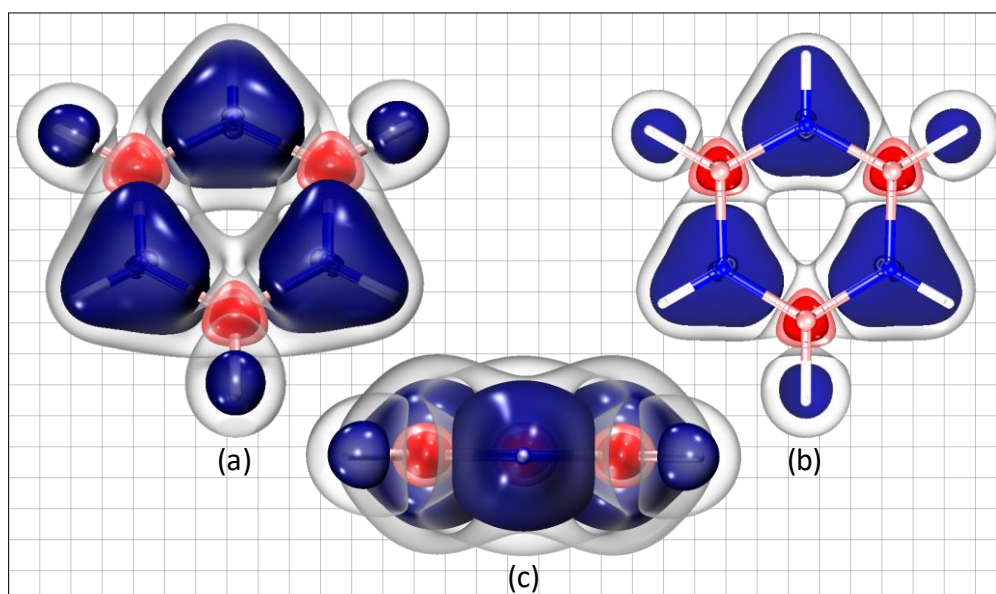


Figure 3-6: *Isotropic shielding isosurfaces for borazine obtained from MP2/6-311++G(2d,2p) calculations. (a) Front view; (b) in-plane cross-section; and top view. The shielding value/colour of the isosurfaces can be defined as: +16 / blue; -16 / red; +7 / transparent; and -5 / transparent red.*

The second pair of shielding values +7/-5 (ppm) were chosen because of their capability to represent the most important magnetic shielding/deshielding details of borazine in a similar manner as +16/-16 do for aromatic molecules. For example, unlike the +16 (ppm) blue isosurface, the +7 (ppm) transparent isosurface can show the cloud of π -electron delocalisation around borazine. Also, comparing these isosurfaces, in terms of their values, can give an approximate aromaticity ratio of borazine to benzene as (7:16). Thus, borazine has a moderate level of aromaticity.

3-3 Borazanaphthalene

Like borazine, the C_{2v} borazanaphthalene geometry was obtained from a DFT B3LYP/cc-pVQZ optimisation with no imaginary frequencies.

The general nuclear shielding trend shows higher responses for the nitrogens than the borons, see table (3-2). The N1 atom has the highest shielding value, whereas the lowest is observed for B4, see figure (3-7) for atom labelling. Interestingly, the bond at the fused location between the rings, N10-B9, connects the least shielded nitrogen, N10, and the most shielded boron, B9. Remarkably, the minimum $|\Delta\sigma_{iso(N-B)}^{0\text{Å}}|$ and the maximum $|\Delta\sigma_{iso(N-B)}^{1\text{Å}}|$ absolute shielding differences can be seen for this bond. The N1-B2 bond shows a trend different from the N10-B9 bond in terms of the shielding difference parameters values, see table (3-3). The uniqueness of N10 and B9 comes from the fact that each of these atoms is linked to three atoms of the other type. Thus, possible effects of charge transfer or electronegativity difference on these two atoms are higher than on other atoms in borazanaphthalene.

Table 3-2: MP2/6-311++G(2d,2p) and HF/6-311++G(2d,2p) isotropic shielding data (σ_{iso}) (in ppm) for the symmetry unique nitrogen and boron nuclei in borazanaphthalene and for points placed 1 Å above the nuclei.

	N		B	
	Nuclear σ_{iso} (ppm)	σ_{iso} 1Å above nuclei	Nuclear σ_{iso} (ppm)	σ_{iso} 1Å above nuclei
MP2	164.99 (N1)	13.82	81.32 (B2)	6.12
	147.13 (N3)	14.52	77.03 (B4)	5.85
	124.40 (N10)	16.29	85.24 (B9)	5.16
HF	168.72 (N1)	14.09	84.16 (B2)	5.36
	151.30 (N3)	14.72	80.67 (B4)	5.15
	133.66 (N10)	16.56	89.03 (B9)	4.42

Table 3-3: Borazanaphthalene MP2/6-311++G(2d,2p) absolute shielding difference (in ppm) between the nuclei of the symmetry unique N-B bonds, $|\Delta\sigma_{iso(N-B)}^{0\text{Å}}|$, and between points at 1 Å above the nuclei, $|\Delta\sigma_{iso(N-B)}^{1\text{Å}}|$.

N-B Bond	$ \Delta\sigma_{iso(N-B)}^{0\text{Å}} $ (ppm)	$ \Delta\sigma_{iso(N-B)}^{1\text{Å}} $ (ppm)	N-B Bond	$ \Delta\sigma_{iso(N-B)}^{0\text{Å}} $ (ppm)	$ \Delta\sigma_{iso(N-B)}^{1\text{Å}} $ (ppm)
N1-B2	83.67	7.70	N3-B4	70.10	8.67
N1-B9	79.75	8.66	N10-B4	47.37	10.44
N3-B2	65.81	8.40	N10-B9	39.16	11.13

Despite the difference in shielding between results obtained from HF and MP2, both methods share similar shielding patterns, see table (3-2).

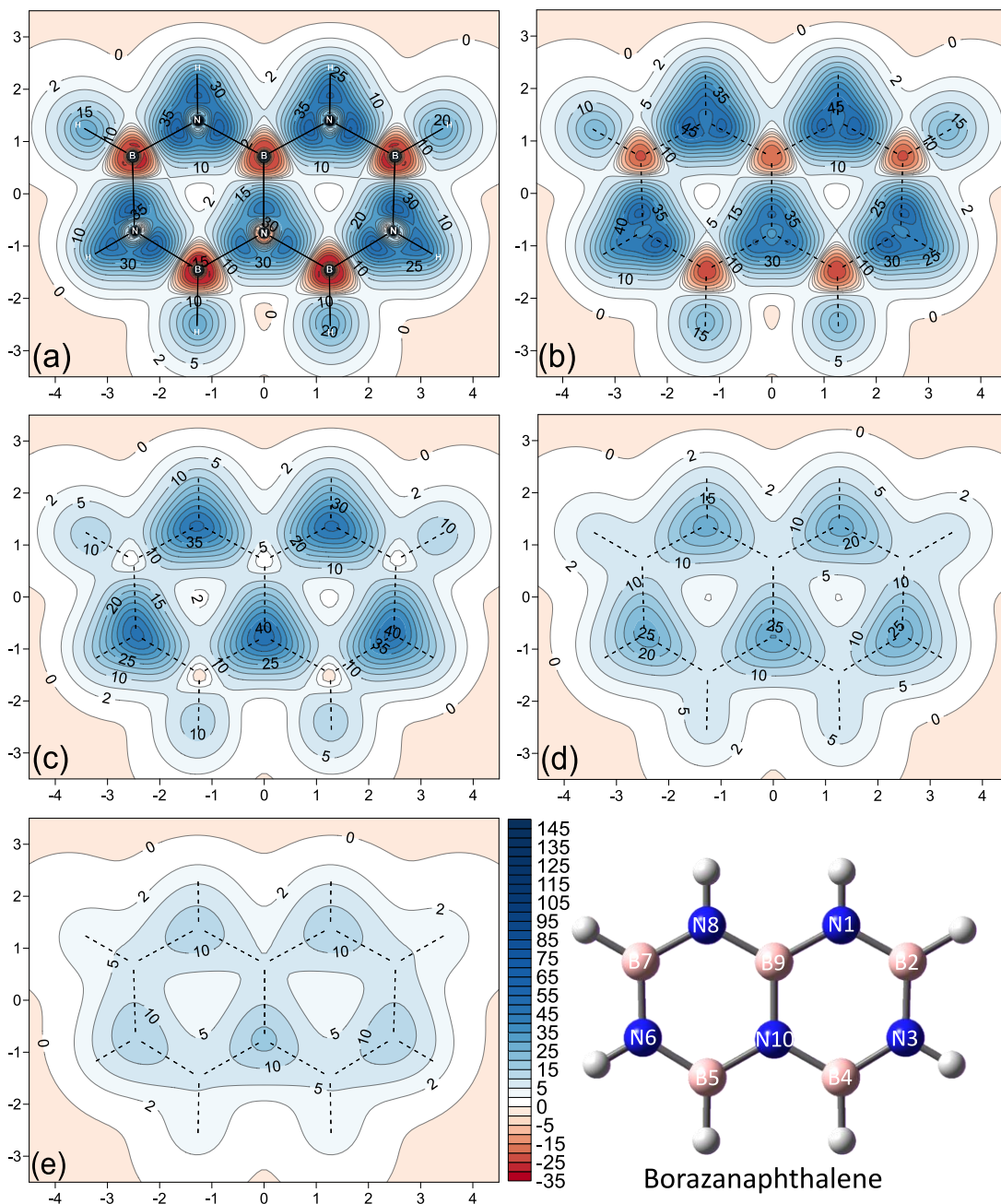


Figure 3-7: Five contour maps of the isotropic shieldings (σ_{iso}) (in ppm) obtained at the MP2/6-311++G(2d,2p) level of theory for borazanaphthalene. (a-e): from grids parallelly placed at 0.00, 0.25, 0.50, 0.75 and 1.00 Å heights above the molecular plane, respectively.

Several shielding observations can be made using figure (3-7). The 2D isotropic shieldings in the molecular plane, map (a), shows that each of the

nitrogen atom is centred a triangular well-shielded cloud which contains the shielding clouds of the N-B and N-H bonds AMBL. Also, the extended cloud of π -electron delocalisation, which contains five higher-shielded clouds (islands) of semi-localised nitrogen lone pairs, is obvious at 1 Å, see figures (3-7 (e)) and (3-8). Deshieldings activities can only be seen at lower heights, between 0.00 to 0.50 Å mainly around borons, see figures (3-7 (a) and (b)). Although the nuclear shielding data in the table (3-2) show the borons as shielded, each of the borons, in fact, has two different shielding features. The first is a small shielded-sphere, see figures (3-7 (a)) and (3-9). The second feature is a deshielded-sphere including a core of the first feature, see figures (3-7 (a,b)) and (3-9).

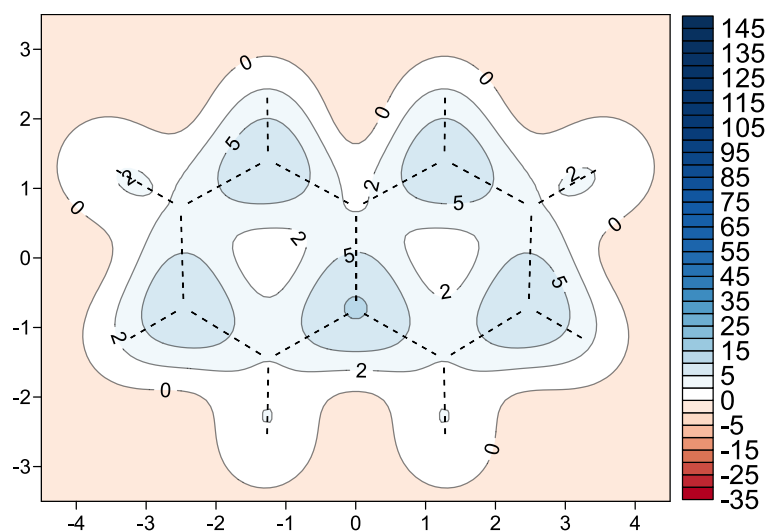


Figure 3-8: Contribution of the vertical-component of the isotropic shielding ($\sigma_{izo(zz)}$) (in ppm) in the total isotropic shielding σ_{izo} of borazanaphthalene, obtained at the MP2/6-311++G(2d,2p) level of theory for a grid placed parallelly at 1.00 Å above the molecular plane.

Evaluating the shielding behaviour at the ring centre showed the presence of LSC, see figure (3-7) and the right-sides of the maps in figure (3-10). The LSC can also numerically be understood via the curve in figure (3-11) which shows that the shielding at the ring centre is 0.67 (ppm), reaching a maximum of 2.06 (ppm) at 1 Å above the ring centre. In comparison, the maximum shielding value is 2.7 (ppm) for borazine and found at 0.94 Å, see figure (3-4). Thus, the π -electron delocalisation above the rings is lower in the case of borazanaphthalene, and consequently, aromaticity is relatively higher in borazine.

The shielding behaviour of the N-B bonds is shown in figures (3-(9,10,12)). As in borazine, all the maps in figure (3-9) show much higher shielding activities around nitrogen than around boron except for a few low differences in maps (e) and (f). Low deshielding activity can be seen at spaces close to the centre of N10 in these two maps, see also figure (3-7 (a)). These deshieldings partially split the shielding cloud into two islands above and below the N10 nucleus. Factors such as the electronegativity difference cause these variations and induce the localisation of lone pairs. These observations show that borazanaphthalene is lower in aromaticity than naphthalene.

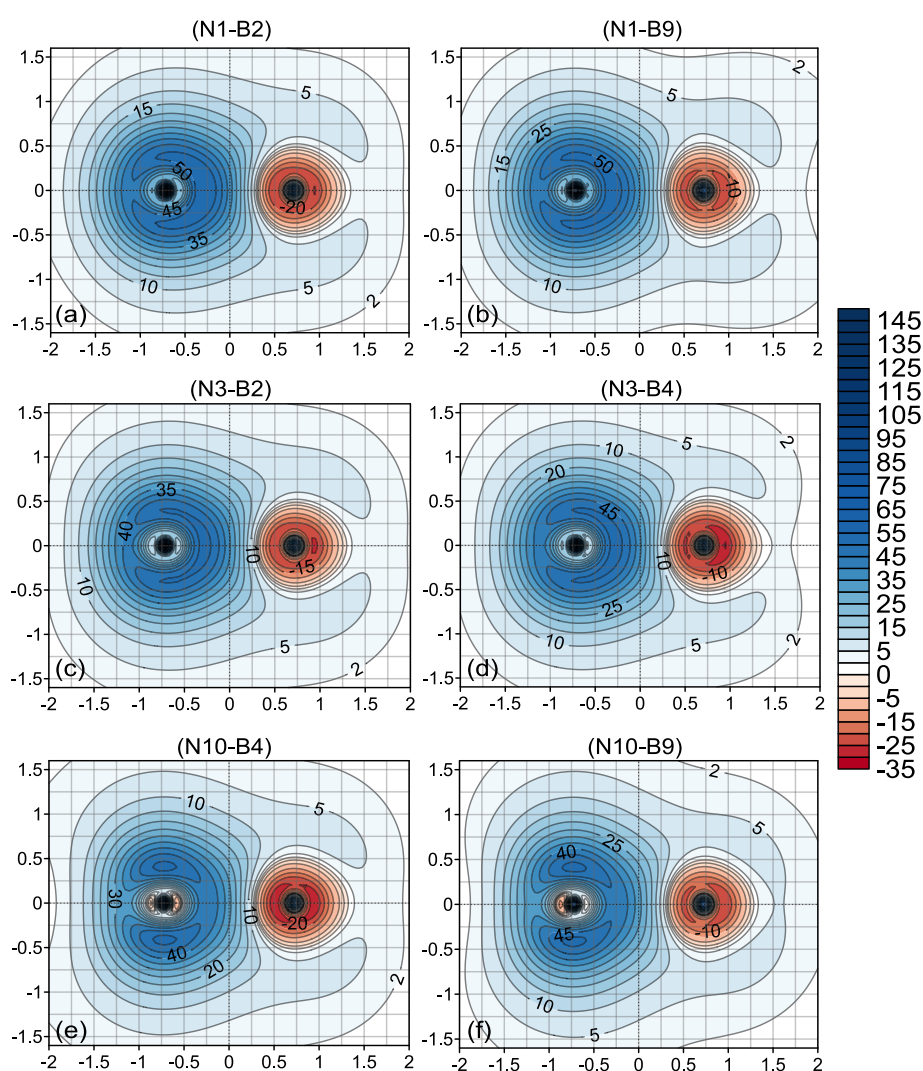


Figure 3-9: MP2/6-311++G(2d,2p) isotropic shielding contour maps (in ppm) for the symmetrically unique N-B bonds of borazanaphthalene. For each map, the left and right well-shielded dots respectively represent the N and B nuclei. Also, the midpoint of each bond corresponds to the (0,0) XY coordinates in these maps.

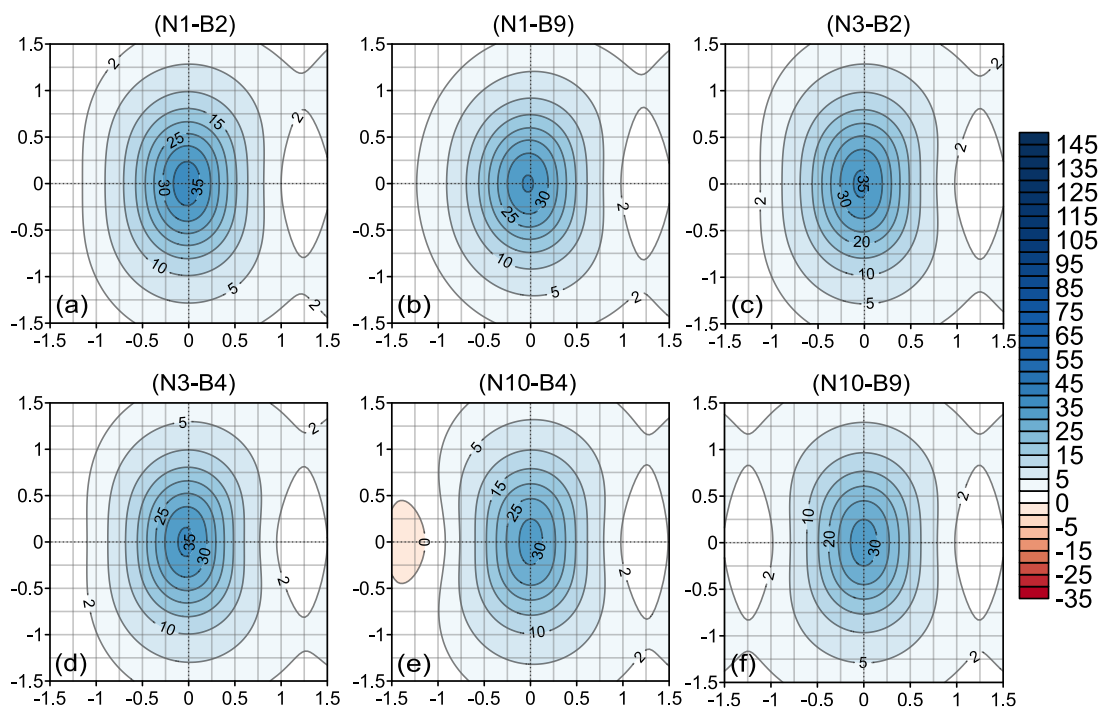


Figure 3-10: MP2/6-311++G(2d,2p) isotropic shielding contour maps (in ppm) of borazanaphthalene obtained by utilising the 2D ghost-atoms grids located perpendicular to and crossing the midpoints of the N-B bonds. For all maps, except (f) which is located between rings, the right side is directed towards the inner side of the ring, which includes the ring centre. Also, the N-B bond in each map is located exactly at the (0,0) X,Y coordinates.

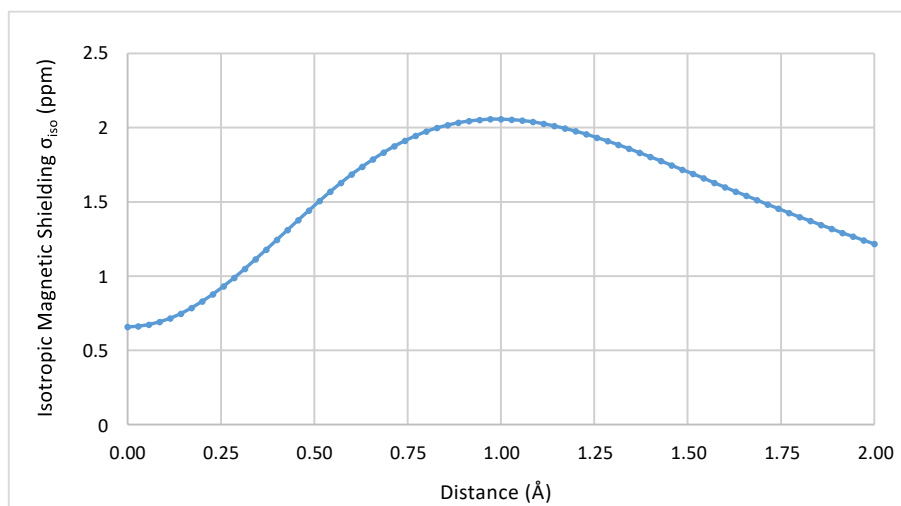


Figure 3-11: Variation in MP2/6-311++G(2d,2p) isotropic shieldings σ_{iso} (in ppm) of borazanaphthalene rings obtained from 71 ghost-atom sets placed perpendicularly from the ring centre to 2 Å height above it.

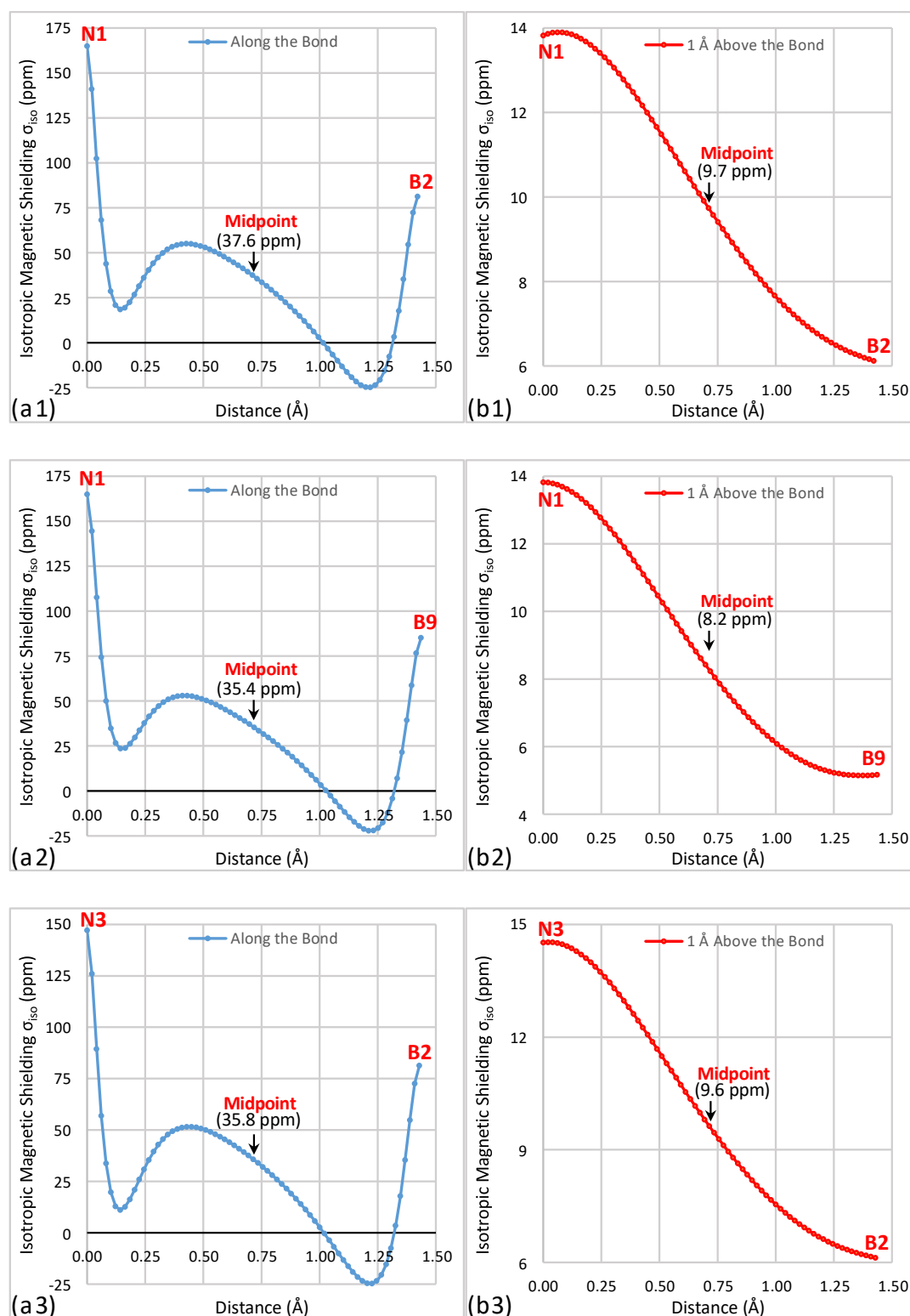


Figure 3-12: Variation in MP2/6-311++G(2d,2p) isotropic shielding (σ_{iso}) (in ppm) of the N-B symmetry unique bonds of borazanaphthalene obtained from 71 ghost-atom sets: (a) positioned along N-B bonds, and (b) positioned 1 Å parallelly above the bonds.

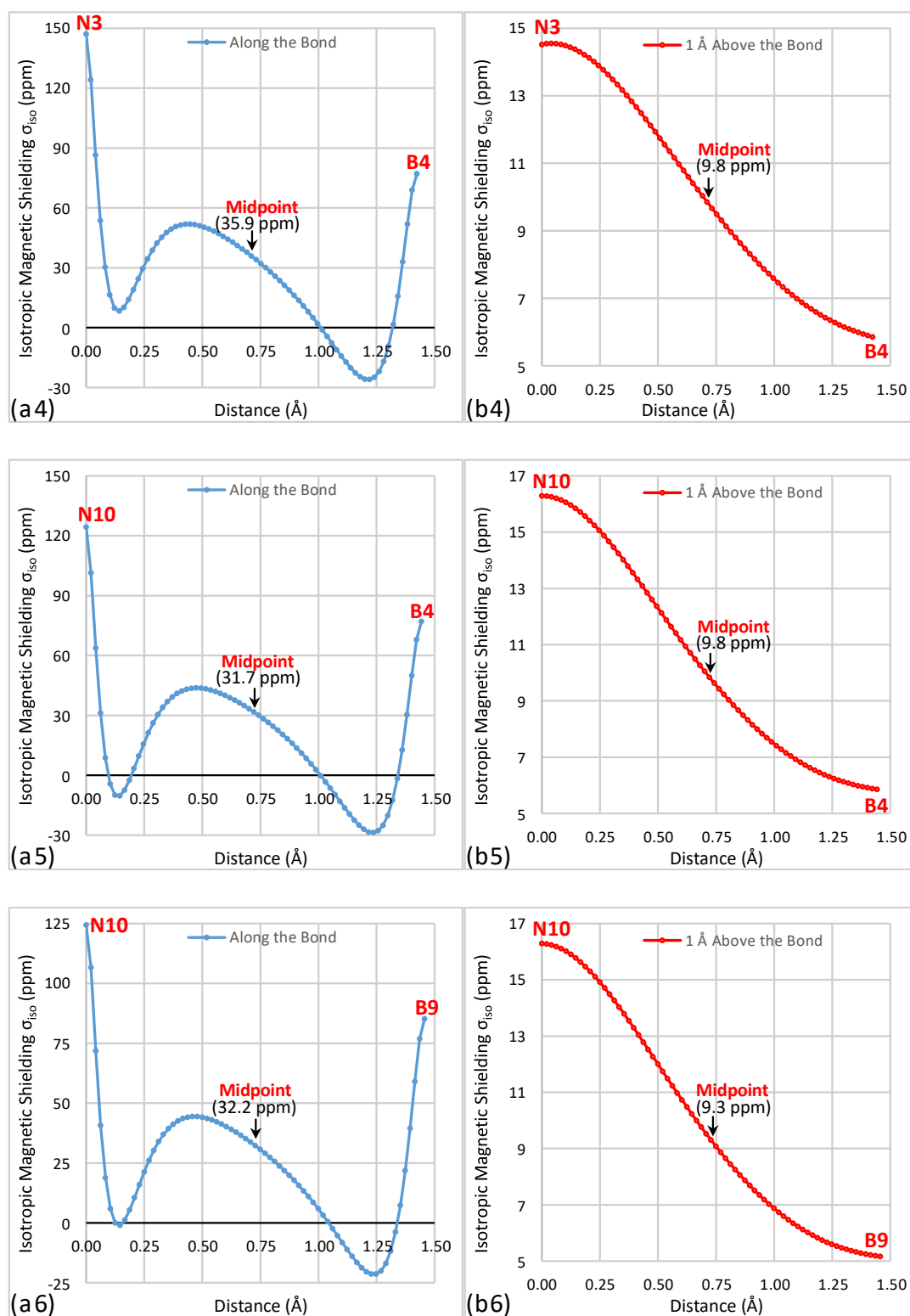


Figure 3-12: Continued.

In addition to the above observations on the N-B bonds, the bonds which include N10, i.e., N10-B4 and N10-B9 show lower shielding at their centres than other bonds, see figure (3-10 (e,f)). Also, in comparison to other bonds, these bonds through the line graphs (a5) and (a6) in figure (3-12) show lower shielding activity by approximately 4 (ppm) as well as the deshielding presence near the N10 atom.

Inspecting the variation of the AMBL shieldings displays the polarisation of the shielding clouds of the N-B bonds towards the nitrogens, see curves (a) in figure (3-12). According to the shielding values at the midpoints of N-B bonds, the most shielded bond is N1-B2, see figure (3-12 (a1)).

Despite the fluctuating shieldings and deshieldings along curves (a) in figure (3-12) of the N-B bonds, a clear and almost-homogeneous shielding profile can be observed at 1Å above the N-B bonds with more shielding above nitrogen than above boron, see curves (b) in the same figure.

In agreement with the 2D isotropic shielding results, the 3D isosurfaces in figure (3-13) display the total 3D shielding activity in borazanaphthalene.

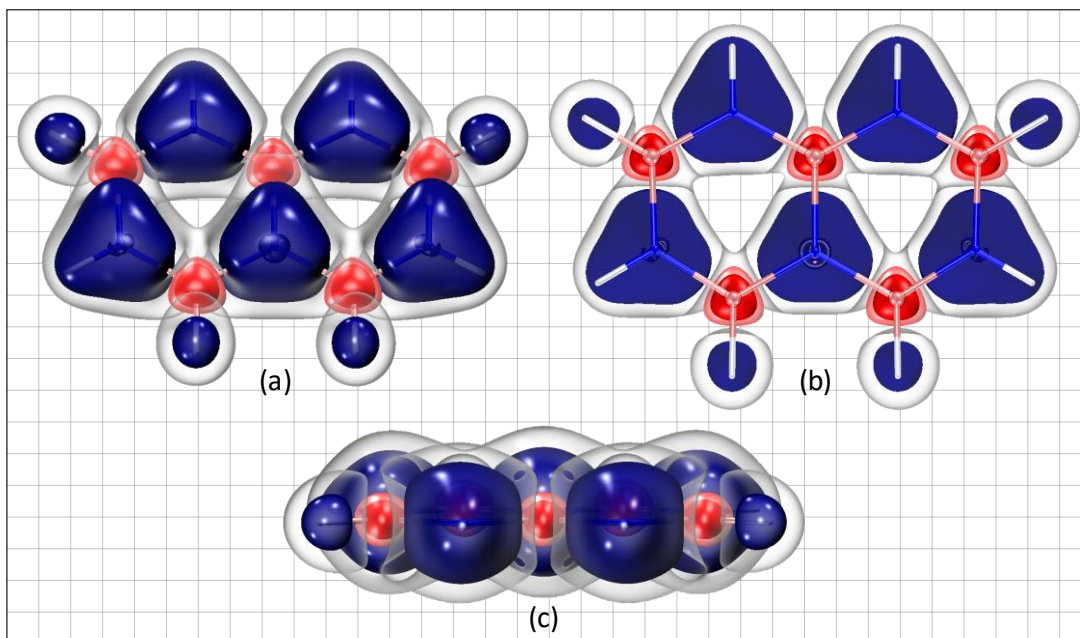


Figure 3-13: Isotropic shielding (σ_{iso}) isosurfaces of borazanaphthalene obtained from MP2/6-311++G(2d,2p) calculations. (a) Front view; (b) horizontal cross-section; and (c) top-view. The isosurfaces visualise the most common range in aromatic molecules, +16 (blue) / -16 (red) (ppm), in addition to a weaker range of +7 (transparent) / -5 (transparent red) (ppm).

As in the 3D treatment of borazine, four isosurfaces from two shielding/deshielding pairs of values are visualised. The first pair, blue/red at +16/-16 (ppm) shows that shieldings around nitrogen atoms behave similarly as those around atoms of aromatic molecules. However, some discontinuities in the shielding clouds over the molecular structure can be seen particularly around the boron centres. This shows the absence of extensive π -electron delocalisation. Therefore, borazanaphthalene magnetically behaves as molecule of lower aromaticity.

The second pair of values is +7/-5 (ppm), transparent / transparent red. This pair describes the shielding / deshielding isosurfaces in the same detail as the +16/-16 (ppm) values for aromatic molecules. Accordingly, visual and numerical comparisons consider borazanaphthalene as less shielding-homogeneous than borazine, with a moderate aromatic extent but much less than in strongly aromatic molecules.

3-4 Conclusions

To summarize this chapter, the results show that there are differences in the isotropic shielding data obtained from HF and MP2 levels of theory. However, the difference in the σ_{iso} between these approaches is less for those points placed at 1 Å above nuclei than at the nuclear positions.

The isotropic shielding behaviour of the nitrogen atoms as well as the boron atoms in borazine and borazanaphthalene shows lower differences. The nitrogen atoms are well-shielded and centred in triangular shielded-clouds including the AMBL clouds of the N-B and N-H bonds. The boron atoms not only have large deshielded-spheres but also display shielded-spheres centred on these deshieldings. Also, the shielding clouds around N-B and N-H bonds show significant shifts in shielding towards the nitrogens.

Utilising the vertical component of the isotropic shielding at 1 Å, $\sigma_{\text{iso}(zz)}$, and comparing its 2D shielding map with the total σ_{iso} map helps in two aspects. Firstly, both maps indicate the existence of (positive) isotropic shielding activities which can help identify localisation and delocalisation activities. Secondly, comparing the shielding profile of the vertical component $\sigma_{\text{iso}(zz)}$ and total σ_{iso} maps can be considered as further evidence of the presence or absence of the antiparallel shieldings at 1 Å above a molecule.

The line graphs used in examining AMBL of the N-B bonds show the polarity of the N-B bonds, which for both molecules were shifted towards nitrogen. According to the shieldings of the parallel lines at 1 Å above the N-B bonds, the shielding above the nitrogens is higher than above the borons. This reflects the partial localisation above the nitrogens. Also, utilising the line graph helped in testing the shielding at the ring centre which numerically proved the presence of LSC and the stronger shielding at π -regions above the planes of both molecules. Also, the maximum shielding value above borazine is higher than above borazanaphthalene which indicates lower aromaticity for the latter.

Visualising the +16 (ppm) isotropic shielding value shows that, except for the borons and their closest surroundings, the shielding for the bonds and for the localised nitrogen lone pairs can be well-illustrated. The -16 (ppm) isosurface displays the deshielding activities around the borons. The discontinuities in the +16 (ppm) shielding isosurface indicate that borazine and borazanaphthalene have lower shieldings in the spaces surrounding the molecular structure than strongly aromatic molecules.

In addition to the above isosurfaces, visualising the +7/-5 (ppm) offered a further way to check the shielding behaviour and to ensure that the low shielding is a global property, in addition to displaying other shielding features of these molecules. These values help visualise molecular magnetic shielding details, such as chemical bonding and electron delocalisation, in a similar way as for aromatic molecules. Comparing the values of +7/-5 with +16/-16 (ppm) highlights the lower extent of the isotropic shielding in these molecules relative to strongly aromatic molecules.

From these results, it can be inferred that borazine and borazanaphthalene possess similar shielding properties, and they have moderate levels of aromaticity. Also, the electron localisation and delocalisation in both molecules can be explained through their isotropic shielding behaviour.

CHAPTER FOUR

CYCLIC OXOCARBON

DIANIONS

4-1 Introduction

Cyclic Oxocarbon dianions is a family of doubly charged monocyclic anions with a general chemical formula of $C_nO_n^{2-}$ which their conjugate acids has the $C_nO_nH_2$ formula. Besides their supposed aromaticity, $n=3$ to 6 dianions are considered as the most popular members of this family which respectively is named as deltate, squarate, croconate and rhodizionate. The first two members are named relative to their geometric shapes. Whereas the Greek words *krokos* and *rhodizein*, which respectively mean yellow and rose-red, are the origin of naming last two members.^[116]

Although the last two members were discovered long time ago, the squaric acid and squarate were prepared in 1959 by Cohen et al.^[117] Accordingly, the high resonance stabilisations were attributed to the contributions of four oxygens. Shortly after Cohen, West and Niu, in 1960, introduced ($n=4-6$) oxocarbon dianions as a new family of electron-delocalised aromatic anions.^[118] West and Niu^[119] also made an effort to generalise a chemical formula of $C_nO_n^m$ to include anions of negative charge of $m=3-4$. About one and a half-decade later, West and Eggerding succeeded in synthesising deltic acid^[120] and its dianion^[121]. Pathways for preparation $n=3-6$ oxocarbons starting from acetylene diether (di-tert-butoxyethyne) was reported by Serratosa.^[122]

Despite the D_{nh} symmetry were reported for deltate,^[123] squarate and croconate,^[124] as well as rhodizionate^[125], most recent papers^[126,127] assigned C_2 symmetry for rhodizionate since the C_2 symmetry represents a minima with an energy content lower than other symmetries.

Aromaticity issue of oxocarbon dianions has been studied in several publications. For instance, Aihara^[128] used graph theory and observed high diatropic and aromatic features for deltate and small resonance energies for other dianions. Jug^[104] utilised the ring current and bond order in assessing aromaticity. Accordingly, he classified all above dianions as moderately aromatic and their aromaticity negatively linked with increasing ring size (i.e., n). Aromatic deltate, moderately aromatic squarate and weakly aromatic croconate and rhodizionate were suggested by Schleyer and co-workers^[126] who examined NICS(0) and NICS(1) indices. In agreement, Frontera et al. also employed NICS(0) and NICS(0.6) and obtained the same aromaticity

classification for the first two oxocarbons^[129,130], whereas the last two were found as non-aromatic^[130].

Herndon^[131] used the valence bond theory and assumed that oxocarbon dianions aromatic due to their resonance stabilisation. He additionally found that the resonance energy per carbonyl unit and per π -electron decrease with increasing the ring size of oxocarbon dianions, however, the greatest gap in the resonance energy per π -electron was observed between deltate and squarate, while fewer differences between other sequenced dianions.^[131]

By using some references of acyclic compounds, Moyano and Serratosa^[132] estimated resonance energy of oxocarbon dianions. Accordingly, oxocarbon dianions described as cycloalkenyl cation rings of $C_n^{(n-2)+}$ and their aromaticity is linked inversely with the amount of perturbations in which caused by (n) of oxygens.

Fowler and co-workers^[133], based on ring currents evaluations, concluded that none of the oxocarbon dianions is aromatic. They found absence of any remarkable π -ring currents in oxocarbon dianion rings, except for deltate which showed around a quarter of benzene π -currents.

Besides their observation about presence of ring currents in oxocarbon dianions, Puebla and Ha^[134] found a relationship between the (n) and bond order. With increasing the (n), the bond order increases for the C-O bonds and decreases for the C-C bonds. Also, the C-C bonds was observed with a bonding character in between single and double bonds, whereas the C-O bonds were found with no electron-donation to carbon besides a pure lone pairs localisation on oxygen.^[134]

Relevantly, increasing the (n) associated with increasing bond distance and decreasing the bond order character of the C-C bonds, while opposite changes are shown by the C-O bonds inline with decreasing charge separation between C and O.^[135] In comparison with the other dianions, more C-C double-bond and C-O single-bond features are found in deltate.^[136]

The purpose of the current chapter is to examine, represent and compare the magnetic shielding features of oxocarbon dianions and then assess their aromaticity.

4-2 Deltate

An optimisation at DFT B3LYP/6-311++G(2d,2p) level was performed. Then, the frequencies of the optimised D_{3h} deltate was checked with no imaginary value. The evaluations of magnetic shielding were performed at HF and MP2 with 6-311++G(2d,2p) basis set. Accordingly, less nuclear σ_{iso} values from HF than MP2, see table (4-1). An inversed trend can be seen for points placed at 1 Å above carbon and oxygen nuclei. Also, σ_{iso} values of oxygen is higher than of carbon by more than four times. While σ_{iso} values at 1 Å above oxygen is around twice that above carbon.

Except for C_2 symmetric rhodizonate, D_{nh} symmetry for other oxocarbon dianions leads to identical carbons and C-C bonds with $|\Delta\sigma_{\text{iso}(C-C)}^{0\text{Å}}|$ and $|\Delta\sigma_{\text{iso}(C-C)}^{1\text{Å}}|$ values equal to zero. Differently, the C-O bond shows obvious gap between the values of both parameters, 179.72 and 6.33 (ppm), respectively.

Table 4-1: MP2/6-311++G(2d,2p) and HF/6-311++G(2d,2p) isotropic shieldings data (in ppm) for deltate C and O nuclei and for points placed 1 Å above the nuclei as well as the vales of $|\Delta\sigma_{\text{iso}(C-O)}^{0\text{Å}}|$ and $|\Delta\sigma_{\text{iso}(C-O)}^{1\text{Å}}|$ shielding parameters.

	C		O		C-O	
	Nuclear σ_{iso} (ppm)	σ_{iso} 1Å above nuclei	Nuclear σ_{iso} (ppm)	σ_{iso} 1Å above nuclei	$ \Delta\sigma_{\text{iso}(C-O)}^{0\text{Å}} $	$ \Delta\sigma_{\text{iso}(C-O)}^{1\text{Å}} $
MP2	51.74	5.92	231.46	12.25	179.72	6.33
HF	47.45	7.07	226.16	12.27	178.71	5.02

Surprisingly, the ring area in figure (4-1 (a,b)), except for the deshielded-spheres around the carbons, is completely well-shielded and forms one shielding domain. Also, a less shielded core LSC at the ring centre cannot be found. Differently, figure (4-2) shows existing of a small less-shielded hole at 1 Å above the ring centre. This does not belong to LSC presence since LSC normally locates much closer to the molecular plane, but rather reflect the profile of π -electron movement at 1 Å height.

Relevantly, shielding variation above the ring-centre is displayed as a curve with a maximum of 34.6 (ppm) locates at the ring centre, see figure (4-3), then, a rapid decrease in shielding intensity occurs at higher heights reaching around one-fourth at 1 Å. The shielding profile of the curve shows that the ring is completely managed by the (positive) isotropic shieldings.

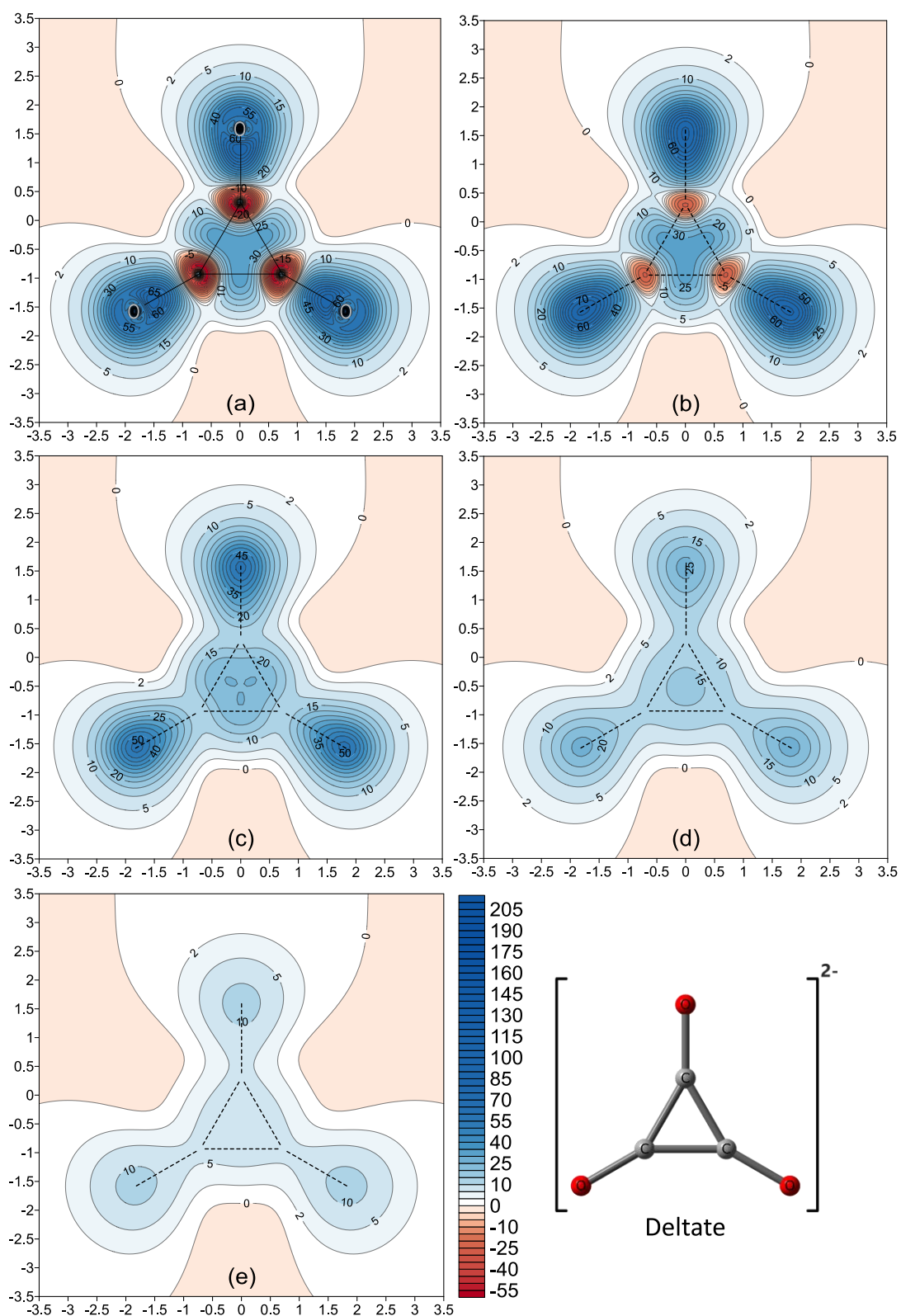


Figure 4-1: Five contour maps of the isotropic shieldings (σ_{iso}) (in ppm) obtained at the MP2/6-311++G(2d,2p) level of theory for deltate. (a-e): from grids placed at 0.00, 0.25, 0.50, 0.75 and 1.00 Å heights above the molecular plane, respectively.

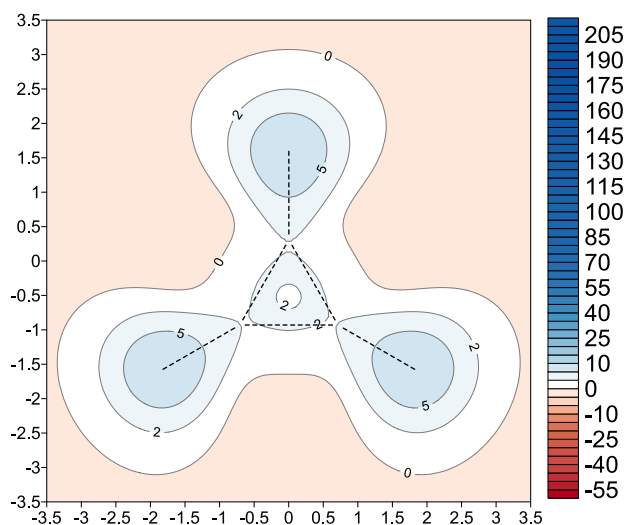


Figure 4-2: Contribution of the vertical-component of the isotropic shielding ($\sigma_{iso(zz)}$) (in ppm) to the total isotropic shielding σ_{iso} of deltate obtained at the MP2/ 6-311++G(2d,2p) level of theory for a grid placed at 1.00 Å above the ring.

Despite the carbon nuclei and their closest areas are magnetically shielded, see table (4-1) and figures (4-1 (a)) and (4-4 (a,b)), their small shielded-spheres are surrounded by strongly deshielded-spheres. In contrast, no such deshieldings surround the well-shielded oxygen nuclei. This reflects the difference in the shielding behaviour around these nuclei of deltate.

Figures (4-1(a)) and (4-4 (a,b)) additionally display the shielding behaviour at and around the C-C and C-O regions. Although these regions show higher σ_{iso} responses than the nearby areas, significant higher shieldings can be seen around the C-O bonds than around C-C bonds. Another observation can be noticed, the C-O shielding cloud shows an extension (about a half of the C-O bond length) to the spaces beyond the oxygen terminal, see figures (4-1) and (4-4 (b)). This extension in the shielding cloud is caused by the oxygen lone-pairs and the polarisation effects together with the electronegativity difference between oxygen and carbon atoms.

Two shielding trends can be seen. Firstly, the shielding clouds of the three C-C bonds are unified in one shielding cloud at the ring, see figure (4-1 (a)) and left side of figure (4-4 (b)). This may be attributed to the geometric feature of deltate since its triangular ring makes the C-C bonds much closer each other. Also, the contribution of the (-2) negative charge in the electron circulation of deltate is high because of the small area of the three-membered ring.

Secondly, comparing the shielding cross-sections at the midpoints of the C-O and C-C bonds leads to observing that the shielding cloud of the C-O bond forms an oval shape with higher shieldings and more vertical expansion than that of the C-C bond, see figures (4-4 (b,c)).

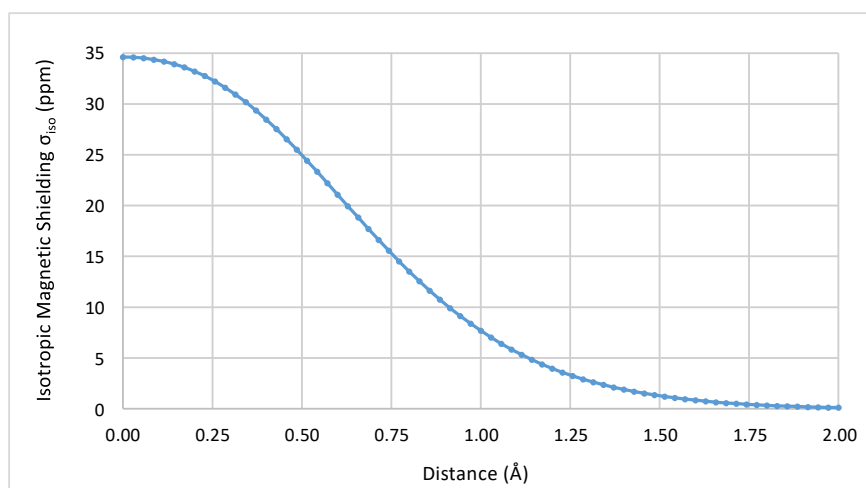


Figure 4-3: Variation in the MP2/6-311++G(2d,2p) isotropic shieldings σ_{iso} (in ppm) above the deltate ring obtained from 71 ghost atoms placed perpendicularly from the ring centre to a 2 Å height above it.

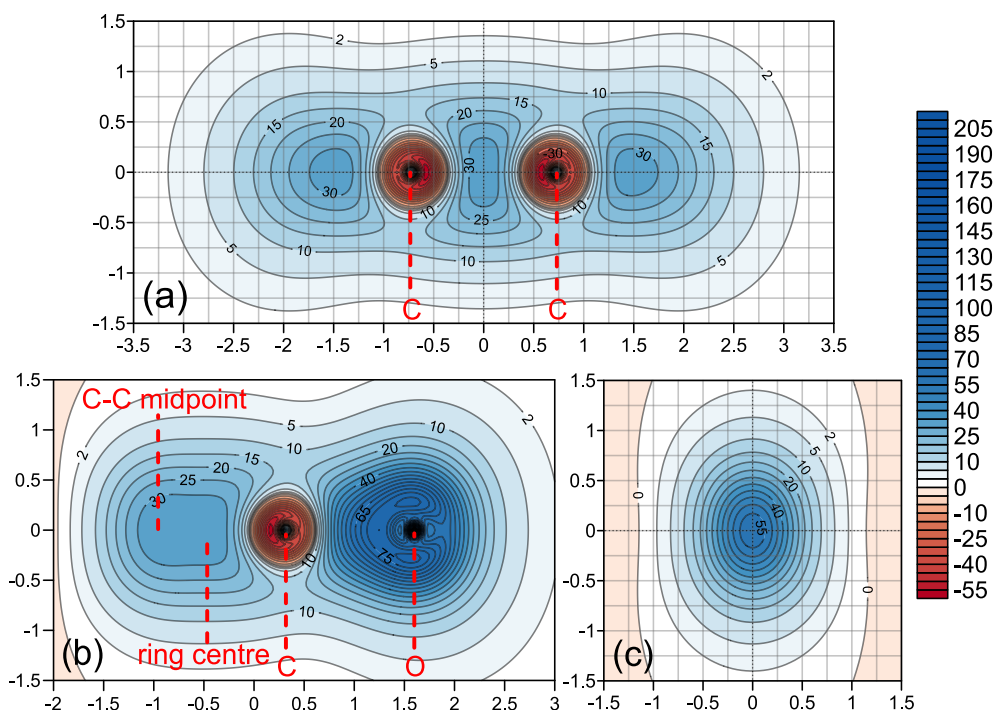


Figure 4-4: MP2/6-311++G(2d,2p) isotropic shielding cross-sections set perpendicularly to the deltate: (a) along C-C bond, (b) along O-C(ring centre)-(C-C midpoint) diagonal and (c) passing through the C-O bond midpoint.

Curves (a) in figure (4-5) indicates that around half of the C-C bond distance is deshielded. Whereas most of the C-O bond line is shielded, except for the deshielded-sphere part near the carbon terminal. The maximum σ_{iso} of the C-C bond AML is 34.4 (ppm) and locates exactly at the bond midpoint. Differently, the maximum σ_{iso} of the C-O bond AML is 80.0 (ppm) which shows a shift from the bond midpoint towards the oxygen terminal. Another point, σ_{iso} value at the C-O midpoint is approximately as twice as that at the C-C midpoint, 59.2 and 34.4 (ppm), respectively.

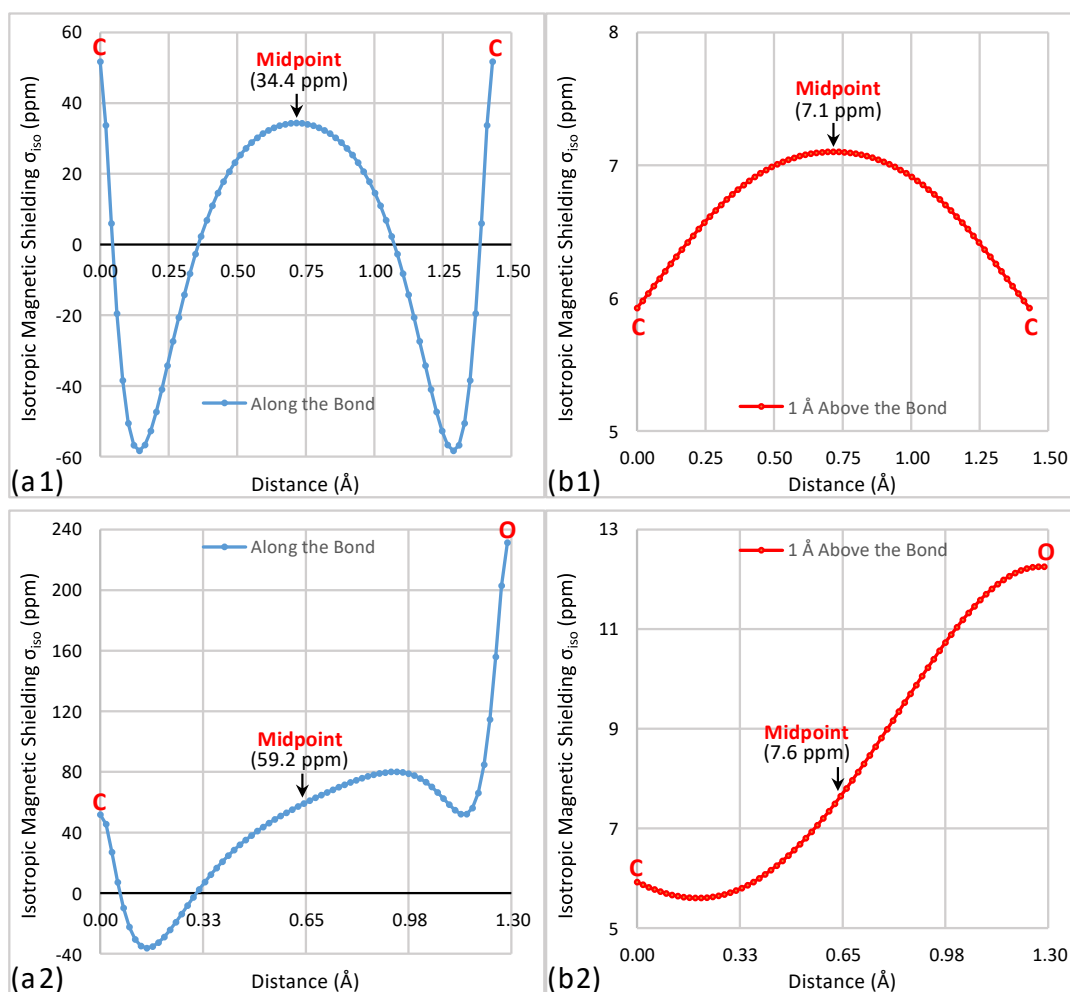


Figure 4-5: Variation in the MP2/6-311++G(2d,2p) isotropic shielding (σ_{iso}) (in ppm) along C-C and C-O bonds in deltat obtained from 71 ghost atoms: (a) placed along the bonds and (b) placed 1 Å parallelly above the bonds.

A different magnetic shielding trend can be noticed at 1 Å, see curves (b) in figure (4-5). Although the shielding activity predominates above both C-C and C-O bonds, the shielding along both curves are unequal. Curve (b1) shows

an increase from 5.92 (ppm) above both C-C bond terminals to 7.10 (ppm) above the bond midpoint. In comparison, curve (b2) shows a higher increase from 5.92 (ppm) above carbon to 12.25 (ppm) above oxygen with $|\Delta\sigma_{\text{iso}}^{1\text{\AA}}(\text{C-O})|$ value of 6.33 (ppm), see table (4-1). Some factors such as bond polarity, lone pairs and electronegativity difference play the main role in the shielding behaviour of curve (b2).

Comparing the previously discussed 2D results of this section with the 3D magnetic shielding isosurfaces in figure (4-6) shows good agreement between them. The blue and the red isosurfaces represent the shielding values of +16 (ppm) and -16 (ppm), respectively.

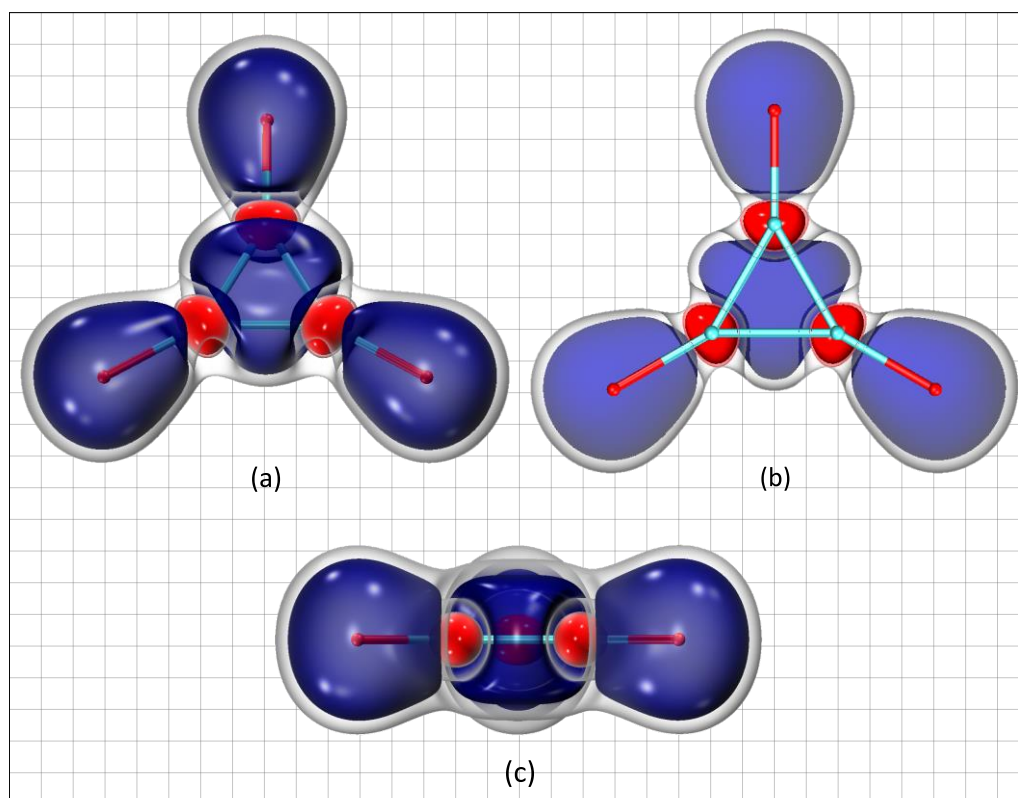


Figure 4-6: Front view (a), cross-section (b) and side view (c) of the 3D isotropic shielding isosurfaces for deltate obtained from MP2/6-311++G(2d,2p) calculations. The isosurfaces visualise (σ_{iso} /colour): +16/blue, -16/red, +10/transparent and -10/transparent red.

Accordingly, these two isosurfaces indicate that the molecular structure, except for the deshielded-spheres of carbons, is managed by shielding activity, i.e., most parts of the deltate behave like aromatic molecules.

However, the discontinuity in the shielding cloud, the blue isosurface, over the carbon deshielded-sphere required further two isosurfaces to check if there is any other shieldings and/or deshieldings at these locations.

The first is the transparent isosurface which displays +10 (ppm). This isosurface precisely affirms the existing of shielding activity over the carbon deshielded-spheres as well as around all other shielding/deshielding isosurfaces surround the molecular structure. Whereas the second isosurface of transparent red visualises -10 (ppm) value and shows a small expansion of the deshieldings of the deshielded-spheres. Besides, this isosurface shows that the expansion of the -10 (ppm) isosurface is much less than that of the +10 (ppm) isosurface. This reflects either the enforcement of the stronger shielding activity to enclose the inner (weaker) deshielding activity in smaller spaces or the localisation of the deshielding activity at these small spaces.

Depending on the findings of this section, the deltate can be classified as an aromatic compound, but less aromatic than strongly aromatic molecules and its geometric features affect its shielding profile.

4-2 Squarate

DFT B3LYP/6-311++G(2d,2p) level of theory was used to optimise squarate structure. The resulted D_{4h} geometry of squarate showed no imaginary frequencies. In comparison to deltate, squarate atoms show two different isotropic shielding trends (see the MP2 results in tables (4-1) and (4-2)). Firstly, the carbon nucleus becomes deshielded -14.0 (ppm), i.e., lower in shielding than that in deltate by 65.8 (ppm). Secondly, σ_{iso} value of oxygen decreased by 183.3 (ppm) and changed from highly shielded in deltate, 231.4 (ppm), to less shielded in squarate, 47.74 (ppm). Moreover, the isotropic shieldings at 1 Å above nuclei of both compounds follow almost the same trend with $|\Delta\sigma_{\text{iso}(C-O)}^{1\text{Å}}|$ value of around 6 (ppm). While the $|\Delta\sigma_{\text{iso}(C-O)}^{0\text{Å}}|$ value decreased from 179.72 in deltate to 61.8 (ppm) in squarate. Like MP2, HF generally shows a similar magnetic profile but with different σ_{iso} values.

Table 4-2: MP2/6-311++G(2d,2p) and HF/6-311++G(2d,2p) isotropic shieldings data (in ppm) for squarate C and O nuclei and for points placed 1 Å above the nuclei as well as the vales of $|\Delta\sigma_{\text{iso}(C-O)}^{0\text{Å}}|$ and $|\Delta\sigma_{\text{iso}(C-O)}^{1\text{Å}}|$ shielding parameters.

	C		O		C-O	
	Nuclear σ_{iso} (ppm)	σ_{iso} 1Å above nuclei	Nuclear σ_{iso} (ppm)	σ_{iso} 1Å above nuclei	$ \Delta\sigma_{\text{iso}(C-O)}^{0\text{Å}} $	$ \Delta\sigma_{\text{iso}(C-O)}^{1\text{Å}} $
MP2	-14.06	6.57	47.74	13.26	61.80	6.69
HF	-21.82	7.16	46.75	13.50	68.57	6.34

Scanning the isotropic shieldings from 0 to 1 Å above molecular plane is represented in figure (4-7) and partly in figure (4-8). Unlike deltate, the C-C shielding clouds of squarate are not unified. Each C-C bond own an individual shielding cloud at its AMBL with a slight location shift towards the spaces outside the ring frame. These shifts are caused by large deshielded-spheres around carbons which occupy large area of the squarate molecular plane, see figures (4-7 (a,b)) and (4-9 (a,d)). Moreover, figure (4-9 (b)) shows the shieldings of the C-C bond as a kidney-shaped cloud with two more shielded islands above and below the C-C bond, see also these islands in figure (4-7(b)). The above shielding behaviour can be considered as a consequence of the high activity of carbon deshielded-spheres at the molecular plane. With decreasing the deshielded-spheres effects at higher heights above the molecular plane, the C-C shielding clouds recover their normal locations and shielding activities, see figure (4-7 (c)).

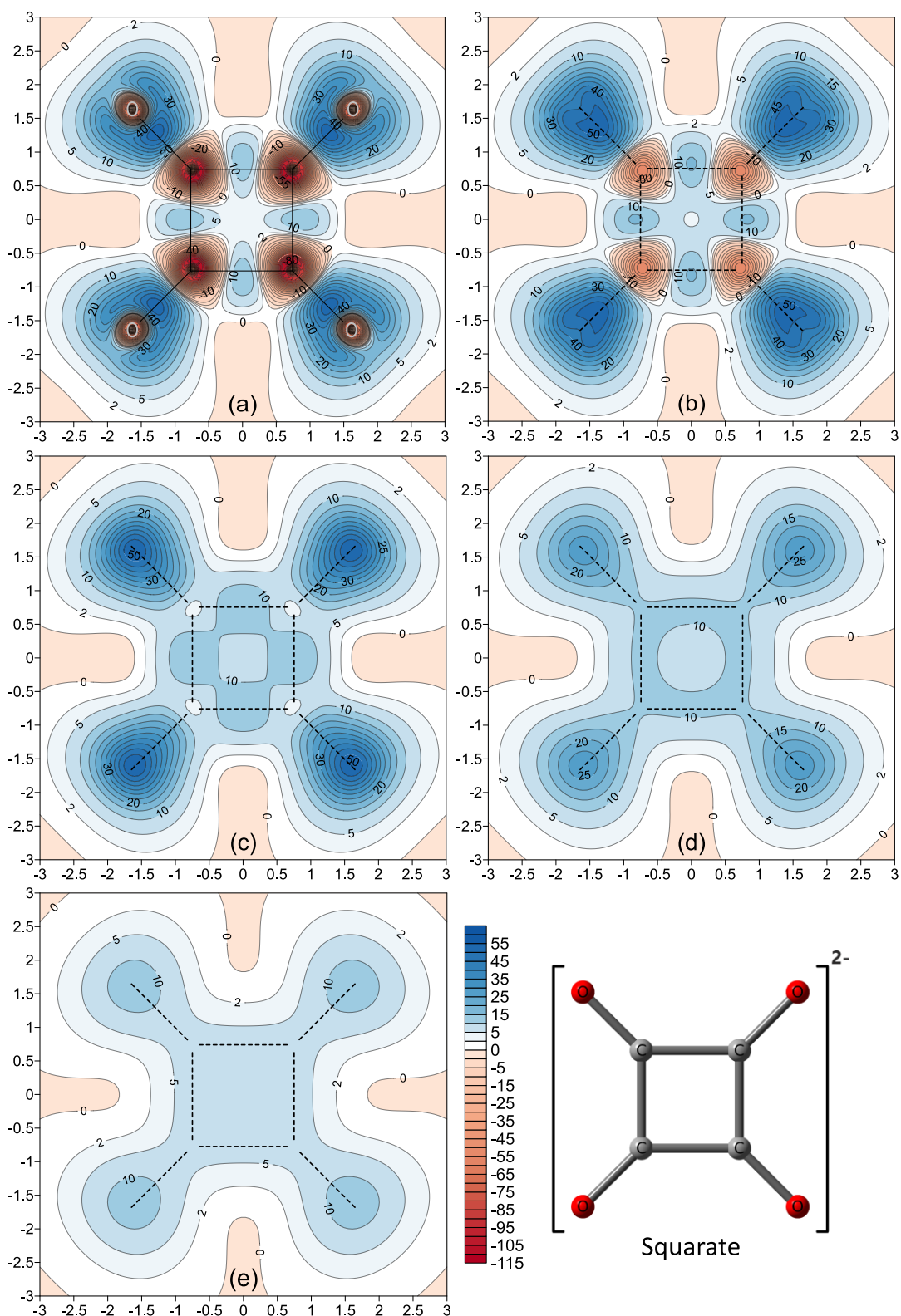


Figure 4-7: Five contour maps of the isotropic shieldings (σ_{iso}) (in ppm) obtained at the MP2/6-311++G(2d,2p) level of theory for squarate. (a-e): from grids placed at 0.00, 0.25, 0.50, 0.75 and 1.00 Å heights above the molecular plane, respectively.

According to figure (4-9), the shieldings along the C-O bond is much higher than that along the C-C bond with a precise shielding polarisation towards the oxygen. Despite the oxygen nucleus is listed as a shielded in table (4-2), a deshielded-sphere of less than 0.25 Å radius surrounds oxygen in figures (4-7 (a,b)) and (4-9 (a)).

The isotropic shielding cloud at around 1 Å height above the squarate plane shows more homogeneous shielding profile than that at the molecular plane, see figures (4-7(a,e)) and (4-9 (a,b)). Similarly, $\sigma_{iso(zz)}$ map agrees with this but with fewer shieldings in particular at the middle area above the ring centre, see figure (4-8). The magnetic shieldings at 1 Å heights indicate presence of π -electron delocalisation. However, the shielding cloud of π -electron circulation shows maximum shielding value about 10 (ppm) at 0.75 Å, see figure (4-7 (d)). At lower vertical heights, the ring centre region shows lower shielding intensity than that at nearby shielded-areas. As a result, LSC centred at the middle area of the squarate ring which can be seen in maps (a) and (b) of figures (4-7) and (4-9).

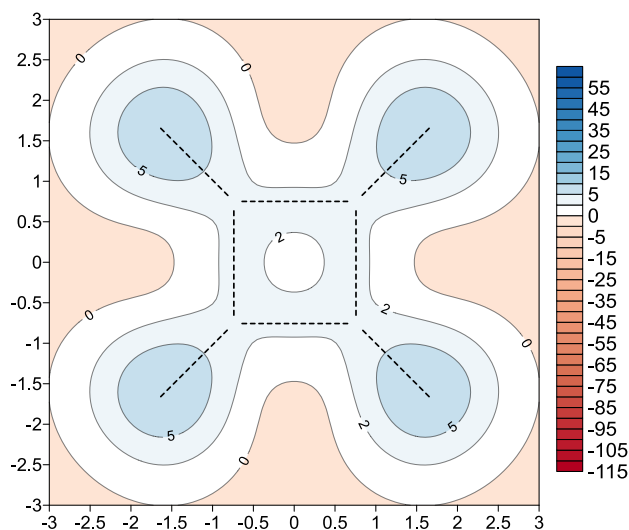


Figure 4-8: Contribution of the vertical-component of the isotropic shielding ($\sigma_{izo(zz)}$) (in ppm) to the total isotropic shielding σ_{izo} of squarate obtained at the MP2/6-311++G(2d,2p) level of theory for a grid placed at 1.00 Å above the ring.

Relevantly, inspecting shielding variation along the curve of figure (4-10) shows that the shielding starts from 3.1 (ppm) at the ring centre which increases and reaching a maximum of 7.2 (ppm) at 0.62 Å vertical height and then decreases at higher heights. This shielding profile approves the presence of LSC and π -electron delocalisation in squarate.

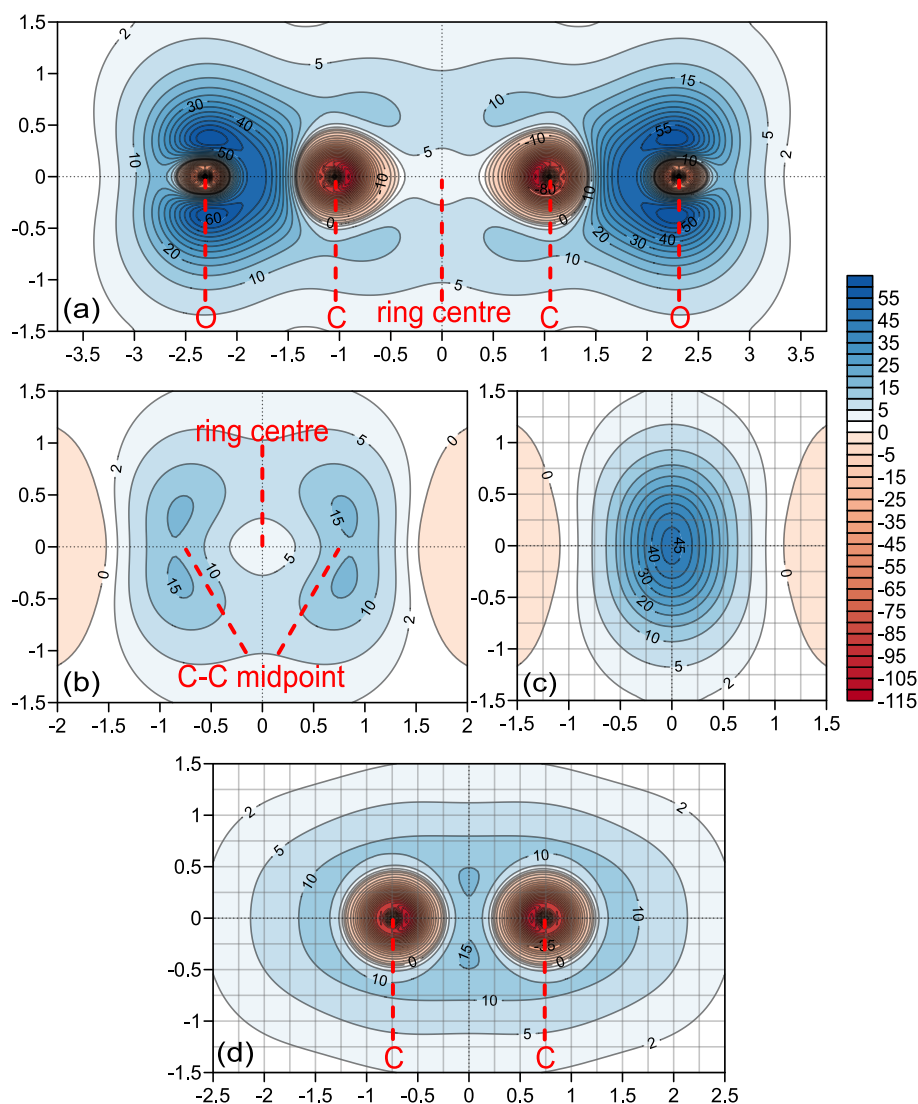


Figure 4-9: MP2/6-311++G(2d,2p) isotropic shielding cross-sections set perpendicularly to squarate: (a) along O-C-(ring centre)-O-C diagonal, (b) along midpoints of two C-C bonds including ring centre, (c) passing through the C-O bond midpoint and (d) along the C-C bond.

According to curve (a1) in figure (4-11), the maximum shielding value along the C-C bond is 13.9 (ppm) and locates at the bond midpoint. Whereas plot (a2) shows a significant shift in the shielding cloud location of the C-O bond ABL towards the oxygen end with a maximum shielding value of 53.9 (ppm). Comparing the C-C bonds shows the ABL comprises about a half and one-third of the total bond distance of deltate and squarate, respectively, see figures (4-5 (a1)) and (4-11 (a1)). These figures also show the maximum deshielding value of deshielded-sphere in deltate and squarate as -58.3 and -108.1 (ppm) respectively. It can be concluded that stronger deshielding

activity of a deshielded-sphere causes more shielding cloud shifts. Similar behaviour can be seen at the oxygen of the C-O bond. Stronger shieldings limit the radius of the weaker deshielded-sphere of oxygen in a less than 0.25 Å radius, see figures (4-9(a)) and (4-11(a2)). Map (c) in figure (4-9) shows a similar effect between the shielding cloud of the C-O bond and the nearby (left and right) deshieldings which affect the shape of the C-O shielding cloud.

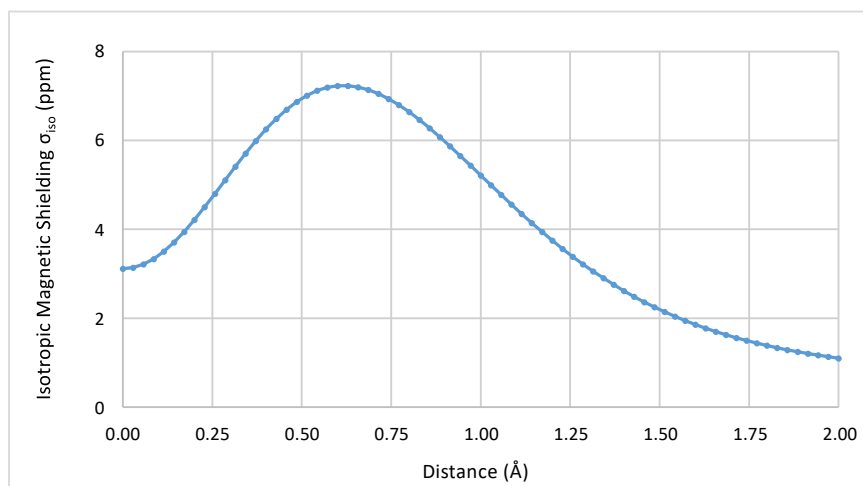


Figure 4-10: Variation in the MP2/6-311++G(2d,2p) isotropic shieldings σ_{iso} (in ppm) above the squarate ring centre obtained from 71 ghost atoms placed perpendicularly from the ring centre to a 2 Å height above it.

Another point, the carbon deshielded-sphere behaves unevenly along the C-C and C-O bonds, see curves (a1) and (a2) in figure (4-11). This can be understood when comparing the shielding values of the deshielded points near the carbon ends of the above curves. The maximum deshielding values near these ends are -108.1 and -87.1 (ppm), respectively. A similar profile can also be observed in deltate, see figure (4-5 (a1,a2)).

Several reasons lead to the above uneven behaviour. This includes the difference in bond nature of covalent C-C and polar C-O bonds, electronegativity difference between carbon and oxygen besides other structural and magnetic influences such as oxygen lone pairs and/or effects of nearby C-C bond AMBL shieldings. These reasons not only affect the shielding behaviour of curves (a) in figure (4-11) but also curves (b) as well. Curve (b2) shows polarisation in shielding activity at 1 Å above C-O bond towards oxygen. Whereas curve (b1) shows the shieldings above the C-C bond tends to be equalised.

Four isosurfaces have been aimed to display the 3D isotropic shielding behaviour of squarate, see figure (4-12). Unlike deltate, the absence of +16 (ppm) blue isosurface around the ring frame of squarate reflects a general weakness in magnetic shieldings at these spaces. The blue isosurface can be seen at spaces of stronger shieldings such as at the oxygen lone pairs and most of the C-O bond AMBL spaces.

Differently, visualising +8 (ppm), the transparent isosurface, represents most of the squarate structure. This includes C-C and C-O bonds, the global shielding region of the π -electron delocalisation and oxygen lone pairs. Comparing +8 (ppm) transparent isosurface of squarate with the identical +10 (ppm) isosurface of deltate indicates lower relative shieldings around squarate, see figures (4-12) and (4-6), respectively.

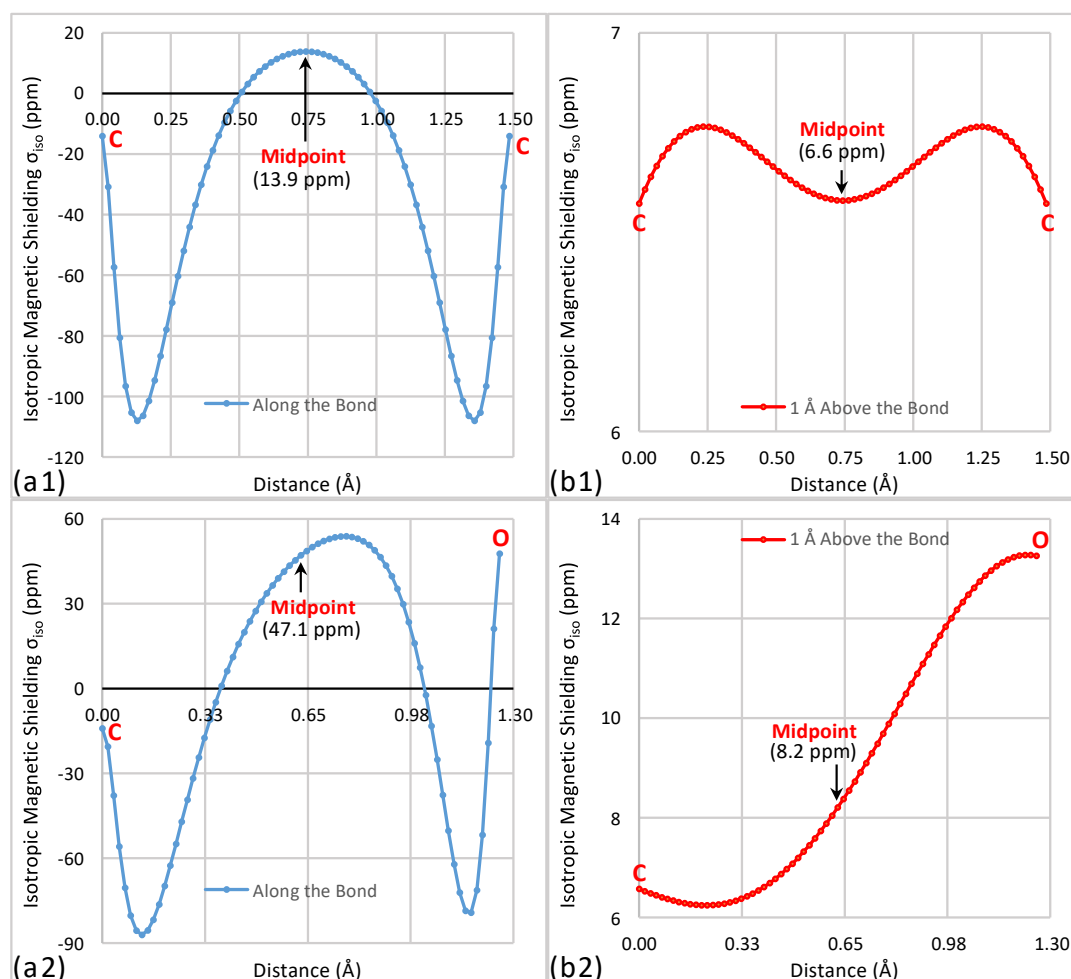


Figure 4-11: Variation in the MP2/6-311++G(2d,2p) isotropic shielding (σ_{iso}) (in ppm) along C-C and C-O bonds in squarate obtained from 71 ghost atoms: (a) placed along the bonds and (b) placed 1 \AA parallelly above the bonds.

The red isosurface of -16 (ppm) represents the deshielding behaviour of squarate. Both deshielded-spheres of carbon and oxygen share similar deshielding profile of aromatic molecules. Moreover, the -8 (ppm) transparent red isosurface highlights the deshielding activity expansion from -16 to -8 (ppm) which occurs in very small spaces surround the deshielded-spheres. In comparison, shielding expansion from +16 to +8 (ppm) occurs through significantly larger spaces, see the isosurfaces of the above shielding values.

Finally, it can be said that squarate has a moderate π -electron circulation and moderate aromaticity but its aromaticity is around a half that of strongly aromatic molecules.

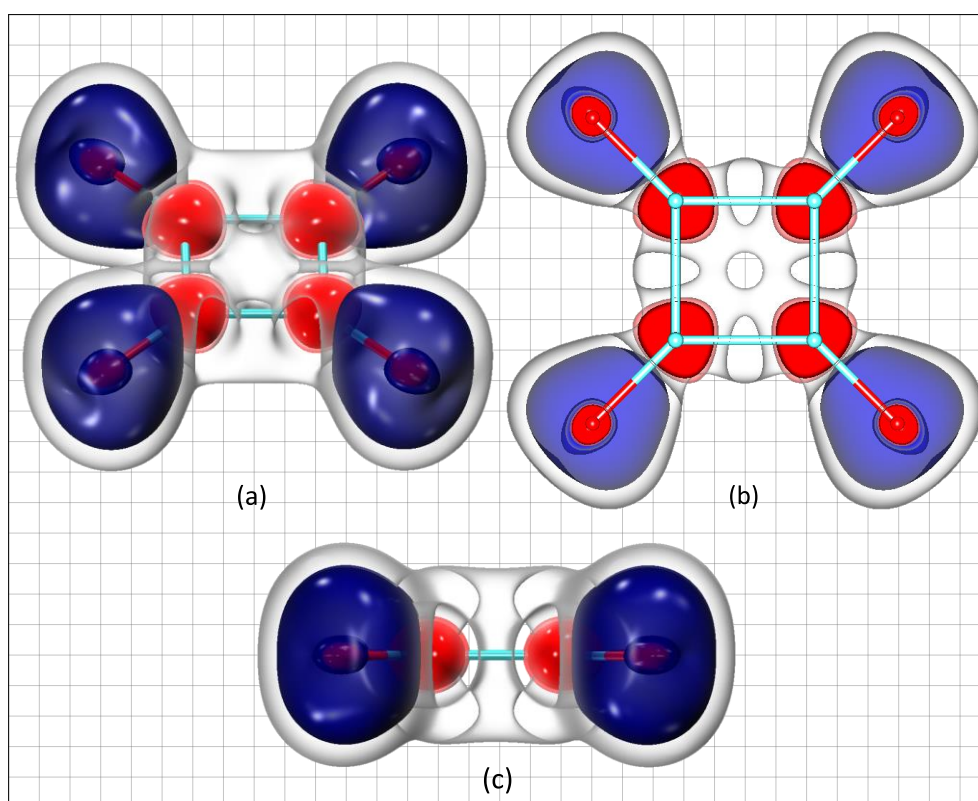


Figure 4-12: Front view (a), cross-section (b) and side view (c) of the 3D isotropic shielding isosurfaces for squarate obtained from MP2/6-311++G(2d,2p) calculations. The isosurfaces visualise (σ_{iso} /colour): +16/blue, -16/red, +8/transparent and -8/transparent red.

4-3 Croconate

Optimising the croconate structure was performed at the DFT B3LYP/6-311++G(2d,2p) level which completed without any imaginary frequency. Then the isotropic shielding calculations were performed under the HF and MP2 levels with 6-311++G(2d,2p) basis set. Comparing σ_{iso} data in table (4-3) with those in tables (4-1) and (4-2) shows an inversion in the nuclear σ_{iso} behaviour of both oxygen and carbon. The oxygen nucleus, according to MP2 results, becomes deshielded and lower in shielding than squarate oxygen by around 85 (ppm). Whereas carbon nucleus regains about 17 (ppm) and becomes shielded like deltate carbon but with lower shielding value. Unlike the similarity in $|\Delta\sigma_{\text{iso}(C-O)}^{1\text{\AA}}|$ value between croconate and the previous two oxocarbons, croconate shows a significant lower $|\Delta\sigma_{\text{iso}(C-O)}^{0\text{\AA}}|$ value than others. Noticeably, nuclear σ_{iso} values obtained from HF are lower than those obtained from MP2. A lower shielding difference between these methods can be seen for those points placed at 1 Å above the carbon and oxygen nuclei, see table (4-3).

Table 4-3: MP2/6-311++G(2d,2p) and HF/6-311++G(2d,2p) isotropic shieldings data (in ppm) for croconate C and O nuclei and for points placed 1 Å above the nuclei as well as the values of $|\Delta\sigma_{\text{iso}(C-O)}^{0\text{\AA}}|$ and $|\Delta\sigma_{\text{iso}(C-O)}^{1\text{\AA}}|$ shielding parameters.

	C		O		C-O	
	Nuclear σ_{iso} (ppm)	σ_{iso} 1Å above nuclei	Nuclear σ_{iso} (ppm)	σ_{iso} 1Å above nuclei	$ \Delta\sigma_{\text{iso}(C-O)}^{0\text{\AA}} $	$ \Delta\sigma_{\text{iso}(C-O)}^{1\text{\AA}} $
MP2	3.47	6.88	-37.64	14.15	41.11	7.27
HF	-6.19	7.39	-48.48	14.67	42.29	7.28

In comparison with delate and squarate, the shielding behaviour of croconate, shows several remarkable changes particularly at the plane of croconate, see figure (4-13). The main change is that the carbon deshielded-spheres extend and join together besides occupying most of the ring area, except for the C-C AMBLs, see figures (4-13 (a,b)) and (4-14 (a)). The shielding clouds of the C-C bond AMBLs show a significant increase in their shifts towards spaces outside the ring frame. Also, these shielding clouds show lowering in their shieldings in particular near the bond midpoints, see (figure 4-13 (a)). At higher vertical heights, the deshieldings fade away which allowing the shielding clouds to recover their shapes and reclaiming their locations at the C-C bond, see figures (4-13 (b,c)) and (4-14 (b,d)).

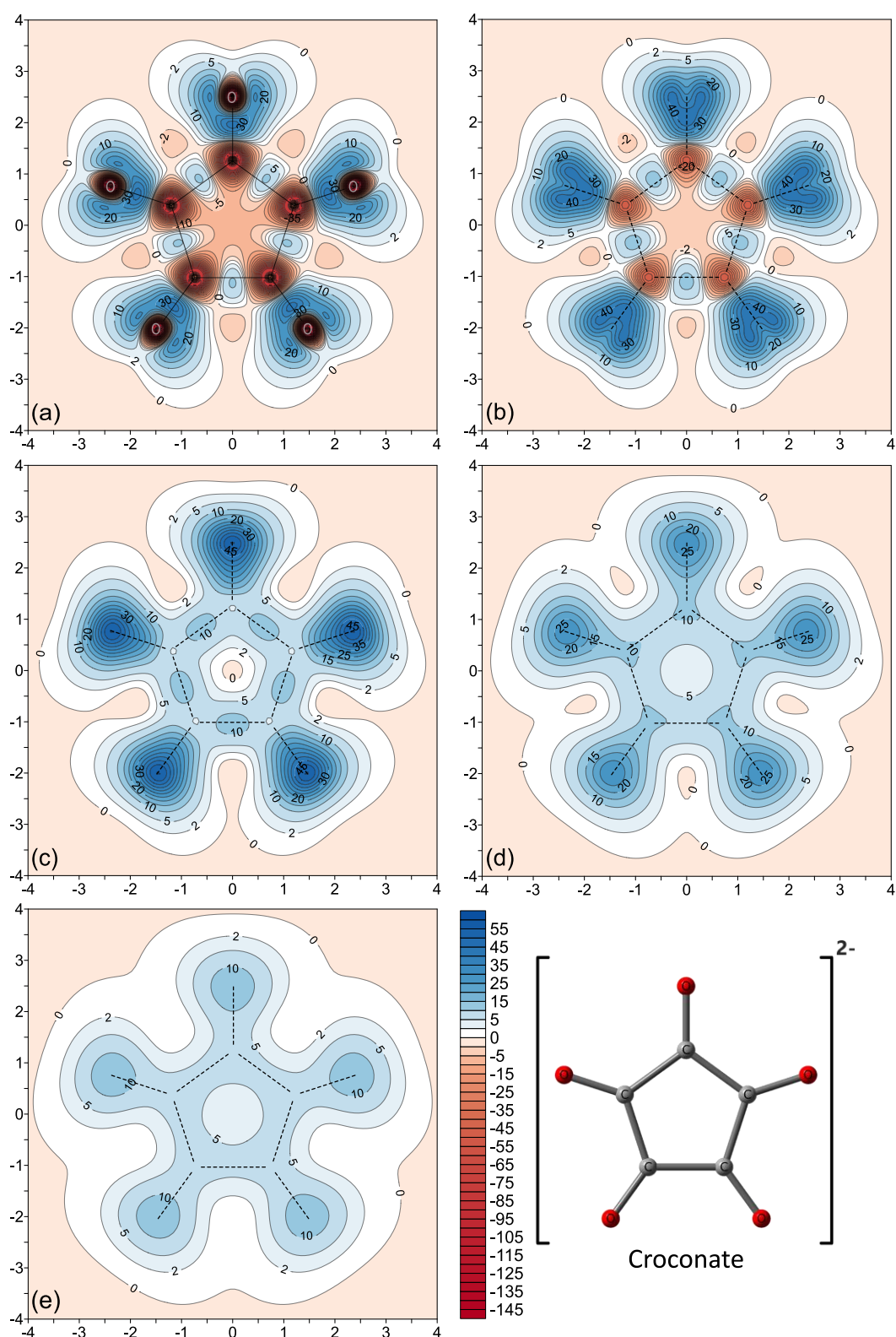


Figure 4-13: Five contour maps of the isotropic shieldings (σ_{iso}) (in ppm) obtained at the MP2/6-311++G(2d,2p) level of theory for croconate. (a-e): from grids placed at 0.00, 0.25, 0.50, 0.75 and 1.00 Å heights above the molecular plane, respectively.

Some noteworthy points regarding the relationship between shielding and deshielding activities in croconate. The shelled-peanut shielding cloud of the C-C bond is caused by deshieldings located at inner and outer ring regions, see figure (4-14 (b)). Besides, these deshieldings also shift C-C shielding clouds towards regions outside the ring frame. This is because of the deshieldings at the inner region of the croconate ring are higher than those at outer regions.

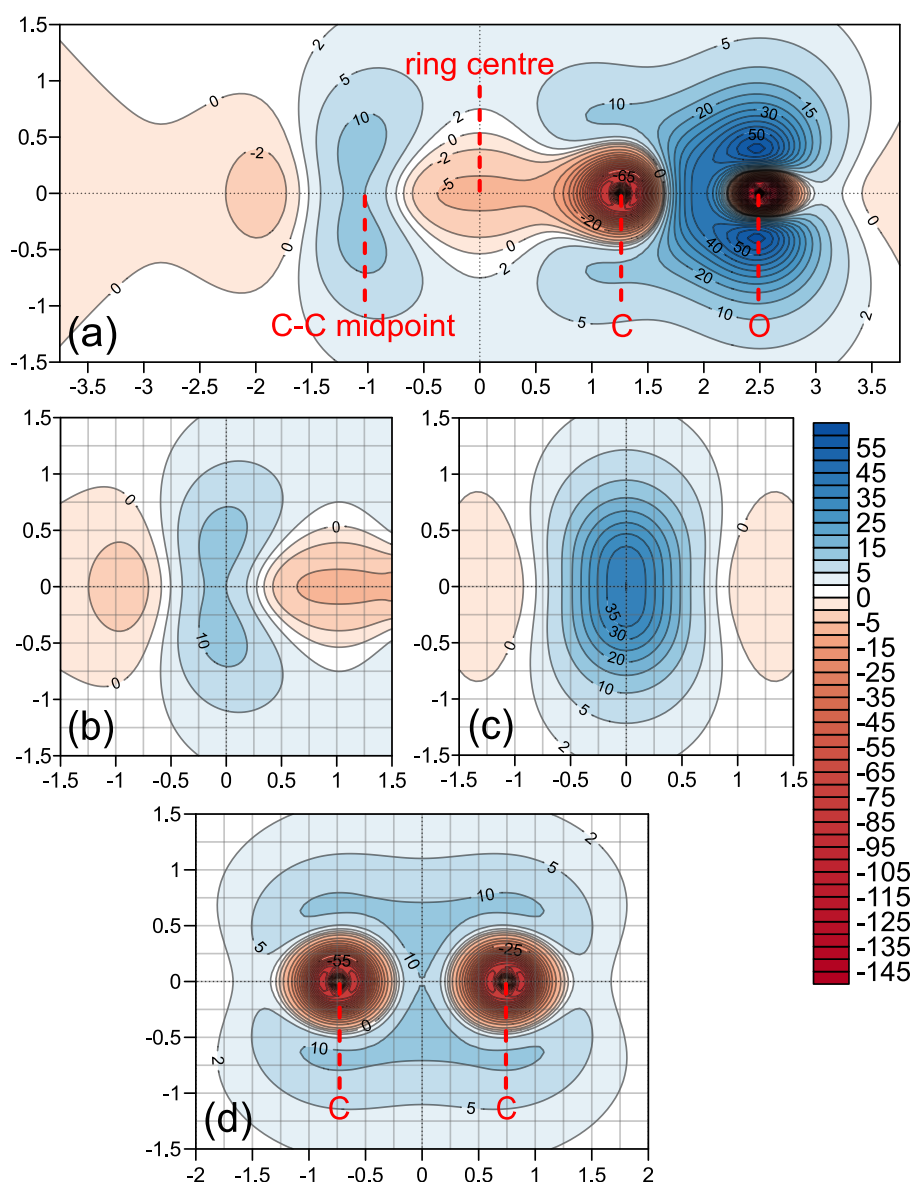


Figure 4-14: MP2/6-311++G(2d,2p) isotropic shielding cross-sections set perpendicular to croconate: (a) along O-C-(ring centre)-(C-C midpoint) diagonal, (b) along midpoint of the C-C bond, (c) passing through the C-O bond midpoint and (d) along the C-C bond.

Comparing map (c) in figures (4-4), (4-9) and (4-14) shows that: closer/stronger deshieldings at left and right sides of these maps cause lowering the shielding cloud width of the C-O bond, i.e., closer opposite shielding/deshielding activities cause more cloud distortions. The stronger magnetic activity has a priority to occupy the available spaces and force the weaker magnetic activity either to shift its location or to distort/shrink its shape/volume.

Despite the strong deshieldings and weak shieldings at/near the molecular plane, the shieldings at higher heights between 0.75 to 1.00 Å show a high level of similarity with shielding activities at these heights for the previous dianions, see maps (d,e) in figures (4-13), (4-7) and (4-11). $\sigma_{\text{iso}(zz)}$ shieldings at 1 Å show a further similarity trend for all the three dianions, see maps (4-15), (4-8) and (4-2). This can be considered as an indication for π -electron delocalisation existence at 1 Å height.

However, for a molecule, it is important to perform, analyse and evaluate the magnetic shielding activities for the whole molecular volume before assessing aromaticity of the molecule. The magnetic shielding observations at/near the molecular plane of croconate behave against the shielding at 1 Å. This magnetic behaviour is similar to the magnetic behaviour of antiaromatic molecules. Therefore, croconate, based on its magnetic behaviour, is an antiaromatic compound.

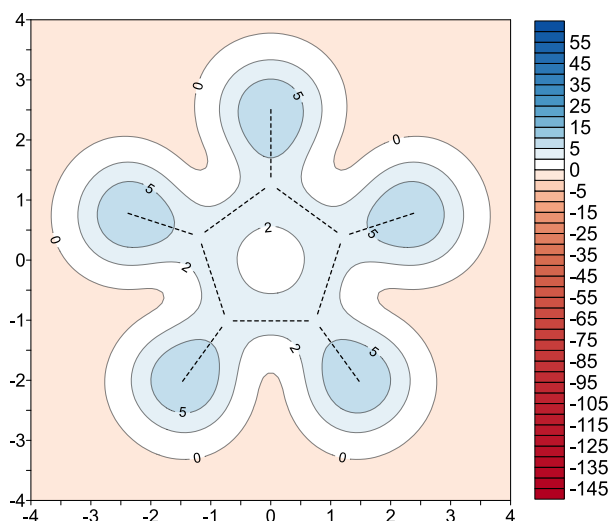


Figure 4-15: Contribution of the vertical-component of the isotropic shielding ($\sigma_{\text{iso}(zz)}$) (in ppm) to the total isotropic shielding σ_{iso} of croconate obtained at the MP2/6-311++G(2d,2p) level of theory for a grid placed at 1.00 Å above the ring.

The issue of the isotropic shielding of the croconate ring centre is represented in figure (4-16). The greatest deshielding value locates at the ring centre, followed by a gradual decrease in deshielding which switches to shielding at 0.6 Å. These findings are in agreement with the 2D shielding maps in figures (4-13) and (4-14 (a)). This fluctuation in the σ_{iso} responses indicates the antiaromatic character of croconate.

Numerical σ_{iso} variation along and above the croconate bonds are shown in figure (4-17). Low isotropic shieldings can be seen at the C-C AML besides that the carbon deshielded-spheres comprise most of the C-C bond, see curve (a1). In addition, the C-O bond AML seems less polarised towards oxygen than that of squarate, see plots (a2) in figures (4-17) and (4-11), respectively. Curves (b2) of these figures not only show the similarity in shielding trend at 1 Å but also show more shielding intensity above the oxygen of croconate than that of squarate. Whereas curves (b1) show less than 1 (ppm) shielding fluctuation along a line placed at 1 Å above the C-C bonds.

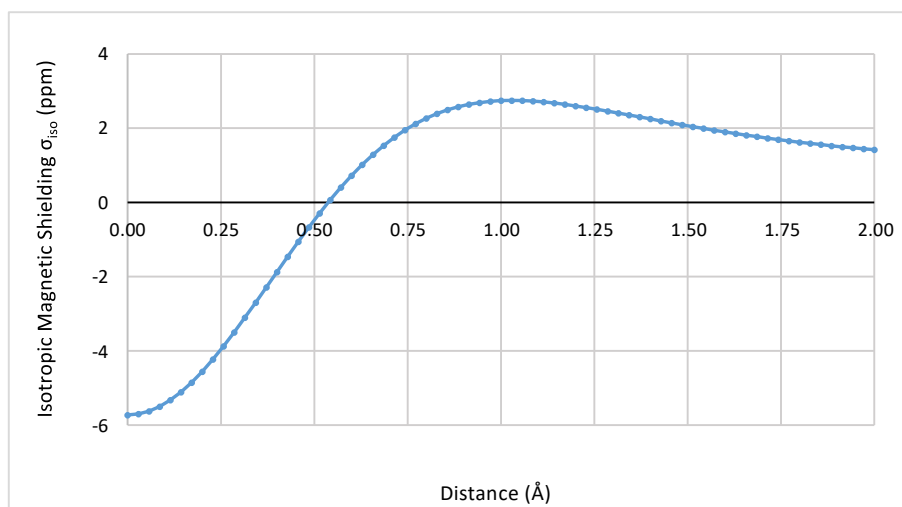


Figure 4-16: Variation in the MP2/6-311++G(2d,2p) isotropic shieldings σ_{iso} (in ppm) above the croconate ring obtained from 71 ghost atoms placed perpendicularly from the ring centre to a 2 Å height above it.

Despite the similarity in the blue/red +16/-16 (ppm) shielding isosurfaces of croconate and squarate, see figures (4-18) and (4-12), respectively, several differences in the isotropic shielding behaviour can be observed.

The -5 (ppm) transparent red isosurfaces shows the carbon deshielded-

spheres extension and their meeting at the middle area of croconate ring. Whereas +8 (ppm) transparent isosurface displays the shieldings around the croconate structure.

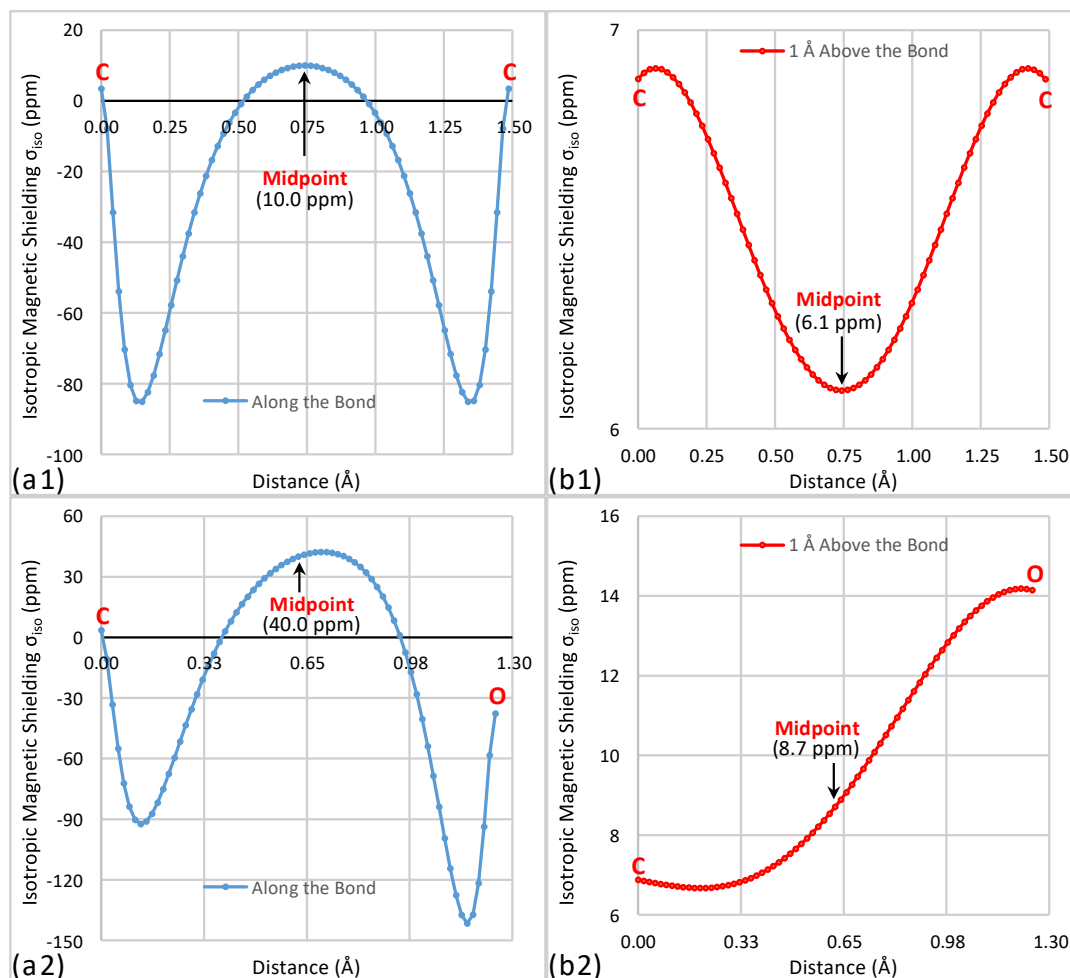


Figure 4-17: Variation in the MP2/6-311++G(2d,2p) isotropic shielding (σ_{iso}) (in ppm) along C-C and C-O bonds in croconate obtained from 71 ghost atoms: (a) placed along the bonds and (b) placed 1 Å parallelly above the bonds.

In agreement with the 2D results, most of the previous findings of this section can be seen in the figure (4-18). For instance, the deshielded tunnels which link all the carbon deshielded-spheres at the ring centre. Another example, the weaker shieldings of C-C bonds besides their shifts towards outside regions of the ring.

Finally, to sum up the isotropic shielding results of croconate, the deshieldings exceed the shieldings, and the overall magnetic shieldings assign the antiaromaticity of croconate.

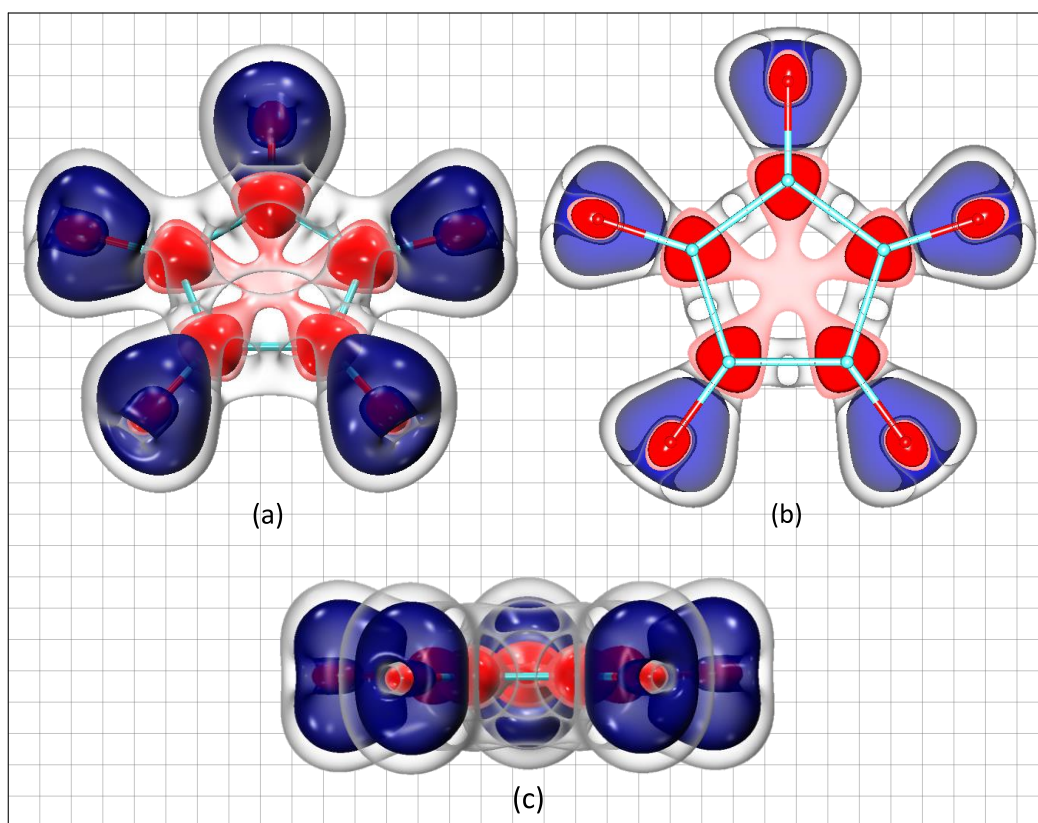


Figure 4-18: Front view (a), cross-section (b) and side view (c) of the 3D isotropic shielding isosurfaces for croconate obtained from MP2/6-311++G(2d,2p) calculations. The isosurfaces visualise (σ_{iso} /colour), +16/blue, -16/red, +8/transparent and -5/transparent red.

4-4 Rhodizonate

Unlike the three smaller planar oxocarbon dianions, the six-membered ring of rhodizonate is nonplanar with a C_2 point group. The C_2 geometry was optimisation under the DFT B3LYP/6-311+G(2d,2p) calculations. The optimisation was checked with no imaginary frequencies.

The nuclear isotropic shielding values for symmetry unique nuclei are listed in table (4-4). In comparison with croconate, more $|\Delta\sigma_{\text{iso}(C-O)}^{0\text{\AA}}|$ difference is found in rhodizonate, besides the carbon and oxygen nuclei continue in increasing their shielding and deshielding, respectively. In addition, the general similarity/dissimilarity of the isotropic shieldings from the MP2 and the HF level of theory are observed in a similar manner of the previous oxocarbon dianions.

Table 4-4: MP2/6-311++G(2d,2p) and HF/6-311++G(2d,2p) isotropic shieldings data (in ppm) for rhodizonate C and O nuclei and for points placed 1 Å above the nuclei as well as the vales of $|\Delta\sigma_{\text{iso}(C-O)}^{0\text{\AA}}|$ and $|\Delta\sigma_{\text{iso}(C-O)}^{1\text{\AA}}|$ shielding parameters.

	C		O		C-O	
	Nuclear σ_{iso} (ppm)	σ_{iso} 1Å above nuclei	Nuclear σ_{iso} (ppm)	σ_{iso} 1Å above nuclei	$ \Delta\sigma_{\text{iso}(C-O)}^{0\text{\AA}} $	$ \Delta\sigma_{\text{iso}(C-O)}^{1\text{\AA}} $
MP2	16.75 (C1)	6.62	-99.16 (O1)	14.28	115.91	7.66
	13.63 (C2)	6.52	-103.73(O2)	13.76	117.36	7.24
	13.92 (C3)	6.98	-103.32 (O3)	14.60	117.24	7.62
HF	6.51 (C1)	6.97	-133.86 (O1)	15.17	140.37	8.20
	4.17 (C2)	6.91	-136.80 (O2)	14.66	140.97	7.75
	4.38 (C3)	7.44	-136.57 (O3)	15.63	140.95	8.19

Due to the nonplanarity of rhodizonate, the first horizontal 2D grid ($z=0.00$) in figure (4-19 (a)) was placed at an averaged position in which only two bonds of C1-O1 and C4-O4 are laid on the 2D grid, whereas the other C-C and C-O bonds are either in- or out-plane of the grid, see figure (4-19) for atoms labelling. The other four grids, (c-e), were parallelly placed above the first grid.

If one inspects figures (4-(19-23,25)), the similarities can easily be noticed between the isotropic shielding behaviour of rhodizonate and croconate. For instance, the σ_{iso} and $\sigma_{\text{iso}(zz)}$ shielding profiles at 1Å above the averaged molecular plane (figures (4-19(e)) and (4-20)), the general shielding profile at and above the ring centre (figure (4-21)), the deshielded-spheres of carbon

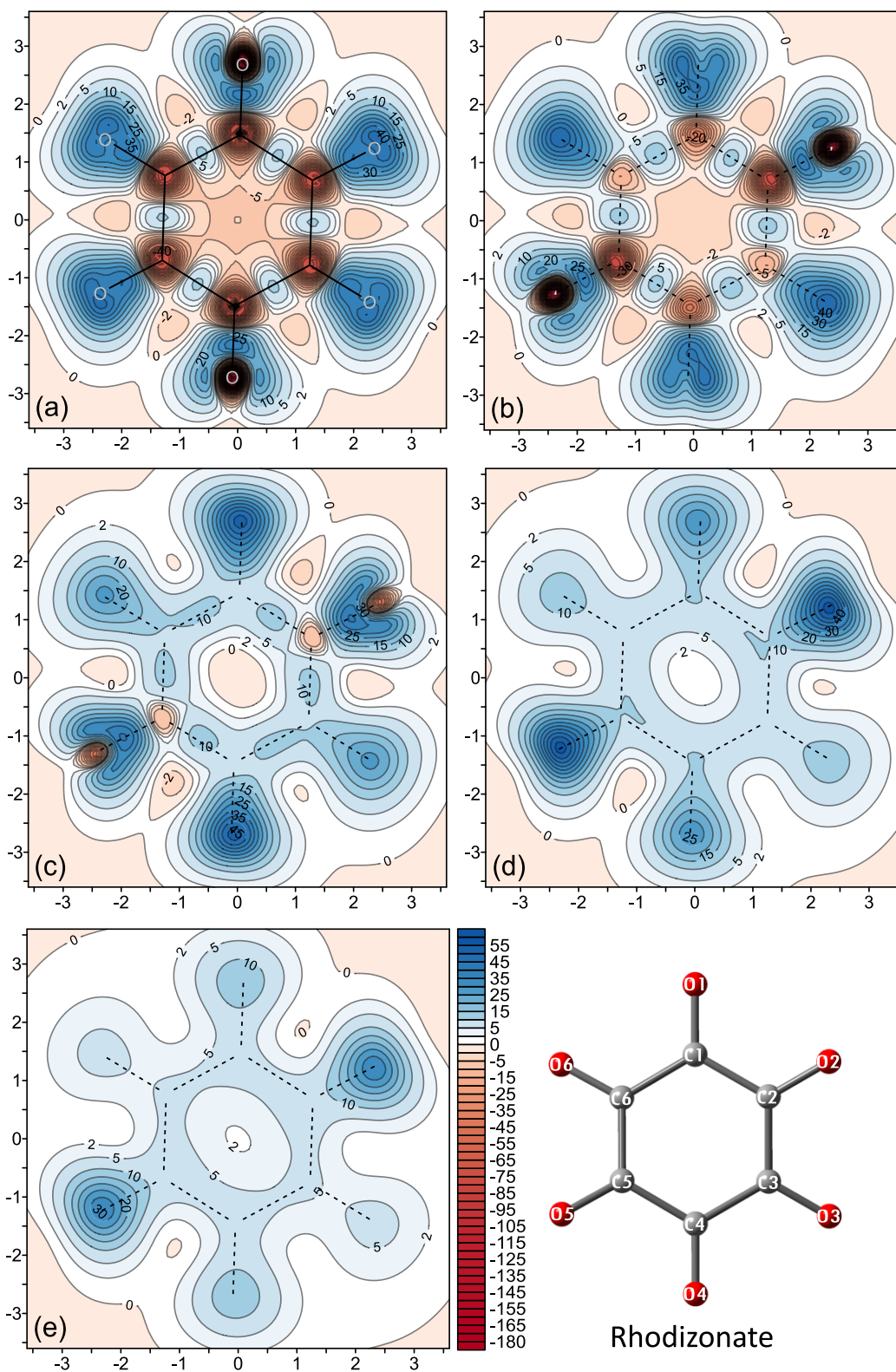


Figure 4-19: Five contour maps of the isotropic shieldings (σ_{iso}) (in ppm) obtained at the MP2/6-311++G(2d,2p) level of theory for rhodizonate. (a): from a grid placed at averaged position at the ring, (b-e) from grids placed at 0.25, 0.50, 0.75 and 1.00 Å heights above the first grid, respectively.

and oxygen as well as the expansion and the meeting of the carbon deshielded-spheres at the ring centre area (figures (4-19(a)) and (4-22(a))), the effects of the deshieldings on the clouds of the C-C and C-O bonds (figures (4-19) and (4-22)), the shielding behaviours of the C-C and C-O bonds (4-23) and finally the general 3D shielding isosurfaces (4-25). However, several differences have been observed between rhodizonate and croconate.

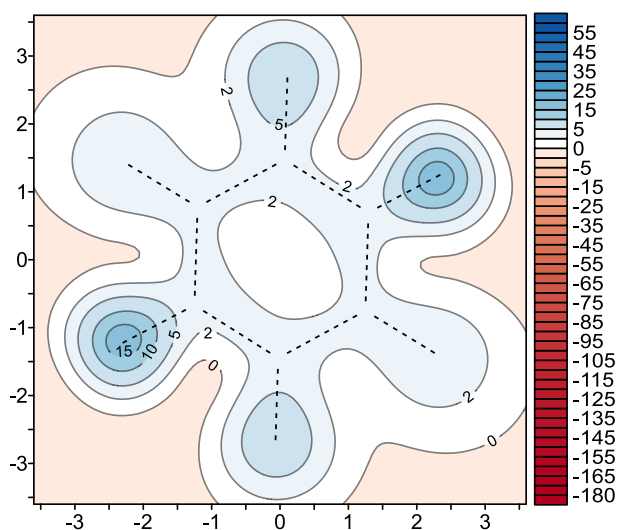


Figure 4-20: Contribution of the vertical-component of the isotropic shielding ($\sigma_{izo(zz)}$) (in ppm) to the total isotropic shielding σ_{izo} of rhodizonate obtained at the MP2/6-311++G(2d,2p) level of theory for a grid placed at 1.00 Å above the ring.

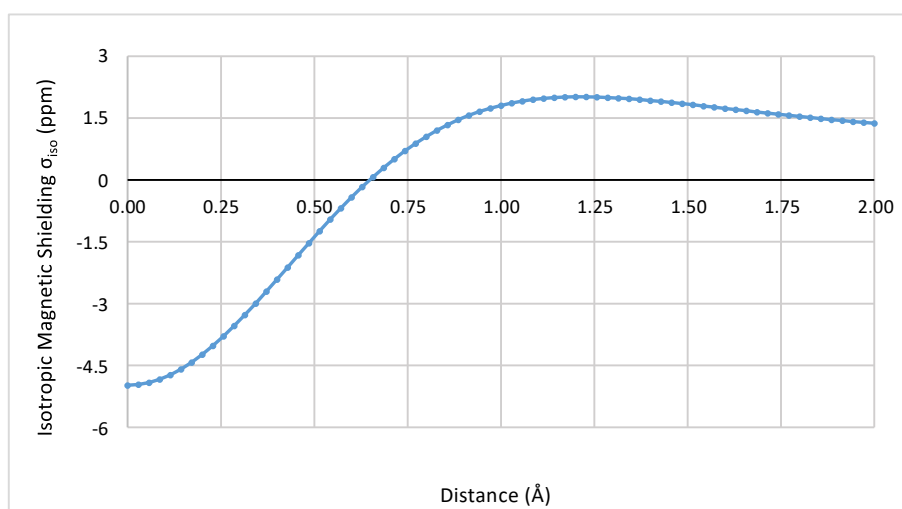


Figure 4-21: Variation in the MP2/6-311++G(2d,2p) isotropic shieldings σ_{izo} (in ppm) above the rhodizonate ring obtained from 71 ghost atoms placed perpendicularly from the ring centre to a 2 Å height above it.

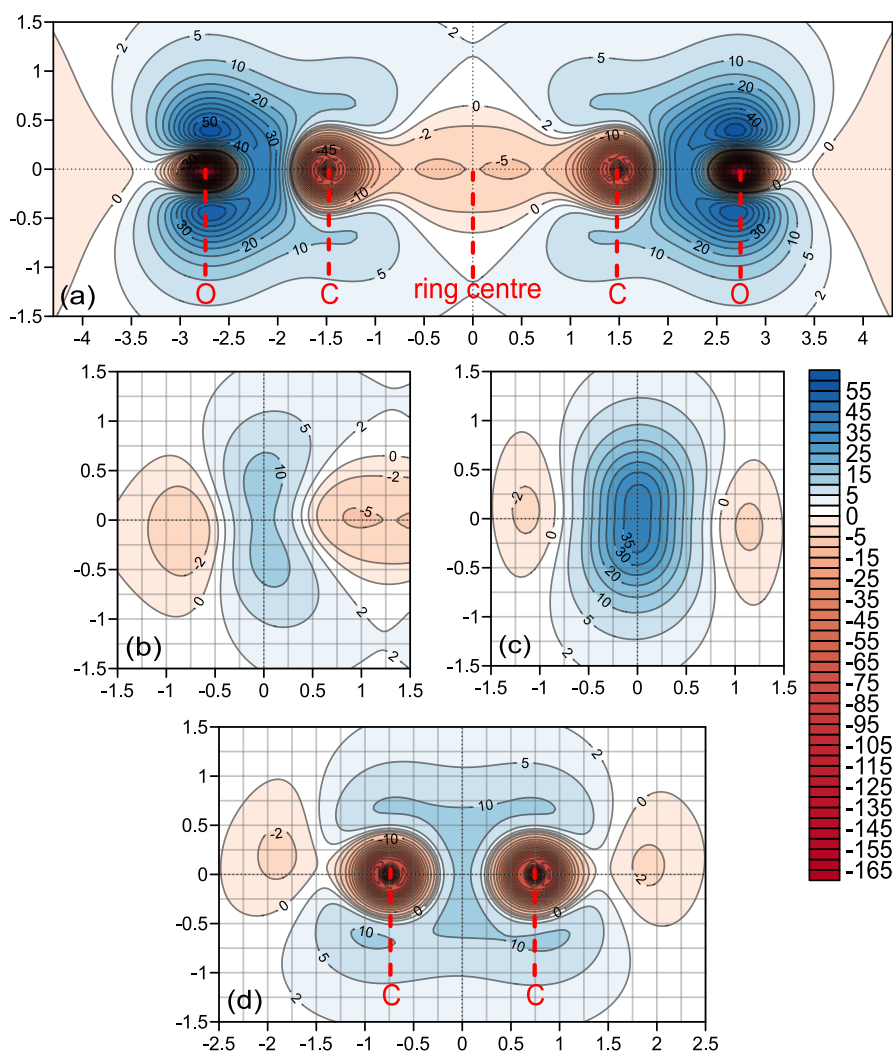


Figure 4-22: MP2/6-311++G(2d,2p) isotropic shielding cross-sections set perpendicularly to rhodizonate: (a) along O-C-(ring centre)-O-C diagonal, (b) along midpoints of the C-C bond, (c) passing through the C-O bond midpoint and (d) along the C-C bond.

The greatest difference is that the deshielded-sphere becomes bigger around oxygen and smaller around carbon. This can be seen horizontally in figure (4-19 (a)) and vertically in figure (4-22 (a)). This belongs to the weakness in the isotropic shieldings around oxygen which allows the sphere expansion. Figure (4-23) shows that the shielding increased for the C-C bond and decreased for the C-O bond with less shielding polarisation of AMBL towards oxygen. In agreement, tables (4-3) and (4-4) show that the carbon nuclei is more shielded in rhodizonate than in croconate by around 13 (ppm).

Besides, figures (4-23 (a1) and 4-17 (a1)) show the maximum deshielding value of carbon deshielded-sphere for rhodizonate and croconate are -75.5

and -85.1 (ppm), respectively. This forms a convenient magnetic environment allowing the shielding clouds of the C-C bonds to recover positions at their bonds, see figures (4-19 (a)) and (4-22(b)). A further lowering in width of the shielding cloud of the C-O bond can be seen in figure (4-22 (c)) due to the increase of the left and right deshieldings besides a weaker C-O shielding cloud, see the C-O bond AMBL in figure (4-23 (a2)).

The isotropic shielding responses at the ring centre indicate lower deshieldings strength in rhodizonate than croconate, see figures (4-21),(4-16) and (4-22(a)),(4-14(a)). The larger six-membered ring area and/or the nonplanarity of the rhodizonate ring cause such lowering in the deshieldings. Therefore, lower deshieldings in rhodizonate than in croconate can represent a lower antiaromaticity profile for the former.

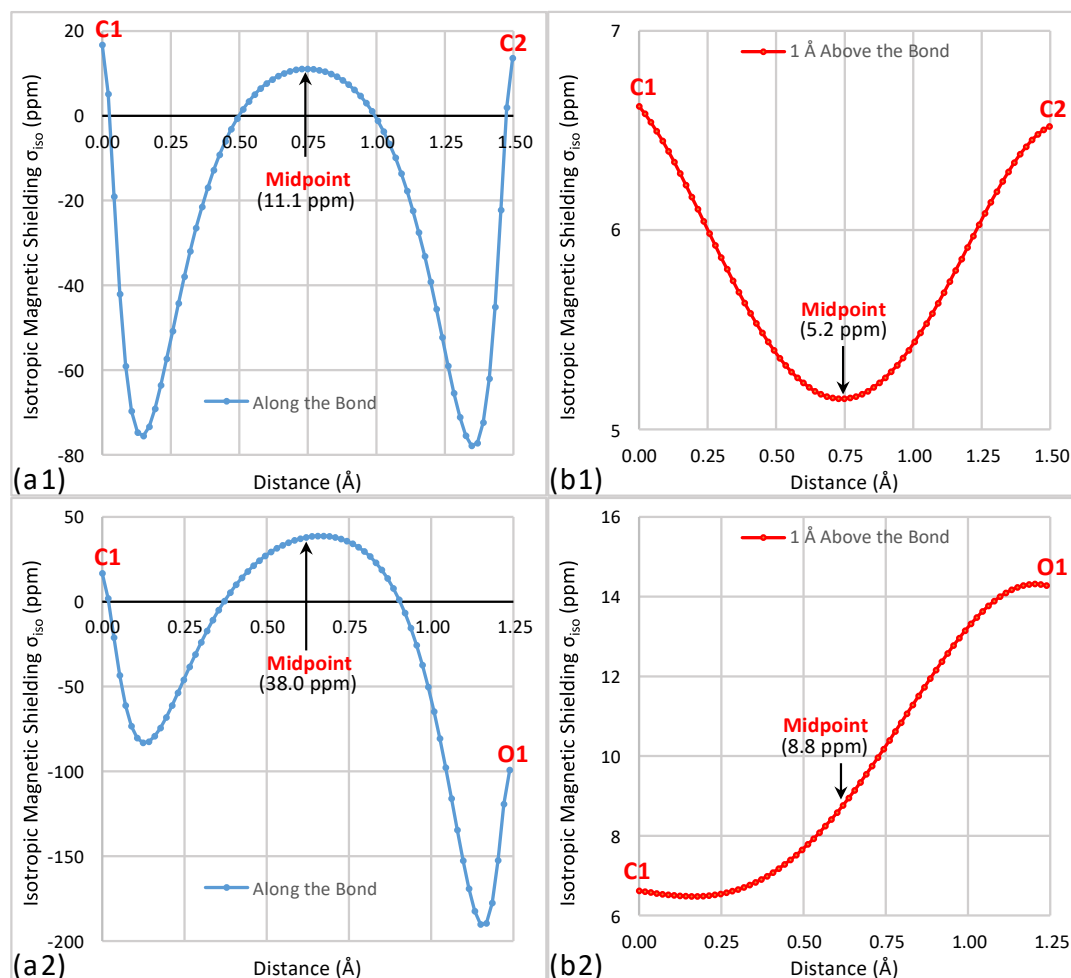


Figure 4-23: Variation in the MP2/6-311++G(2d,2p) isotropic shielding (σ_{iso}) (in ppm) along C1-C2 and C1-O1 bonds in rhodizonate obtained from 71 ghost atoms: (a) placed along the bonds and (b) placed 1 Å parallelly above the bonds.

Deltate and squarate tend to show electron delocalisation which can be concluded from their magnetic shieldings. The larger oxocarbons have a tendency to become like cross-conjugated dianions. For instance, although the suggested resonance mechanism of rhodizionate is representable through six resonance structures of (1-6) as shown in figure (4-24(a)) below, the equivalent structure (i) is inconsistent with the shielding behaviour of rhodizionate. In contrast, structure (ii), as a dianionic cross-conjugated system, gives better description of the electronic features of rhodizionate.

In more detail, increasing the number (n) of $C_nO_n^{2-}$ of the oxocarbon dianions affects the isotropic shielding behaviour in two ways. Firstly, with increasing (n), the ring area increases too. This means that, when adding ($-2e$) charge to a larger ring, the value of ($-2e/\text{ring area}$) (or $-2e/\text{volume}$) will decrease. Thus, the smallest three-membered ring of deltate gains the highest ratio. Secondly, increasing the number (n) will increase the number of the $C=O$ bonds, which act as electron-withdrawing groups. This can be considered as an additional factor in reducing the electron density per volume of a ring. Thus, with increasing the (n), the electron circulation, magnetic properties and aromaticity decrease.

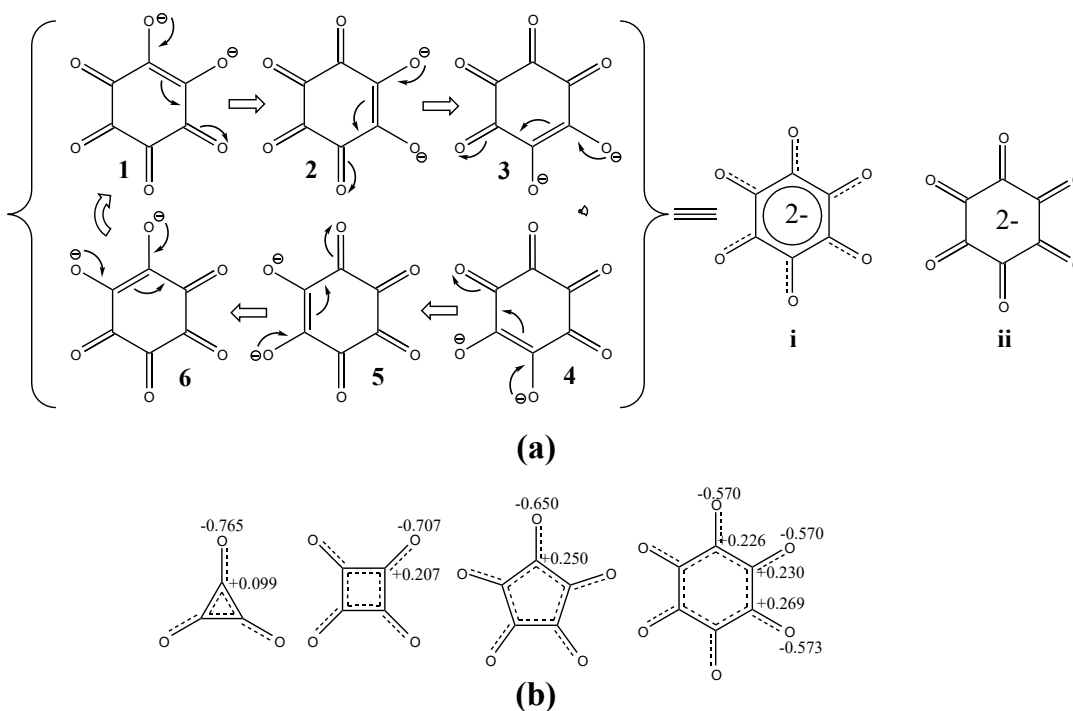


Figure 4-24: Resonance structures of rhodizionate, (a), and Mulliken charge distribution values for carbon and oxygen of oxocarbon dianions, (b), which were calculated at DFT B3LYP/6-311++G(2d,2p) level of theory.

Mulliken charge distribution values of the oxocarbon dianions, figure (4-24 (b)), support the above suggestions. Increasing the oxocarbon dianion size causes the oxygen atoms to become less negatively charged, while the positive charge of carbon atoms is increased. Remarkably, deltate shows the smallest carbon positive charge and highest oxygen negative charge, 0.099 and -0.765, respectively. This also directly affects the electron delocalisation and lead to the same conclusion, that the deltate shows a stronger shielding and aromatic profile. In contrast, the delocalisation destabilised the larger oxocarbon dianions due to the above factors.

All the 3D isosurfaces of rhodizonate were visualised by the same colours/shielding/deshielding parameters of croconate, see figures (4-25) and (4-18), respectively. Most points mentioned in the discussion of this section can be seen in figure (4-25).

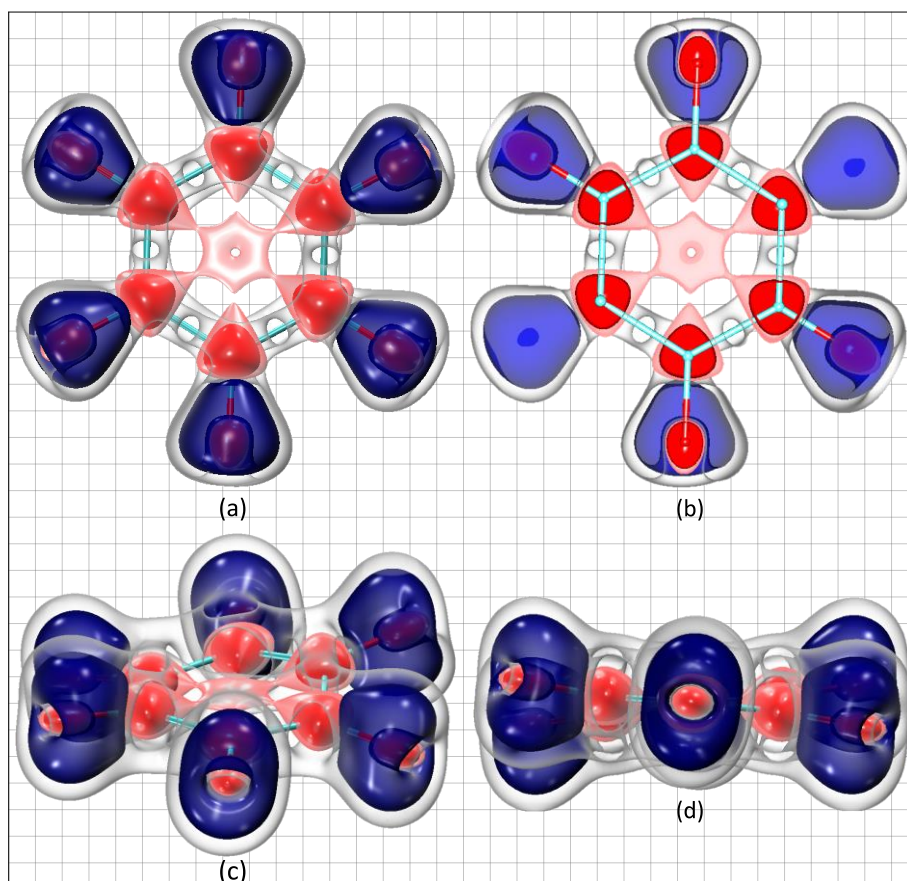


Figure 4-25: Front view (a), cross-section (b) and top views (c and d) of the 3D isotropic shielding isosurfaces of rhodizonate obtained from MP2/6-311++G(2d,2p) calculations. The isosurfaces visualise (σ_{iso} /colour): +16/blue, -16/red, +8/transparent and -5/transparent red.

The most remarkable one is that the recovery of the C-C shielding clouds their locations at the bonds with shielding increase at their AMBLs, see also the deshieldings lowering at the inner region of the ring. Moreover, the shrinking of the blue clouds around the C-O bonds is partly because of the deshielded-spheres of oxygen become larger in size and higher in deshielding and partly because the weakness in their shielding strength. Another point, the twisting of the shielding clouds of the C-C bonds can also be seen since the nonplanarity of the ring skeleton. Thus, rhodizonate is antiaromatic but less antiaromatic than croconate.

4-5 Conclusions

Employing different types of isotropic shielding investigations on the oxocarbon dianions lead to several important observations. One of these, the ability to follow up the isotropic shielding behaviour not only through the spaces of each of the oxocarbons but also via comparing the shielding behaviour among the members of the oxocarbon dianions.

Both HF and MP2 showed a similar magnetic theme but with lower nuclear isotropic shielding values from HF than from MP2 calculations. A reversed trend is found for the shielding values of points placed at 1 Å above the nuclei.

The $|\Delta\sigma_{\text{iso}(\text{C}-\text{O})}^{0\text{Å}}|$ and $|\Delta\sigma_{\text{iso}(\text{C}-\text{O})}^{1\text{Å}}|$ parameters with line graphs placed along and above the C-O bonds show the isotropic shielding variation degree for nuclei of a bond and for points located vertically above the bond. The $|\Delta\sigma_{\text{iso}(\text{C}-\text{O})}^{1\text{Å}}|$ for the C-O bonds of the studied oxocarbon dianions seems to be the same, whereas the $|\Delta\sigma_{\text{iso}(\text{C}-\text{O})}^{0\text{Å}}|$ show a remarkable decrease with increasing the size of planar dianion, whereas a significant increase is observed for rhodizonate.

Curves show the highest shielding at the C-C bond midpoints is for deltate followed by squarate with a remarkable decrease, then the lowest for croconate, while rhodizonate shows slightly more shielding than croconate. the polarisation degree and the shieldings at C-O bond AMBLs decrease with increase the ring size. Also, the isotropic shielding of oxygen changed from well-shielded with no deshielded-sphere in deltate to very-deshielded with large deshielded-sphere in croconate and rhodizonate. Differently, the lines placed at 1 Å above bonds show the predominance of the isotropic shieldings in all the oxocarbon dianions with slight differences in shielding values.

Greatest shieldings at ring centre is shown by deltate, which is followed by squarate, while croconate is the highest in the deshielding activities at the ring centre followed by rhodizionate.

Moreover, the 2D shielding maps represent the deltate ring as one shielding cloud unified with the C-C bonds shielding clouds. Whereas squarate has a moderate shielding, the ring of croconate and rhodizionate are managed by deshielding activities of the carbon deshielded-spheres which showed an expansion towards the ring centre.

Also, the five parallel 2D layers show that all the deshielding effects are found at lower heights near the molecular plane, whereas at higher heights, even for highly deshielded rings, the shielding activity is the predominant. In agreement, $\sigma_{\text{iso}(zz)}$ maps show a similar shielding profile and indicate the ring currents existence. However, aromaticity evaluation must depend on several magnetic investigations though whole the molecular and the nearby spaces.

The shielding clouds extend beyond that of the oxygen atom of the of the C=O bonds themselves. Also, these bonds show a polarisation in shielding clouds towards oxygen. This behaviour is due to C=O bond polarity, electronegativity difference between oxygen and carbon and oxygen lone pairs localisation.

The shielding/deshielding activities tend to avoid each other. A weaker activity tries either change its location, expand its activity in available nearby spaces, or shrink its sphere to a smaller size when it is fully surrounded by an opposite and stronger magnetic activity. For instance, the shifts of the shielding cloud of the C-C bonds to outside ring frame in squarate and croconate. Another example, the shrinkage of the oxygen deshielded-sphere of croconate.

With increasing the number (n) of $\text{C}_n\text{O}_n^{-2}$, the ring area increases and $(-2e)/\text{ring area}$ decreases for larger area. Also, increasing the (n) means increasing the number of the C-O bonds in which act as electron withdrawing groups. Thus, the electron density per volume unit of a ring decreases and electron movements/aromaticity decreases too.

Finally, depending on the isotropic shielding findings, the aromaticity degree of the studied oxocarbon dianions can follow this classification: Deltate aromatic, squarate moderately aromatic and croconate and rhodizionate antiaromatic.

CHAPTER FIVE

DISULFUR DINITRIDE

5-1 Introduction

Disulfur dinitride, the inorganic four-membered heterocyclic ring with a chemical formula of S_2N_2 , has been known since the start of the twentieth century.^[137] S_2N_2 can be prepared thermally by passing S_4N_4 as gaseous vapour (heated up to 300°) over silver wool to depolymerise S_4N_4 to S_2N_2 .^[138,139] The crystals of the latter are insoluble in water but they have a good solubility in several organic solvents^[138] and they can be polymerised to polysulfur nitride^[140], $(SN)_x$, which exhibits superconductivity^[141] and metallic conductivity^[142].

Because of the unusual nature of the smallest inorganic six π -electron aromatic molecule, namely S_2N_2 , many attempts have been made to understand its chemical and structural features. For example, there are several suggestions for the electronic structure of S_2N_2 , see figure (5-1) which schematically shows the most popular models of S_2N_2 , (see also references [143] and [52]). According to Greenwood and Earnshaw,^[138] the structure of S_2N_2 is shaped as D_{2h} square-planar with two different N-S bond lengths, 1.651 and 1.657 Å and the measurements of S-N-S and N-S-N angles are 90.4 and 98.6 degrees, respectively. Similar structural measurements were reported by Findlay et al.^[144] who employed *ab initio* calculations. They also concluded that the S_2N_2 molecule has no cross-ring bonds, i.e., no S-S or N-N bridged-bonds (see models (i) and (iii) in figure (5-1)).

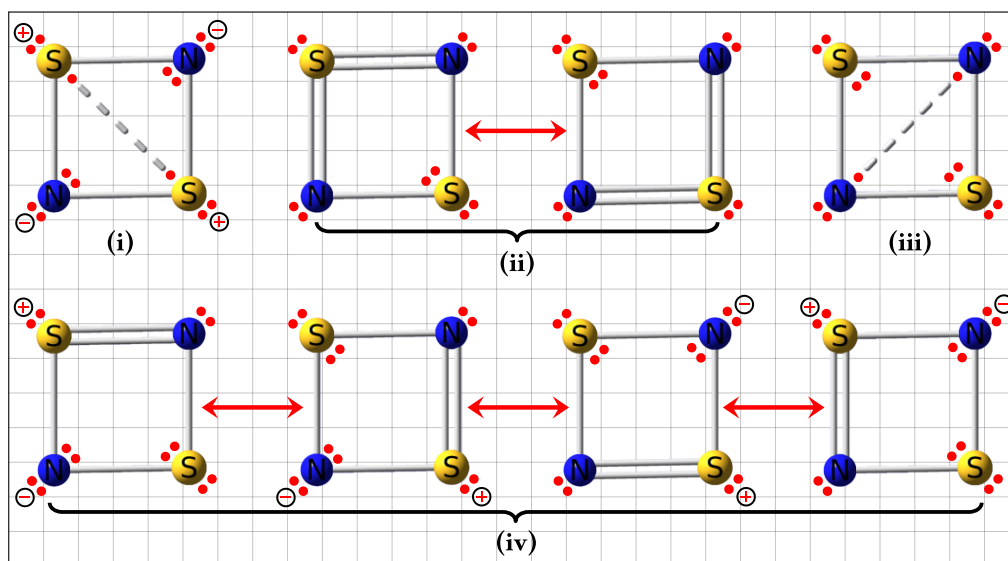


Figure 5-1: The most common electronic structure suggestions for disulfur dinitride.

In contrast to this, Gerratt and co-workers^[145] suggested, via the π -space spin-coupled bond method, that S_2N_2 has singlet diradical features. In addition, to this suggestion, each atom of S_2N_2 has one electron lone pair, centred about nitrogen, or, in the case of sulfur, coupled across the S-S diagonal. See model (i) in figure (5-1)).

The S-N bond of S_2N_2 was described^[146] as polar bond because of the charge transfer from sulfur to nitrogen. The back-bonding from p_π of nitrogen to d_π of sulfur was reported by Brant and co-workers.^[147] They found that the back-bonding is not necessary for the S-N bonding in S_2N_2 .

Head-Gordon and collaborators^[143] pointed out the consistency between the formal charges, i.e., N(-) and S(+) shown in figure (5-1), and the electronegativity difference between nitrogen and sulfur since nitrogen has higher electronegativity. Head-Gordon et al.^[143] also found that the natural and Mulliken atomic charges are positive for sulfur and negative for nitrogen. This charge profile is in agreement with other findings.^[145,148]

The S_2N_2 aromaticity can also be considered as a topic of interest. For instance, Head-Gordon et al.^[143], according to structural and magnetic criteria, suggested that the S_2N_2 molecule follows the pattern of 2π aromatic systems with an S-N bond order of around 1.25.

Braïda et al.^[149] employed *ab initio* valence bond calculations to evaluate the S_2N_2 aromaticity. They represented the collective π -electron flow by utilising successive one-electron transfers via an eight-steps cycle chart which includes six models of (i); (iii) and (iv) shown in figure (5-1)). They confirmed the S_2N_2 aromatic features and stated that there is no contradiction between diradical character and aromaticity.^[149] The 6π -aromaticity was also studied by Zandwijk and coworkers^[150] who employed *ab-initio* molecular orbital methods and considered S_2N_2 as aromatic because of its geometric and stability properties.

Finally, we^[52] extensively researched the electronic states of S_2N_2 including the ground state; (S_1 - S_8); and (T_1 - T_8). The investigations of the isotropic magnetic shieldings, as it will be shown in this chapter, included the ground state, S_0 , the lowest first singlet state, S_1 (as $1\ ^1A_u$ for $\pi \rightarrow \pi^*$ excitation), and the lowest triplet state, T_1 (as $1\ ^3B_{3u}$ for $\pi \rightarrow \pi^*$ excitation).

5-2 Ground State (S_0) of S_2N_2

The isotropic shielding calculations for the ground state of S_2N_2 , as well as for other electronic states in this chapter, were performed at the CASSCF(22,16)/cc-pVTZ level of theory. The semi-experimental D_{2h} geometry of S_2N_2 , which was obtained by Perrin et al.^[151], was used during all the isotropic shielding calculations.

As it can be seen from table (5-1), both the sulfur and nitrogen nuclei are deshielded but the deshielding of the latter is significantly higher. A different shielding profile at 1 Å above the nuclei can be observed. The shielding values decreased to about one-tenth of the nuclear shieldings. If the absolute difference values of $|\Delta\sigma_{iso(S-N)}^{0\text{Å}}|$ and $|\Delta\sigma_{iso(S-N)}^{1\text{Å}}|$ are compared, one can notice that the value of the latter is much lower than the former.

Table 5-1: CASSCF(22,16)/cc-pVTZ isotropic shielding data (σ_{iso}) (in ppm) of ground state of S_2N_2 for sulfur and nitrogen nuclei and for points placed 1 Å above them as well as absolute shielding difference values of the S-N bond nuclei, $|\Delta\sigma_{iso(S-N)}^{0\text{Å}}|$, and of points located 1 Å above the nuclei, $|\Delta\sigma_{iso(S-N)}^{1\text{Å}}|$.

	Nuclear σ_{iso} (ppm)	σ_{iso} 1 Å above nuclei	$ \Delta\sigma_{iso(S-N)}^{0\text{Å}} $	$ \Delta\sigma_{iso(S-N)}^{1\text{Å}} $
S	-77.79	9.50	42.50	2.57
N	-120.29	12.07		

More shielding details are displayed by the 2D shielding maps, see figure (5-2). In general, the shielding assigns aromatic features to S_2N_2 . The S-N bond domains are obviously well-shielded. Interestingly, although the sulfur nuclei are deshielded, see table (5-1), they are surrounded by very highly shielded-spheres. In contrast to this, the nitrogens are also surrounded by deshielded-spheres. Both types of sphere have radii of around 0.5 Å, see maps (a,b).

Three other shielding features can also be observed from figure (5-2). The first regards the shielding cloud corresponding to π -electron delocalisation which correspond to contour level of 1-5 (ppm) shaped as a hollowed-centre four-pointed star, see maps (a-e). However, at 0.75 Å, see map (d), another star-shaped cloud of 10 (ppm) represents the maximum activity of the π -electron delocalisation at that height, which decreases to 7.5 (ppm) at 1 Å, see map (e).

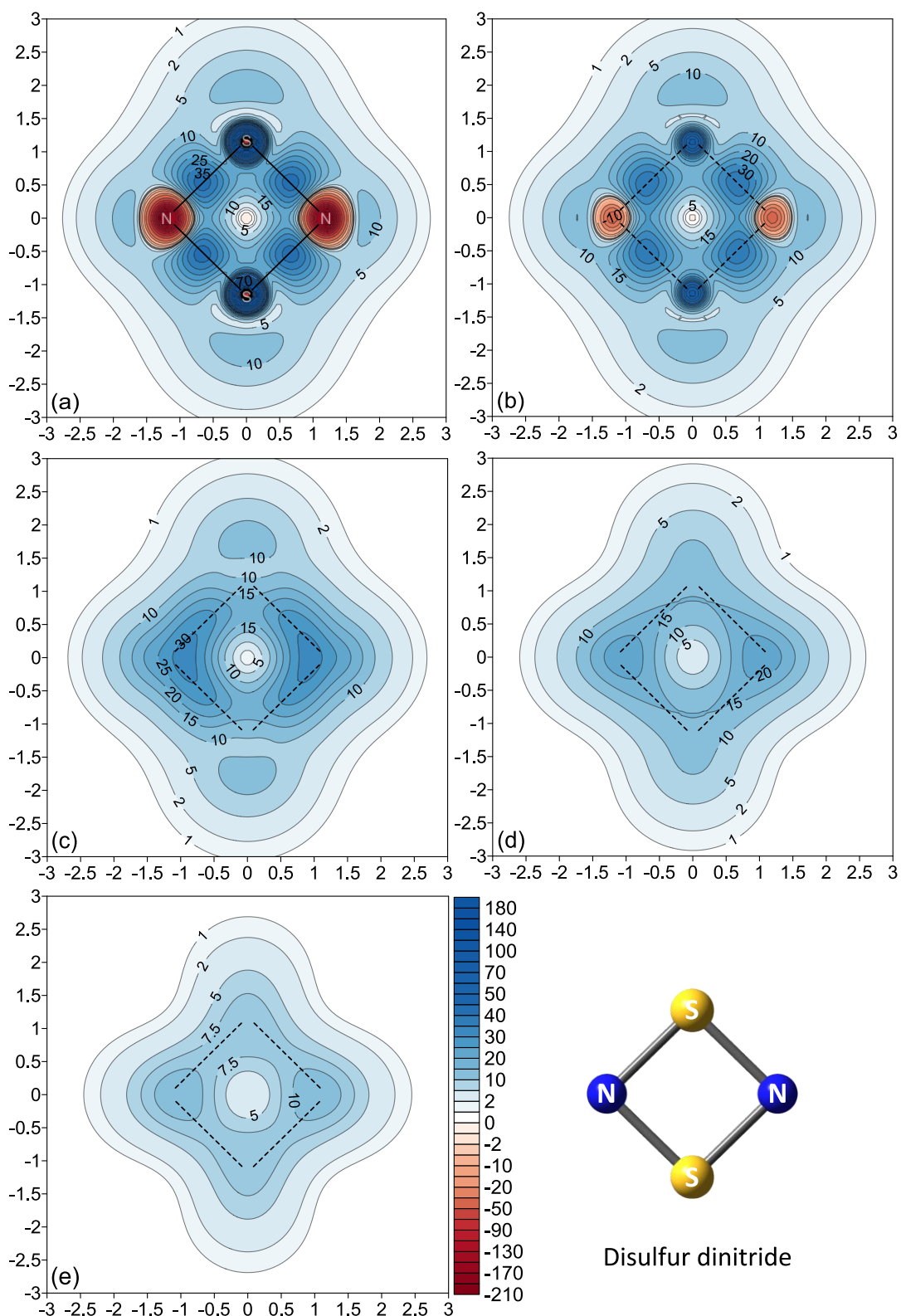


Figure 5-2: Five contour maps of isotropic shieldings (σ_{iso}) (in ppm) obtained at the CASSCF(22,16)/cc-pVTZ level of theory for the ground state of disulfur dinitride. (a-e): grids parallelly placed at 0.00, 0.25, 0.50, 0.75 and 1.00 Å heights above the molecular plane, respectively.

The second point shown by figure (5-2) relates to the shielding clouds of the lone pairs. The shielding islands located at the corners of above-mentioned star shapes in maps (a-c) besides two shielding islands above the nitrogens in maps (d,e) represent the shielding activity of the lone pairs of the nitrogens and sulfurs. When comparing these shielding activities of the lone pairs, it is obvious that higher contributions come from the nitrogens rather than the sulfurs.

Both points mentioned above can also partially be noticed in figure (5-3) showing the vertical component of the isotropic shielding $\sigma_{\text{iso}(zz)}$.

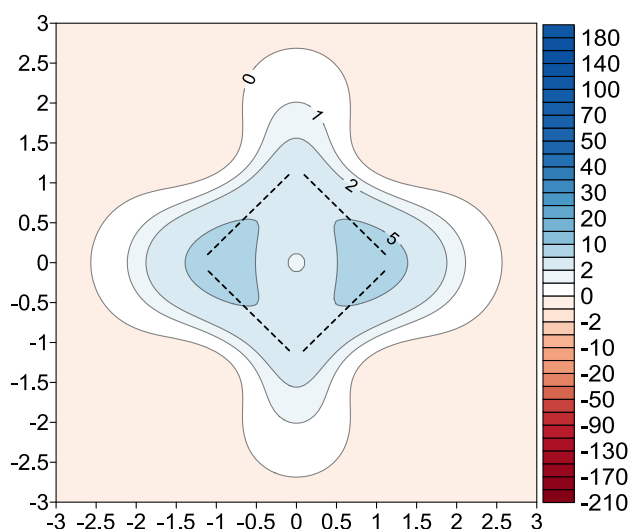


Figure 5-3: Contribution of the vertical-component of the isotropic shielding ($\sigma_{\text{iso}(zz)}$) (in ppm) in the total isotropic shielding σ_{iso} of ground state S_2N_2 , obtained at the CASSCF(22,16)/cc-pVTZ level of theory for a grid placed parallelly at 1.00 Å above the molecular plane.

The third point is that the less shielded core, LSC, of S_2N_2 becomes not only “lower in shielding” but also becomes “deshielded”. This most probably belongs to the small size of the ring of S_2N_2 which makes the σ -bonds closer, which, in turn, affects the shielding activity of the ring centre.

A clearer shielding profile above the ring centre is shown in figure (5-4). The maximum deshielding value is found at the ring centre, -0.99 (ppm). Above this point, the deshielding activity gradually fades away till 0.32 Å at which there is a switch to shielding which increases till reaching a maximum value of +2.65 (ppm) at 1.02 Å above the ring centre. Figure (5-5) shows cross-sectionally an ovoid LSC centred on the S_2N_2 ring.

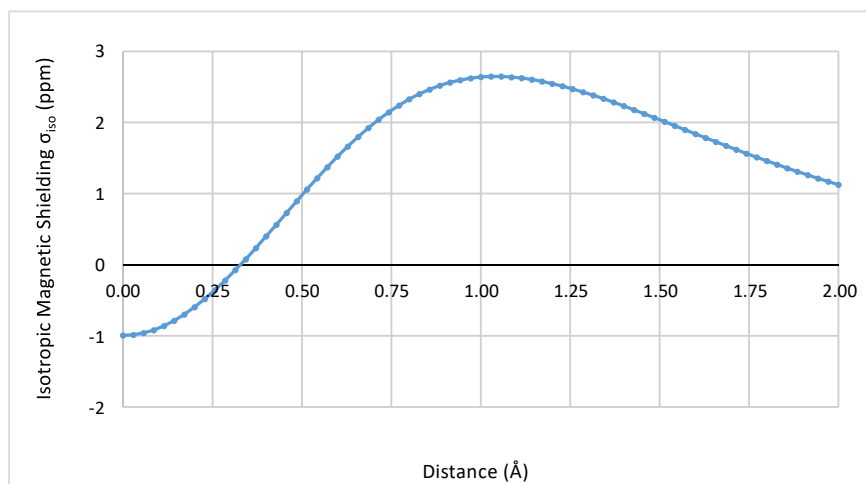


Figure 5-4: Variation in the CASSCF(22,16)/cc-pVTZ isotropic shielding σ_{iso} (in ppm) of the ground state of S_2N_2 obtained from 71 ghost atoms placed perpendicularly from the ring centre to a 2 Å height above it.

By comparing the close surroundings of the nuclei in maps (a) and (b) in figure (5-5), one can notice strongly shielded and deshielded spheres that surround sulfur and nitrogen, respectively. Outside these spheres, shielding activity about the nitrogen exceeds that about sulfur. In other words, there are higher contributions from nitrogen in S-N bonding and π -delocalisation than from sulfur. Also, the presence of two islands above and below each nitrogen in map (b) corresponds to the shielded-triangles of nitrogen lone pairs that are shown in figure (5-2 (c)). The reason for the shielding variation of both nuclei most probably belongs to the electronegativity difference and to other possible reasons mentioned in the introduction of this chapter (see section (5-1)).

Inspecting the two outer shielding borders at 1 and 2 (ppm) of the three maps in the figure (5-5) clearly highlights the shielding combination above and below the ring centre which can be considered as a characteristic feature of π -electron delocalisation at these places. The maps show no sign of diagonal shieldings along S-S or N-N bonds which can be seen in figure (5-1 (i) and (iii)). The conclusion is that such bonds do not exist.

Cross-sections of the S-N bond shielding are shown in figure (5-6). Map (a) indicates a shift of the shielding cloud from the midpoint towards nitrogen. Several factors may cause this, the delocalisation as well as the lone pair above and below the nitrogen atom promote such shifting towards nitrogen, see figure (5-2 (c-e)). The maximum shielding at the midpoint of the S-N bond

in figure (5-6 (b)) is around 40 (ppm), centred in a less-shielded triangular cloud. However, the map shows a slight shift of the above cloud towards the space outside the ring. The existence of deshielding of LSC at the ring centre, which counteracts with nearby shielding activities, is the cause of this shift. Interestingly, an example of shielding/deshielding avoidance can be observed in the shielded/deshielded spheres around sulfur represented by curve (a) in figure (5-7). The very strongly shielded-sphere, located at the sulfur with maximum shielding of +169.5 (ppm) shows a tendency to enforce the shrinkage of the inner-deshielded sphere to occupy the smallest volume possible, see also map (a) in figures (5-5) and (5-6).

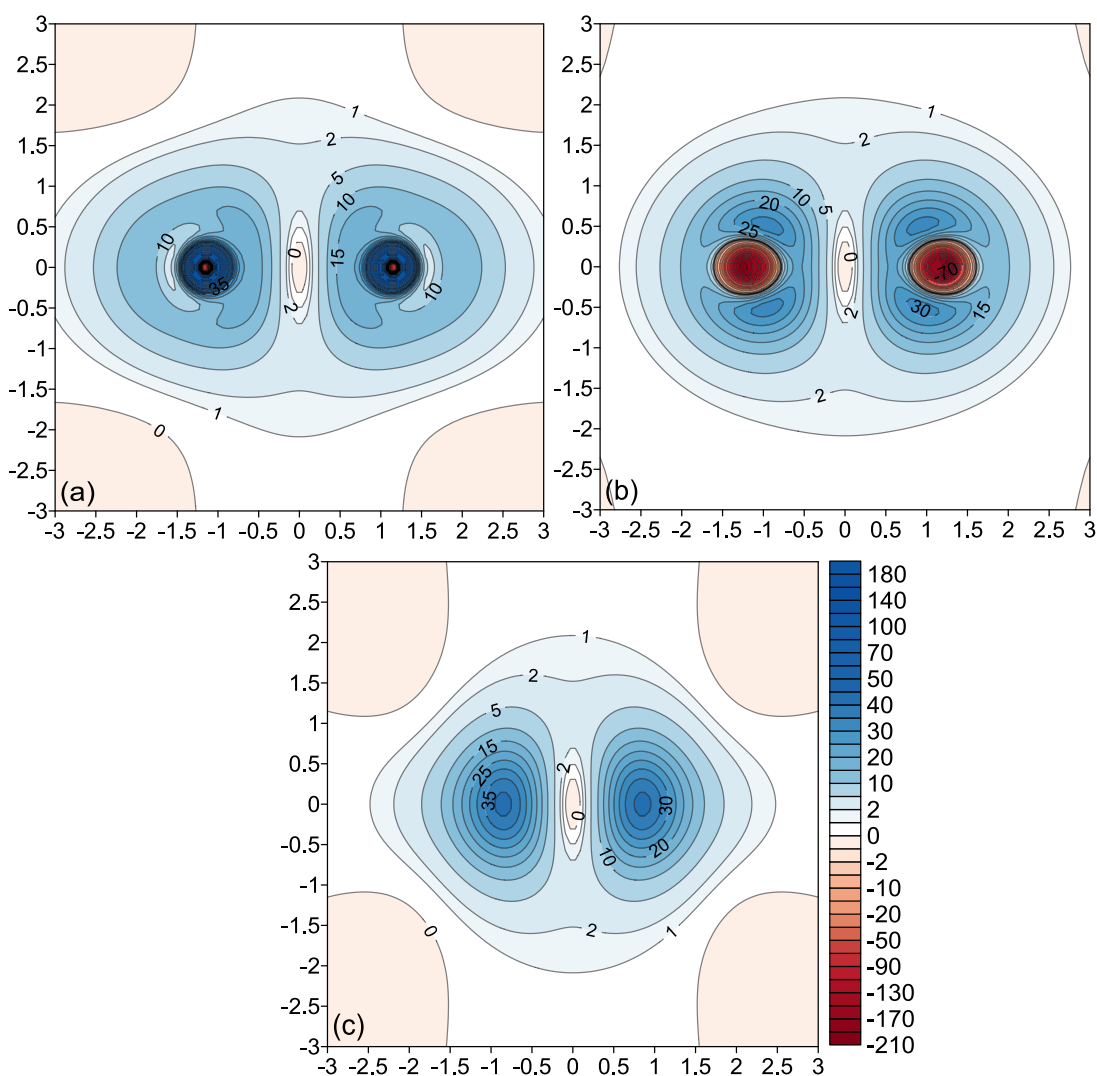


Figure 5-5: Ground state CASSCF(22,16)/cc-pVTZ isotropic shielding map obtained by utilising 2D grids placed perpendicularly to the S_2N_2 molecular plane, diagonally passing through sulfurs (a) and nitrogens (b) as YZ and XZ planes, respectively, evenly bisecting the ring and opposite S-N bonds (c).

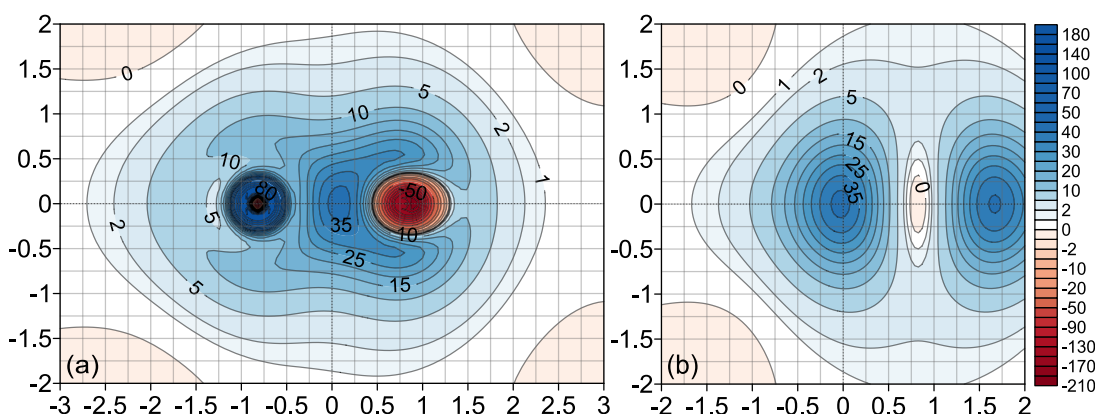


Figure 5-6: CASSCF(22,16)/cc-pVTZ isotropic shielding contour maps (in ppm) of ground state S_2N_2 obtained by utilising 2D ghost-atoms grids located perpendicularly to and passing along an S-N bond, (a), or bisecting and crossing the bond at its midpoint (b). The (0,0) X,Y point is located at the bond midpoint.

The above shielding behaviours of sulfur and nitrogen, as well as of the S-N bond, can be analysed numerically via figure (5-7). The maximum shielding value of the S-N bond AMLB is 42.6 (ppm) which is located about 0.1 Å away from the bond midpoint towards nitrogen. Also, both shielded/deshielded-spheres can be observed as shielded/deshielded peaks near the nuclei. However, the shielded-sphere of sulfur surrounds a smaller deshielded-sphere of around 0.07 Å radius. Curve (b) shows a more homogenous shielding trend than curve (a). However, the points above and near nitrogen are higher in shielding than those around sulfur.

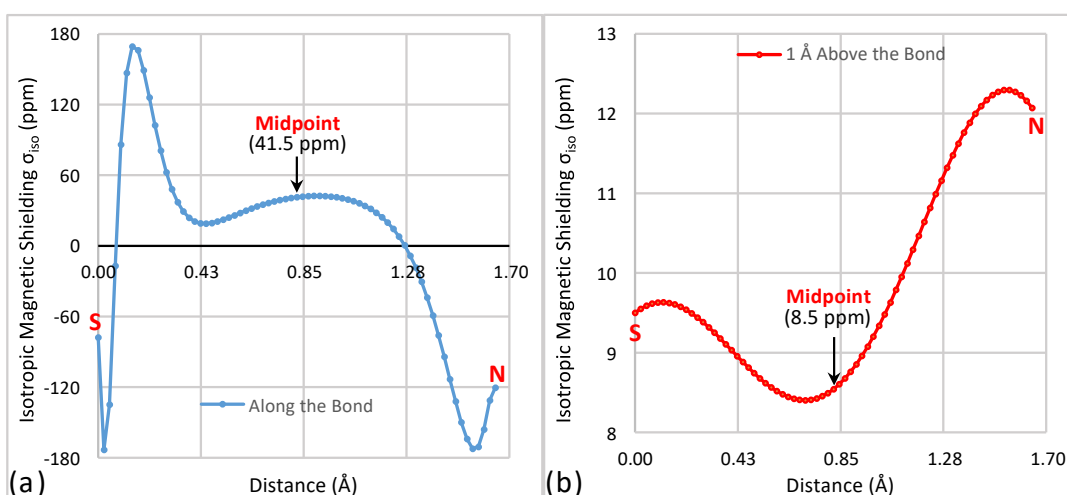


Figure 5-7: Variation in the CASSCF(22,16)/cc-pVTZ isotropic shielding (σ_{iso}) (in ppm) of the S-N bond of ground state S_2N_2 obtained from 71 ghost atoms: (a) positioned along the S-N bond, and (b) placed 1 Å parallelly above the bond.

Clearly, the blue isosurface in figure (5-8), which corresponds to +16 (ppm), indicates that S_2N_2 , in general, shares the shielding behaviour of aromatic molecules. However, the shrinking of this isosurface in regions near S-N bonds indicates lower shielding and aromatic content than aromatic molecules. The transparent isosurface at +7 (ppm) serves as a comparative tool which shows how much S_2N_2 is lower in shielding and aromaticity than aromatic molecules. The expansion trend of this isosurface is similar to that of +16 (ppm) in aromatic molecules. Thus, the ratio of +7 to +16 isosurface extents may reflect aromaticity content of S_2N_2 relative to strongly aromatic molecules.

Finally, unlike the sulfurs, the nitrogens behave like the atoms in aromatic rings because of the deshielded-spheres presence about the nitrogens. This is shown by the red isosurface of -16 (ppm) in figure (5-8).

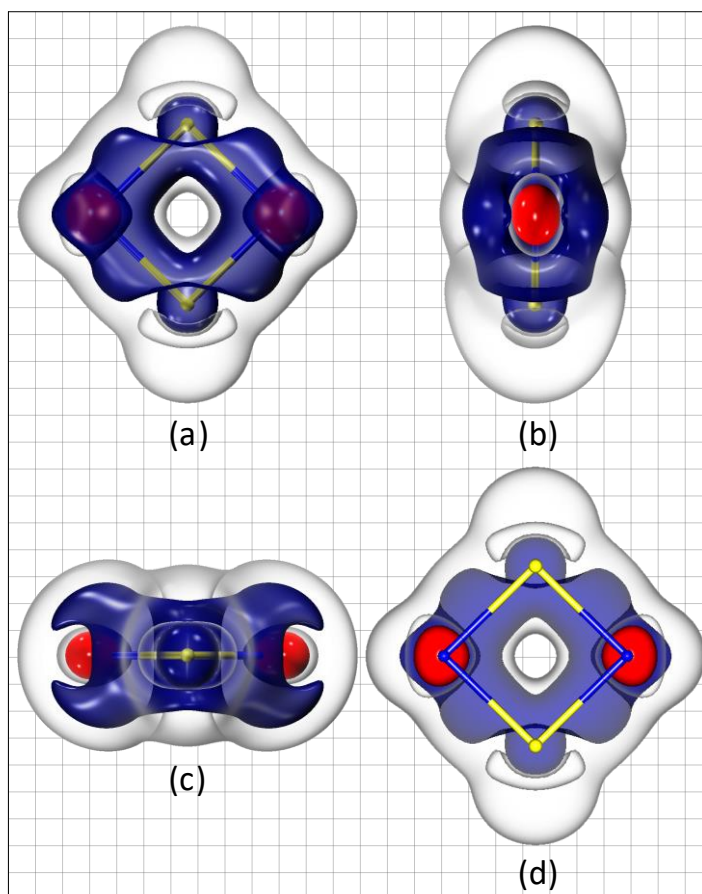


Figure 5-8: CASSCF(22,16)/cc-pVTZ isotropic shielding (σ_{iso}) isosurfaces of ground state S_2N_2 , (a) front view, (b) and (c) side views along the X- and Y-axis, respectively, (d) horizontal (in-plane) cross-section. The isosurfaces colour/shielding value are defined as transparent/+7; blue/+16; and red/-16.

5-3 First Singlet (S_1) Excited State of S_2N_2

The S_1 state was confirmed as 1^1A_u . Table (5-2) shows that the deshielding becomes more pronounced for both N and S atoms in the S_1 state. However, in contrast to ground state data in table (5-1), sulfur becomes more deshielded than nitrogen in S_1 S_2N_2 and the absolute shielding difference increases between the nuclei. Also, despite the decrease in the $|\Delta\sigma_{iso(S-N)}^{1\text{\AA}}|$ value, both isotropic shielding values at 1 Å above the nuclei become deshielded.

Table 5-2: CASSCF(22,16)/cc-pVTZ isotropic shielding data (σ_{iso}) (in ppm) of the S_1 state of S_2N_2 for sulfur and nitrogen nuclei and for points placed 1 Å above them as well as absolute shielding difference values of the S-N bond nuclei, $|\Delta\sigma_{iso(S-N)}^{0\text{\AA}}|$, and of points located 1 Å above the nuclei, $|\Delta\sigma_{iso(S-N)}^{1\text{\AA}}|$.

	Nuclear σ_{iso} (ppm)	σ_{iso} 1 Å above nuclei	$ \Delta\sigma_{iso(S-N)}^{0\text{\AA}} $	$ \Delta\sigma_{iso(S-N)}^{1\text{\AA}} $
S	-284.79	-48.82	132.96	0.93
N	-151.83	-49.75		

Switching from the ground to the S_1 state hugely affects the isotropic shielding scene of S_2N_2 . As it can be seen from figure (5-9), the ring centre is occupied by a very strong semi-cylindrical deshielding region of a radius around 1.3 Å. As a result, all shielding features adapt to avoid this strong deshielded region. For example, the lone pairs of nitrogen move to side locations next to the S-N-S angles. Such shifts can be considered as an avoidance action of the “shielded” lone pairs to move away from the deshielded region at the ring centre. Similar behaviour is followed by the shielding clouds of the S-N bonds, which join the shielding clouds of the nitrogens lone pairs and form two shielding clouds similar to parentheses in shape over S-N-S, see maps (a,b) in figure (5-9). The deshielding activity of the ring centre and the sulfur inner deshielded-sphere (see section 5-2) prevent the merging of these two parentheses. In more detail, on one hand, the sulfur outer shielded-sphere, as it is strong enough, tries to keep its location and avoid location shifting to outside the ring. On the other hand, the strong deshielding of the ring centre joins the inner deshielded-sphere along the Y-axis, and, at the same time, distorts and compresses the outer shielded-sphere to a smaller size. Thus, the outer shielded-sphere is distorted to a ring-ovoid shape which is symmetric about the Y-axis, see the XZ-cross-section in figure (5-10 (a)).

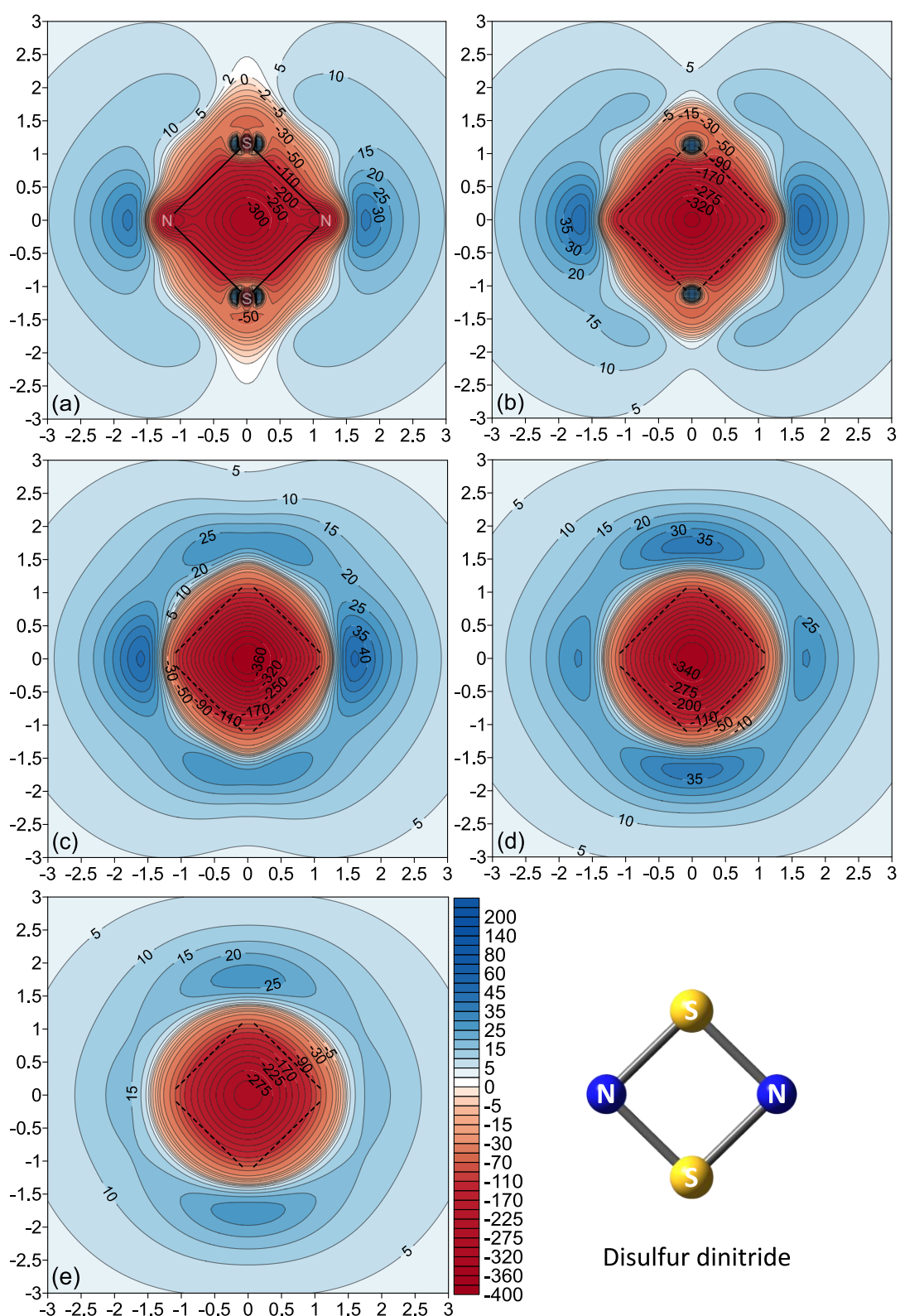


Figure 5-9: Five contour maps of isotropic shieldings (σ_{iso}) (in ppm) obtained at the CASSCF(22,16)/cc-pVTZ level of theory for the S_1 state of disulfur dinitride. (a-e): grids parallelly placed at 0.00, 0.25, 0.50, 0.75 and 1.00 Å heights above the molecular plane, respectively.

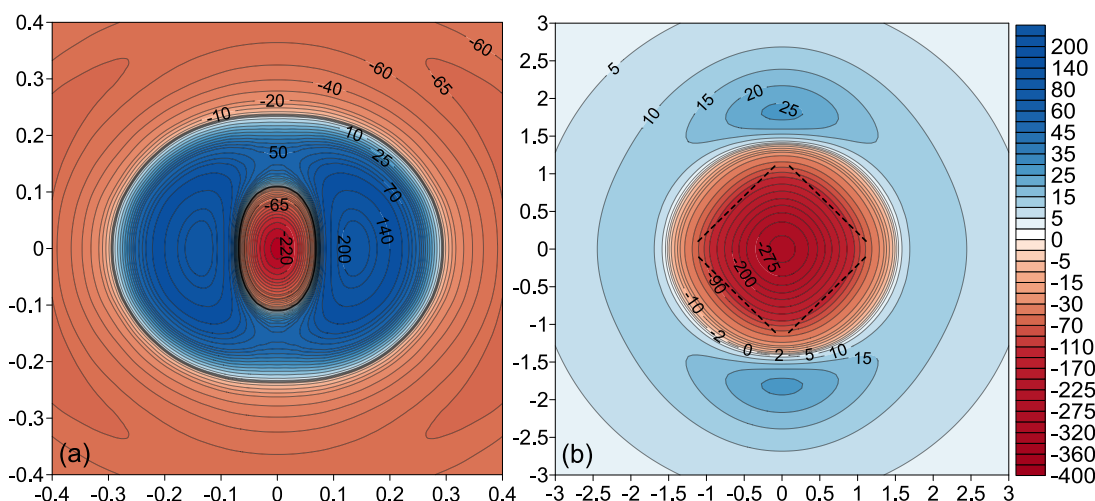


Figure 5-10: Isotropic shielding σ_{iso} (in ppm) of the S_1 state of S_2N_2 for (a) XZ-cross-section shielding map (from a 0.025 \AA grid) showing the distortion of the shielded-sphere of sulfur, (b) the contribution of the vertical-component of the isotropic shielding ($\sigma_{iso(zz)}$) in the total isotropic shielding σ_{iso} obtained from a grid placed parallelly at 1.00 \AA above the molecular plane.

Thus, the inner deshielded-sphere of sulfur acts as a tunnel linking the deshielding activities on both sides of the tunnel. The linked deshieldings, as a repulsive factor, compress the sulfur ovoid-shaped shielded-sphere. Also, the overall deshielding splits the shielding cloud of the sulfur lone pairs and moves each segment higher than the semi-split clouds of nitrogen lone pairs, see figures (5-11 (a,b)) and (5-12 (a)). On the other hand, the ovoid-shaped shielded-sphere of sulfur weakens the deshielding cloud at the ring centre making the deshielding clouds above and below the ring centre stronger, see figures (5-11); see also figure (5-13) which shows the maximum deshielding value of -398.1 (ppm) located at 0.54 \AA , not at 0.00 \AA . These stronger deshieldings with other deshielding contributions force the shielding-related activities of both lone pairs and S-N bonds to shift outside the S_2N_2 ring.

As it can be seen from figures (5-11 (c) and 5-12 (b)), the S-N bond shielding cloud shows similar features of splitting-up and shifting-out due to reasons identical to those mentioned above. Also, the S-N bond shielding cloud prefers to link the similar “shielded” clouds of the lone pairs of sulfur and nitrogen. These splitting and linkage effects make the shielding associated with π -electron delocalisation show a maximum value of 20 (ppm) at 0.50 - 0.75 \AA height, see figure (5-9 (c,d)), which reduces to around 15 (ppm) at 1 \AA , see figure (5-9 (e)); see also figure (5-10 (b)).

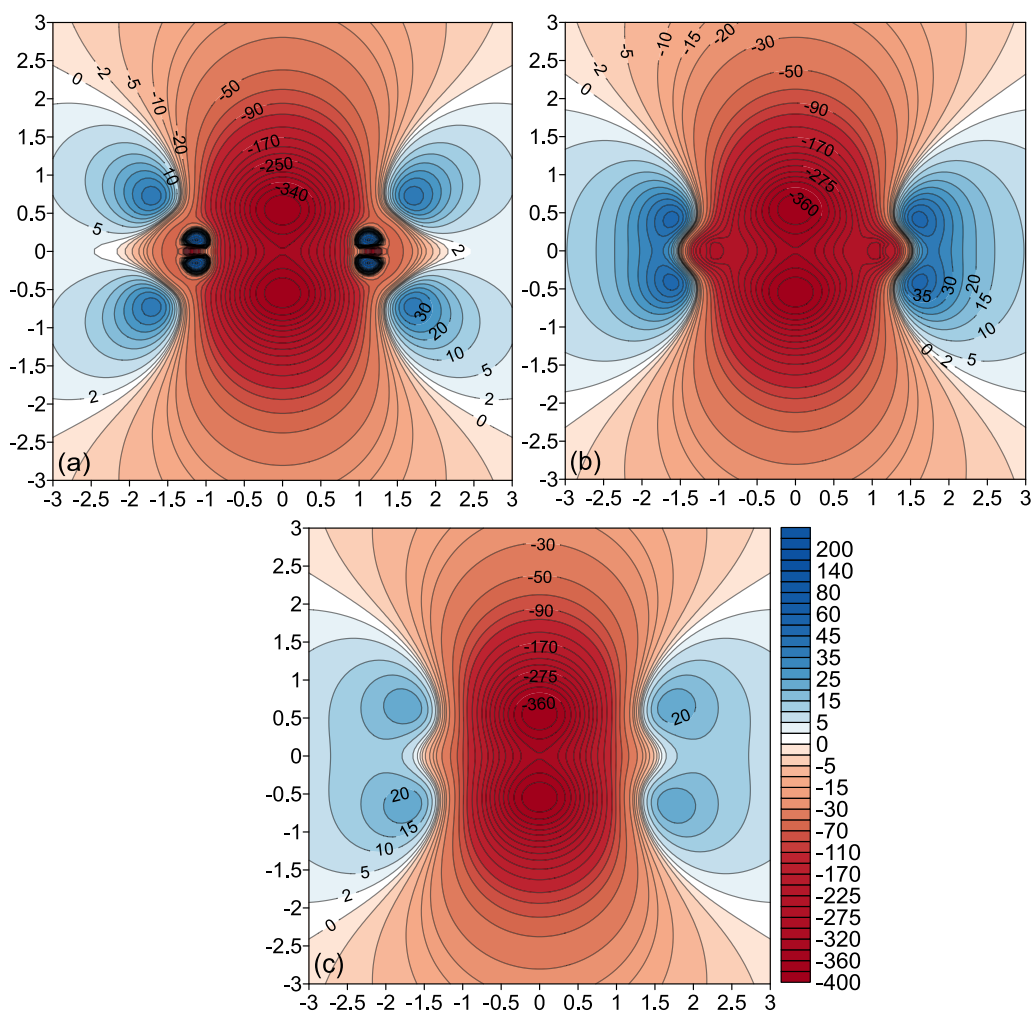


Figure 5-11: S_1 state CASSCF(22,16)/cc-pVTZ isotropic shielding map obtained by utilising 2D grids placed perpendicularly to the S_2N_2 molecular plane, diagonally passing through sulfurs (a) and nitrogens (b) as YZ and XZ planes, respectively, evenly bisecting the ring and opposite S-N bonds (c).

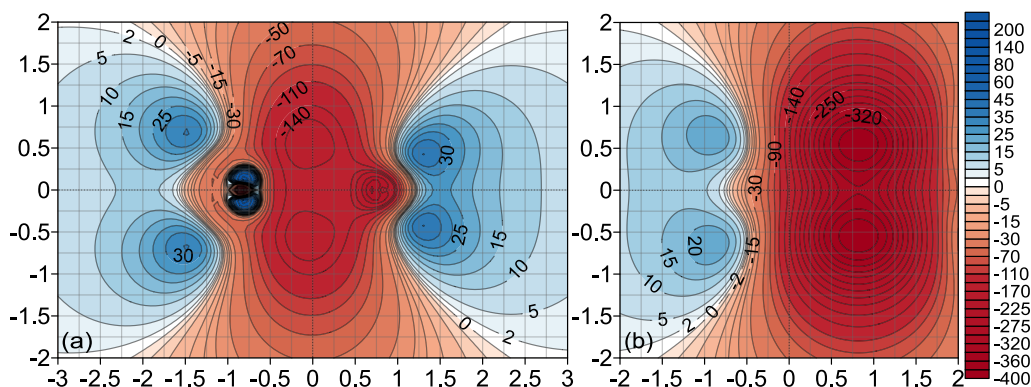


Figure 5-12: CASSCF(22,16)/cc-pVTZ isotropic shielding contour maps (in ppm) of S_1 state S_2N_2 obtained by utilising 2D ghost-atoms grids located perpendicularly to and passing along an S-N bond, (a), or bisecting and crossing the bond at its midpoint (b). The (0,0) X,Y point is located at the bond midpoint.

In addition to figure (5-12), further shielding details of the S-N bond are given in figure (5-14). As it can be seen from curve (a), the deshielding feature is dominant except for a few shielded points, see also the S-N bond in figures (5-9 (a)) and (5-12 (a)). Also, the most deshielding points near nitrogen in curve (a) correspond to the combination of the nitrogen deshielded-sphere with the deshielding of the ring inner-region. The full deshielded curve in figure (5-14 (b)) shows the deshielding at 1 Å above the bond, see also the dashed line above S-N bond in figure (5-9 (e)).

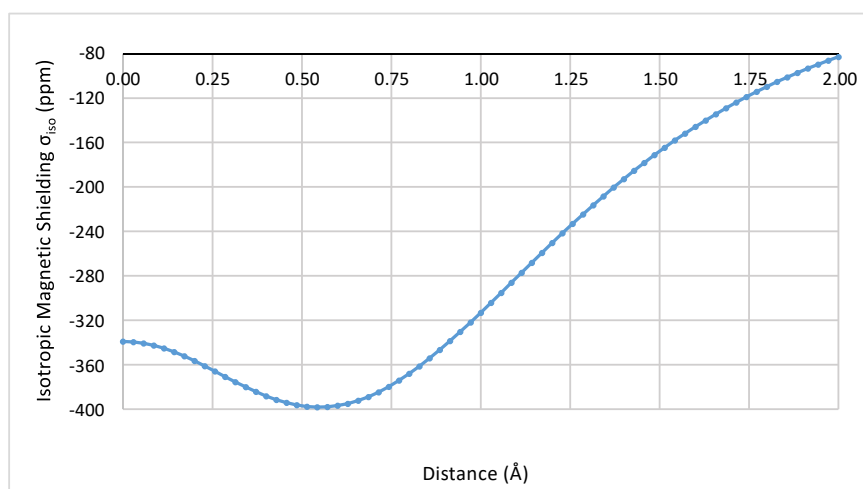


Figure 5-13: Variation in the CASSCF(22,16)/cc-pVTZ isotropic shielding σ_{iso} (in ppm) of the S_1 state of S_2N_2 obtained from 71 ghost atoms placed perpendicularly from the ring centre to a 2 Å height above it.

3D shielding isosurfaces of the S_1 state S_2N_2 are shown in figure (5-15). Most of the shielding features discussed previously can be seen in the isosurfaces. For instance, the shielding clouds shift to outside the S_2N_2 ring, the stronger deshielding above and below the ring centre, the expansion of the deshielding of the inner region of the ring, the rapid decrease of the extent of deshielding in the direction from inside to outside the ring, the more pronounced splitting of the shielding clouds of the sulfur lone pairs and S-N bonds which is less pronounced for nitrogen, the ovoid-shaped shielded-sphere of sulfur, and the linked profile of the shielding clouds. All of these features are demonstrated by the isosurfaces in figure (5-15).

At the end, all data indicates that the S_1 state of S_2N_2 can be described magnetically as strongly antiaromatic.

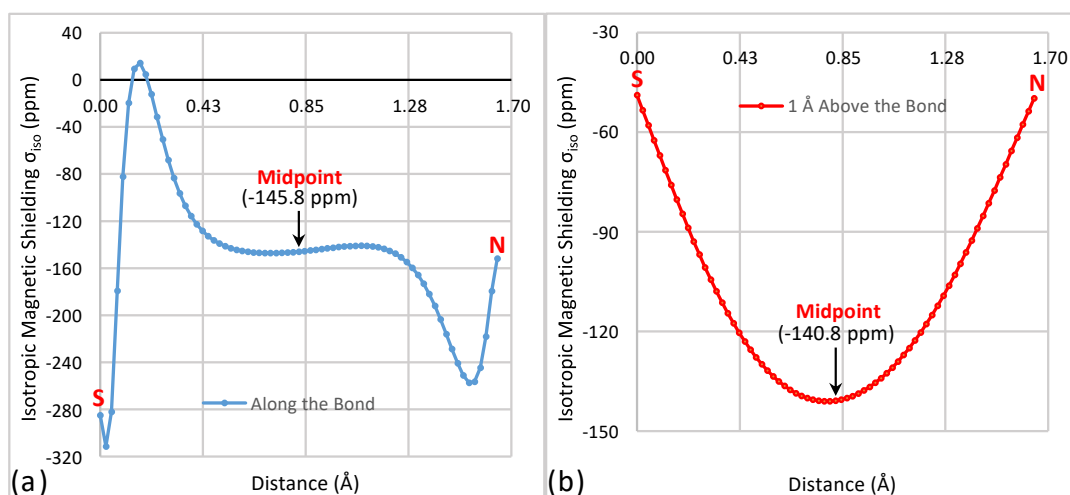


Figure 5-14: Variation in the CASSCF(22,16)/cc-pVTZ isotropic shielding (σ_{iso}) (in ppm) of the S-N bond of S_1 state S_2N_2 obtained from 71 ghost atoms: (a) positioned along the S-N bond, and (b) placed 1 Å parallelly above the bond.

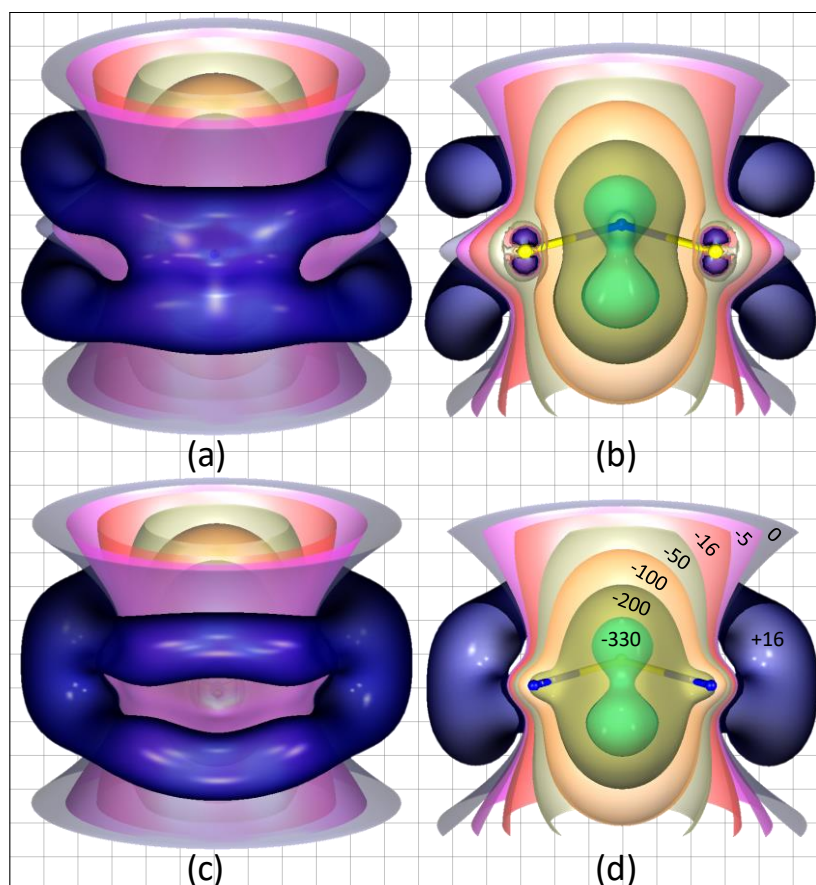


Figure 5-15: CASSCF(22,16)/cc-pVTZ isotropic shielding (σ_{iso}) isosurfaces of S_1 state S_2N_2 . The atoms, which are located at page level, are sulfurs in (a,b), and nitrogens in (c,d). Also, the shielding values for the full isosurfaces (a,c), and their cross-sections (b,d), are labelled in (d).

5-4 First Triplet (T_1) Excited State of S_2N_2

The T_1 state was confirmed as 1^3B_{3u} . In comparison to the S_1 state, the T_1 state shows fewer deshielding features, see tables (5-2) and (5-3), respectively. More pronounced changes are observed at N than at S atoms, which is directly reflected on the $|\Delta\sigma_{iso(S-N)}^{0\text{Å}}|$ value (218.38 (ppm)). Also, the shieldings at 1 Å above the nuclei become again positive as in the S_0 state.

Table 5-3: CASSCF(22,16)/cc-pVTZ isotropic shielding data (σ_{iso}) (in ppm) of T_1 state of S_2N_2 for sulfur and nitrogen nuclei and for points placed 1 Å above them as well as absolute shielding difference values of the S-N bond nuclei, $|\Delta\sigma_{iso(S-N)}^{0\text{Å}}|$, and of points located 1 Å above the nuclei, $|\Delta\sigma_{iso(S-N)}^{1\text{Å}}|$.

	Nuclear σ_{iso} (ppm)	σ_{iso} 1 Å above nuclei	$ \Delta\sigma_{iso(S-N)}^{0\text{Å}} $	$ \Delta\sigma_{iso(S-N)}^{1\text{Å}} $
S	-227.96	4.32	218.38	2.53
N	9.58	1.79		

A quick glance to figures (5-16 to 5-22) and a comparison with analogous figures from the two previous sections, demonstrate that the T_1 state is antiaromatic but less S_0 shielding features than the S_1 state. In more detail, figure (5-16) shows that the shielding clouds of the S-N bonds, to some extent, recover their S_0 locations, but with some shifts to outside the ring.

A similar recovery of properties is observed for the shielded/deshielded spheres of sulfur/nitrogen. However, some other features of S_1 remain, such as the vertical deshielding in the inner region of the ring and the diagonal deshielding expansion along the S-S line, both features interrupt the shielding cloud surrounding the ring. The most shielded cloud, which follows form of the π -electron flow, is located at 0.75 Å, see map (d). The deshielded-sphere around nitrogen, together with the deshielding cloud along S-S diagonal (Y-axis) give rise to repulsion effects which push the lone pairs shielding clouds of both nitrogen and sulfur atoms to 0.75-1.00 Å height above the ring plane, see figure (5-16(d,e)) and (5-17).

Unlike the S_1 state, because of the normal shape recovery of the sulfur shielded-sphere, together with the lower deshieldings at the ring inner-region, the maximum deshielding value can be found at the ring centre, see figure (5-18).

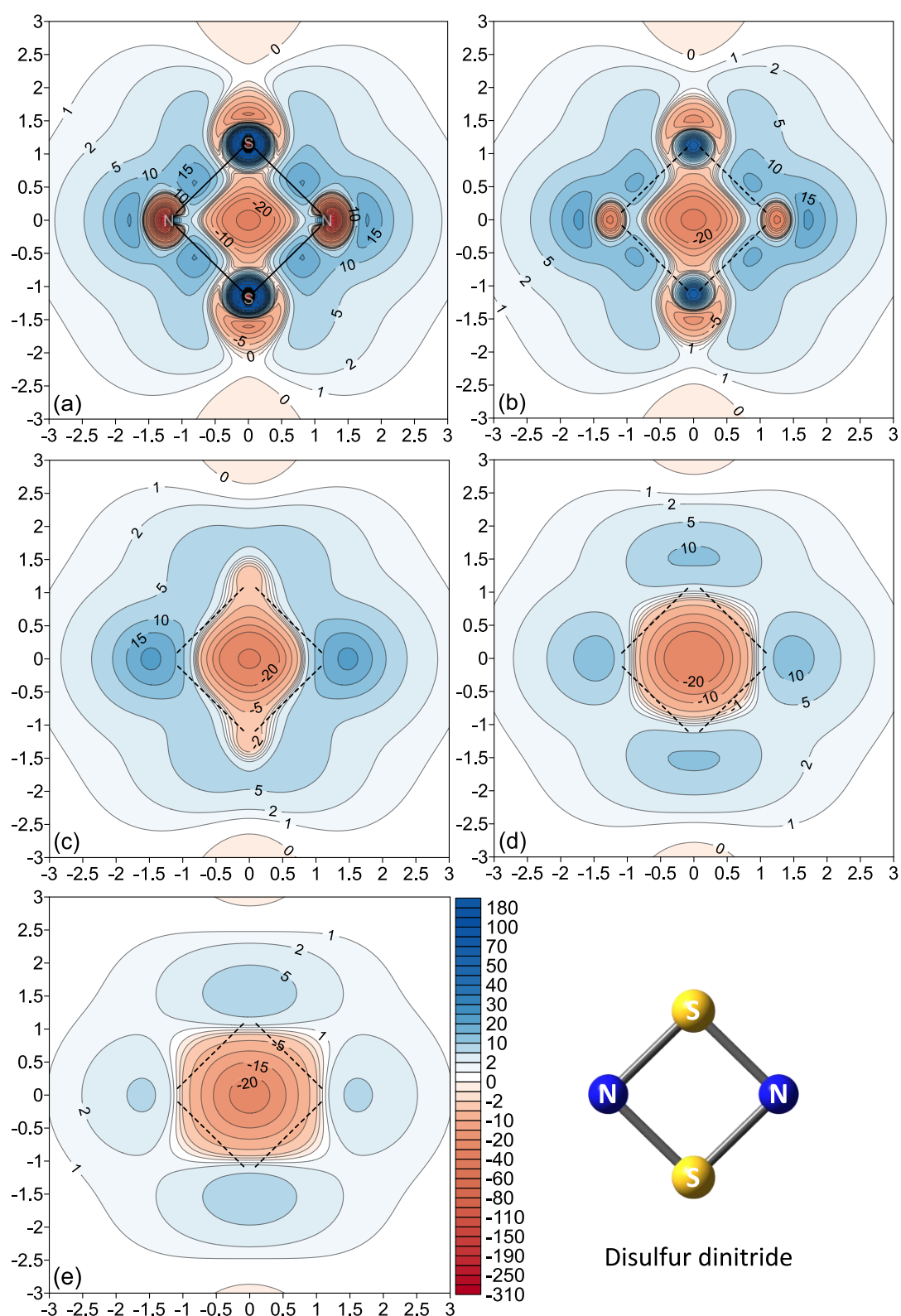


Figure 5-16: Five contour maps of isotropic shieldings (σ_{iso}) (in ppm) obtained at the CASSCF(22,16)/cc-pVTZ level of theory for the T_1 state of disulfur dinitride. (a-e): grids parallelly placed at 0.00, 0.25, 0.50, 0.75 and 1.00 Å heights above the molecular plane, respectively.

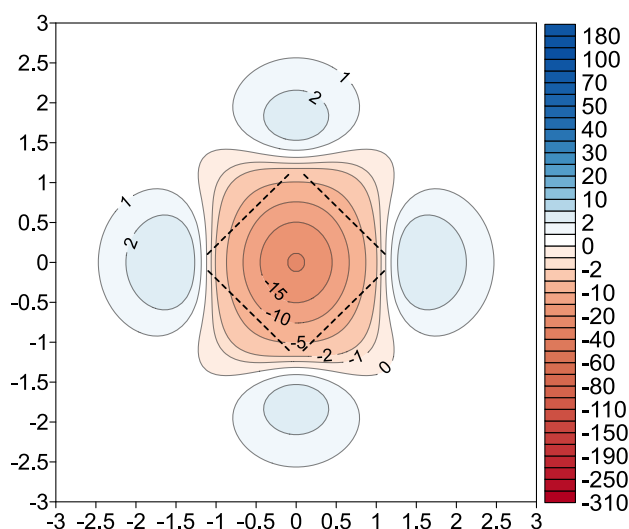


Figure 5-17: Contribution of the vertical-component of the isotropic shielding ($\sigma_{iso(zz)}$) (in ppm) in the total isotropic shielding σ_{iso} of T_1 state S_2N_2 , obtained at the CASSCF(22,16)/cc-pVTZ level of theory for a grid placed parallelly at 1.00 Å above the molecular plane.

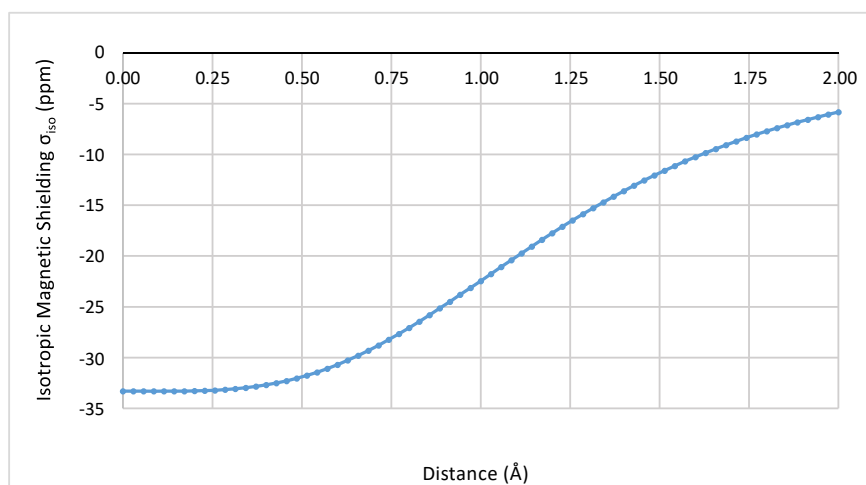


Figure 5-18: Variation in the CASSCF(22,16)/cc-pVTZ isotropic shielding σ_{iso} (in ppm) of the T_1 state of S_2N_2 obtained from 71 ghost atoms placed perpendicularly from the ring centre to a 2 Å height above it.

For the same reasons, the T_1 shielding clouds are influenced by less deshielding effects than in the S_1 state, see figures (5-19) and (5-11), respectively. Namely, as can be seen in figure (5-19): (i) although the S-S diagonal deshielding splits the shielding clouds of the lone pairs, they remain almost above the sulfurs (see map (a)); (ii) a shielding cloud almost fully surrounds each nitrogen (see map (b)); and (iii) the clouds around the S-N bonds are very close to the bond line (see map (c) and figure (5-20 (b))).

However, due to the different deshielding contributions, a shift in the ABL shielding cloud of the S-N bond towards nitrogen and a shift to outside the ring can be seen in figures (5-20) (a) and (b), respectively. More details about these shifts can also be seen in figures (5-16 (a)) and (5-21 (a)).

Plot (b) in figure (5-21) shows that deshieldings effects dominate the curve except for the terminals above the nuclei at 1 Å. In this context, the shielding maps in figures (5-16) and (5-19) show that the deshielding cloud around the ring centre region prefers vertical expansion with avoiding the lower shielding activities present at higher regions.

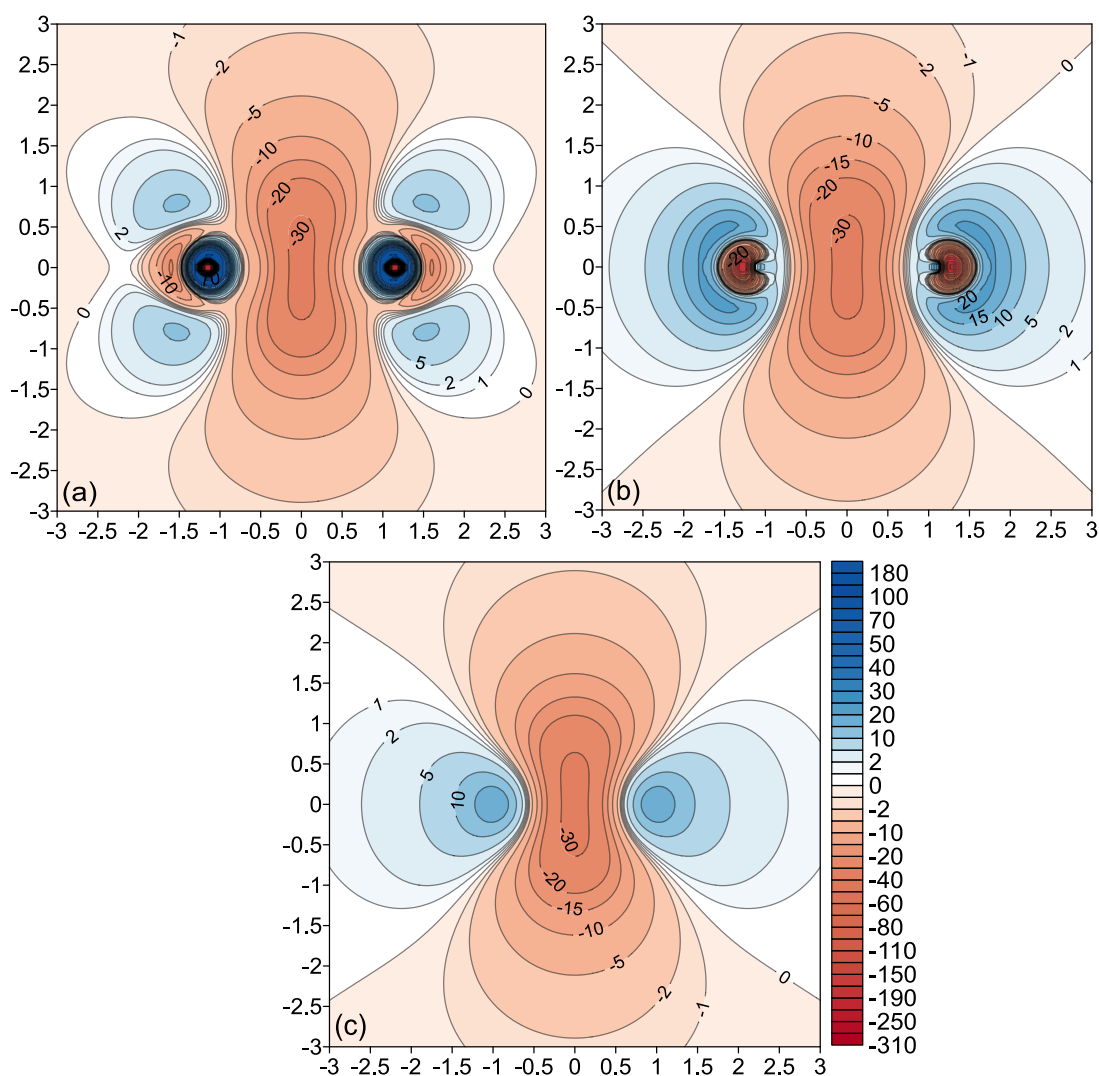


Figure 5-19: T_1 state CASSCF(22,16)/cc-pVTZ isotropic shielding map obtained by utilising 2D grids placed perpendicularly to the S_2N_2 molecular plane, diagonally passing through sulfurs (a) and nitrogens (b) as YZ and XZ planes, respectively, evenly bisecting the ring and opposite S-N bonds (c).

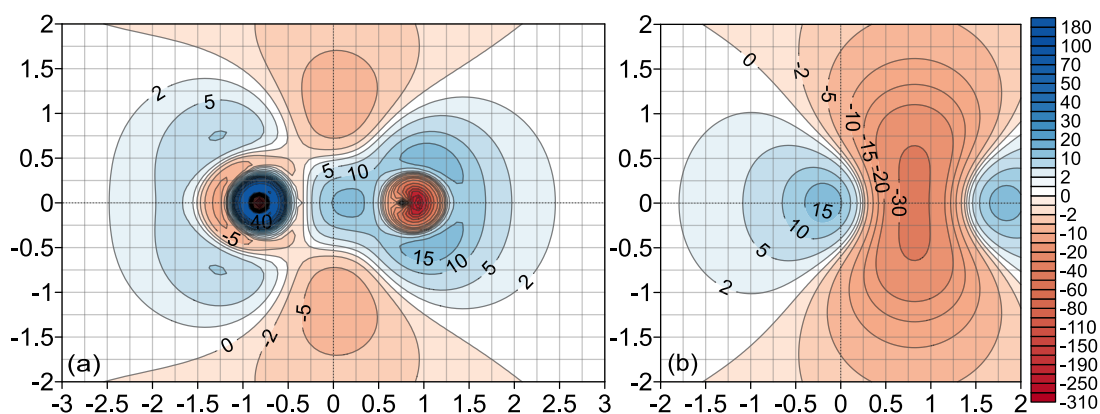


Figure 5-20: CASSCF(22,16)/cc-pVTZ isotropic shielding contour maps (in ppm) of T_1 state S_2N_2 obtained by utilising 2D ghost-atoms grids located perpendicularly to and passing along an S-N bond, (a), or bisecting and crossing the bond at its midpoint (b). The (0,0) X,Y point is located at the bond midpoint.

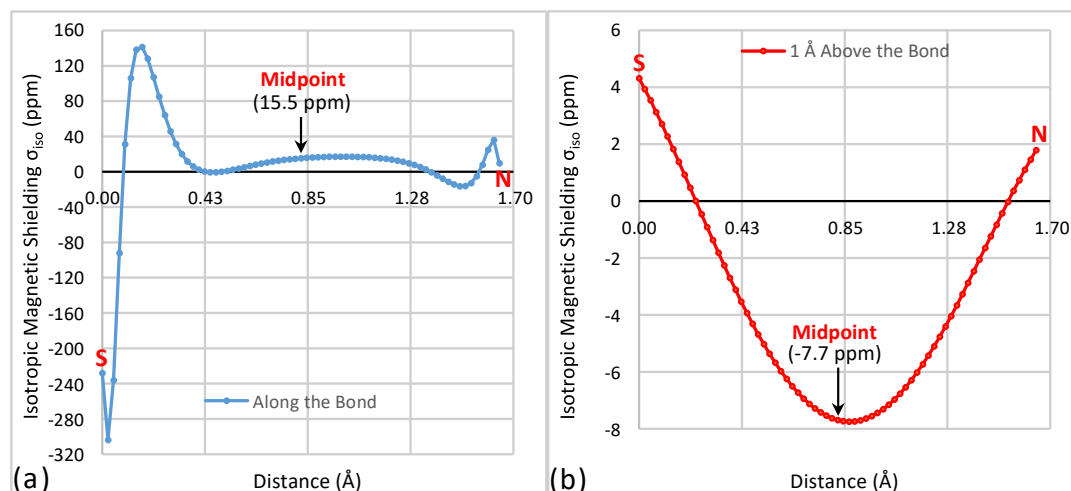


Figure 5-21: Variation in the CASSCF(22,16)/cc-pVTZ isotropic shielding (σ_{iso}) (in ppm) of the S-N bond of T_1 state S_2N_2 obtained from 71 ghost atoms: (a) positioned along the S-N bond, and (b) placed 1 \AA parallel above the bond.

The most pronounced deshieldings are shaped like a capsule centred on the ring and are surrounded by less pronounced deshieldings which through deshielding expansion form two identical deshielding pyramids attached via their apexes, see figures (5-16) and (5-22 (a)). In the S_1 state, the analogous expansion of the deshielded region forms two cones instead of pyramids (see figure (5-15)). The reason for this relative difference belongs to the intensity ratios of shielding to deshielding in the two states,

To provide higher clarity, figure (5-22 (a)) shows separately isosurface values

at -16, -10; -3 in addition to 0 (ppm). The +16; +5; and -16 (ppm) isosurfaces are shown in illustrations (b) to (d) in figure (5-22). The aim of the image (a) is to show the deshielding expansion behaviour. Another aim is to show the contribution of the deshielded region around each sulfur in distorting and repelling the shielding clouds of the sulfur lone pairs which makes their shape similar to a bagel, see images (b-d). The bagels serve as bridges linking the shielding parentheses-shaped regions of π -electrons shielding activity represented by the +5 (ppm) transparent grey isosurface, see images (b-d).

The blue isosurface at +16 (ppm) shows some S_0 shielding character recovery in the T_1 state. Partial return to the S_0 picture in the shielding clouds of the nitrogen lone pairs and S-N bonds can be seen in figure (5-22 (b-d)). The isosurface not only shows the +16 (ppm) shielding distribution but also highlights the extent of similarity between S_0 ; S_1 ; and T_1 states.

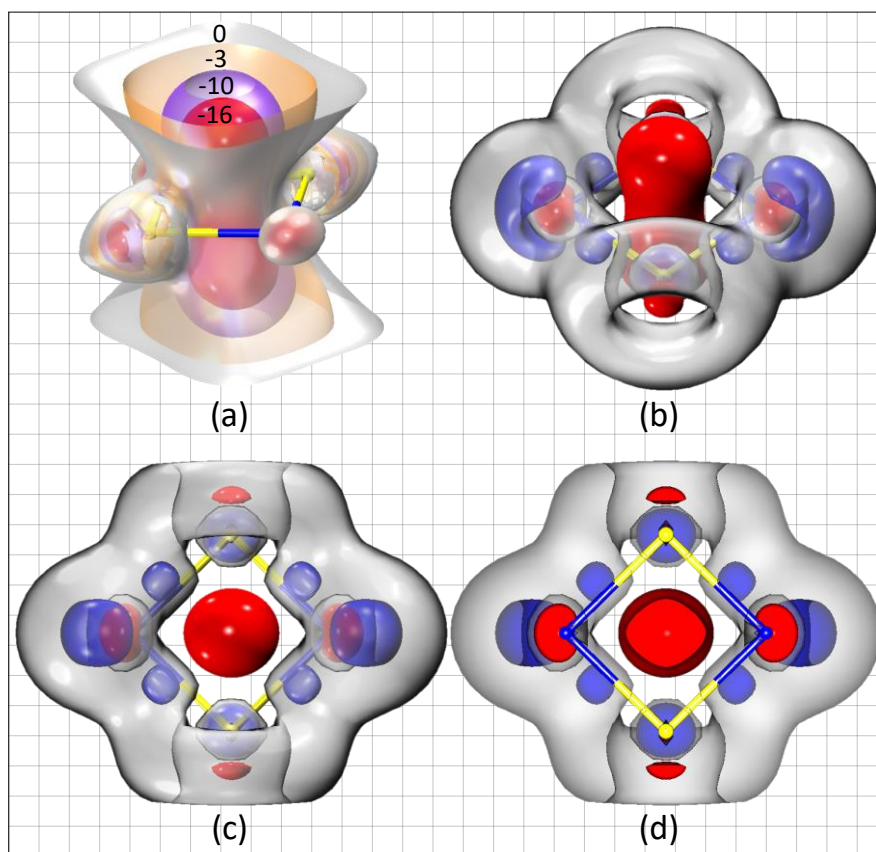


Figure 5-22: CASSCF(22,16)/cc-pVTZ isotropic shielding (σ_{iso}) isosurfaces for T_1 state S_2N_2 represented as (a) different deshielding values. (b-d) side; top; and in-plane cross-section views in which the shielding value/colour is given as: -16/red; +16/blue; and +5/transparent grey.

5-5 Conclusions

Remarkable changes in the isotropic magnetic shielding in S_2N_2 occur with the vertical excitations from the ground state to the S_1 and T_1 excited states. These changes were illustrated and discussed in detail. The sulfur nucleus keeps its deshielded character in the ground, S_1 and T_1 states, with the maximum deshielding in the S_1 state. A similar trend is shown by nitrogen, except for a reversal in shielding sign from shielded in the S_1 to deshielded in the T_1 state. However, although the nuclear shielding values of sulfur and nitrogen are informative, the overall magnetic changes accompanying transitions between electronic states could not be understood without performing multidimensional shielding analyses.

In this context, the 2D contours and 3D isosurfaces demonstrate a variety of magnetic features. For example, the lone pairs and S-N bonds show S_0 shielding which is similar to that in aromatic molecules. In addition, the different shielding contributions of the lone pairs and the π -electron shielding delocalisation above the S_2N_2 ring form a combined shielding cloud of 10 (ppm) at 0.75 Å which is a further sign of the aromaticity of ground state S_2N_2 .

The nitrogen and sulfur nuclei are surrounded by shielded and deshielded spheres, respectively. The latter can be considered as a feature similar to atoms of aromatic rings, whereas the difference in shielding behaviour around the atoms might be attributed to the difference in electronic charges and/or electronegativities. The higher shielding around nitrogen together with the higher vertical extension of its lone pairs suggest the conclusion that nitrogen is the main contributor in π -bonding and circulation in $S_0 S_2N_2$. A contributing factor can be the existence of deshielded-spheres around the nitrogens which promote such vertical shifts and consequently, π -shielding delocalisation.

A conclusion that S-S or N-N bonds do not exist was made by examining 2D grids set vertically to S-S and N-N diagonals, which show no shieldings that identify such bonds.

As the 3D isosurface at +7 (ppm) behaves like those at +16 (ppm) for aromatic molecules, the ratio between these numbers can be considered as an approximate aromaticity comparison between S_2N_2 and other aromatic molecules.

The small size of the four-membered ring S_2N_2 brings S-N bonds and their σ -bonding interferences much closer, which, in turn, reflects on the magnetic activity of LSC. At higher distances above the ring centre, the contribution of π -delocalisation is shown precisely. This is the main reason which makes the LSC deshielded instead of less-shielded than the nearby locations of the ring inner region.

Regarding the isotropic shielding behaviour of the S_1 state, the most significant magnetic feature is the extraordinary strong deshieldings, about -400 (ppm), which occupies the inner region of the ring. These deshieldings destroy and reconstruct most magnetic features observed in the ground state. As a consequence, similar magnetic effects are combined together, while opposite effects are separated further. For instance, the (inner) deshielded-spheres of (sulfur) and nitrogen nuclei are combined with the deshieldings of the inner region of the ring. On the other hand, the shieldings of the lone pairs and the S-N bonds are split and shifted to locations outside the ring. However, the intensity of the shielding/deshielding effects plays a key role in resisting or promoting such shifts. For example, the outer (distorted) shielded-sphere of sulfur keeps its location as it is strongly-shielded and its maximum shielding is about +220 (ppm).

Most features observed in the S_1 state can also be seen in the T_1 state with: (i) significantly lower shielding/deshielding intensities, (ii) less distortion in the shielding/deshielding spheres, (iii) less shielding clouds splitting and shifts to out of ring locations, and (iv) the nitrogen/sulfur deshielded/shielded spheres mostly remain in their S_0 locations and forms. Similarly, the S-N bond shielding cloud partially returns to its S_0 location but is still not aligned along the S-N bond line. Also, the deshieldings along the S-S diagonal (Y-axis), or more specifically, the deshieldings around sulfurs, split the global shielding cloud in which encloses it. The global cloud, which consists of lone pairs and S-N bonds shielding contributions, bridges its parts above and below the deshieldings near N-S-N angle and forms shielded-bagels surrounding the deshieldings.

Finally, the aromaticity classification according to the current findings for S_2N_2 is as follows: the ground state is (moderately) aromatic, the S_1 is strongly antiaromatic and T_1 is also antiaromatic but significantly less S_0 than S_1 .

CHAPTER SIX

NAPHTHALENE

6-1 Introduction

Naphthalene, one of the best-known compounds in chemistry, was discovered around two centuries ago. The oldest reported description of naphthalene as a compound coming from coal tar decomposition was given by Kidd and Wollaston William in 1821.^[152]

Naphthalene has attracted considerable interest as it is the smallest polycyclic benzenoid compound which contains two fused benzene rings. The first estimate of the C-C interatomic distances for naphthalene in the literature was reported by Pauling and co-workers in 1935.^[153] Since that time, there have been numerous studies of various properties of naphthalene. In this context, a recent structure of D_{2h} naphthalene has been obtained by Baba et al.^[154] These authors used ultrahigh-resolution laser spectroscopy in addition to *ab initio* calculations.

There is no doubt that the aromaticity of naphthalene can be considered as the most important and well-known property of this compound. We continue with a brief overview of naphthalene aromaticity from literature survey, which, in most cases, depended on finding the difference in a physical property relative to benzene.

Dewar and de Llano^[155] calculated the resonance energy for some cyclic and acyclic conjugated molecules. Naphthalene was found to have higher resonance energy than benzene. Resonance energies were also obtained via a new approach based on Hückel molecular orbital theory (HMO) by Hess and Schaad^[156]. These authors also employed the approach in another study^[157] to calculate the resonance energy per π -electron for a wide range of benzenoid hydrocarbons, the values for benzene and naphthalene were found as 0.065 and 0.055 β , respectively.

Based on HMO, Milun et al.^[158] introduced a new index as a tool for measuring the aromatic stabilisations of cyclic molecules. The indices for benzene and naphthalene were found to be 0.44 and 0.56 β , respectively. Aihara^[159] also calculated and compared resonance energies obtained from other approaches. According to his comparison, naphthalene has approximately twice the resonance energy of benzene.

In a further report by Aihara^[160] the resonance energy per a C-C bond was

calculated. The value for the C-C bond of benzene was found to be greater than those for the C-C bonds of naphthalene. This author also observed a similar trend for the bond orders, except the C1-C2 bond of naphthalene, which showed the largest bond order amongst all bonds of both molecules.

Several physical properties of some polycyclic hydrocarbons were calculated by Wiberg.^[161] He found that the delocalisation energy per C=C bond for both benzene and naphthalene is equal, 12 kcal/mol, whereas the delocalisation energies for these molecules were 36 and 60 kcal/mol, respectively. Jug and coworkers^[162] introduced a new way of calculating the delocalisation energy depending on the difference in energy between a cyclic compound and an identical compound in which its π -delocalised orbitals are replaced by localised orbitals. They found that the delocalisation energy indices of benzene and naphthalene were 21.5 and 19 kcal/mol, respectively.

As an indicator of aromaticity, the diamagnetic susceptibility exaltation was reported for naphthalene as more than twice that of benzene.^[28,163,164] According to the NICS approach, Schleyer^[18] et al. found that naphthalene is slightly more aromatic than benzene with NICS values of -9.9 and -9.7 (ppm), respectively.

The average g-factor index, Δg , was introduced by Uzun and Tokatli as procedure for evaluating the aromaticity of mono and polycyclic benzenoid hydrocarbons.^[165] They estimated Δg from the difference between the g-factor of the free electron (as in a hydrogen atom) and for a cyclic system including that hydrogen atom positioned at a 1.2 Å vertical height above the ring centre. Their findings indicate that naphthalene is less aromatic than benzene by about one-sixth. According to the elliptical bond approach by Dominikowska and Palusiak^[166], naphthalene has around 60 % of the aromaticity of benzene.

The local ring current for naphthalene is slightly higher than that for benzene, as observed by Aihara.^[167] In addition, Aihara utilised the percentage of topological resonance energy as a comparative scale of aromatic content. Benzene was found to have a higher percentage of topological resonance energy than naphthalene, 3.53 and 2.92, respectively.^[167]

Steiner and Fowler^[168] calculated the ring current density at 1 Bohr above benzene as well as above a set of linear polycyclic molecules from

naphthalene to heptacene. They showed, through 2D current maps, that the current circulation in each six-membered ring of these molecules is formed not only by the diamagnetic circulation of the π -current but also by a paramagnetic σ -current which circulates in opposite direction around the centres of these rings.

Since the weakest bond order can be considered as the magnitude of the ring current, Jug^[104] utilised this bond as an index for calculating the ring current in order to assess aromaticity. For naphthalene and benzene, the ring current are 1.751 and 1.514, respectively. In contrast, the currents for these molecules according to Steiner and Fowler^[168] are 0.099 and 0.0104 au.

By employing semiempirical valence bond calculations, Li and Jiang^[169] succeeded in calculating the relative local hexagon energy as a local index of aromaticity for each ring of a selected set of benzenoid hydrocarbons. This depended on finding the energy ratio by dividing the energy of each ring in these molecules by the energy of benzene. For naphthalene and benzene, the ratios were 0.945 and 1.000, respectively.

Regarding the kinetic stability, a reduced HOMO-LUMO energy gap was calculated^[170] as a ratio of HOMO-LUMO energy of a molecule / HOMO-LUMO energy of a hypothetical polyene reference. The gap in naphthalene is slightly less than the gap in benzene, 1.932 and 1.748, respectively, indicating high stability for both molecules.

The heat of formation was calculated theoretically using the *ab initio* SCF 6-31G* calculations.^[171] The heat of formation ratio of benzene to that of naphthalene is 4:7. The same ratio can be found from experimentally estimated results.^[172]

As it is shown above, different approaches produce different results for the aromaticity and physical properties of naphthalene. In many cases, there are disagreements in the assessments. Therefore, the aim of this chapter is to evaluate the aromaticity of naphthalene through isotropic shielding σ_{iso} calculations. The assessment is carried out not only for the ground state of naphthalene but also for some lowest excited states such as the first singlet state (S_1 as $^1B_{2u}$), the second singlet state (S_2 as $^1B_{1u}$) and the first triplet state (T_1 as $^3B_{1u}$). All these excited states occur within $\pi \rightarrow \pi^*$ electronic transition.

6-2 Ground State (S_0) of Naphthalene

All isotropic shielding calculations of the different naphthalene electronic states in this chapter were carried out at the CASSCF(10,10)/6-311+G(d) level of theory. In the isotropic shielding calculations, the naphthalene structure reported by Baba et al.^[154], which was mentioned earlier in the introductory section of this chapter, has been used not only for the ground state of naphthalene but also for different excited states.

The isotropic shielding data in table (6-1) show that the lowest nuclear σ_{iso} value is observed for the carbons of the fused C-C bond, i.e., C8a and C4a (see figure (6-1) for atom numbering). On the other hand, the largest $\sigma_{\text{iso}}^{1\text{\AA}}$ is located above these two nuclei. The $|\Delta\sigma_{\text{iso}}^{0\text{\AA}}(\text{C-C})|$ and $|\Delta\sigma_{\text{iso}}^{1\text{\AA}}(\text{C-C})|$ for C1-C8a and C1-C2 are 8.66 / 2.51 and 2.19 / 2.04 (ppm), respectively. This means that the nuclei of the C1-C2 bond have the lowest shielding difference not only between the nuclei but also at 1 Å above them. The other C-C bonds, on the other hand, have zero shielding differences due to the identical carbon nuclei in these bonds.

Table 6-1: CASSCF(10,10)/6-311+G(d) isotropic shielding data (σ_{iso}) (in ppm) for ground state naphthalene for symmetry unique carbon nuclei, and for points placed 1Å above these nuclei.

	Nuclear σ_{iso} (ppm)	σ_{iso} 1 Å above nuclei (ppm)
C1	75.16	13.84
C2	77.35	15.88
C8a	66.50	16.35

The 2D σ_{iso} maps of ground-state naphthalene are shown in figures (6-1 to 6-5). It is obvious that the 2D shielding map, figure (6-1), shows strong shielding profiles at different vertical heights. The middle region of the C-C bonds shows higher shielding than nearby areas. Similar behaviour is observed for the C-H bonds but with lower shielding strength and higher shielding closer to hydrogens rather than carbons. Although each of the carbon nuclei is well-shielded, see table (6-1) and figures (6-1(a)) and (6-5), these nuclei are surrounded by deshielded-spheres with wider horizontal extents and less than 0.5 Å vertical radii, see figures (6-1 (a,b)) and (6-5). No such spheres are found around the hydrogens.

Several important points can be noticed from the 2D shielding maps. One of these, at 0.50-1.00 Å vertical height, the C-C bonds shielding clouds show significant shifts from the ring frames to the inner areas of the rings, see figure (6-1 (c-e)). The maximum shifts of the clouds can be seen at 1 Å above the molecular plane.

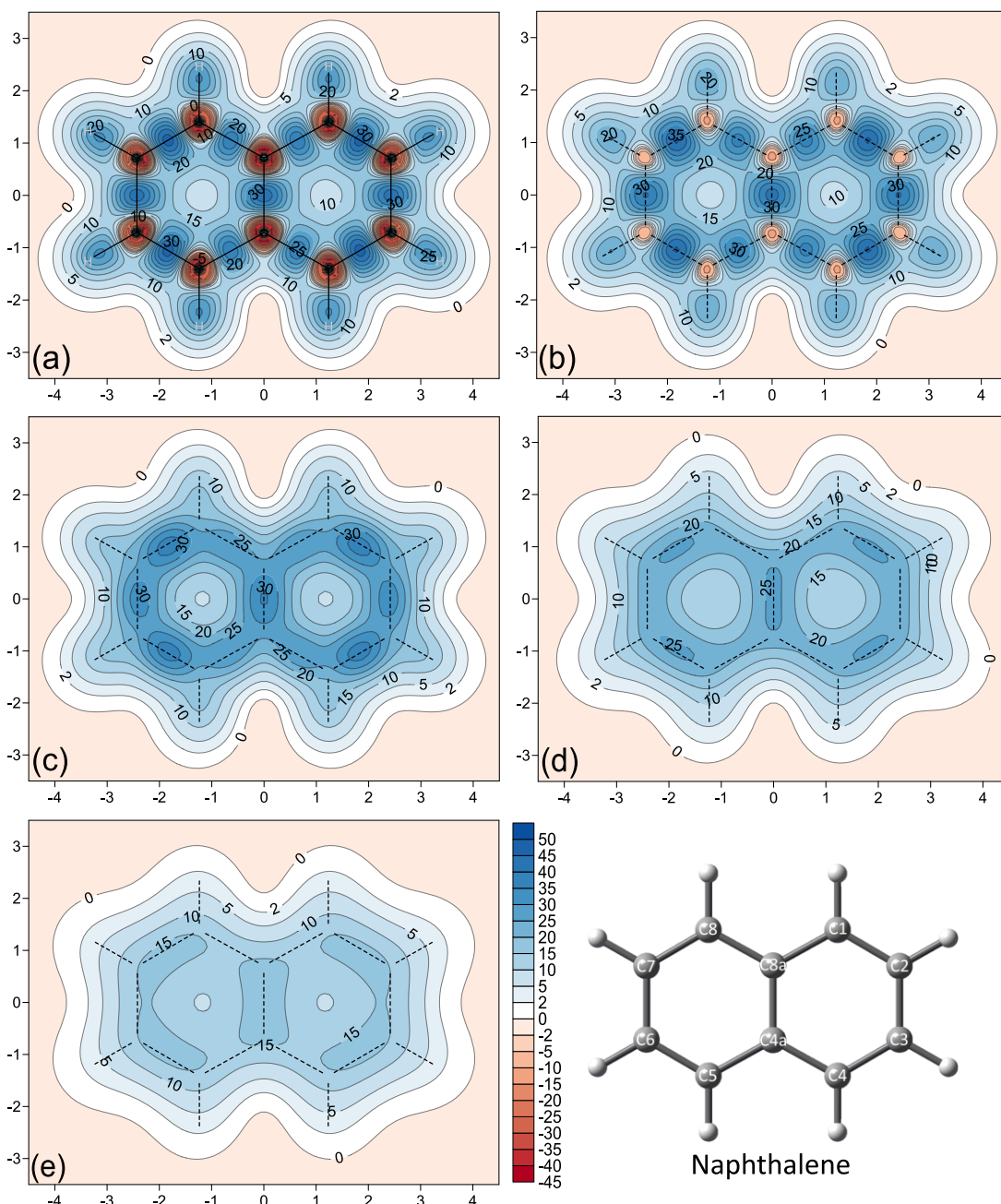


Figure 6-1: Contour maps of the isotropic shieldings (σ_{iso}) (in ppm) obtained at the CASSCF(10,10)/6-311+G(d) level of theory for ground state naphthalene. (a-e): for grids respectively placed at 0.0, 0.25, 0.50, 0.75 and 1.00 Å vertical heights above the molecular plane.

In agreement with this, figure (6-6) also shows that the maximum σ_{iso} is 10.16 (ppm) which is located vertically at 0.77 Å above the ring centre. From the observations associated with the two figures, one can find that the maximum isotropic shielding activities occupy a vertical height between 0.75 to 1.00 Å.

This leads to a further suggestion, in addition to what has been put forward in earlier chapters. It relates to shielding and deshielding activities and their preferred ways of avoiding each other. Here, in the absence of deshielding activity at the inner regions of a ring, the shielding clouds show strong π -electron delocalisation above and below the molecular plane and prefer the region inside the ring. This trend can be enhanced by the strongly-shielded ring centre as a similar magnetic activity, i.e., there is no need for any type of avoidance. The shielding behaviour in figures (6-1) to (6-4) and figure (6-6) support this suggestion which is related to the aromaticity of naphthalene.

Another relevant point, the contribution of the vertical component, $\sigma_{\text{iso}(zz)}$, of the isotropic shielding to the total isotropic shielding, σ_{iso} , shows that most of the total σ_{iso} at 1 Å is due to $\sigma_{\text{iso}(zz)}$, see figures (6-1 (e)) and (6-2), respectively. Both figures indicate strong π -electron shielding delocalisation at that height. Additionally, the XZ cross-section map shows a remarkable vertical expansion of the σ_{iso} cloud which surrounds the whole molecule, see figure (6-3). Also, the shielding clouds are joined together above the ring centre at around 0.75 Å, which is consistent with figure (6-6), indicating a high degree of π -electron shielding delocalisation at that height.

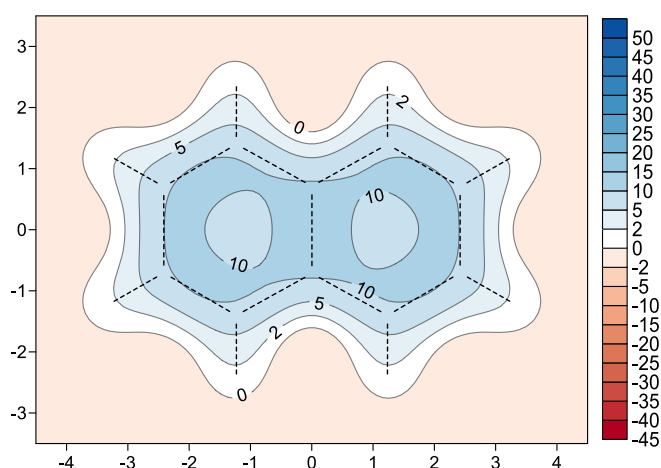


Figure 6-2: Contribution of the vertical-component of the isotropic shielding ($\sigma_{\text{iso}(zz)}$) (in ppm) to the total isotropic shielding σ_{iso} of ground state naphthalene, obtained at the CASSCF(10,10)/6-311+G(d) level of theory for a grid placed vertically at 1.00 Å above the molecular plane.

A further observation about the shielding behaviour of the C-C bonds, the C1-C2 bond has the greatest σ_{iso} density, while the lowest is observed for the C1-C8a bond (see figures (6-1), (6-4) and (6-5)). Although each C-C bond has an individual shielding cloud in the molecular plane ($z=0.0$ Å, see figure 6-1(a)), these shielding clouds tend to be shared over most of the bonds at 1 Å, except for that over the C1-C8a bond, (see figure 6-1(e)). This is shown more precisely in the $\sigma_{\text{iso}(zz)}$ map (see figure (6-2)) with a slightly lower shielding above the C1-C8a bond.

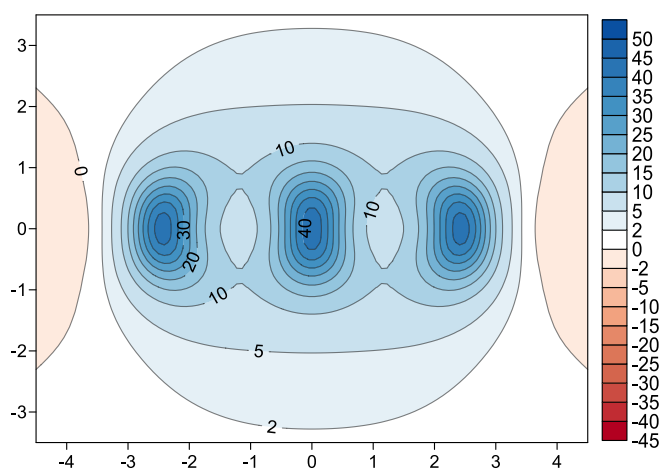


Figure 6-3: XZ cross-section isotropic shielding map (in ppm) for ground state naphthalene, obtained at the CASSCF(10,10)/6-311+G(d) level of theory for a grid placed vertically and bisecting the molecular plane at its X and Z axes.

The sizes of the deshielded-spheres surrounding the carbons suggest that the shapes of these spheres are influenced by shielding activity, see figure (6-5). In more detail, each of the deshielded-spheres is affected by two C-C bond shielding clouds as well as by the shielding of the inner ring region. In contrast, the regions outside the ring frame near the C-C-C angle experiences less of these shielding effects. This makes the deshielded-spheres prefer these spaces for expansion, see figure (6-1 (a)). Besides, the C-H bond shielding clouds, which shift towards hydrogens and have a weaker magnetic shielding strength, also influence the shape of the deshielded-spheres as they offer less-shielded space for expansion.

The centre of the shielding cloud of each C-C bond corresponds to the physical centre of each of these bonds. The vertical cross-sections at midpoints as well as along these bonds clearly support this observation, see figures (6-4) and (6-5), respectively. This can be considered as a sign of the

homogeneity of the σ_{iso} distribution about the bonds. In addition, this not only affects the homogeneity of the shielding activities but also has a similar effect on deshielding activities as these are considered as a repelling factor in reorienting the shielding clouds.

In order to avoid any confusion which may arise from the above paragraph, it is useful to mention here that the above discussion deals with shielding behaviour in the molecular plane as well as at close vertical heights. This, therefore, does not introduce any inconsistency with the previous suggestion about the C-C bond shielding clouds shifts to the inside regions of the rings. What is more, focusing on the top part of each of the semi-kidney-shaped region in figure (6-4) shows the shifts in the shielding clouds towards the inside part of the ring. Also, the LSC can be seen in the maps of the figure.

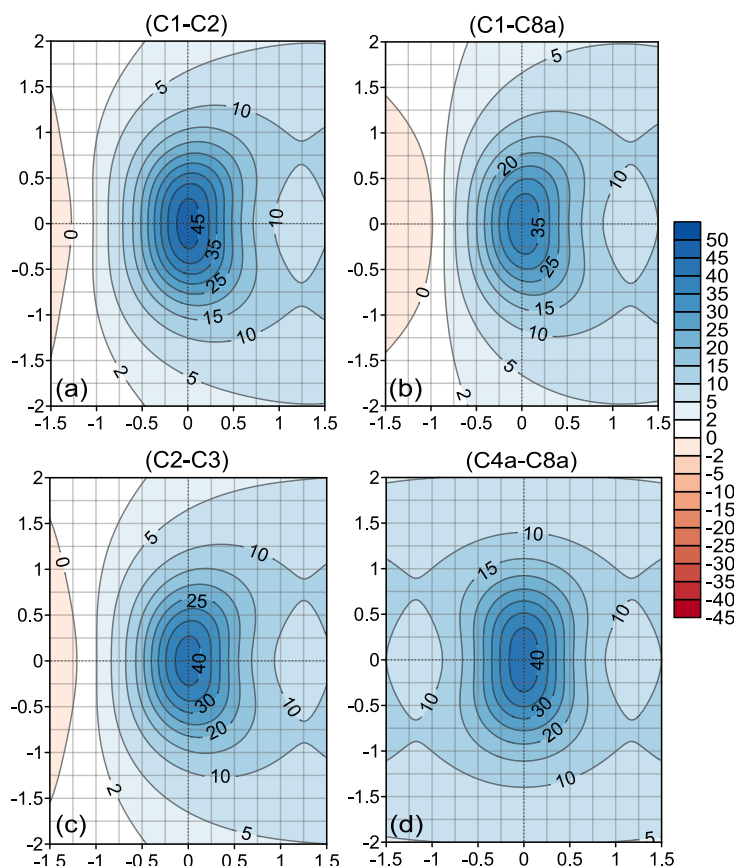


Figure 6-4: CASSCF(10,10)/6-311+G(d) isotropic shielding contour maps (in ppm) of ground state naphthalene. The figures result from 2D ghost-atom grids located perpendicularly to and crossing the midpoints of symmetry unique C-C bonds. Note that for all maps above, the right side is directed towards the inner part of the ring, which includes the ring centre. Also, the C-C bond in each map is located exactly at the (0,0) X,Y coordinates.

Inspection of figure (6-5) shows that the highest value in an isotropic shielding cloud of a C-C bond is for the C1-C2 bond, followed by the C4a-C8a and C2-C3 bonds. The C1-C8a bond has the weakest shielding and its shielding cloud shows less symmetry than other C-C bonds (see map (b)). Although the C2-C3 and C4a-C8a bonds seem to have the same levels of shielding, the latter bond has significantly higher shielding at vertical heights between 1.5 and 2.0 Å (see figure (6-5) (c) and (d)).

The isotropic shielding properties of the C-C bonds were also examined numerically with the aid of a 1D ghost atom set, see figure (6-7). Excellent agreement is observed between the above-mentioned order of the C-C bonds according to their shielding strength in figure (6-5) and the order of the bonds according to the curves (a) in figure (6-7). In addition, the C1-C8a bond shows not only the lowest shielding along the bond but also at 1 Å above it, see curves (a2) and (b2) in figure (6-7), respectively. However, for lines placed at 1 Å parallelly above the C-C bonds, the shielding values at the midpoints of these lines, see curves (b), shows a minor difference. The highest shielding is located above C4a-C8a (not C1-C2), followed by C1-C2; C2-C3; and C1-C8a.

For each of the blue curves, (a1-a4), the maximum shielding value of the AMBL is located at the bond midpoint. In contrast, none of the corresponding red curves, (b1-b4), shows a maximum shielding at its midpoint. Also, the red curves show different fluctuation details of the isotropic shieldings at 1 Å above the C-C bonds. However, it is difficult to associate these fluctuations with particular bond properties.

Finally, the 3D shielding isosurfaces confirm most of the findings discussed earlier, see figure (6-8). The +16(blue)/-16(red) isosurfaces clearly illustrate the magnetic shielding variation, especially the continuity of the shielding isosurface over the naphthalene structure. This highlights the π -electron shielding delocalisation and so proves strong aromaticity. Also, the deshielded-spheres around the carbons are represented via the red isosurface. Noticeably, the minor unevenness in the shielding isosurface agrees with curves (b) of figure (6-7) about the shielding fluctuations over C-C bonds. Also, figures (6-8 (c)) and (6-7 (b4)) agree on the observation that the C4a-C8a bond has the highest shielding at a height of 1 Å.

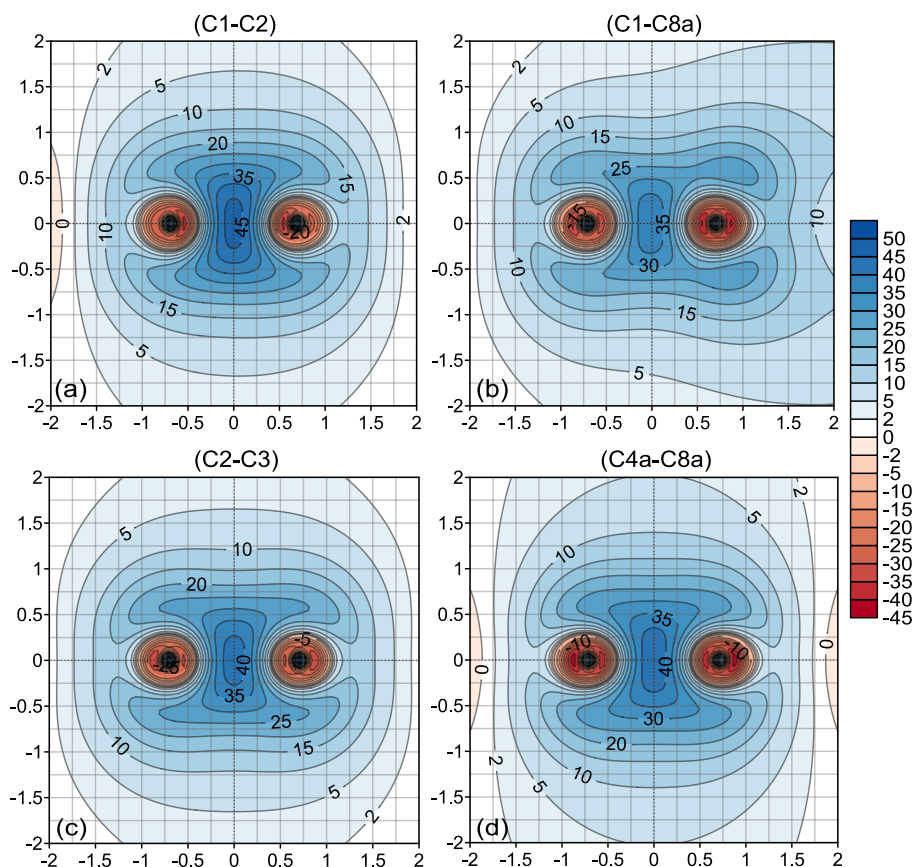


Figure 6-5: CASSCF(10,10)/6-311+G(d) isotropic shielding contour maps (in ppm) for the symmetry unique C-C bonds of ground state naphthalene. In each map, the left and right well-shielded dots represent the C nuclei of the correspondingly bond. Also, the midpoint of each bond corresponds to the (0,0) X,Y coordinates.

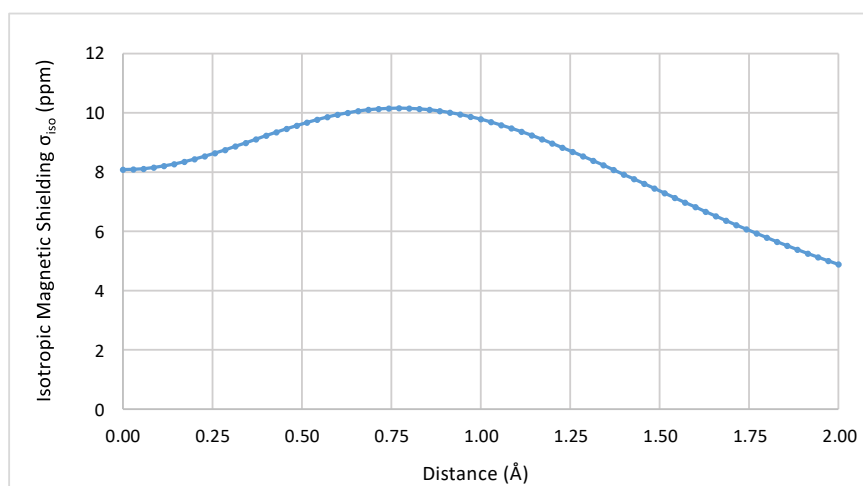


Figure 6-6: Variation in CASSCF(10,10)/6-311+G(d) isotropic shielding σ_{iso} (in ppm) of ground state naphthalene obtained from 71 ghost-atoms located perpendicularly from the ring centre to a height of 2 Å above it.

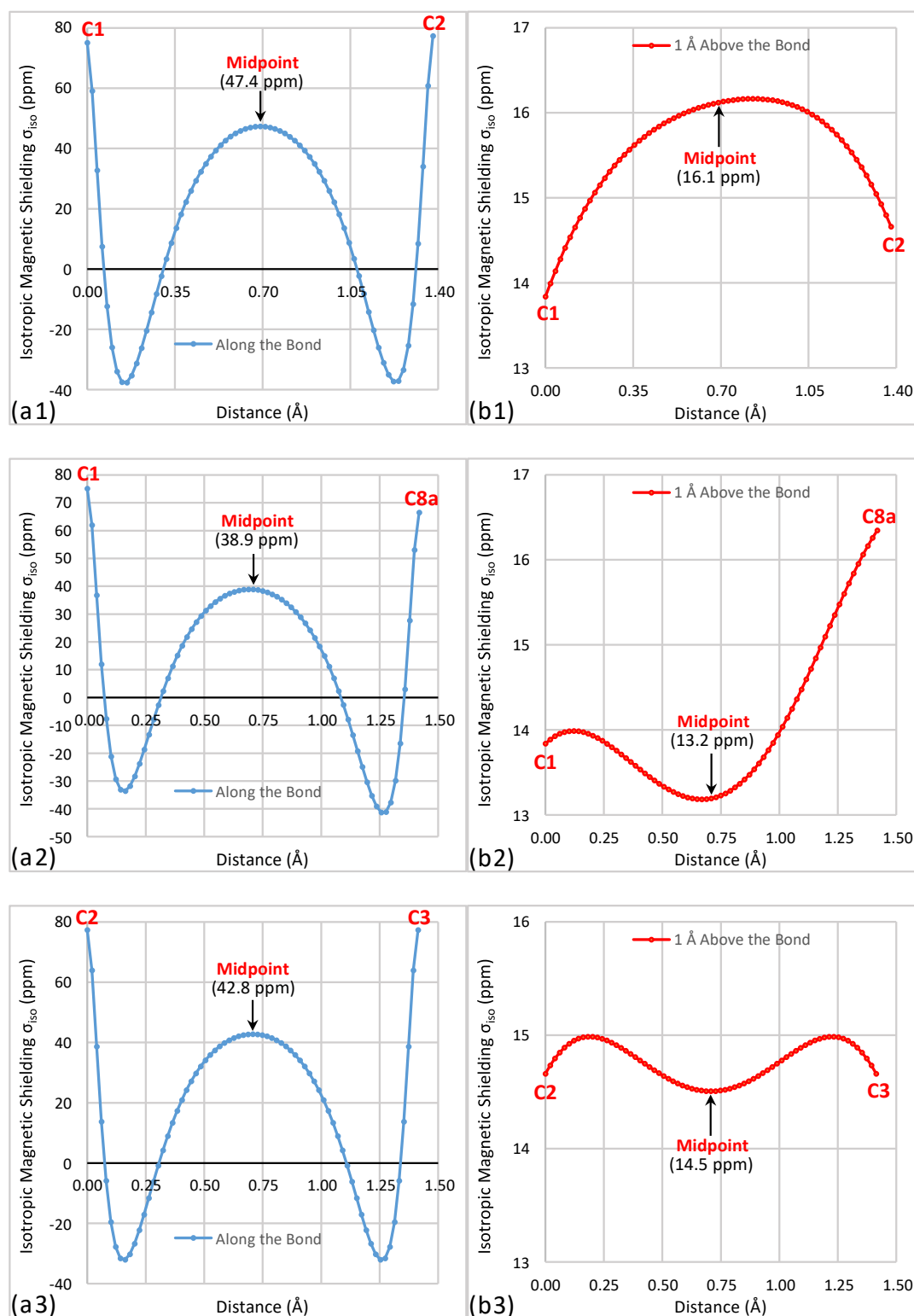


Figure 6-7: Variation in CASSCF(10,10)/6-311+G(d) isotropic shielding (σ_{iso}) (in ppm) of the symmetry unique C-C bonds of ground state naphthalene obtained from 71 ghost-atoms: (a) positioned along C-C bonds, and (b) positioned 1 Å vertically above the bonds.

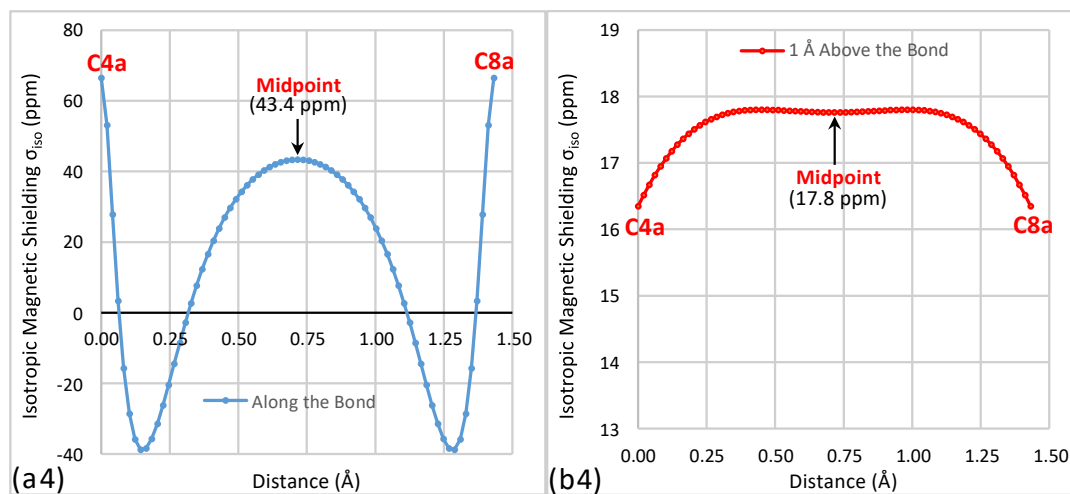


Figure 6-7: Continued.

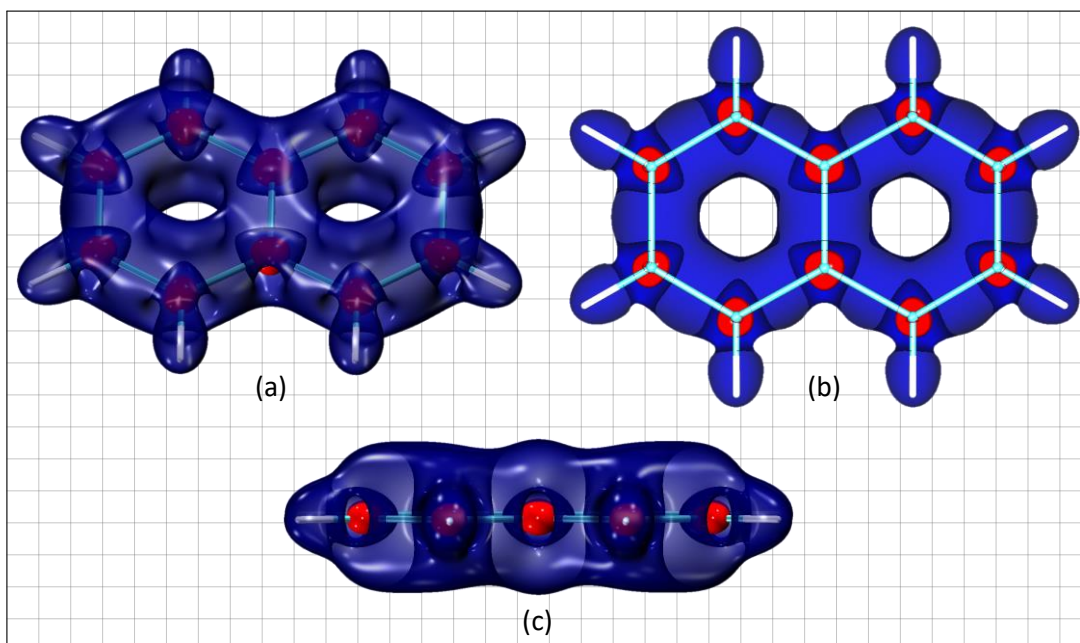


Figure 6-8: Front (a); cross-section (b); and axial side-view (c) of the isotropic shielding (σ_{iso}) isosurfaces of ground state naphthalene obtained from CASSCF(10,10)/6-311+G(d) calculations. The isosurfaces visualise the most common shielding values for aromatic molecules, +16(blue)/-16(red) (ppm).

6-3 The First Singlet State (S_1) of Naphthalene

The isotropic shielding results for the first singlet excited state, S_1 (as ${}^1B_{2u}$), are included in this chapter. Clearly, comparing data in tables (6-2) and (6-1) indicates that all nuclear σ_{iso} values for the S_1 state are lower than those for the ground state but the values of the C1 and C2 show lower decreases than that for C8a. The differences become much more pronounced for the points at 1 Å above these nuclei, especially above C8a. The $|\Delta\sigma_{\text{iso}(C-C)}^{0\text{Å}}|$ value for C1-C2 is 3.23 (ppm) which is much lower than the value of 18.35 (ppm) for C1-C8a. The $|\Delta\sigma_{\text{iso}(C-C)}^{1\text{Å}}|$ values above these bonds are 1.36 and 11.3 (ppm), respectively. This gives an initial idea about the differences in isotropic shielding behaviour between the ground and S_1 states of naphthalene.

Table 6-2: CASSCF(10,10)/6-311+G(d) isotropic shielding data (σ_{iso}) (in ppm) for S_1 naphthalene for symmetry unique carbon nuclei, and for points placed 1Å above these nuclei.

	Nuclear σ_{iso} (ppm)	σ_{iso} 1 Å above nuclei (ppm)
C1	72.66	3.23
C2	75.89	1.87
C8a	54.31	-8.07

However, the full magnetic picture cannot be understood without the 2D shielding maps shown in figures (6-9) to (6-13). Major areas inside the ring frames are dominated by deshielding activities. Maps (a) and (b) in figure (6-9) show that the shielding clouds at AMBL locations are shifted of towards the outer sides of the ring frames. This comes as the result of the opposite effects of two magnetic activities. One of these is the C-C bond shieldings, and the second one is associated with the strongly deshielded rings. These opposite effects dominate not only the ring area at the molecular plane but also continue at higher vertical heights up to 1 Å, see figure (6-9 (c-e)). As a result, the delocalised shielded-clouds are shifted towards regions outside the rings. The $\sigma_{\text{iso}(zz)}$ map, see figure (6-10), agrees with this observation with a small difference that some degree of shielding clouds localisation at the C-H bonds. All 2D shielding maps of figures (6-(9 to 13)) show fully or in part the strongly-deshielded ring centre. Figure (6-14) shows the deshielding details inside the ring starts from -37.7 at the ring centre to -11.7 (ppm) at 2 Å above the centre.

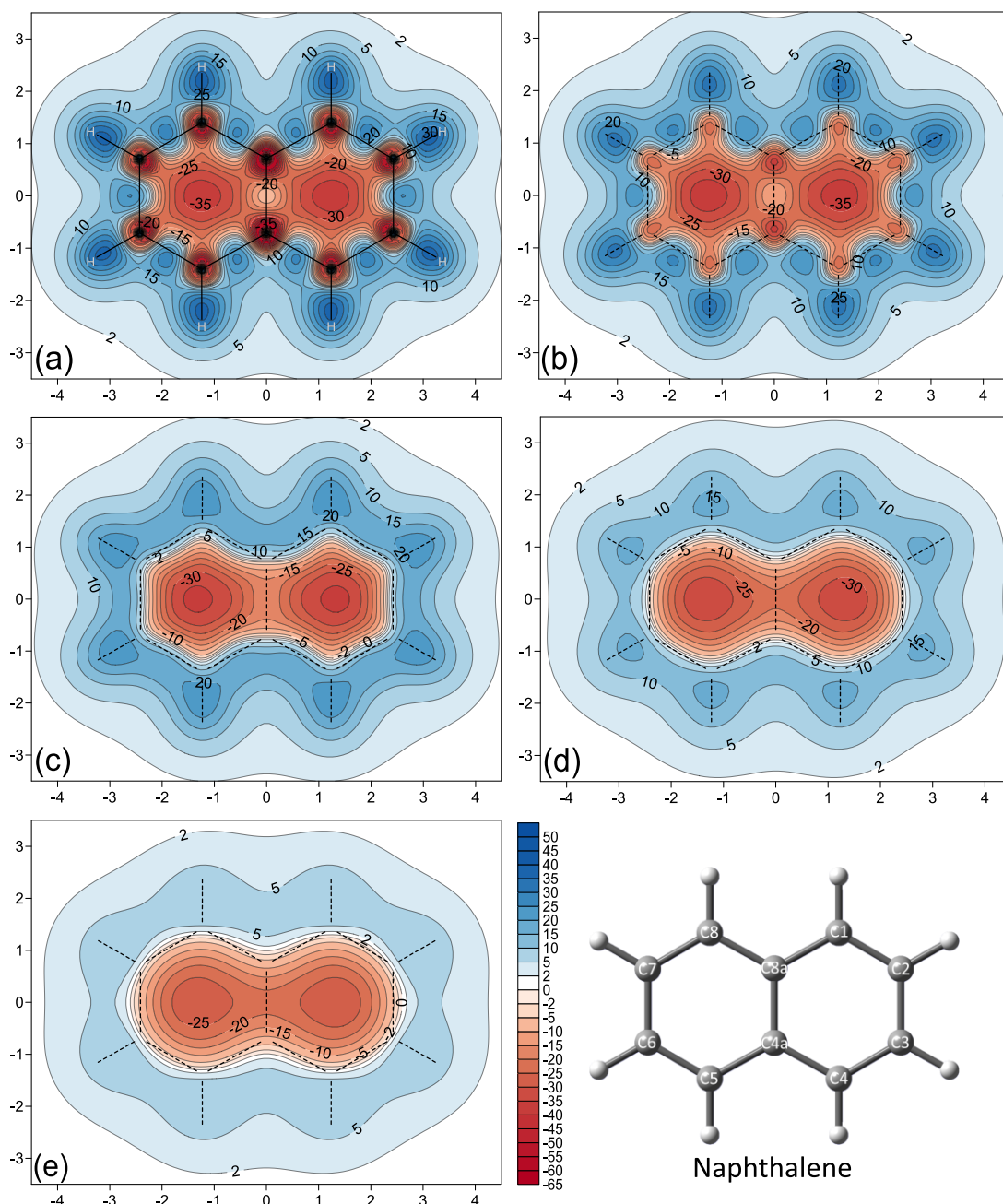


Figure 6-9: Contour maps of the isotropic shieldings (σ_{iso}) (in ppm) obtained at the CASSCF(10,10)/6-311+G(d) level of theory for S_1 naphthalene. (a-e): for grids respectively placed at 0.0, 0.25, 0.50, 0.75 and 1.00 Å vertical heights above the molecular plane.

The deshielded-spheres around carbon are linked with the deshielded region inside the rings, and the deshielded clouds of both rings are merged together. Focusing on the deshielding behaviour of bond C4a-C8a supports the suggestion that shielding and deshielding activities work against one another, i.e., they compete to occupy space according to their strengths. From the

significantly lower degree of deshielding around the C4a-C8a bond in figures (6-9 (a)); (6-11); (6-12 (d)) and (6-13 (d)), it seems that the bond ABL of this bond is originally shielded and only averaging with the strong deshieldings of the two rings yields the final σ_{iso} profile. Accordingly, curves (a4) and (b4) in figure (6-15) show the midpoint of the bond as the least deshielded point, while the most deshielded value is found at 1 Å above the bond midpoint, -6.9 and -21.5 (ppm), respectively. This deshielding behaviour is the opposite of the deshielding trend at the ring centre, which was mentioned earlier, see figure (6-14).

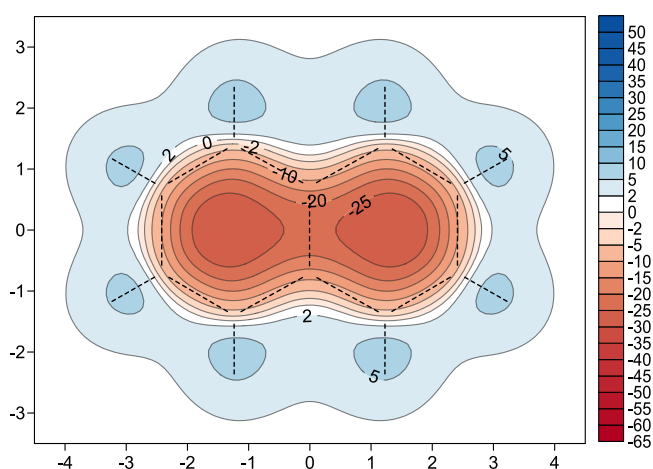


Figure 6-10: Contribution of the vertical-component of the isotropic shielding ($\sigma_{\text{iso}(zz)}$) (in ppm) of S_1 naphthalene, obtained at the CASSCF(10,10)/6-311+G(d) level of theory for a grid placed vertically at 1.00 Å above the molecular plane.

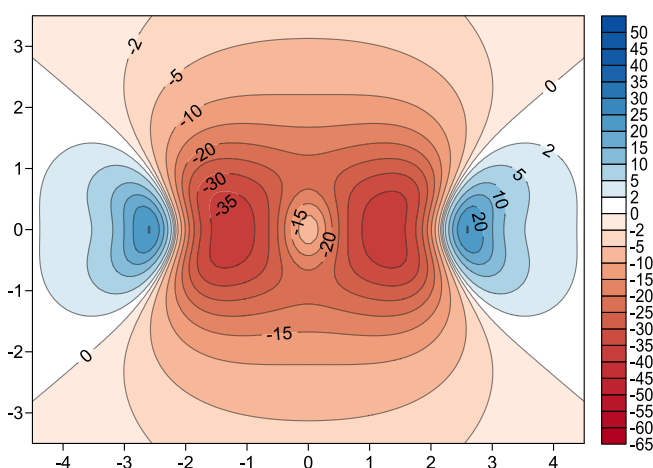


Figure 6-11: XZ cross-section isotropic shielding map (in ppm) of S_1 naphthalene, obtained at the CASSCF(10,10)/6-311+G(d) level of theory for a grid placed vertically and bisecting the molecular plane at its X and Z axes.

Three observations related to figure (6-11): Firstly, the contrast between shielded and deshielded areas is very noticeable. Secondly, there is a less deshielded oval-shaped core centred on the C4a-C8a bond. Thirdly, the two well-deshielded clouds at the middle region of the rings, which occupy up to just under than 1 Å vertical height, are enclosed in a central, larger and less-deshielded cloud with a vertical height of more than 3 Å.

Due to the shifts in the locations of the shielding clouds of the C-C bonds, it is not sufficient to depend on one vertical cross-section map to understand shielding behaviour see figures (6-12) and (6-13). The C4a-C8a bond is an exception as it shows no shifts in its shielding cloud since the magnetic environment surrounding this bond is fully symmetric.

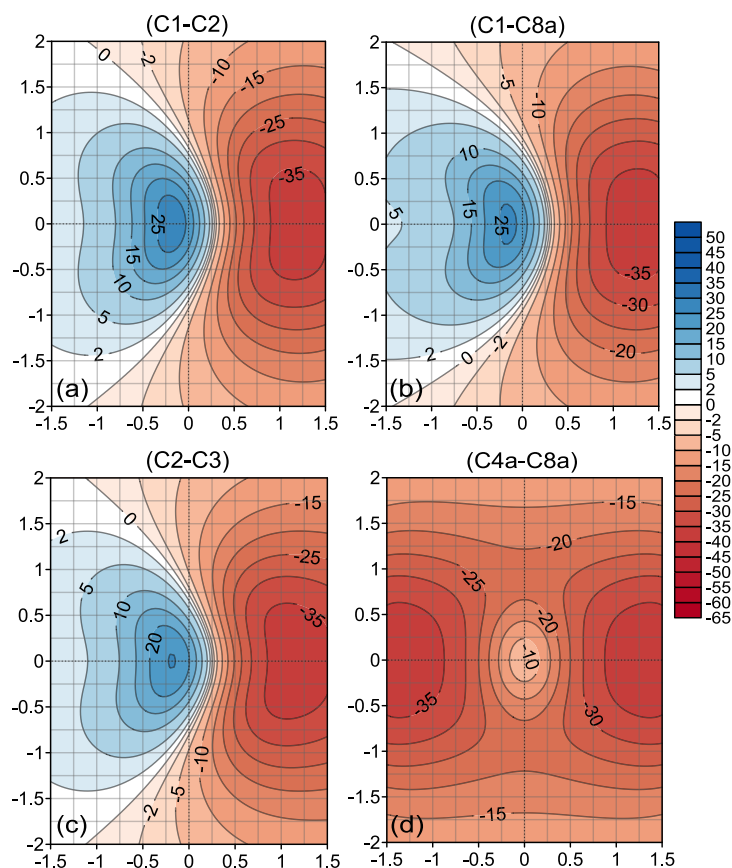


Figure 6-12: CASSCF(10,10)/6-311+G(d) isotropic shielding contour maps (in ppm) of S_1 naphthalene. The figures result from 2D ghost-atom grids located perpendicularly to and crossing the midpoints of symmetry unique C-C bonds. Note that for all maps above, the right side is directed towards the inner part of the ring, which includes the ring centre. Also, the C-C bond in each map is located exactly at the (0,0) X,Y coordinates.

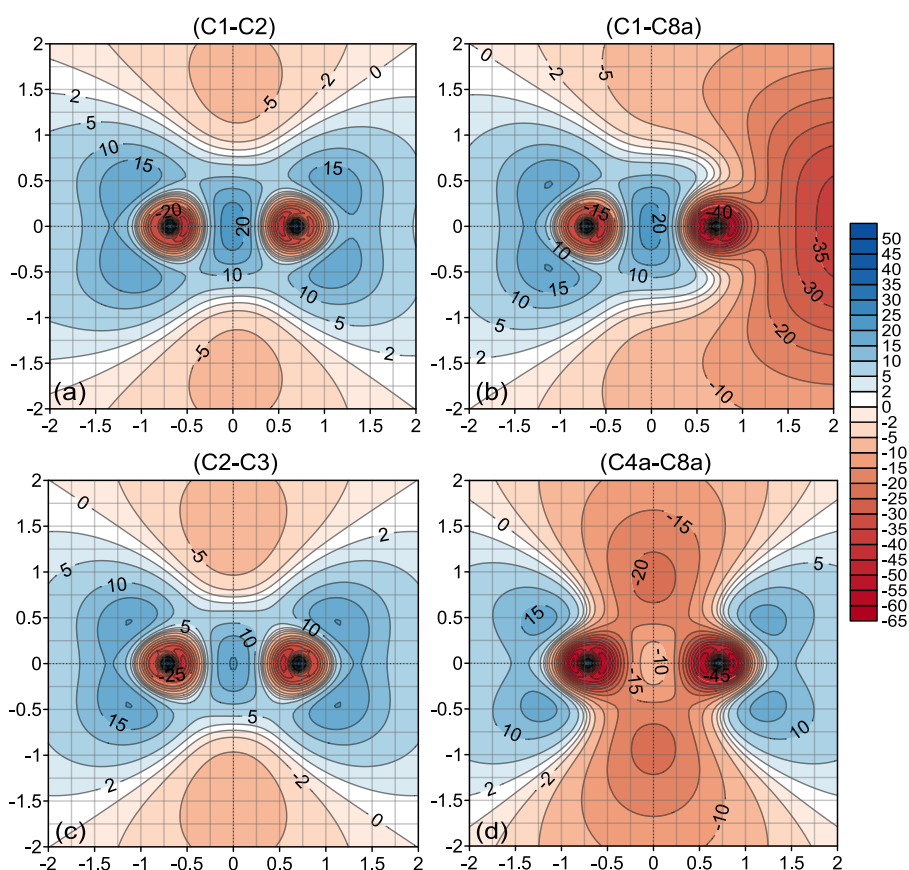


Figure 6-13: CASSCF(10,10)/6-311+G(d) isotropic shielding contour maps (in ppm) for the symmetry unique C-C bonds of S_1 naphthalene. In each map, the left and right well-shielded dots represent the C nuclei of the correspondingly bond. Also, the midpoint of each bond corresponds to the (0,0) X,Y coordinates.

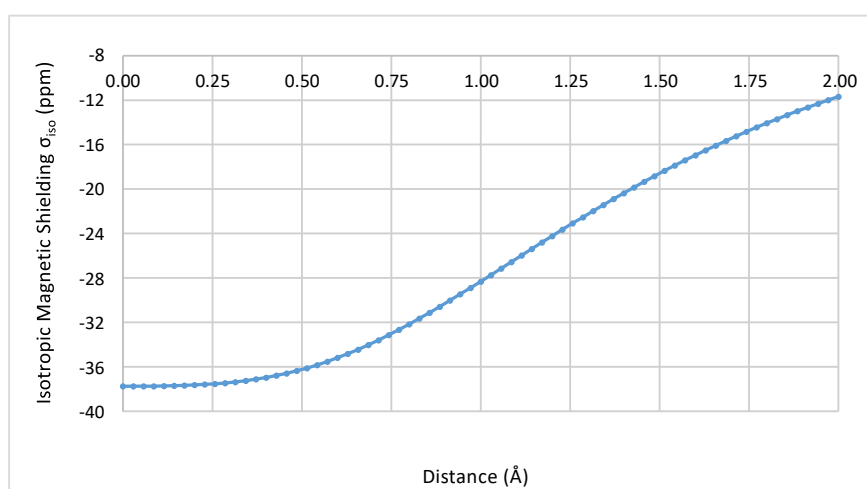


Figure 6-14: Variation in CASSCF(10,10)/6-311+G(d) isotropic shielding σ_{iso} (in ppm) of S_1 naphthalene obtained from 71 ghost-atoms located perpendicularly from the ring centre to a height of 2 Å above it.

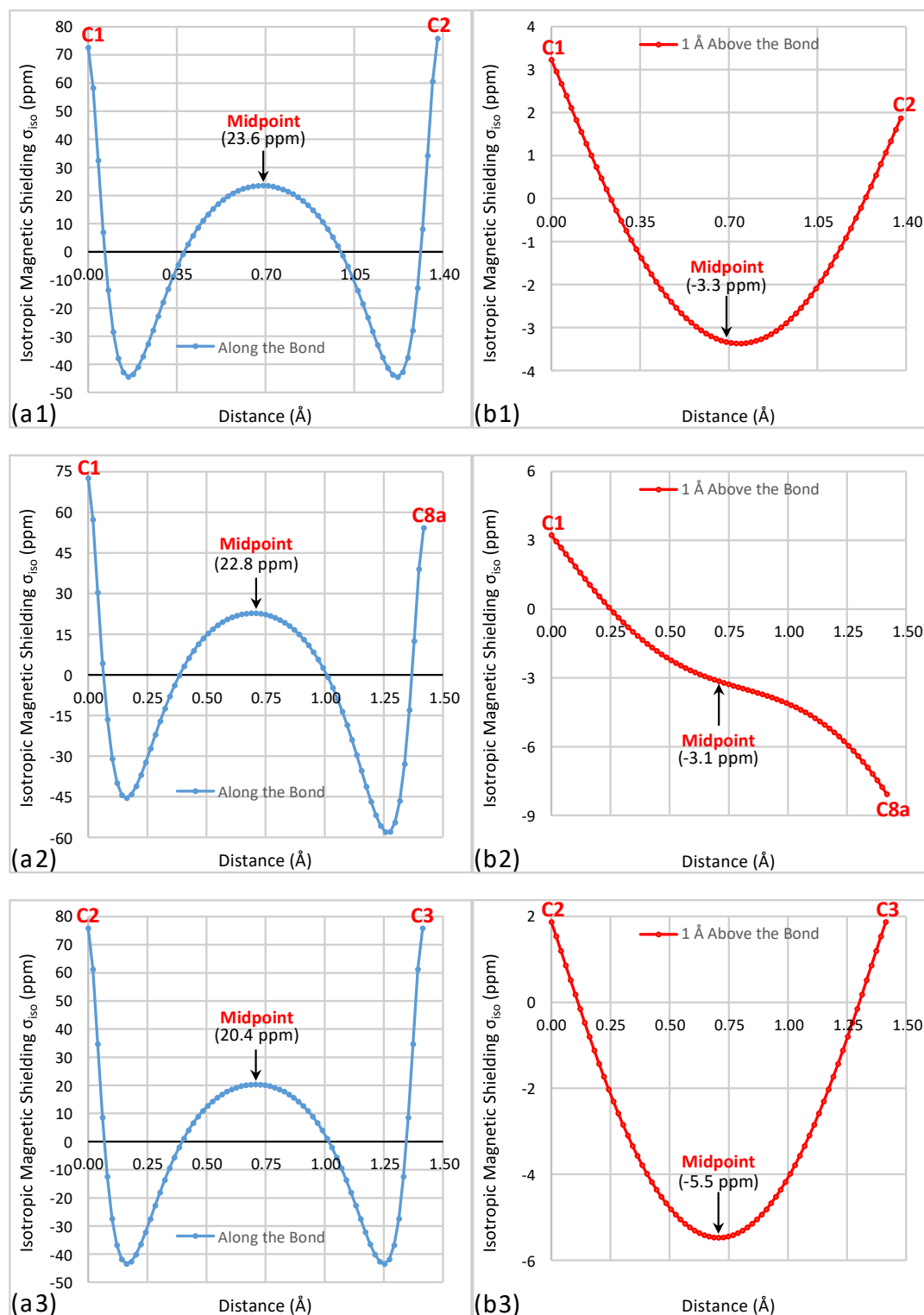


Figure 6-15: Variation in CASSCF(10,10)/6-311+G(d) isotropic shielding (σ_{iso}) (in ppm) of the symmetry unique C-C bonds of S_1 naphthalene obtained from 71 ghost-atoms: (a) positioned along C-C bonds, and (b) positioned 1 Å vertically above the bonds.

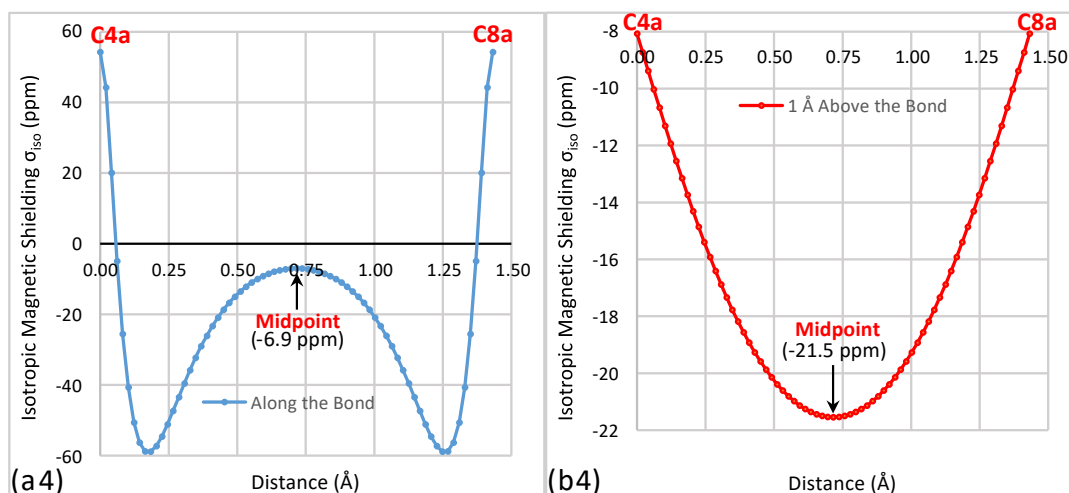


Figure 6-15: Continued.

According to the shielding values on the maps in figure (6-12), the σ_{iso} shielding of the C-C bonds follow the order: C1-C2 = C1-C8a > C2-C3 >>> C4a-C8a. The ordering of the first two bonds seems to be inconsistent with the values in the figure (6-13). This can be attributed to the migration of the shielding cloud far from the C-C bond lines towards the region outside the ring frame.

Similar effects can be seen when comparing the σ_{iso} variation along the bonds, and at 1 Å above the bonds (see figure (6-15)).

All magnetic data for S_1 naphthalene shows that this electronic state is strongly antiaromatic. The difference becomes obvious when comparing the S_1 and ground state results, see section (6-2). The main antiaromatic feature is the deshielding inside the two rings which can also be illustrated using 3D isosurfaces.

The 3D σ_{iso} results for S_1 naphthalene are shown in figure (6-16). Which includes four isosurfaces. In order to compare S_1 with the ground state, the blue/red isosurfaces visualise the values of (+16) / (-16) (ppm), respectively. The other two isosurfaces, the transparent/transparent red, visualise the values (+9)/(-9), respectively, and aim to show the expansion tendency of the shielding and deshielding activities around the molecule.

Clearly, the deshielded-spheres around carbon are linked with the deshielding cloud which occupies the inner space of the rings. The shielding cloud shift

towards the outside of the ring frame is obvious not only for the (+16) shielding value but also for the lower value of (+9), see the blue and the transparent isosurfaces, respectively. These isosurfaces illustrate the horizontal expansion tendency of the shieldings. The red and the transparent red isosurfaces, illustrate vertical expansion. Both expansions prove the avoidance between the opposing activities. Finally, image (d) shows clearly the unusual deshielding activity around the C4a-C8a bond which was mentioned earlier.

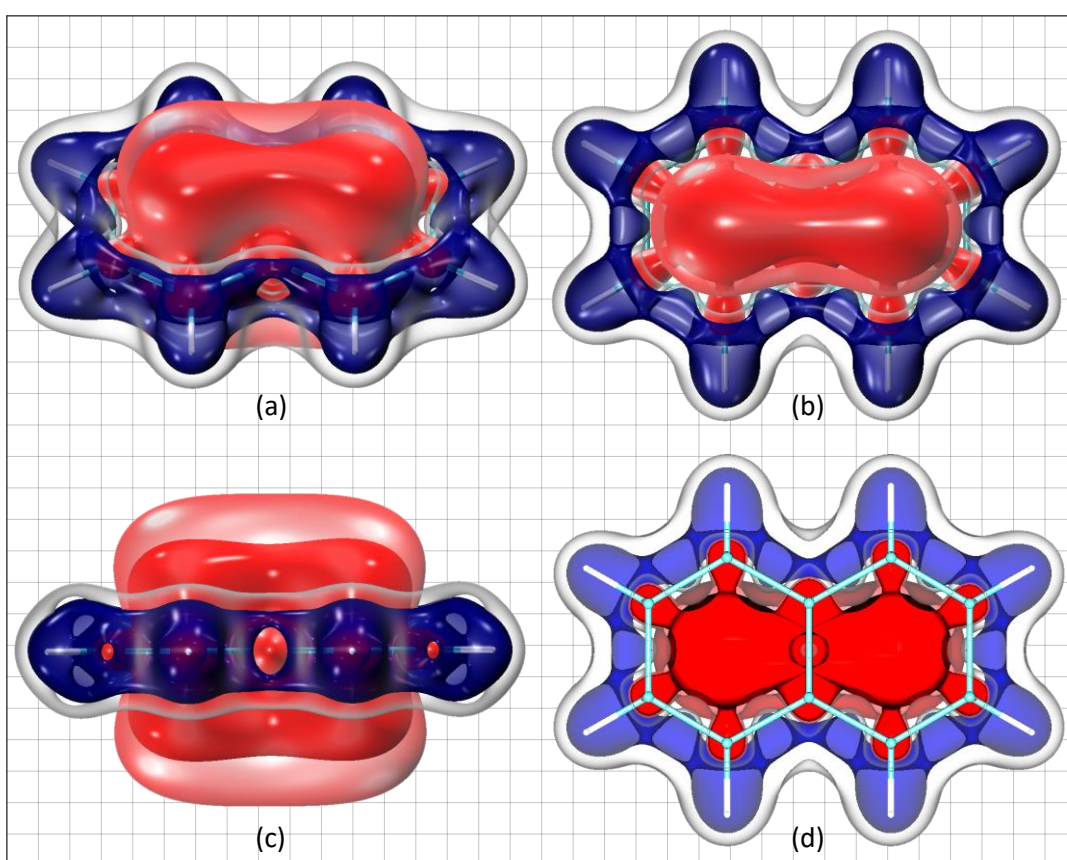


Figure 6-16: Front (a-b); side (c); and horizontal cross-section views of the isotropic shielding (σ_{iso}) obtained from CASSCF(10,10)/6-311+G(d) calculations for S_1 naphthalene, visualised by four isosurfaces as value(ppm)/colour of: +16/blue ; -16/red ; +9/transparent; and -9/transparent red.

6-4 The Second Singlet State (S_2) of Naphthalene

The second singlet state, S_2 (as ${}^1B_{1u}$), shows higher shielding values of both nuclear (σ_{iso}^0) and σ_{iso}^1 than in the ground state of naphthalene, see tables (6-3) and (6-1), respectively. However, the increase for the σ_{iso}^1 values is larger than that for σ_{iso}^0 . For the S_2 state, the increase is around one-third more than of S_0 state value. Interestingly, all the carbon nuclei in S_2 naphthalene show a significant shielding increase but C8a nucleus shows the largest increase in both σ_{iso}^0 and σ_{iso}^1 parameters. As a result, the C4a-C8a bond has different shielding profile in comparison to the previous two states.

The $|\Delta\sigma_{\text{iso(C-C)}}^0|$ and $|\Delta\sigma_{\text{iso(C-C)}}^1|$ values for the C1-C8a and C1-C2 bonds are (3.87 / 12.53) and (2.79 / 2.42) (ppm); respectively. This shows that the maximum variation is observed for the points at 1 Å above the ends of the C1-C8a bond. Also, the high σ_{iso} values in table (6-3) can be considered as a sign of the strong shielding and aromaticity of this electronic state.

Table 6-3: CASSCF(10,10)/6-311+G(d) isotropic shielding data (σ_{iso}) (in ppm) for S_2 naphthalene for symmetry unique carbon nuclei, and for points placed 1Å above these nuclei.

	Nuclear σ_{iso} (ppm)	σ_{iso} 1 Å above nuclei (ppm)
C1	83.68	20.77
C2	80.89	23.19
C8a	79.81	33.30

Comparing the 2D results from the previous two sections to those for the S_2 state shows a substantial increase in shielding, see figures (6-(17 to 21)). A glance at figure (6-17) shows immediately that the isotropic shielding of the S_2 state is very much the opposite of that for the S_1 state. Both rings are well-shielded, with intensive shielding clouds around the bonds. However, the shielding clouds of the C-C bonds show significant shifts towards the inside region of the rings (see map (a)). Also, the most intensive circular shielding clouds inside each ring are found at heights of 0.50-1.00 Å, see maps (c-e). This indicates strong shielding activity at those heights. Surprisingly, the figure shows the highly shielded areas prefer to be much more contracted inside the rings than what has been found for the ground state (see figure (6-1)). σ_{iso} at

1 Å is dominated by $\sigma_{\text{iso}(zz)}$ because of the high similarity between the σ_{iso} and $\sigma_{\text{iso}(zz)}$ plots in figures (6-17 (e)) and (6-18).

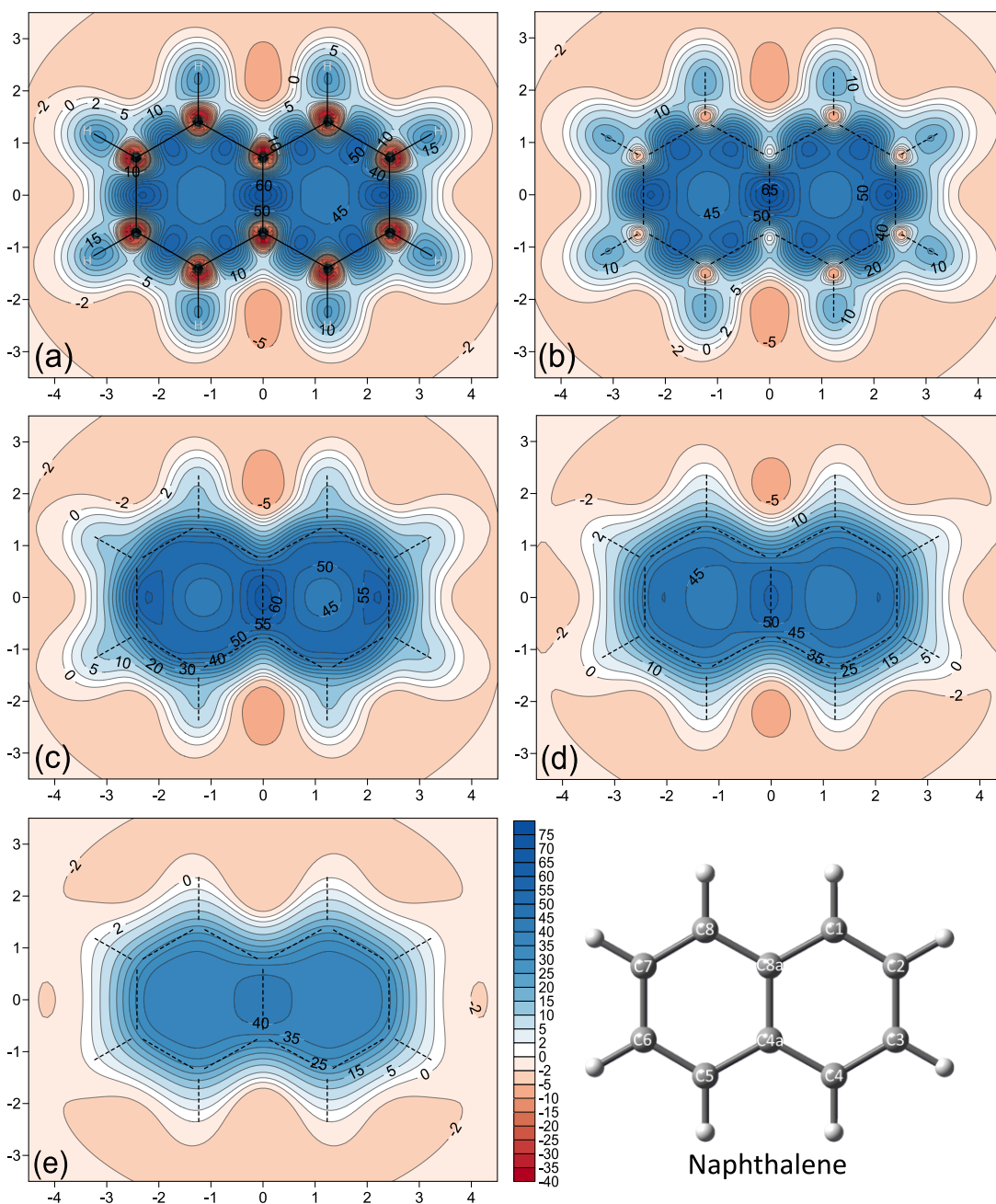


Figure 6-17: Contour maps of the isotropic shieldings (σ_{iso}) (in ppm) obtained at the CASSCF(10,10)/6-311+G(d) level of theory for S_2 naphthalene. (a-e): for grids respectively placed at 0.0, 0.25, 0.50, 0.75 and 1.00 Å vertical heights above the molecular plane.

It can be argued that when electron delocalisation becomes more pronounced, the ring current and the resulting shielding clouds prefer shorter circular paths inside the rings. These strong ring shielding clouds prepare an

adequate magnetic environment which works as an attractive factor causing the C-C bonds shielding clouds to be shifted to the inner regions of the rings.

The shielding at different heights above the ring centre shows similar behaviour. This behaviour is hard to notice in figures (6-17,19,20) but the curve in figure (6-22) is easier to follow. When comparing the shielding profile of this curve to that for the ground state in figure (6-6), we notice important differences. For the ground state, the maximum isotropic shielding is 10.16 (ppm) at 0.77 Å. The value for the S_2 state is 42.52 (ppm) at 0.51 Å. This means the highest shielding associated with electron delocalisation moves much closer to the molecular plane when the overall shielding of the ring increase (i.e. with an increase in the aromaticity).

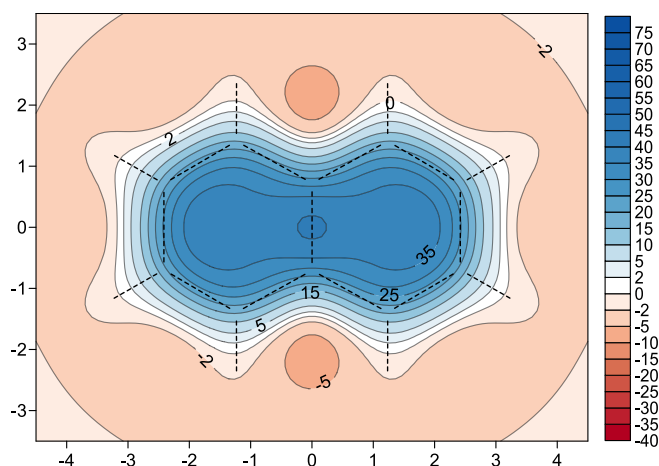


Figure 6-18: Contribution of the vertical-component of the isotropic shielding ($\sigma_{iso(zz)}$) (in ppm) of S_2 naphthalene, obtained at the CASSCF(10,10)/6-311+G(d) level of theory for a grid placed vertically at 1.00 Å above the molecular plane.

As it can be seen in figure (6-19), the shielded region has a considerable vertical bulk. It reaches 3.5 Å in height, which is much higher than that in the ground state (see figure (6-3)). Both figures show similarities in shielding behaviour. For both states, deshielded regions are found at the left and the right sides of the molecule.

Another important observation is that the shielding of the C4a-C8a bond is much higher than those around other C-C bonds. As a consequence, the deshielded-spheres of this bond behave differently from the general trend for the other C-C bonds, see figures (6-17 (a,b)) and (6-21 (d)).

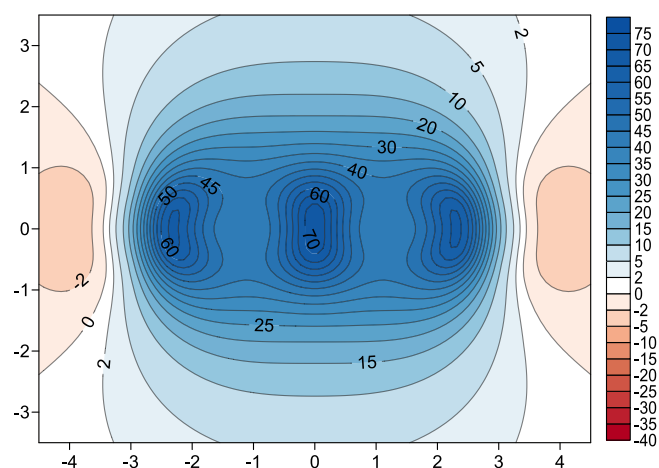


Figure 6-19: XZ cross-section isotropic shielding map (in ppm) of S_2 naphthalene, obtained at the CASSCF(10,10)/6-311+G(d) level of theory for a grid placed vertically and bisecting the molecular plane at its X and Z axes.

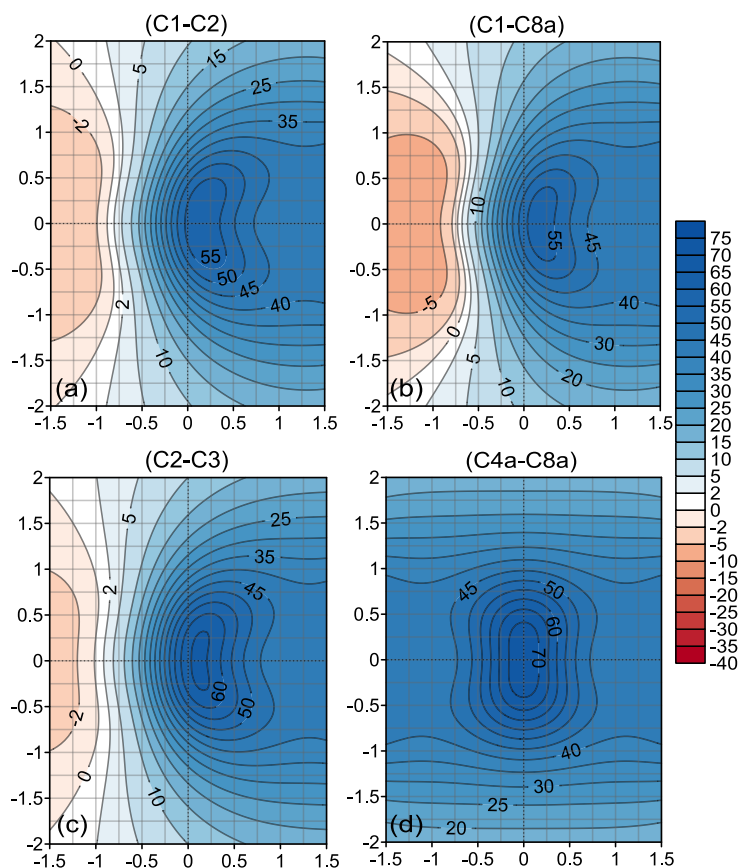


Figure 6-20: CASSCF(10,10)/6-311+G(d) isotropic shielding contour maps (in ppm) of S_2 naphthalene. The figures result from 2D ghost-atom grids located perpendicularly to and crossing the midpoints of symmetry unique C-C bonds. Note that for all maps above, the right side is directed towards the inner part of the ring, which includes the ring centre. Also, the C-C bond in each map is located exactly at the (0,0) X,Y coordinates.

The deshielded-spheres of the nuclei in the C4a-C8a bond show distortions in their shapes, they are not centred on the carbon nuclei, and incorporate significant variations in their levels of deshielding. As it can be seen in figure (6-21 (d)), the lowest levels of deshielding in these spheres are observed inside the bond. The most deshielded parts are located outside the bond. Further details can be seen in curves (a1-a4) in figure (6-23). The deshielding parts of the C4a-C8a bond are the shortest ones in comparison to other C-C bonds, while most of the curve is strongly shielded. Also, the lowest deshielding values in the figure are within the deshielded-spheres of this bond. All these features are caused by the strong shielding of the bond. This is a feature example of competition between shielding and deshielding activities.

The arrangement the C-C bonds according to shielding levels is as follows: C4a-C8a > C2-C3 > C1-C2 > C1-C8a, see figures (6-20,21,23). Although this order differs from that in the ground state, however, the bond with weakest shielding is C1-C8a in both states.

A further observation associated with figure (6-23). The shielding at 1 Å above the C-C bonds is shown by the red curves (b) which follows the same order as that mentioned above for the corresponding bonds, curves (a). Additionally, the shielding above the bonds shows that the minimum shielding values are located above the nuclei, except that the above C8a nucleus in the C1-C8a bond, see curve (b2). The reason for this exception can be explained by looking at figure (6-17 (e)) and curve (6-21 (b)). The two maps show that the shielding clouds of the two rings are linked over the C4a-C8a bond, making the spaces at 1 Å above these nuclei much more shielded. There are no such shielding effects over the C1 nucleus or any other carbon nuclei.

Due to the very high isotropic shielding of S₂ naphthalene, the +16 (ppm) blue isosurface, does not show much details of the overall 3D shielding behaviour. Therefore, another value, +44 (ppm), has also been selected for a second shielding isosurface, the green isosurface, see figure (6-24).

On the other hand, deshielding activity can be well-represented by the -16 (ppm) isosurface only due to no more deshielding features to be shown by a further value.

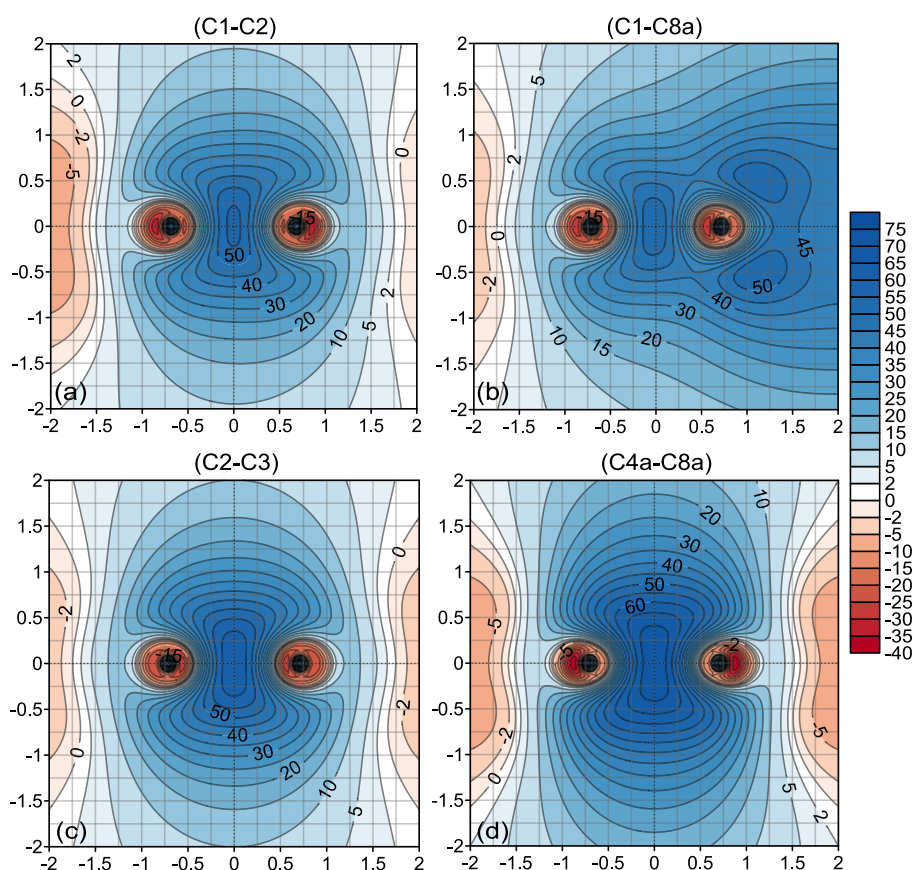


Figure 6-21: CASSCF(10,10)/6-311+G(d) isotropic shielding contour maps (in ppm) for the symmetry unique C-C bonds of S_2 naphthalene. In each map, the left and right well-shielded dots represent the C nuclei of the correspondingly bond. Also, the midpoint of each bond corresponds to the (0,0) X,Y coordinates.

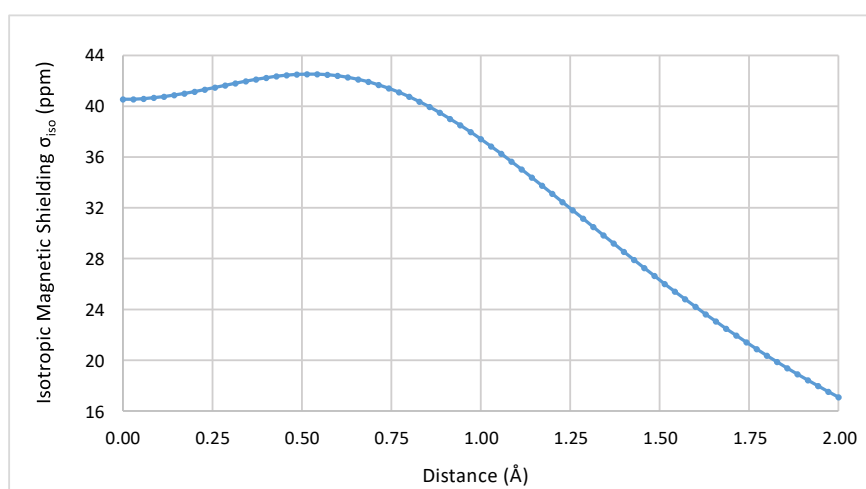


Figure 6-22: Variation in CASSCF(10,10)/6-311+G(d) isotropic shielding σ_{iso} (in ppm) of S_2 naphthalene obtained from 71 ghost-atoms located perpendicularly from the ring centre to a height of 2 Å above it.

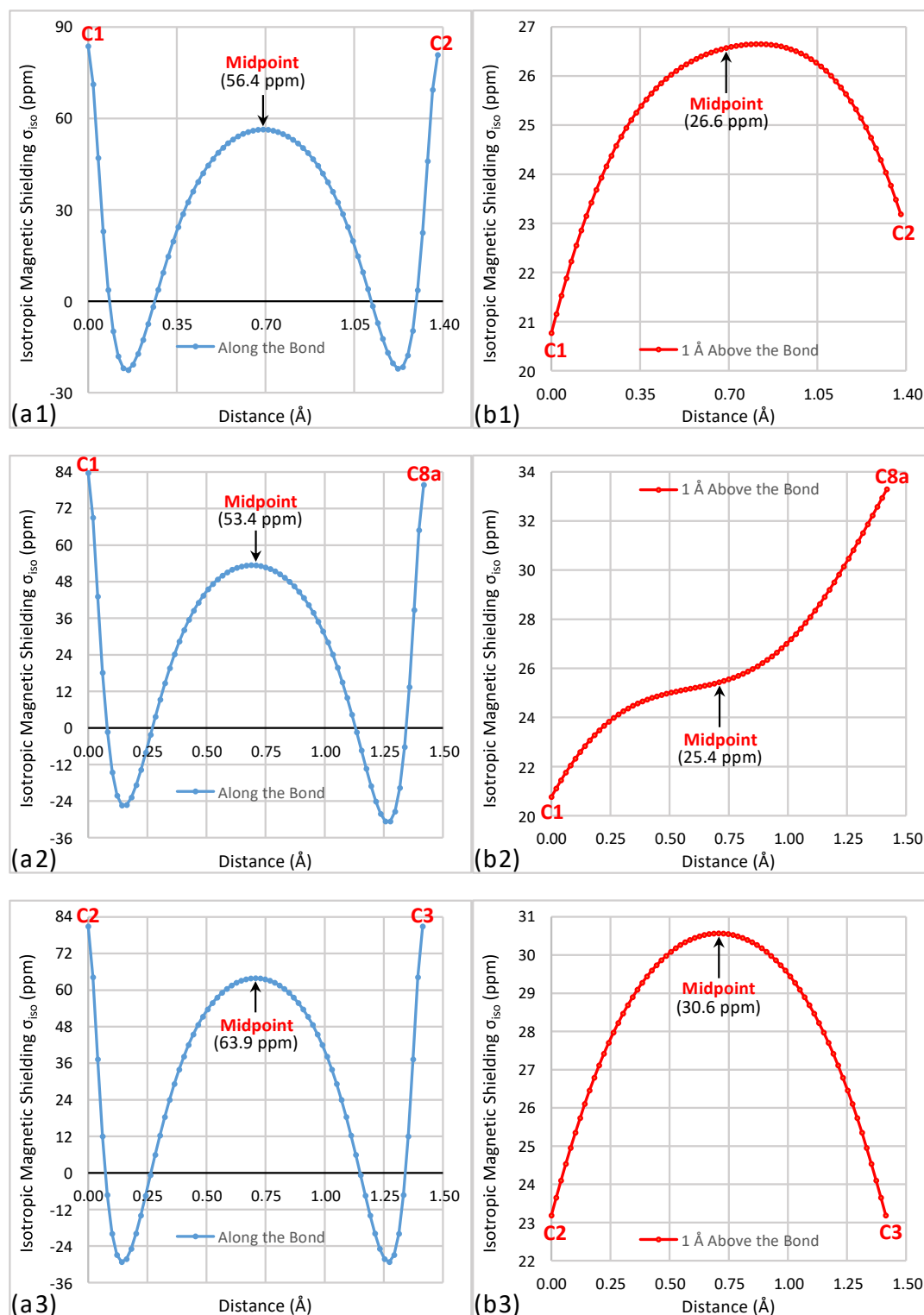


Figure 6-23: Variation in CASSCF(10,10)/6-311+G(d) isotropic shielding (σ_{iso}) (in ppm) of the symmetry unique C-C bonds of S_2 naphthalene obtained from 71 ghost-atoms: (a) positioned along C-C bonds, and (b) positioned 1 Å vertically above the bonds.

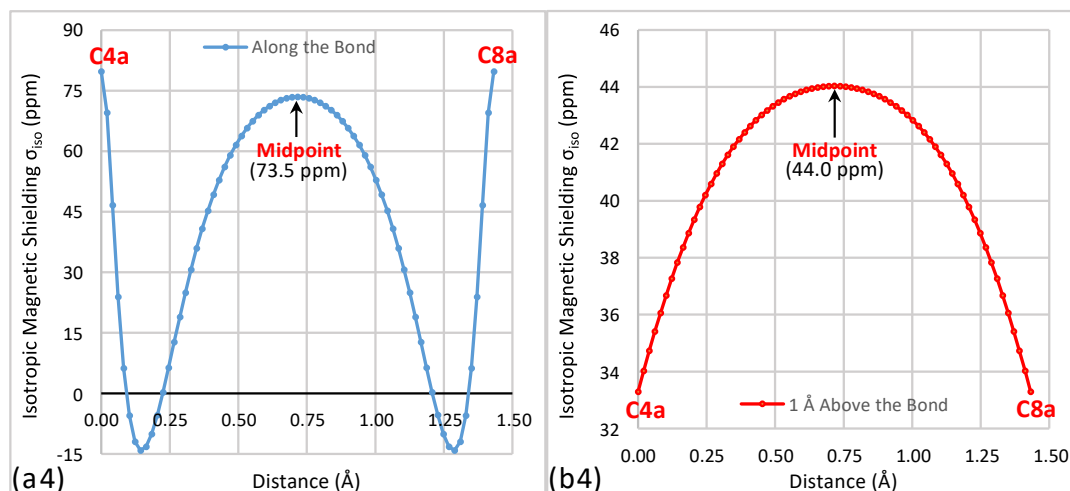


Figure 6-23: Continued.

As it can be seen from the shielding profiles in figure (6-24 (a,b)), the blue isosurface represents the common trend in the shielding of aromatic molecules. The shielding cloud surrounds the molecule and shows a considerable vertical bulk. The shieldings over the C-H bonds are also displayed by this isosurface. These findings indicate that S_2 naphthalene is strongly aromatic.

However, several details can only be understood by looking at the +44 (ppm) green isosurface in figure (6-24 (c,d)). This green isosurface illustrates the vertical and the horizontal shrinkage of the strongly shielded region towards the insides of the rings. When comparing the expansion tendencies of the green and the blue isosurfaces, it becomes obvious that the stronger shieldings are closer to the molecular plane. The displacements in the locations of the shielding clouds of the C-C bonds can also be seen via the green isosurface. The higher isotropic shielding of the C4a-C8a bond, which links the shielding clouds of the two rings, cannot be seen in the +16 (ppm) isosurface, but is well-represented by the +44 (ppm) green isosurface.

Finally, the results reported in this section, show clearly that the shielding in the S_2 state is much stronger than in ground state, S_0 , naphthalene. Consequently, the S_2 state has much more pronounced aromatic features.

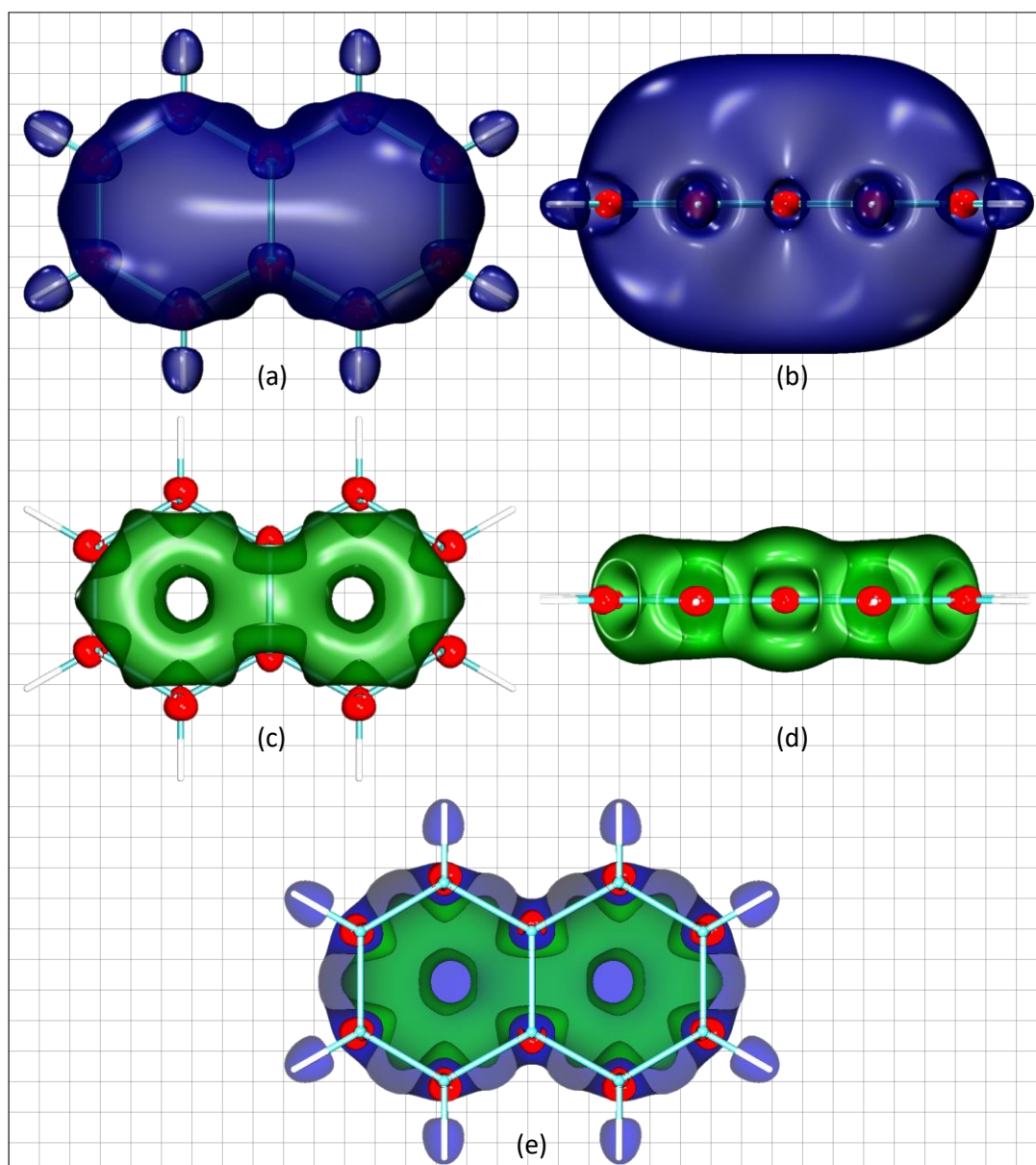


Figure 6-24: Isotropic shielding (σ_{iso}) isosurfaces of S_2 naphthalene obtained from CASSCF(10,10)/6-311+G(d) calculations. The blue isosurface corresponds to the +16 (ppm) shielding value. The green isosurface corresponds to the +44 (ppm) shielding value. Isotropic deshieldings are represented by the red isosurface which corresponds to -16 (ppm). (a,c) show the front-view; (b,d), show two side-views; (e) shows the cross-section of the three isosurfaces.

6-5 The First Triplet State (T_1) of Naphthalene

The first triplet state, T_1 , was confirmed as ${}^3B_{1u}$. All isotropic shielding data for T_1 naphthalene in table (6-4) are positive, both the nuclear σ_{iso} and the $\sigma_{\text{iso}}^{1\text{\AA}}$ of C8a are the lowest values amongst the carbons. In other words, the carbon nuclei of the C-C bond at the fused location and the points at 1 Å above them show the lowest isotropic shieldings. This behaviour is similar to that of the S_1 state reported in table (6-2). Also, the $\sigma_{\text{iso}}^{1\text{\AA}}$ values, in general, are smaller than those for the ground or the S_2 states, see tables (6-1) and (6-3), respectively, but higher in shielding than those for the S_1 state, see table (6-2).

In addition, the $|\Delta\sigma_{\text{iso(C-C)}}^{0\text{\AA}}|$ and $|\Delta\sigma_{\text{iso(C-C)}}^{1\text{\AA}}|$ values are (6.48 / 0.32) and (25.24 / 3.68) (ppm) for C1-C2 and C1-C8a bonds, respectively. This indicates that the maximum nuclear shielding difference amongst the C-C bonds is observed for the C1-C8a bond.

Table 6-4: CASSCF(10,10)/6-311+G(d) isotropic shielding data (σ_{iso}) (in ppm) for T_1 naphthalene for symmetry unique carbon nuclei, and for points placed 1Å above these nuclei.

	Nuclear σ_{iso} (ppm)	σ_{iso} 1 Å above nuclei (ppm)
C1	82.78	7.61
C2	76.30	7.93
C8a	57.54	3.93

In addition to what was mentioned above about the similarity in the shielding data between the T_1 and S_1 states, comparing all S_1 state isotropic shielding results, see figures (6-(9-16)), to the corresponding T_1 state results reported in this section, see figures (6-(25-32)), strongly suggests that the shielding/deshielding trends for these two states are very similar.

However, there are several important differences. For instance, despite the similarity in the deshielding regions inside the rings, the levels of deshielding are much lower in the T_1 state in comparison to the S_1 state. As a result, the necessity to shift shielding clouds to outside of the ring frames decreases. Therefore, it can be observed that the shielding clouds over C-C bonds are less shifted in T_1 than in the S_1 state, see maps (a,b) in figures (6-25) and (6-9), respectively. For the same reason, these maps also show that the horizontal expansion of the shielding clouds is smaller in the T_1 state.

As the avoidance between deshielding and shielding effects becomes less pronounced, the intensities and locations of the clouds around C-C and C-H bonds try to get back to the S_0 picture. Maps (a-c) in figures (6-25) and (6-9) indicate that the C-C bond shieldings become higher in T_1 in comparison to S_1 state, while the C-H bond clouds show a change in the opposite direction.

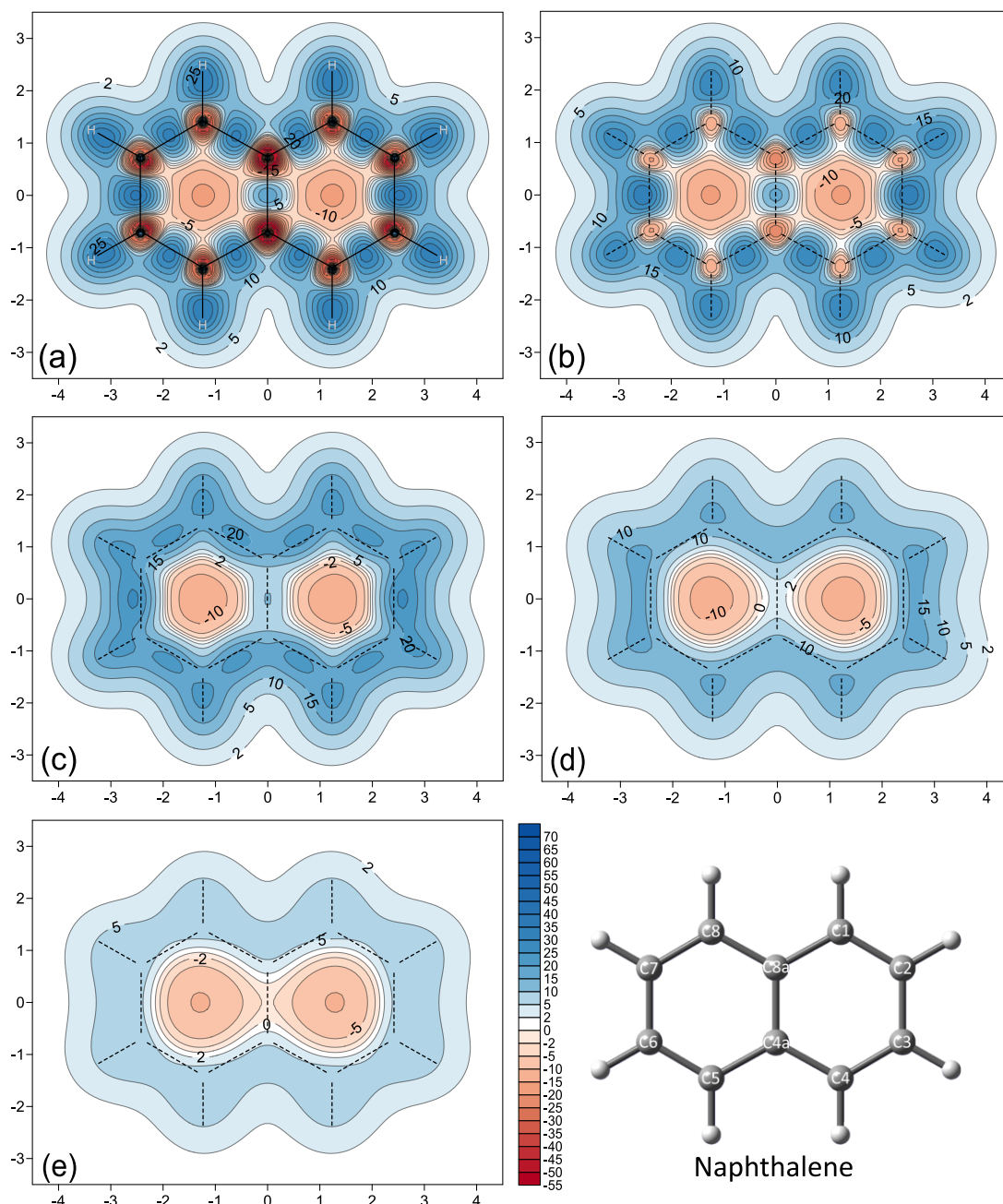


Figure 6-25: Contour maps of the isotropic shieldings (σ_{iso}) (in ppm) obtained at the CASSCF(10,10)/6-311+G(d) level of theory for T_1 naphthalene. (a-e): for grids respectively placed at 0.0, 0.25, 0.50, 0.75 and 1.00 Å vertical heights above the molecular plane.

Comparing the shieldings of the electron circulation at heights of 0.50-1.00 Å shows another difference, see maps (c-e) in these figures. The shielding cloud has better alignment over the ring frame in the T_1 than in the S_1 state because of the weaker deshielding inside the rings in the T_1 state.

The C4a-C8a bond shieldings in the T_1 state, see figures (6-25 (a-c)); (6-27); (6-28 (d)) and (6-29 (d)), are in line with the discussion about the shielding behaviour of this bond in the S_1 state. At the bond location, the higher shielding of this bond dominates the weaker deshieldings. As a result, averaging the shielding/deshielding activities produces an overall shielding effect. Also, this helps in understanding the lower shielding of this bond when comparing its shielding to those of other C-C bonds, see figures (6-28,29,31).

In general, the shielding/deshielding of the two rings in all naphthalene states shows a tendency towards merging over the fused location, i.e. the C4a-C8a bond. However, the presence or absence of similarly magnetic nature of the rings and that of the bonds is of key importance here. As figures (6-25) and (6-27) show, there are remarkable differences in the shielding behaviour inside the rings at different heights. The C4a-C8a bond shielding acts as a barrier between the deshieldings of the two rings, (see the plots at heights 0.00-0.75 Å). Once outside the shielding zone of the bond, the two rings re-associate their deshielding clouds. This is observed at 1 Å over the bond, see figures (6-26) and (6-27).

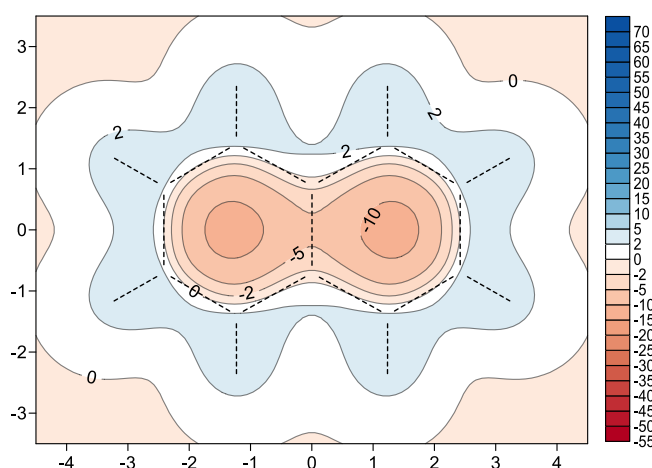


Figure 6-26: Contribution of the vertical-component of the isotropic shielding ($\sigma_{iso(zz)}$) (in ppm) of T_1 naphthalene, obtained at the CASSCF(10,10)/6-311+G(d) level of theory for a grid placed vertically at 1.00 Å above the molecular plane.

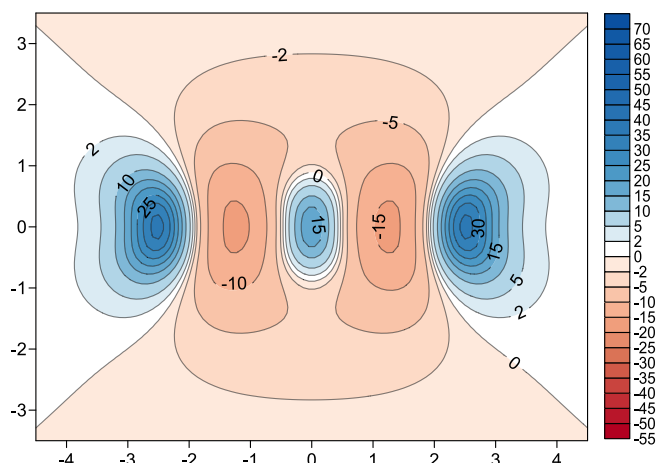


Figure 6-27: XZ cross-section isotropic shielding map (in ppm) of T_1 naphthalene, obtained at the CASSCF(10,10)/6-311+G(d) level of theory for a grid placed vertically and bisecting the molecular plane at its X and Z axes.

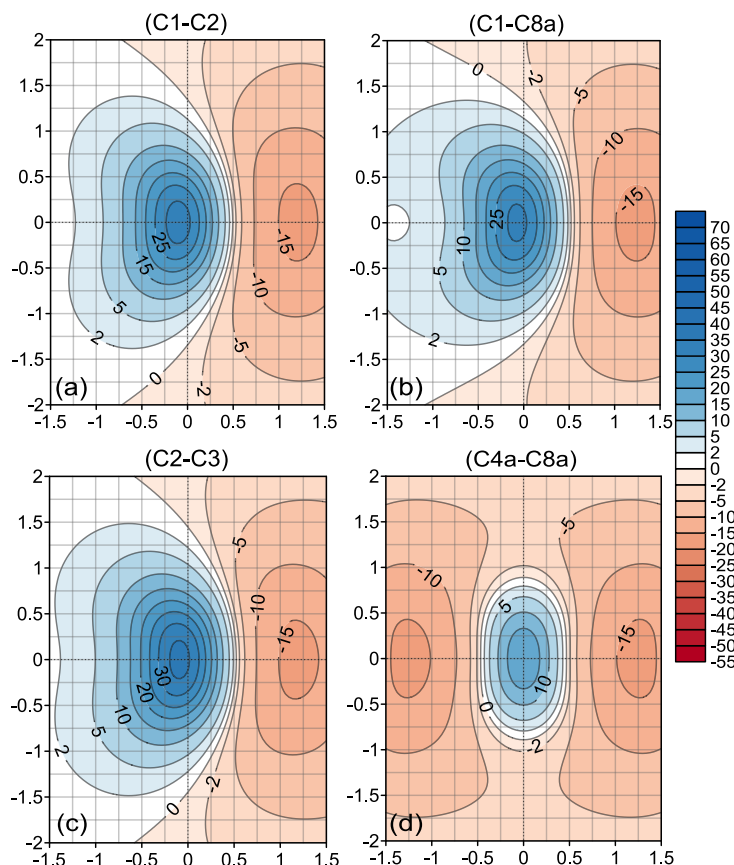


Figure 6-28: CASSCF(10,10)/6-311+G(d) isotropic shielding contour maps (in ppm) of T_1 naphthalene. The figures result from 2D ghost-atom grids located perpendicularly to and crossing the midpoints of symmetry unique C-C bonds. Note that for all maps above, the right side is directed towards the inner part of the ring, which includes the ring centre. Also, the C-C bond in each map is located exactly at the (0,0) X,Y coordinates.

If we ignore shielding values, the general trends of the shielding around the ring centre for the T_1 and S_1 states of naphthalene show a high degree of similarity, see figures (6-30) and (6-14), respectively. Looking at the numbers, the shielding value at the ring centre in the case of the T_1 state is approximately one-third of that in the S_1 state. For example, the shielding value for each ring centre at the molecular plane is -16.1 and -37.7 (ppm) for the T_1 and S_1 states, respectively. The extent of the deshielding above a ring centre decreases gradually with heights and the shielding values at 1 Å become -10.3 and -28.3 (ppm) for these states, respectively. If the extent of deshielding is taken as a measure of aromaticity, then one can say that the T_1 state is much less antiaromatic than the S_1 state.

Figures (6-(28,29,31)) show further details of the shielding around C-C bonds in the T_1 state. According to shielding content, these bonds can be arranged in the order: C2-C3 > C1-C2 \approx C1-C8a > C4a-C8a. For comparison, the order of the bonds is different from that in the S_1 state. The reason for this is, as mentioned earlier, that shielding and deshielding follow different patterns in the space surrounding naphthalene in each of these electronic states. The shielding clouds around bonds in the T_1 state regain much of their S_0 strengths and locations. The above shielding bond ordering is valid not only along the bonds but also at 1 Å above the bonds.

The overall 3D shielding of the T_1 state is shown in figure (6-32). The 3D isosurfaces are generally similar to those for the S_1 state, see figure (6-16), with lower deshielding intensities than in S_1 . The σ_{iso} values chosen for isosurfaces are +16; -16; +8; and -3 (ppm). These corresponding isosurfaces are displayed in blue; red; transparent; and transparent red, respectively.

The behaviour of the deshielding clouds of the two rings around the linkage, which was discussed earlier, is shown clearly in figure (6-32). This figure confirms the effect of the shielding around the C4a-C8a which counteracts the deshielded clouds on both sides of the bond. The figure also shows other magnetic features such as the shifts in the shielding clouds for the C-C bonds as well as the overall shielding behaviour. All antiaromaticity features are noticeably weaker than those in the S_1 state.

The transparent red isosurface, see figure (6-32 (d)), shows that the deshielded spheres have weaker linkages with the central deshielding clouds

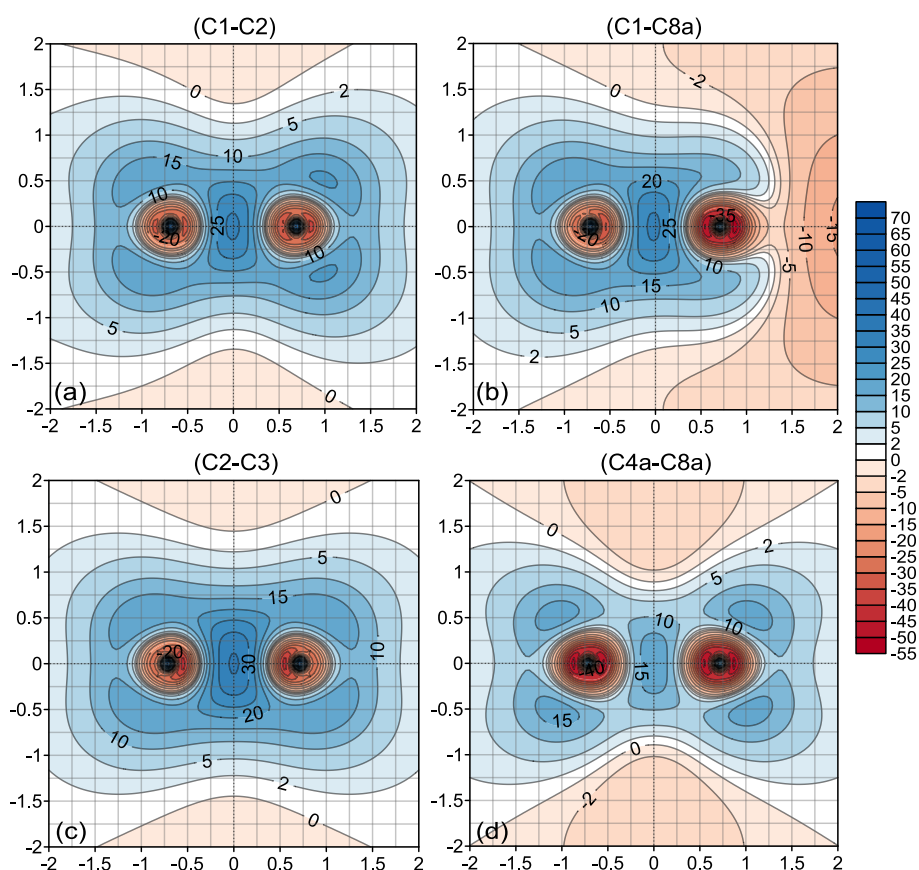


Figure 6-29: CASSCF(10,10)/6-311+G(d) isotropic shielding contour maps (in ppm) for the symmetry unique C-C bonds of T_1 naphthalene. In each map, the left and right well-shielded dots represent the C nuclei of the correspondingly bond. Also, the midpoint of each bond corresponds to the (0,0) X,Y coordinates.

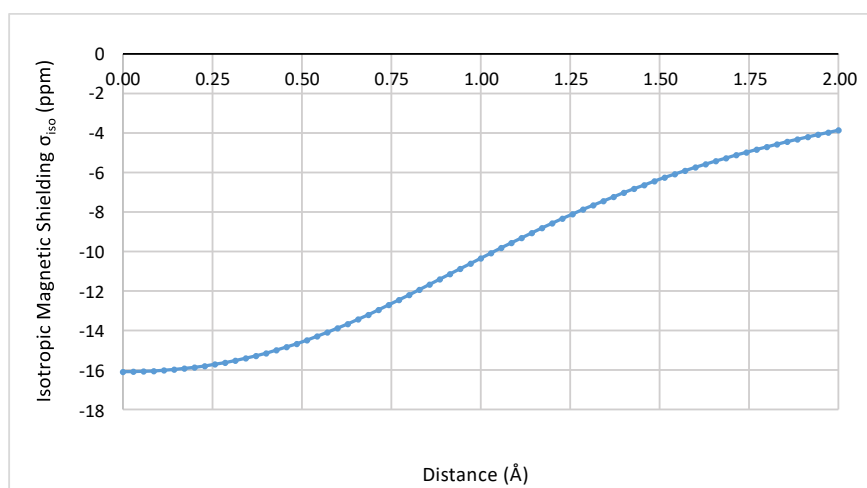


Figure 6-30: Variation in CASSCF(10,10)/6-311+G(d) isotropic shielding σ_{iso} (in ppm) of T_1 naphthalene obtained from 71 ghost-atoms located perpendicularly from the ring centre to a height of 2 Å above it.

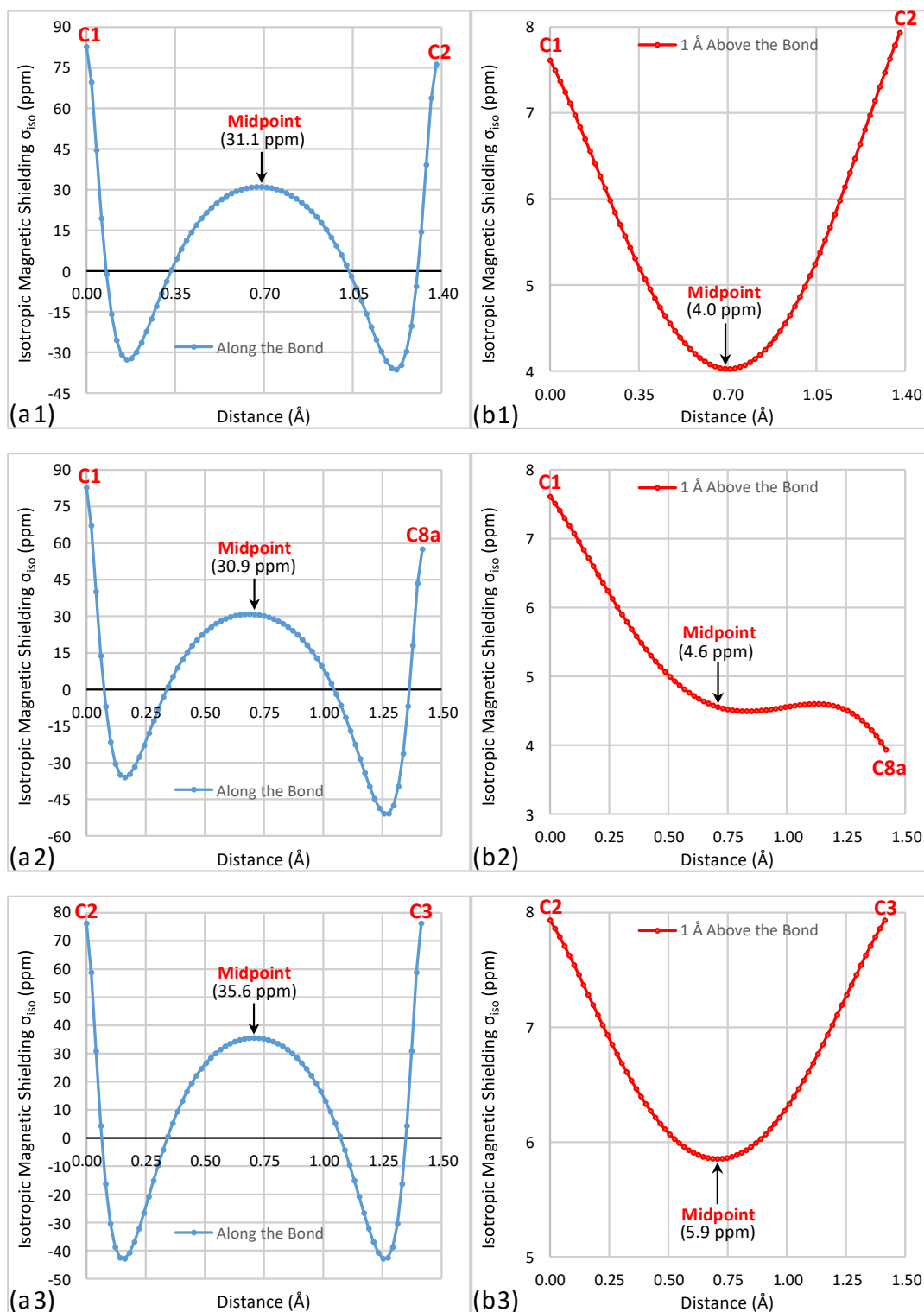


Figure 6-31: Variation in CASSCF(10,10)/6-311+G(d) isotropic shielding (σ_{iso}) (in ppm) of the symmetry unique C-C bonds of T_1 naphthalene obtained from 71 ghost atoms: (a) positioned along C-C bonds, and (b) positioned 1 \AA vertically above the bonds.

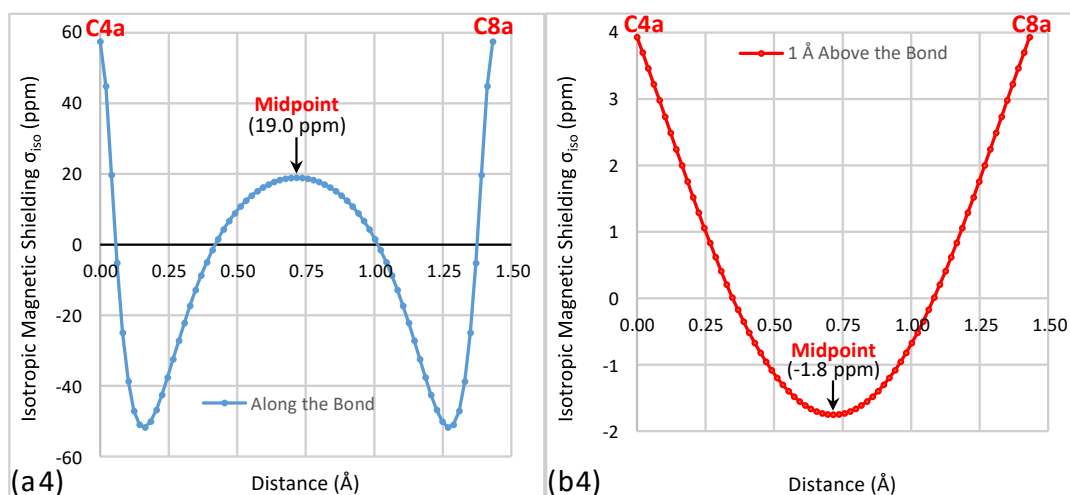


Figure 6-31: Continued.

in each ring than the linkages shown in figure (6-16 (d)) due to stronger shieldings at the C-C bond AMBLs. Map (a) in figures (6-25) and (6-9) illustrate this observation which highlights the weaker deshielding and stronger shielding effects in the T_1 state in comparison to the S_1 state.

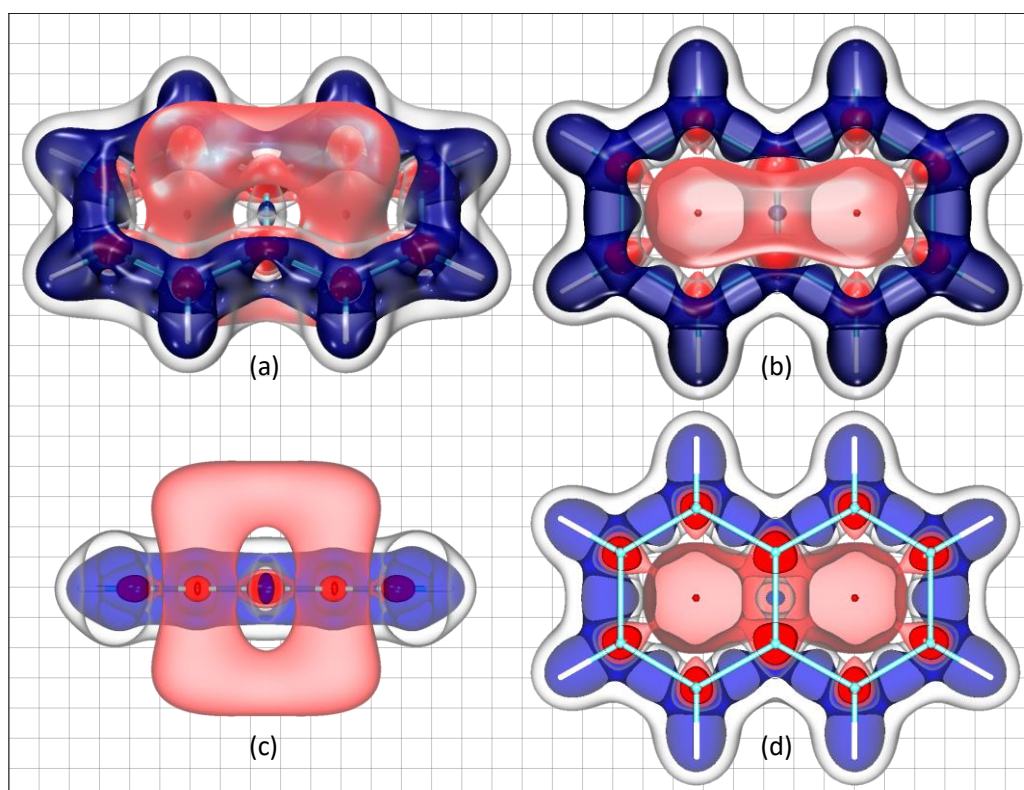


Figure 6-32: Axial (a,b); vertical (c) and horizontal (d) cross-section views of the isotropic shielding (σ_{iso}) isosurfaces for T_1 naphthalene obtained from CASSCF(10,10)/6-311+G(d) calculations. The isosurfaces value(ppm)/colour are defined as: +16/(blue), -16/(red), +8/transparent, and -3/transparent red.

6-6 Conclusions

The isotropic shielding clouds can adopt several strategies in order to deal with different magnetic environments established around the molecular framework. Similarity between separate shielding or deshielding effects increases the possibility of association of similar effects. On the other hand, if there is dissimilarity between magnetic effects, the stronger effects either repels or modifies the shape of the weaker effect. Examples include, the shifts of the locations of the shielding clouds of the C-C bonds in the S_2 state to inside the rings, or the displacements of these clouds outside the rings observed in the T_1 state and to a larger extent, in the S_1 state. An example of the shape reconstruction is given by the deshielded-spheres of the carbons in the C4a-C8a bond in the S_2 state. There is no need for such adaptations if the magnetic environment for a specific space is largely homogeneous, as in the S_0 .

Three features indicate increased aromaticity. Firstly, most shielded parts of the overall shielding cloud, contract to inside the rings. Secondly, σ_{iso} variations at the ring centre of S_2 and the ground state naphthalene demonstrate that, with the increase of shielding at the ring centre, the maximum σ_{iso} value becomes much closer to the ring centre in the molecular plane (i.e., maximum σ_{iso} is found closer to $z=0.00$). To summarise, with the increase in aromaticity, the most shielded areas inside the rings experience vertical and horizontal shrinking. Thirdly, the vertical extent of the shielding cloud above and under the molecular plane increases with the increase in aromaticity.

In addition to the useful σ_{iso} 2D grids, looking at the $\sigma_{\text{iso}(zz)}$ maps can be helpful as it indicates to what extent this component contributes to the total σ_{iso} value, and shows whether there is any localisation in the shielding cloud at a height of 1 Å above the molecular plane.

According to the isotropic shielding distribution around naphthalene in different electronic states, the highest shieldings were found in the S_2 state, followed by the ground state. Deshielding can be seen in the T_1 state, but it is weaker than the deshielding in the S_1 state. In each state, the C-C bonds have a unique ordering according to shielding extent. The four electronic states of naphthalene can be arranged in order of decreasing aromaticity as: $S_2 > S_0 >>> T_1 > S_1$.

CHAPTER SEVEN

ANTHRACENE AND

PHENANTHRENE

7-1 Introduction

This chapter aims to follow the change in isotropic shielding behaviour and aromaticity when switching from bicyclic naphthalene, discussed in the previous chapter, to tricyclic linear anthracene and angular phenanthrene.

For both of these isomeric benzenoid compounds, the historical, chemical, and spectral properties, in addition to some of their reactions have been discussed by Clar.^[10] The total π energies for anthracene and phenanthrene was calculated by Hess and Schaad^[156] as 19.31 and 19.45 β , as well as by Aihara^[173] as 19.314 and 19.448 β , respectively. The hardness^[174], the resonance energy obtained by Dewar^[155] and other researchers^[156,159,175,176] showed that phenanthrene has greater resonance energy than that for anthracene.

Most of the published papers agree that the terminal rings of phenanthrene are more aromatic than the central ring, however, the controverting about the aromaticity of anthracene ring is still not settled.

According to Schleyer and coworkers^[18], the anthracene central ring has the most negative NICS value, -13.3 (ppm), followed by the terminal rings of phenanthrene, -10.2 (ppm). These values exceeded NICS of the benzene ring, -9.7 (ppm). The phenanthrene central ring shows the least negative NICS value, -6.5 (ppm).^[18] The same study showed that the magnetic susceptibility exaltations (Λ) for anthracene and phenanthrene are respectively -49.8 and -47.9 (ppm cgs).^[18] Schleyer et al. also^[177] performed a similar evaluation for linear acenes. Accordingly, the NICS(0)/NICS(1) are (-11.5/-13.1) and (-7.6/-9.9) (ppm) for the central and terminal rings of anthracene, respectively.

Solà et al.^[178] evaluated the para-delocalisation index (PDI) as well as the harmonic oscillator model of aromaticity (HOMA) for several molecules. Their findings are in agreement with the above NICS trends for the rings of both molecules. Another study by Portella et al.^[15] showed that the PDIs for the anthracene rings tend to be almost the same, whereas HOMA for the central ring is higher than that for the terminal rings. They also found that the NICS values for the rings are similar to those reported by Schleyer et al.^[18] Thus, the HOMA and PDI indices follow the general behaviour of NICS in terms of dealing with these two molecules. In a further study, Portella et al.^[179]

assessed these three indices for several polycyclic aromatic hydrocarbons (PAHs) to find to what extent Clar's qualitative π -sextet models are valid. The anthracene central ring and the phenanthrene terminal rings were found to have the highest index values. The latter trend was also pointed out by Cyrański et al.^[180] who evaluated the HOMA and NICS(0) and NICS(1) indices. They found that NICS(1) is more negative than NICS(0) above each ring in both molecules. π -current density maps at 1 Bohr above the molecular plane of these molecules obtained by Ligabue et al.^[181], as well as the ring aromaticity index by Giambiagi et al.^[182] support the Schleyer trends.

Mandado et al.^[183] calculated the scaled 6-centres delocalisation indices and the effective scaled electron delocalisation and they found that the indices for the anthracene terminal rings are lower than that for central ring. Additionally, they concluded that the n -centre delocalisation indices of local rings cannot be used to assess the total aromaticity since they are unable to probe information about the π -electron delocalisation to neighbouring rings.^[183]

In contrast, other research showed that NICS is not able to measure the aromaticity degree of a ring in a polycyclic compound.^[184-187] Furthermore, Howard and Krygowski^[188] found that the HOMA index were inconsistent with the NICS indices published by Schleyer et al.^[18] Despite his doubt about the validity of NICS indices as a measure of aromaticity, Stanger^[187] scanned NICS changes at different heights over the ring centres of both molecules. He found a similar magnetic trend to the above mentioned for the rings. As his scan was along a single vertical line, the shape of the shielding clouds around the molecules was not taken into account, which has an important impact on the quality of the results.

While trying to evaluate local aromaticity for some PAHs, Bultinck and coworkers^[185] found that NICS deviated from expectations when assessing local aromaticity of the anthracene rings. Also, they found that NICS have the lowest correlation with the Polansky and six-centre index (SCI) in their study.

Bultinck et al.^[184,189] attributed the inaccurate local aromaticity measured by NICS for different six-membered rings of a polycyclic system to the contributions of the non-local in addition to local circuits of that system. Anthracene, for example, has six circuits which contribute to the ring currents and NICS.^[184] Although NICS locally probe shielding at one ring (local circuit),

this cannot avoid the contributions of other circuits. Thus, NICS can be considered as a sum of the contributions of all circuits.^[184]

Other studies of the local aromaticity of the rings of some PAHs have been reported.^[15,186,190] Aihara^[186] computed the topological resonance energy (TRE) and the bond resonance energy. He found that the bond resonance energy decreases with the increase of the polyacene size. Also, he stated that the current density cannot assess aromaticity in an accurate manner.

In spite of the research carried out so far, a detailed description of the magnetic behaviour of the individual rings in PAHs is still not available. Such a description could reveal the reason why the central ring of linear PAHs is more reactive than the terminal rings, as it is considered as the preferred location for Diels-Alder reactions. According to Clar^[10], the reactivity of linear polyacenes increase with increasing the number of rings. Moreover, Schleyer^[177] reported that the resonance energy per π -electron for linear acenes stays almost the same with increasing the size (and the reactivity) of the acenes. Another point worth noting, there is only one sextet ring that can be observed for a linear PAH while the other rings can be classified as non-sextet. This leads to another question. What is the effect of increasing length of the conjugated system in PAHs on the aromaticity and the magnetic behaviour of the rings? Schleyer et al. partially answered this question by concluding that the contribution of remote π -C-C bonds to NICS(π) is small (less or equal to 10%).^[177] It has been argued that delocalisation of π -electrons over bridged carbons at the fused locations increases the aromaticity of the molecule and, at the same time, decreases the π -electron delocalisation of each local ring.^[183] Clearly, establishing the local and global aromaticity of linear PAHs is a challenging task.

In this chapter, we show the behaviours of the isotropic shielding in PAHs using 1D shielding plots, 2D shielding maps, and 3D shielding isosurfaces. As an attempt to measure global aromaticity, we calculated a global average shielding, $\sigma_{iso(global)}$, for a polycyclic PAH, see equation (7.1), as the average the shieldings of all ring centres in the PAH. $\sigma_{iso(global)}$ values then are plotted against heights to find the maximum value.

$$\sigma_{iso(global)} = \frac{\sum \sigma_{iso} \text{ at the centres of all rings at a specific height}}{\text{Number of the rings}} \quad \dots (7.1)$$

7-2 Anthracene

The ground state geometry of anthracene was optimised using DFT at the B3LYP/cc-pVQZ level of theory. The vibrational frequencies of the D_{2h} structure obtained are positive which confirms that it is a true minimum.

This D_{2h} B3LYP/cc-pVQZ geometry of anthracene was used in all isotropic shielding calculations. These calculations were performed at the MP2-GIAO / 6-311+G(d) level of theory. As intermediate results, the calculations produced HF-GIAO / 6-311+G(d) shieldings, which are also reported and discussed in some cases.

Table (7-1) shows the isotropic shielding values for the symmetry unique nuclei of anthracene, see figure (7-1) for the structure and for labelling of atoms. The differences between the σ_{iso} values obtained using the MP2 and HF methods are around 10 (ppm). Although the nuclear isotropic shieldings obtained using MP2 are higher than those obtained using HF, HF yields a slightly higher shieldings (by about 1 (ppm)) for points placed at a height of 1 Å above the nuclei.

According to both methods, the C2 and C9a nuclei have the highest and the lowest shieldings, respectively. The highest shielding at a height of 1 Å above the nuclei is found above C9a, the bridge carbon at the fused location between rings. In this way, the behaviour of C9a here is similar to that of the carbon at the fused location of naphthalene (see chapter six), namely, the C4a nucleus. Our HF shielding values are in excellent agreement with those published by Ligabue et al.^[181]

Table 7-1: Isotropic shielding data (σ_{iso}) (in ppm) obtained at the MP2-GIAO/6-311+G(d) and HF-GIAO/6-311+G(d) levels of theory for the symmetry unique carbon nuclei and for points placed 1Å above these nuclei in anthracene.

	HF		MP2	
	Nuclear σ_{iso} (ppm)	σ_{iso} 1Å above nuclei	Nuclear σ_{iso} (ppm)	σ_{iso} 1Å above nuclei
C1	60.69	14.11	71.25	13.35
C2	64.35	15.28	74.27	14.49
C9	63.47	14.72	72.68	13.55
C9a	56.06	17.74	65.04	16.74

The shielding differences between the carbon nuclei of non-symmetric bonds, as well as at heights of 1 Å above these bonds, $|\Delta\sigma_{iso(C-C')}^{0\text{Å}}|$ and $|\Delta\sigma_{iso(C-C')}^{1\text{Å}}|$, are listed in table (7-2). The largest $|\Delta\sigma_{iso(C-C')}^{0\text{Å}}|$ difference is observed between the nuclei of the C9-C9a bond. The C1-C2 bond shows the lowest shielding variations not only between its nuclei, but also between the points located 1 Å above the nuclei. For this bond, the low shielding variation reflects the homogeneity of the magnetic environment of the bond.

Table 7-2: Anthracene MP2-GIAO/6-311+G(d) isotropic shieldings differences (in ppm) for non-asymmetric C—C' bonds, $|\Delta\sigma_{iso(C-C')}^{0\text{Å}}|$, and for ghost atoms located 1Å above these nuclei, $|\Delta\sigma_{iso(C-C')}^{1\text{Å}}|$.

C—C' Bond	$ \Delta\sigma_{iso(C-C')}^{0\text{Å}} $ (ppm)	$ \Delta\sigma_{iso(C-C')}^{1\text{Å}} $ (ppm)
C1-C2	3.02	1.14
C1-C9a	6.21	3.39
C9-C9a	7.64	3.19

As shown in figure (7-1), the anthracene structure is well shielded by the isotropic shielding cloud, except for the deshielded-spheres around carbons. In the molecular plane, see map (a), the shielded regions around C-C bonds are more shielded and more evenly centred between the nuclei than those for the C-H bonds. Also, the shieldings around the C1-C2 and C4a-C9a bonds at 0.75 Å are higher than those for other C-C bonds with the isotropic shielding over the C4a-C9a bond higher than that over the C1-C2 bond, see map (d).

Looking at the differences in shielding at different vertical heights, there are two noteworthy points, see maps (a-e) in figure (7-1). Firstly, the isotropic shieldings of the rings in anthracene are remarkably high. The shielding of the central ring is significantly higher than those of the terminal rings. This is more difficult to observe at the lowest vertical height, except for the shielding values at the ring-centre areas, see map (a), but becomes much more noticeable at higher heights. Secondly, with the exception of shielding map (a), which shows the σ -bonding zone, it can be seen from the other maps that the shielding clouds of the C-C bonds exhibit shifts towards the inner region of the rings with the increase the height above the molecular plane.

Both features can also be seen in figure (7-2). In addition, unlike the central ring, the terminal rings show clearly lower shieldings at their centres.

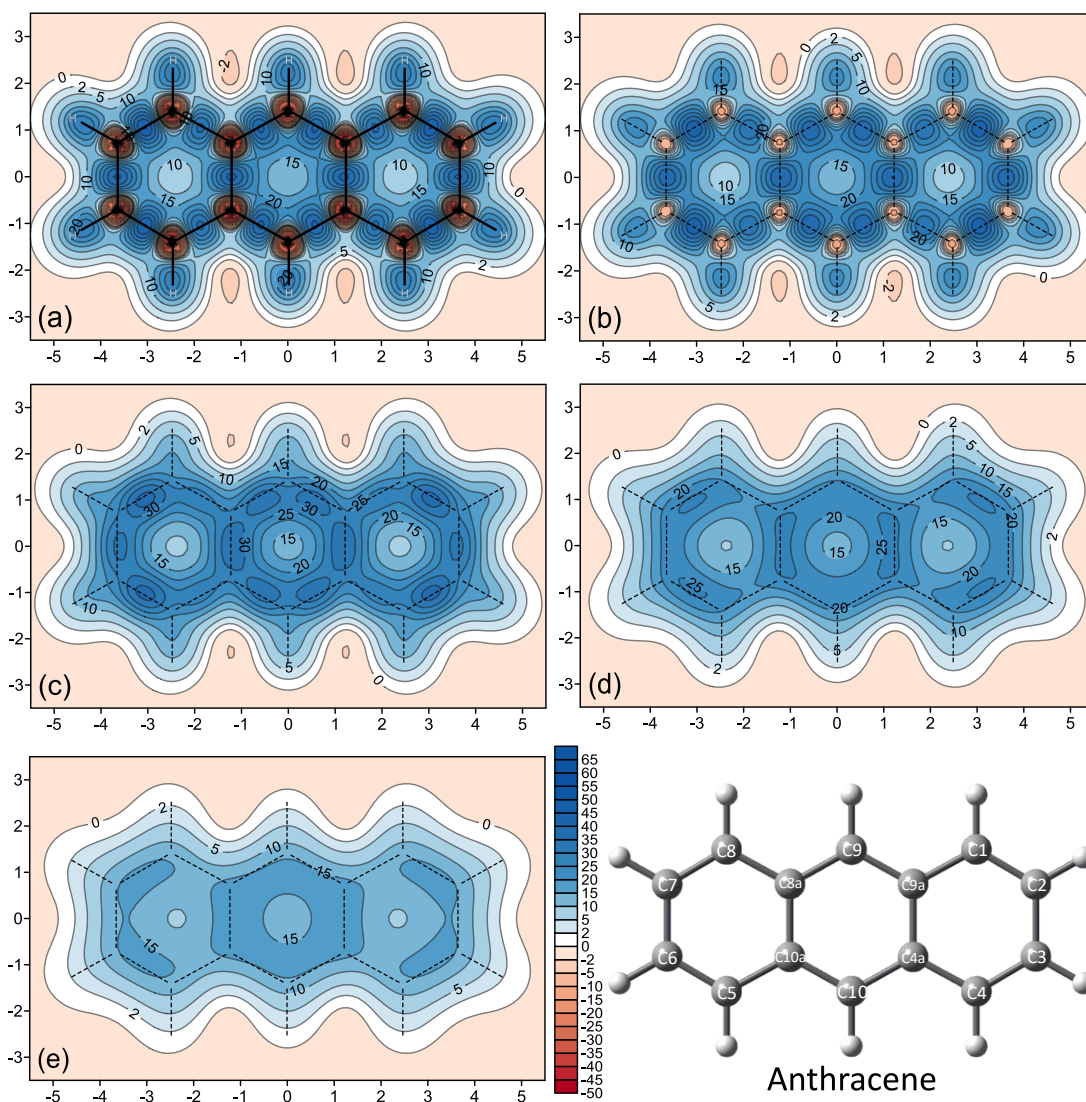


Figure 7-1: Five contour maps of the isotropic shieldings (σ_{iso}) (in ppm) obtained at the MP2-GIAO/6-311+G(d) level of theory for anthracene. (a-e): for grids placed at 0.00, 0.25, 0.50, 0.75 and 1.00 Å heights above the molecular plane, respectively.

Further information about the isotropic shielding of the anthracene ring centres is shown in figure (7-3). The black line shows that the maximum global average shielding value, $\sigma_{iso(\text{global})}$, see equation (7.1), is 11.14 (ppm). The value can be compared to that of phenanthrene, as discussed in the next section. Clearly, the shielding of the central ring is higher than that of the terminal rings. The maximum isotropic shielding values and their heights above ring centres are (13.71)/(0.74) and (9.88)/(0.83) (ppm/Å), for the central and terminal rings, respectively. The numbers suggest that the height of the maximum isotropic shielding is in an inverse relationship with its magnitude.

In other words, higher isotropic shieldings are closer to the molecular plane. A similar observation was made for the shielding above the ring centre for the ground and second singlet states of naphthalene, see figures (6-6) and (6-22), respectively.

The LSC can be thought of as being formed by joining clouds of the C-C σ -bonds and the cloud of delocalised π electrons. The red and blue curves in figure (7-3) show that the central ring has more shieldings in its LSC than the terminal rings. In agreement, figure (7-4) shows this observation in a more comparable manner.

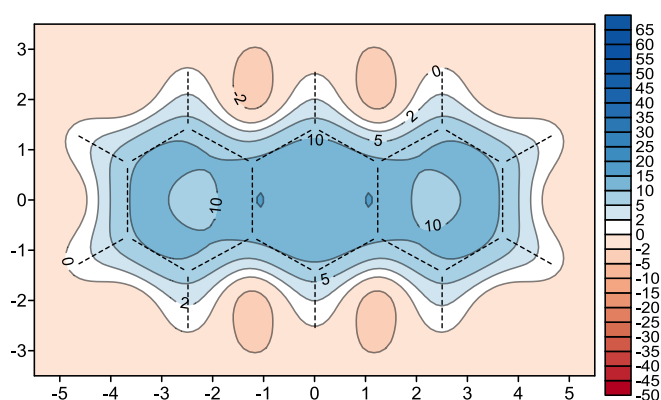


Figure 7-2: Contribution of the vertical-component of the isotropic shielding ($\sigma_{iso(zz)}$) (in ppm) to the total isotropic shielding σ_{iso} of anthracene, obtained at the MP2-GIAO/6-311+G(d) level of theory for a grid placed at 1.00 Å above the molecular plane.

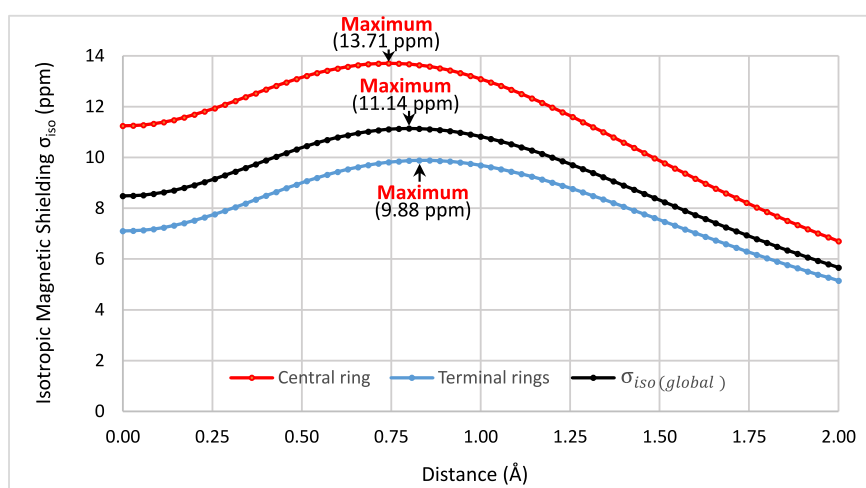


Figure 7-3: Variation in the MP2-GIAO/6-311+G(d) isotropic shieldings σ_{iso} (in ppm) above the anthracene rings obtained using 71 ghost atoms placed perpendicularly to the ring centre up to a 2 Å height above it.

In addition to LSCs mentioned above, the contour map (7-4), which obtained by setting an XZ 2D-grid bisecting and perpendicular to the three rings, clearly shows that the shielding above the central ring is more homogeneous and stronger than those over terminal rings. Besides, the figure shows that the shielding above the central ring is higher even at a vertical height of 2.50 Å.

As the central ring in anthracene has a higher isotropic shielding than the terminal rings, it is logical to suggest that the central ring is more aromatic than the terminal rings.

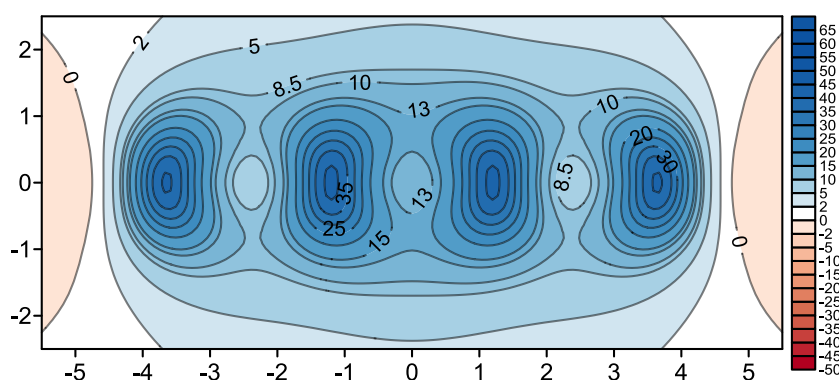


Figure 7-4: MP2-GIAO/6-311+G(d) isotropic shielding map obtained for a 2D grid placed perpendicularly to the molecular plane and evenly bisecting the three rings of the anthracene.

The isotropic shielding variations around C-C bond are shown in figures (7-5) to (7-7). These shielding findings indicate that the centre of the C1-C2 bond is more shielded than those for the other C-C bonds, see figure (7-5 (a)). In contrast, the C1-C9a bond shows the lowest shielding at its centre, see map (b). The highest isotropic shieldings at the centres of these bonds are around 45 and 35 (ppm), respectively. The highest shieldings at the centres of the remaining C-C bonds are about 40 (ppm).

Despite most of the maps in figure (7-5) show the shielding clouds centre (0,0) X,Y point, maps (b) and (e) show how the centre of the shielding clouds of the C1-C9a and C9-C9a bonds shift towards the respective ring centres. As the C4a-C9a bond is shared between two rings, its shielding cloud shows distorting, above and below the molecular plane, towards the centres of both rings. However, the distortion towards the centre of the better shielded central ring is more pronounced.

Another view of the shielding surrounding C-C bonds is provided by figure (7-6). The shielding clouds for all C-C bonds are evenly centred between the carbon nuclei, except for C1-C9a and C9-C9a, which include the C9a nucleus, see maps (b) and (e), respectively. The centres of the shielding clouds show minor cloud-shifts towards C1 or C9 away from C9a. This might be due to the stronger deshielding of the deshielded-sphere of C9a. This feature is discussed when we examine the shielding curves for the C-C bonds (see below).

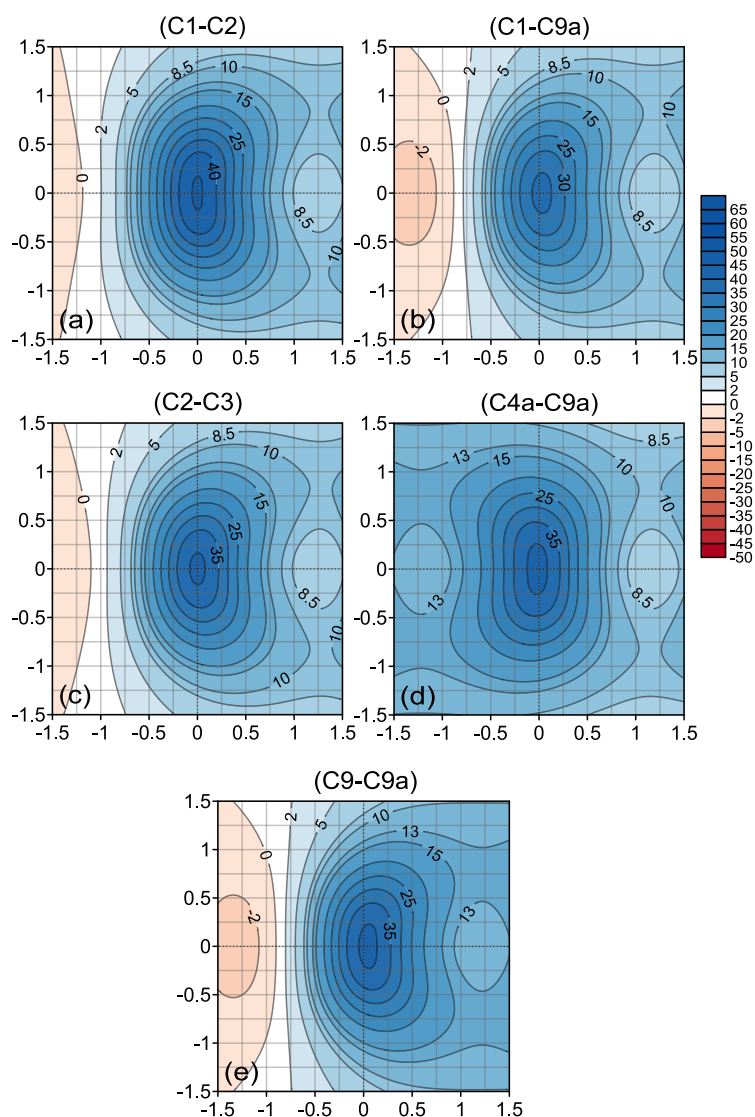


Figure 7-5: MP2-GIAO/6-311+G(d) isotropic shielding contour maps (in ppm) for anthracene obtained by using 2D ghost-atoms grids perpendicular to and passing through the midpoints of the C-C bonds. In all maps, except for (d) which is located between rings, the right side is oriented towards the inner side of the ring, which includes the ring centre. The C-C bond in each map is located exactly at the (0,0) X,Y coordinates.

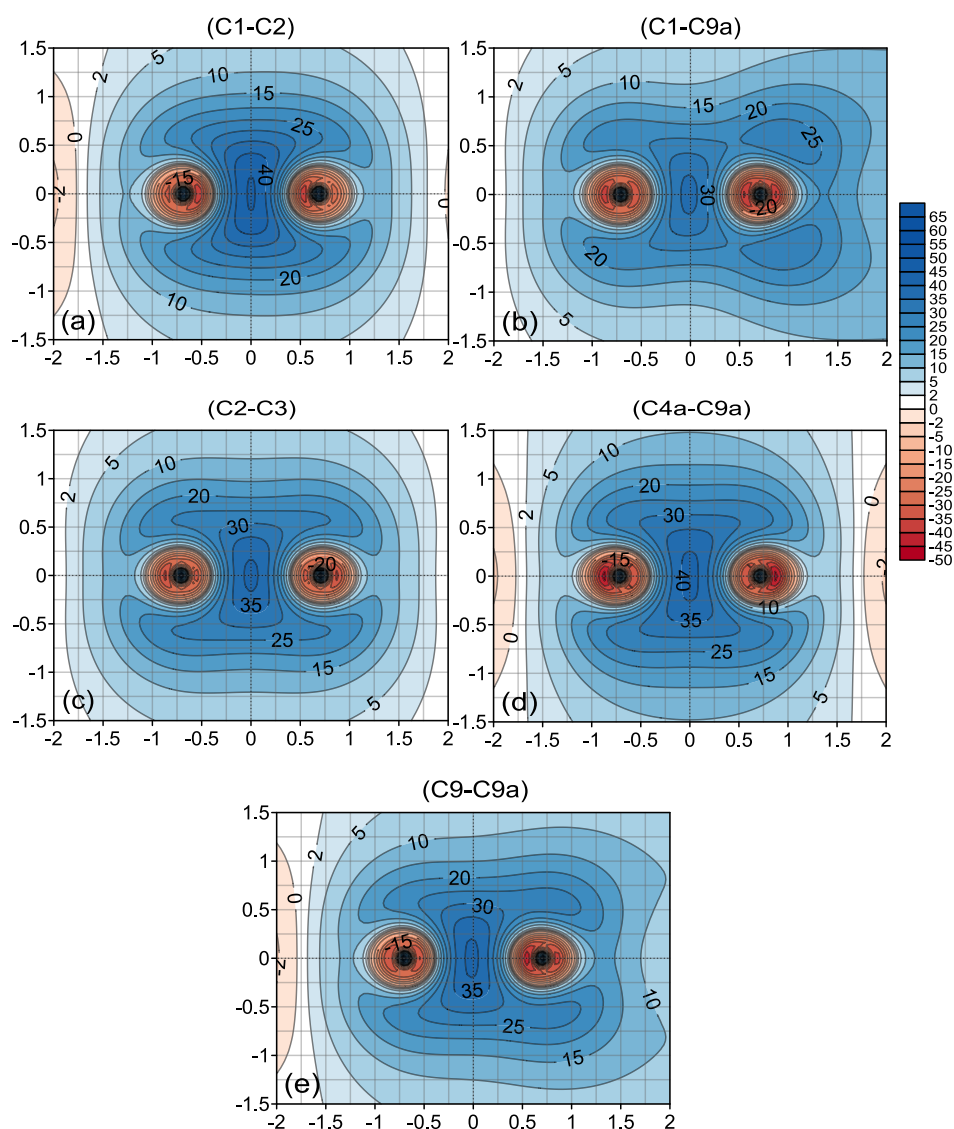


Figure 7-6: MP2-GIAO/6-311+G(d) isotropic shielding contour maps (in ppm) for the symmetry unique C-C bonds of anthracene. In each map, the left and right well-shielded dots represent C nuclei. The midpoint of each bond is placed at the (0,0) X,Y coordinates..

Additional details about the isotropic shielding along C-C bonds are shown in figure (7-7). Details of the deshielding around the C9a nucleus can be seen in plots (a2) and (a5). The lowest shielding values observed are -35.12, -41.27, -35.12 and -43.58 (ppm) next to the C1, C9a, C9 and C9a nuclei in the C1-C9a and C9-C9a bonds, respectively. These values support the previous observation that the deshielding around the C9a is more pronounced than those around the other nuclei in these bonds. The more pronounced deshielding next to C9a shifts the shielding clouds located between C1-C9a

away from C9a.

Plots (b2) and (b5) show that at a height of 1 Å, the isotropic shielding is higher above C9a. This can be considered as a consequence of avoidance shielding and deshielding regions, with the pronounced deshielding around C9a pushing out the shielding cloud around the bond away from this nucleus.

Curve (b4) highlights isotropic shieldings at 1 Å above the C4a-C9a. A remarkable higher isotropic shielding can be seen above this bond than shielding above other C-C bonds, see curves (b). This can also be observed via the 3D isosurfaces, see figure (7-8 (b)).

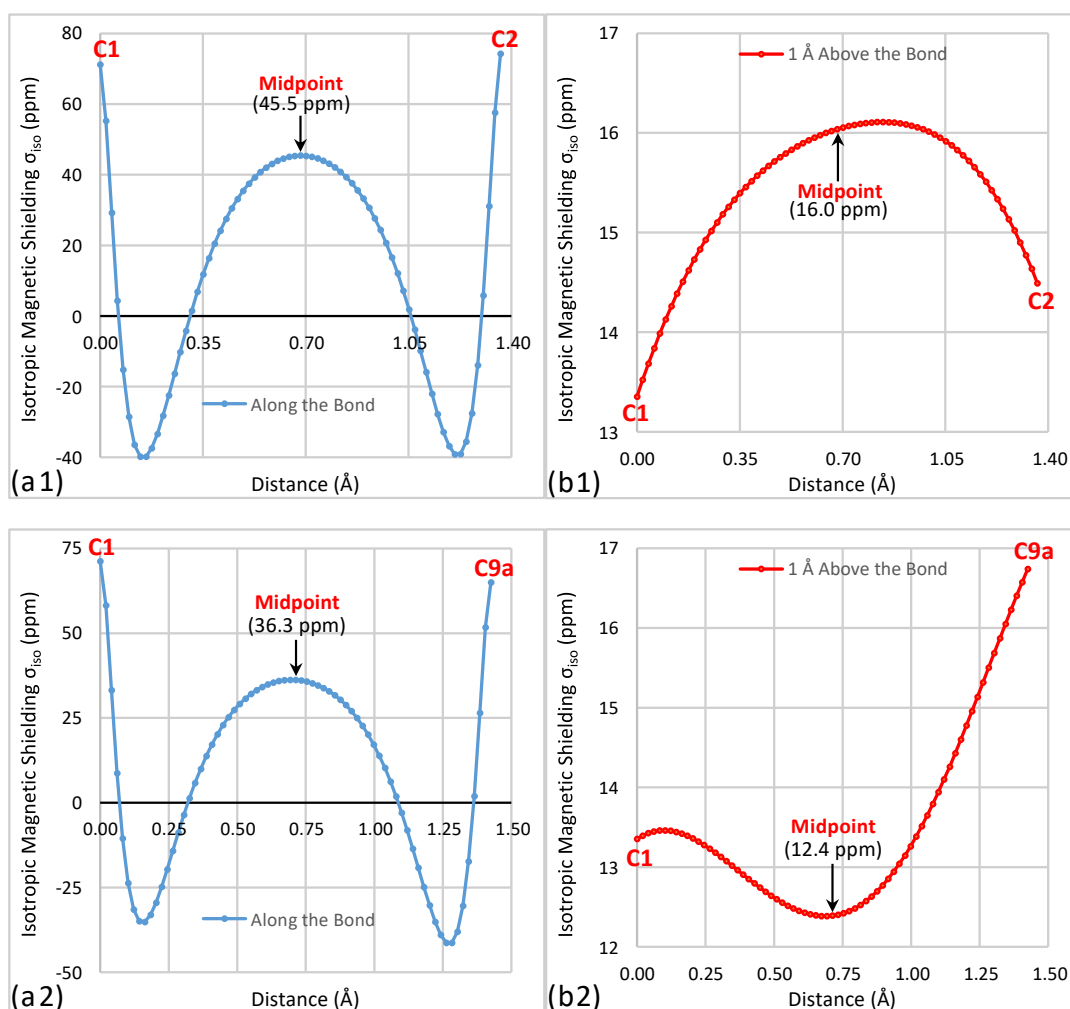


Figure 7-7: Variation in the MP2-GIAO/6-311+G(d) isotropic shielding (σ_{iso}) (in ppm) of the symmetrically unique C-C bonds of the anthracene obtained using 71 ghost atoms: (a) positioned along the C-C bonds, and (b) positioned 1 Å parallelly above the bonds.

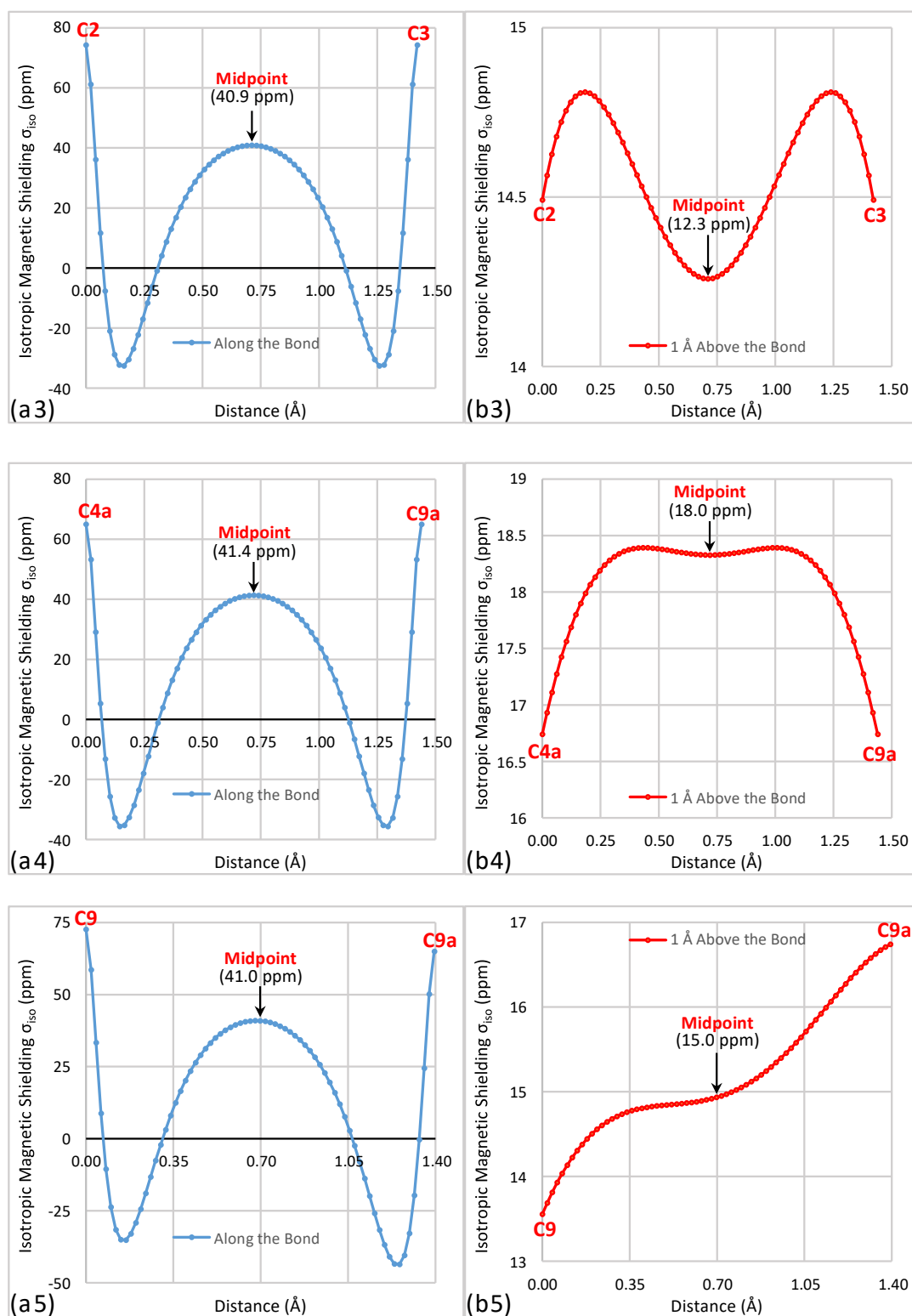


Figure 7-7: Continued.

If a comparison is made between the deshielding along different directions of bonds in which connected to a specific deshielded-sphere around a specific nucleus, one can observe different levels of deshielding. For example, the most deshielded value next to the C1 nucleus in the C1-C2 bond is -39.8 (ppm), see curve (a1) in figure (7-7). Whereas the most deshielded value next to this nucleus in the C1-C9a bond is -35.1 (ppm), see curve (a2). Similar deshielding difference are observed around C9a in the C1-C9a and C4a-C9a bonds, curves (a2) and (a4), respectively. Thus, the deshielding of a deshielded-sphere surrounds a nucleus is affected by and/or affects the shielding of the bonds terminating of this nucleus. 1D shielding plots along bonds are particularly convenient for investigating this deshielding behaviour.

The 3D shielding isosurfaces for anthracene shown in figure (7-8). As it was mentioned in section (2-2-3-2), the 3D shielding calculations for anthracene were performed using the new technique which was outlined in that section. The blue and red isosurfaces correspond to shielding values of +16 and -16 (ppm), respectively.

As it can be seen in figure (7-8), the size and shape of the blue isosurface indicate that the isotropic shielding around anthracene is similar to those around strongly aromatic molecules. The red isosurface shows the deshielding behaviours around carbon nuclei. Both isosurfaces are similar to those for ground state naphthalene, see figure (6-8).

Some of the features of the isotropic shielding in anthracene, which were discussed earlier in this section, can be seen clearly in figure (7-8). The shielding cloud about the middle ring is noticeably thicker than those around terminal rings. Also, the shielding cloud around the C4a-C9a bond is bulkier than those around other C-C bonds.

The shielding clouds around the C-H bonds show less bulk than those around C-C bonds. As in other aromatic molecules, there are no deshielded regions around hydrogen nuclei.

To summarise the above results, anthracene can be classified as a strongly aromatic molecule. The current work strongly suggests that the anthracene central ring is more aromatic than the terminal rings.

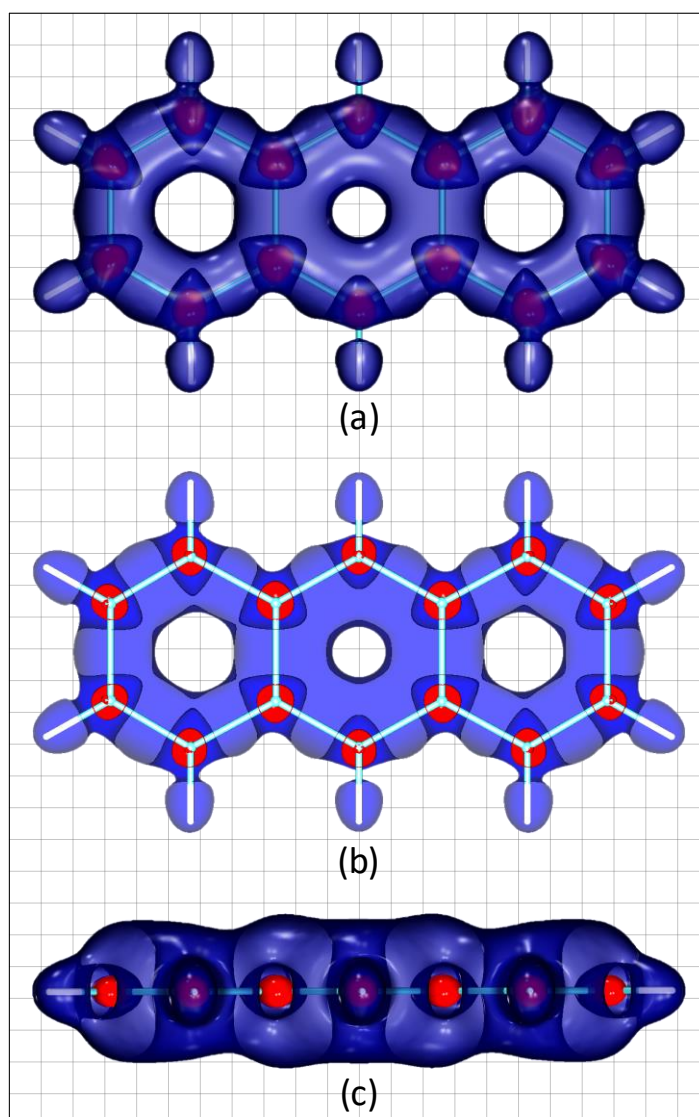


Figure 7-8: (a) Front; (b) horizontal cross-section; and (c) axial side-view of the isotropic shielding (σ_{iso}) isosurfaces of the anthracene obtained from MP2-GIAO/6-311+G(d) calculations. The isosurfaces show the most common shielding values for aromatic molecules; +16(blue)/-16(red) (ppm).

7-3 Phenanthrene

The geometry optimisation and the isotropic shielding calculations for phenanthrene were performed in exactly the same manner as those for anthracene, see the preceding section. Since phenanthrene belongs to the C_{2v} point group, table (7-3) shows the isotropic shielding data for the symmetry unique carbon nuclei only, see figure (7-9) for the phenanthrene structure and for atoms labelling. Clearly, the nuclear σ_{iso} values, which were obtained at the MP2 level, are higher than those coming from HF calculations. The difference between the MP2 and HF values is around 10 (ppm). The opposite shielding trend between results obtained with these two methods can be seen for points located at a height of 1 Å above the nuclei. The nuclear HF shieldings are in agreement with the findings of Ligabue et al.^[181] The lowest shielding values are observed for the carbon nuclei at the fused bond locations. These are the C4a and C10a nuclei, which are shared by two rings. However, the shielding at the ghost atoms above these two nuclei are higher than those above other nuclei. This behaviour is similar to what was observed for the ground states of naphthalene and anthracene, see tables (6-1) and (7-1) for the shieldings in these molecules, respectively.

Looking at the nuclear σ_{iso} values, the highest shielding value is that for the C4 nucleus, whereas the lowest one is for the C10a nucleus. A reversal of this order is observed for the shielding values at 1 Å above these nuclei. The factors affecting the isotropic shielding trends will be discussed alongside the 2D shielding maps.

Table 7-3: Isotropic shielding data (σ_{iso}) (in ppm) obtained at the MP2-GIAO/6-311+G(d) and HF-GIAO/6-311+G(d) levels of theory for the symmetry unique carbon nuclei and for points placed 1Å above these nuclei in phenanthrene.

	HF		MP2	
	Nuclear σ_{iso} (ppm)	σ_{iso} 1Å above nuclei	Nuclear σ_{iso} (ppm)	σ_{iso} 1Å above nuclei
C1	60.78	15.00	70.64	13.98
C2	62.75	15.82	72.96	14.84
C3	62.82	15.80	72.98	14.82
C4	65.67	14.96	77.19	14.07
C4a	56.78	15.82	66.60	14.88
C10	63.01	13.77	72.60	12.95
C10a	55.29	16.93	64.72	15.96

As shown in table (7-4), the highest $|\Delta\sigma_{\text{iso}}^{0\text{Å}}(\text{C}-\text{C}')|$ values correspond to bonds

which include a carbon nucleus at the fused location, i.e., C4a and C10a. In contrast, the C4a-C10a bond shows a much lower shielding difference value. While the lowest $|\Delta\sigma_{iso(C-C')}^{1\text{\AA}}|$ values are above the bonds of the side rings, which do not include the C4a and C10a nuclei. These are the C1-C2, C2-C3 and C3-C4 bonds.

Table 7-4: Phenanthrene MP2-GIAO/6-311+G(d) isotropic shieldings differences (in ppm) for non-symmetric C—C' bonds, $|\Delta\sigma_{iso(C-C')}^{0\text{\AA}}|$, and for ghost atoms located 1Å above these nuclei, $|\Delta\sigma_{iso(C-C')}^{1\text{\AA}}|$.

C—C' Bond	$ \Delta\sigma_{iso(C-C')}^{0\text{\AA}} $ (ppm)	$ \Delta\sigma_{iso(C-C')}^{1\text{\AA}} $ (ppm)
C1-C2	2.32	0.68
C1-C10a	5.92	1.98
C2-C3	0.02	0.02
C3-C4	4.21	0.75
C4-C4a	10.59	0.81
C4a-C10a	1.88	1.08
C10-C10a	7.88	3.01

More details about the isotropic shielding variation in phenanthrene can be seen in figure (7-9). At heights lower than 0.50 Å above the molecular plane, see maps (a,b), the shielding surroundings of the C-C and C-H bonds are well shielded and it is possible to distinguish the deshielded-spheres around the carbon nuclei. The C1-C2, C3-C4, C4a-C10a and C9-C10 bonds are more shielded than the other C-C bonds. Comparing the shielding behaviour along C-C bonds becomes easier at heights of 0.50 and 0.75 Å, see maps (c,d), respectively. It is obvious that the surroundings of the central ring are noticeably less shielded than those of the terminal rings.

The shieldings at the ring centres can be compared via the shielding maps in figure (7-9) and the map of the vertical component of the isotropic shielding $\sigma_{iso(zz)}$, see figure (7-10). Both figures indicate that the C-C bonds of the terminal rings have much higher shielding than the central ring.

Figure (7-11) shows the variation of σ_{iso} at different heights above the phenanthrene ring centres. The terminal ring centres are more shielded than the central ring centre at all heights. The shielding behaviour shown in the figure confirms what was noticed for naphthalene, see figures ((6-6) and (6-22)), and for anthracene, see figure (7-3). Namely, when the shielding above the ring centre becomes stronger, the maximum shielding value is observed

much closer to the molecular plane. As it can be seen from the figure, the maximum σ_{iso} above the ring centre of the central ring is 8.39 (ppm) at 0.91 Å. For the terminal rings, the corresponding value is 10.94 (ppm) at 0.80 Å above the ring centre. The maximum global average shielding value, $\sigma_{\text{iso}(\text{global})}$, is 10.08 (ppm), see the black curve in figure (7-11) which was calculated using equation (7.1). This value is slightly lower than the value for anthracene, 11.14 (ppm). This shows that the global isotropic shielding and the aromaticity of phenanthrene are lower than those for anthracene.

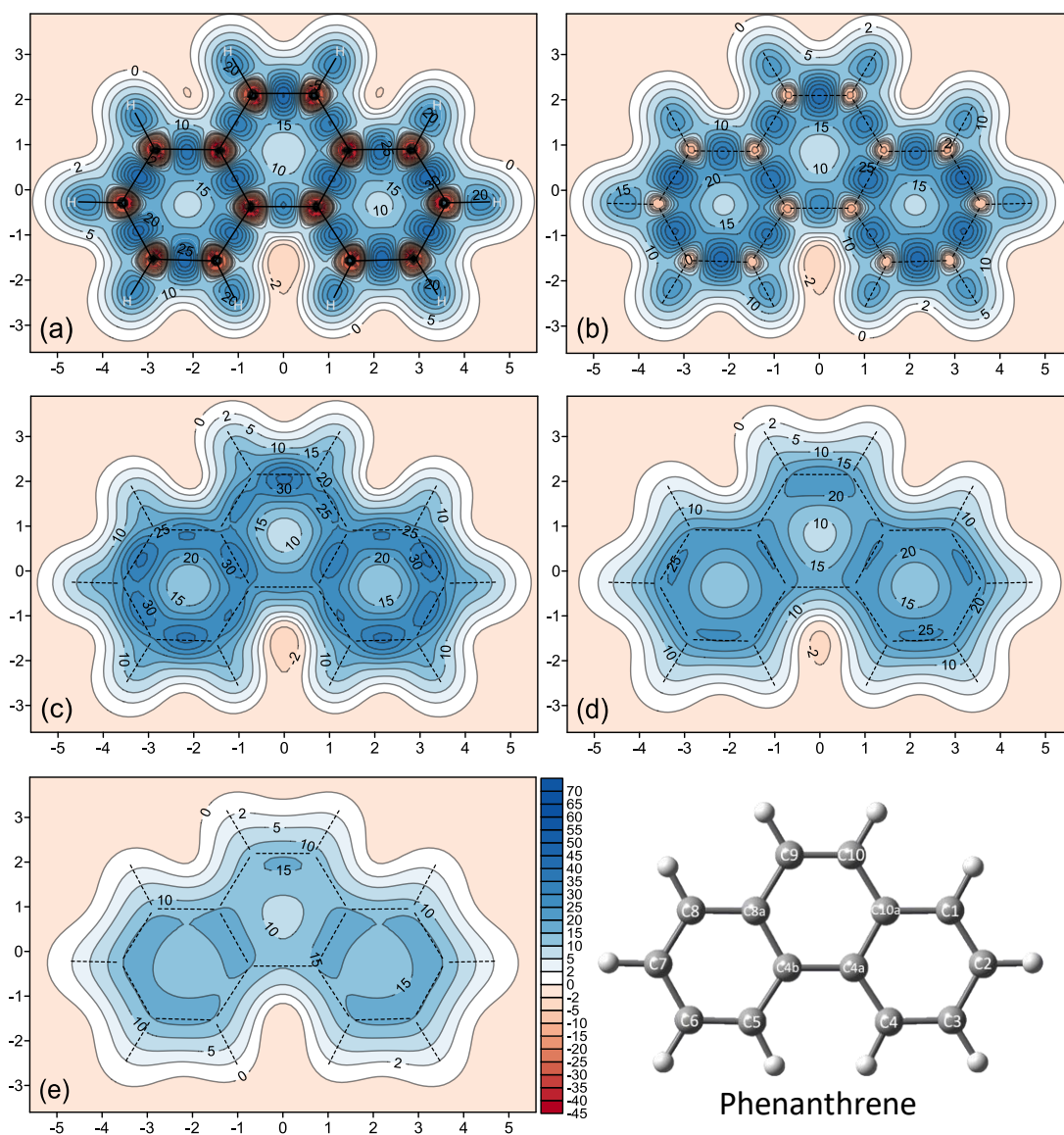


Figure 7-9: Five contour maps of the isotropic shieldings (σ_{iso}) (in ppm) obtained at the MP2-GIAO/6-311+G(d) level of theory for phenanthrene. (a-e): for grids placed at 0.00, 0.25, 0.50, 0.75 and 1.00 Å heights above the molecular plane, respectively.

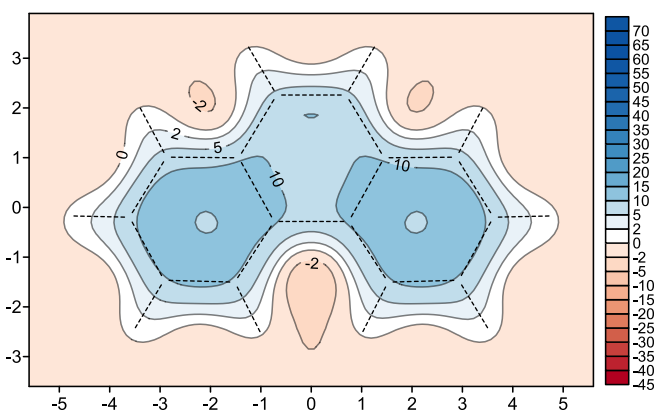


Figure 7-10: Contribution of the vertical-component of the isotropic shielding ($\sigma_{izo(zz)}$) (in ppm) to the total isotropic shielding σ_{izo} of phenanthrene, obtained at the MP2-GIAO/6-311+G(d) level of theory for a grid placed at 1.00 Å above the molecular plane.

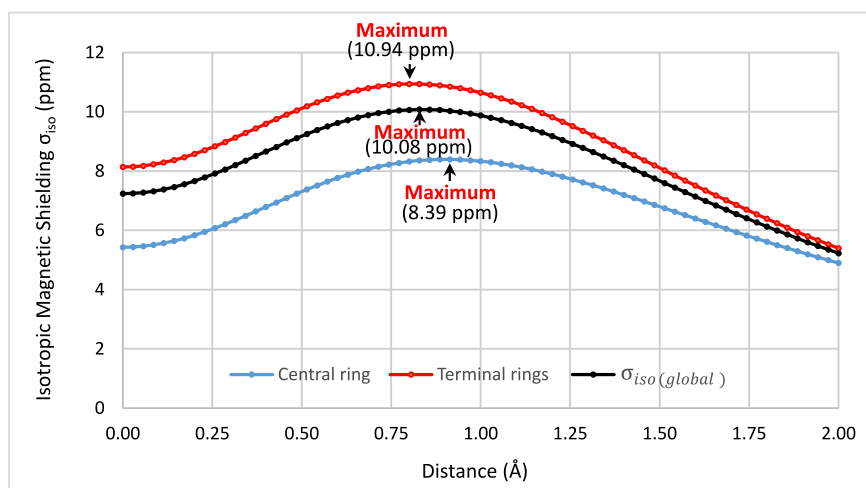


Figure 7-11: Variation in the MP2-GIAO/6-311+G(d) isotropic shieldings σ_{izo} (in ppm) above the phenanthrene rings obtained using 71 ghost atoms placed perpendicularly to the ring centre up to a 2 Å height above it.

To provide additional information about the shielding behaviour above the rings of phenanthrene, a composite V-shaped 2D grid was set in a vertical direction perpendicular to the three rings of the phenanthrene and passing through their centres. Figure (7-12) shows the corresponding shielding map. Clearly, the shielding around the terminal rings is much higher than that around the central ring. Also, at heights between 0.50 and 1.50 Å above the terminal rings, the 10 (ppm) shielding contours are joined above and below the ring centres and form LSC at the centre of these two rings. This can be considered as a consequence of stronger π -electron shielding activities in the terminal rings.

Comparing the isotropic shielding distribution in phenanthrene to these of anthracene, see previous section, shows important differences. The shielding properties of the terminal and central rings in the two molecules are diametrically opposed. In phenanthrene, the central ring shows lower π -electron shielding activities and is less aromatic than the terminal rings. The change in fusion pattern between anthracene and phenanthrene leads to major changes in local aromaticity.

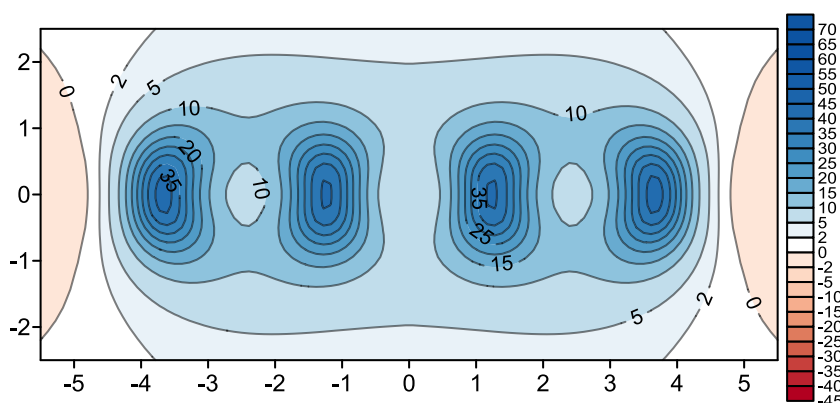


Figure 7-12: MP2-GIAO/6-311+G(d) isotropic shielding map obtained for a composite V-shaped 2D grid placed perpendicularly to the molecular plane and evenly bisecting the three rings of the phenanthrene.

The shielding properties of the C-C bonds were investigated via 2D grids perpendicular to the bonds passing through their midpoints and along the bonds, see figures (7-13) and (7-14), respectively. Looking at figure (7-13), the highest isotropic shielding can be seen at the centre of the C9-C10 bond, see map (h). The lowest σ_{iso} is observed at the centre of the C4a-C4b bond, see map (f). The remaining C-C bonds can be divided into two groups according to the shielding at the bond centre.

The first group includes the bonds of $\sigma_{\text{iso}} \geq 40$ (ppm) at their centres of C1-C2, C2-C3, C3-C4, C9-C10 and the slightly less shielded C4a-C10a. The first four bonds from the first group have $\sigma_{\text{iso}} \geq 15$ (ppm) shielded areas over or next to them in figure (7-9 (e)) (height of 1 Å). The second group includes the bonds of $\sigma_{\text{iso}} \geq 35$ (ppm) at their centres of C1-C10a, C4-C4a, and the slightly less shielded C10-C10a bonds. None of these bonds has a $\sigma_{\text{iso}} \geq 15$ (ppm) shielded area in figure (7-9 (e)). When comparing the shieldings of the C-C bonds, it becomes clear that the better shielded bonds from the first group highlight the preferred resonance structure for phenanthrene.

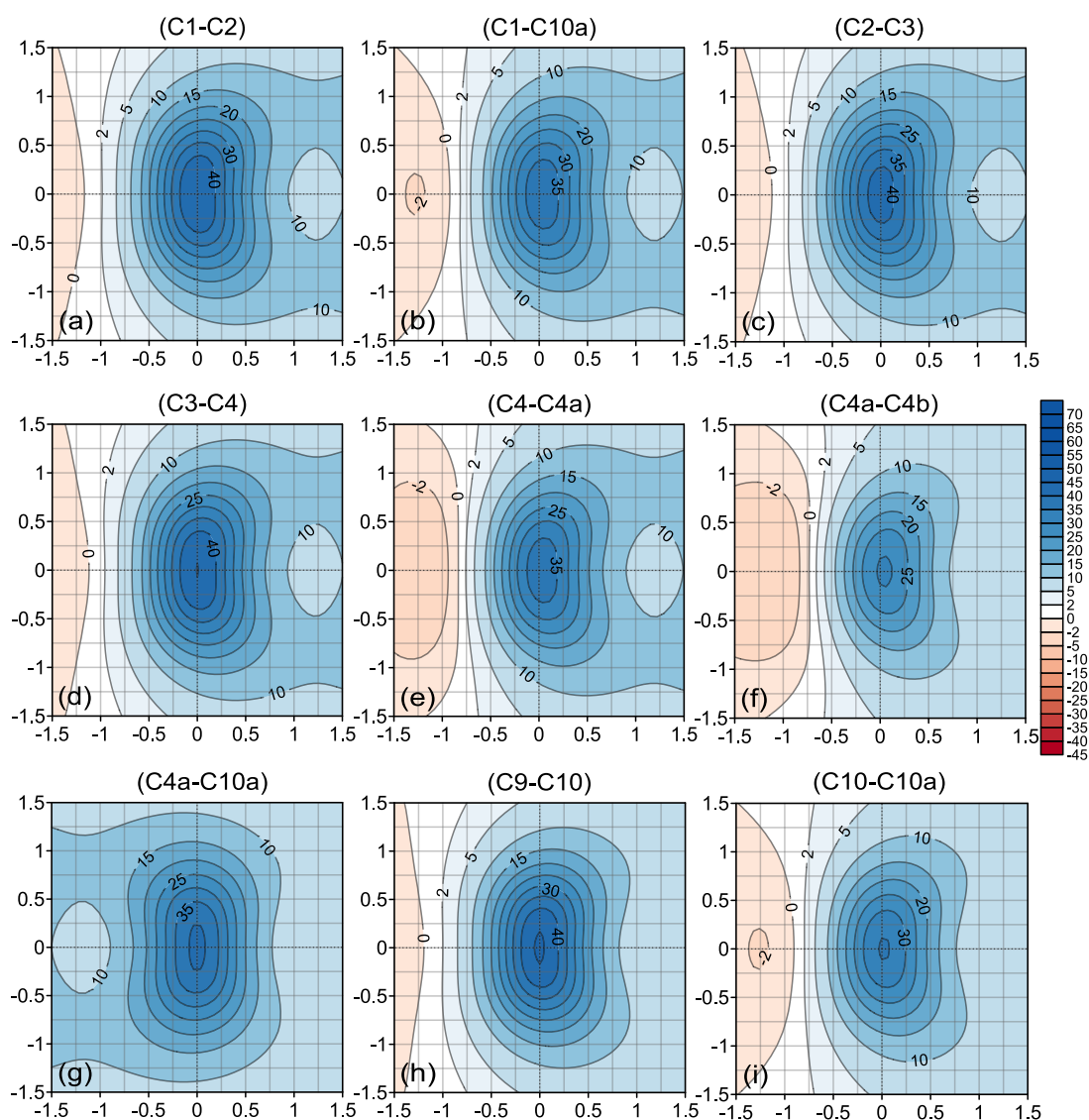


Figure 7-13: MP2-GIAO/6-311+G(d) isotropic shielding contour maps (in ppm) for phenanthrene obtained by using 2D ghost-atoms grids perpendicular to and passing through the midpoints of the C-C bonds. In all maps, except for (g) which is located between rings, the right side is oriented towards the inner side of the ring, which includes the ring centre. The C-C bond in each map is located exactly at the (0,0) X,Y coordinates.

All contour plots in figure (7-13) demonstrate a tendency for the better-shielded areas to move towards a ring centre with the increase of the height above the molecular plane. Similar tendencies were observed in ground state naphthalene and anthracene (see the chapters of these molecules).

The details of the deshielding along the C-C bonds in phenanthrene, see figure (7-14) confirm the observations made while analysing figure (7-13).

For completeness, the curves in figure (7-15) show how shielding changes along each of the C-C bonds in phenanthrene (blue curves, plots (a)), as well as along a line parallel to the bond and placed a height of 1 Å above it (red curves, plots (b)). The ordering of the C-C bonds according to the shielding at their midpoints is as follows (see curves (a)): C9-C10 > C3-C4 > C1-C2 > C2-C3 > C4a-C10a > C1-C10a > C4-C4a > C10-C10a > C4a-C4b.

Looking at the shielding behaviour at 1 Å above each of the C-C bonds (plots (b)) shows that shielding values larger than 15 (ppm) can be observed over bonds with no connection to the C4a-C10a bond at the fused location. However, the highest isotropic shielding value is found over that C4a-C10a bond.

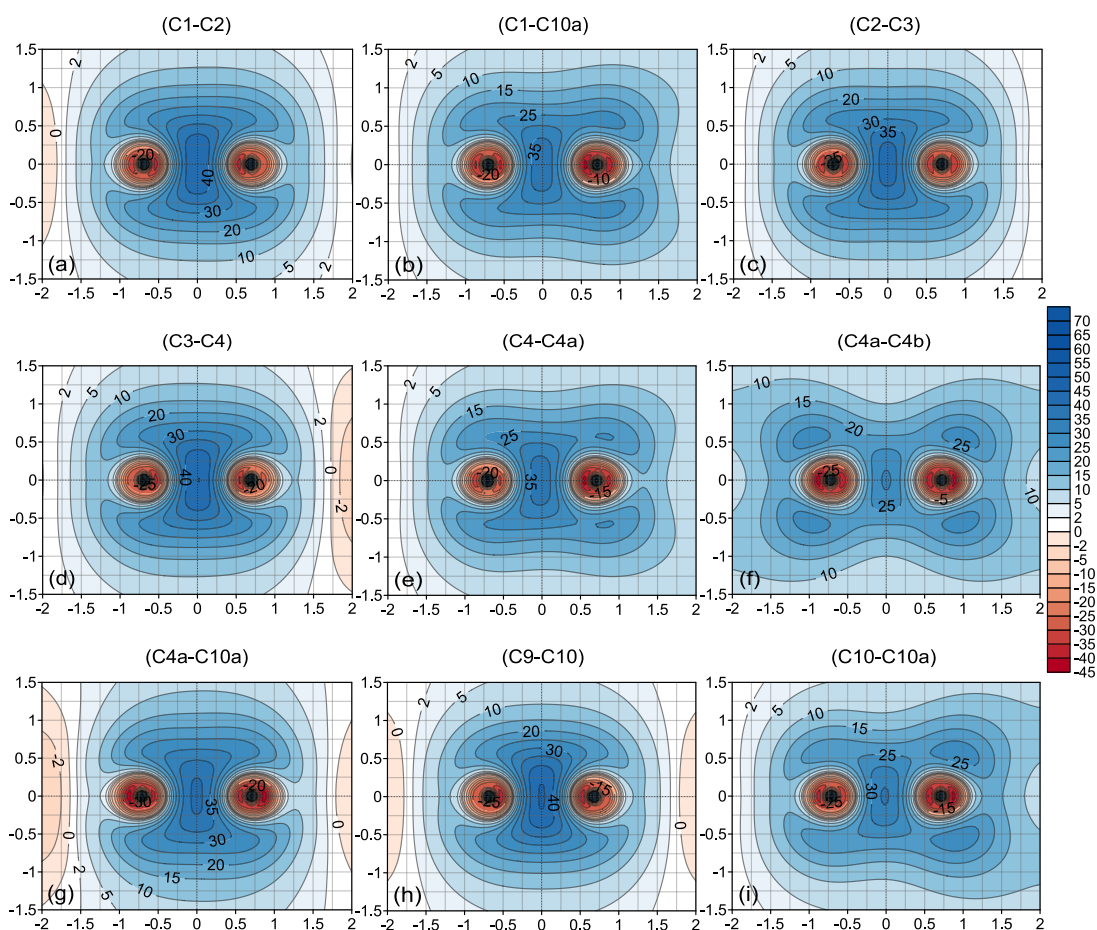


Figure 7-14: MP2-GIAO/6-311+G(d) isotropic shielding contour maps (in ppm) for the symmetry unique C-C bonds of phenanthrene. In each map, the left and right well-shielded dots represent C nuclei. The midpoint of each bond is placed at the (0,0) X,Y coordinates.

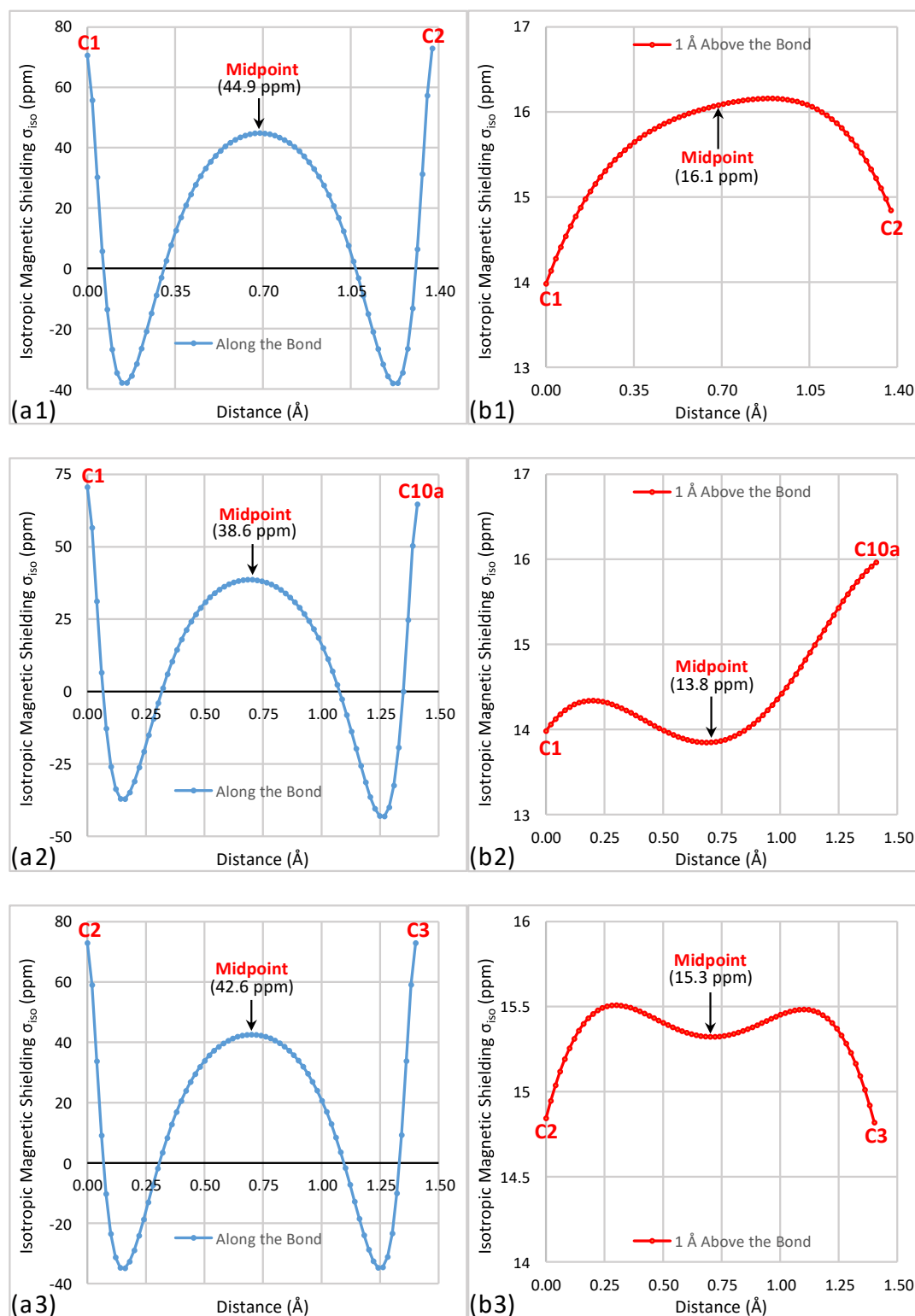


Figure 7-15: Variation in the MP2-GIAO/6-311+G(d) isotropic shielding (σ_{iso}) (in ppm) of the symmetrically unique C-C bonds of the phenanthrene obtained using 71 ghost atoms: (a) positioned along the C-C bonds, and (b) positioned 1 Å parallelly above the bonds.

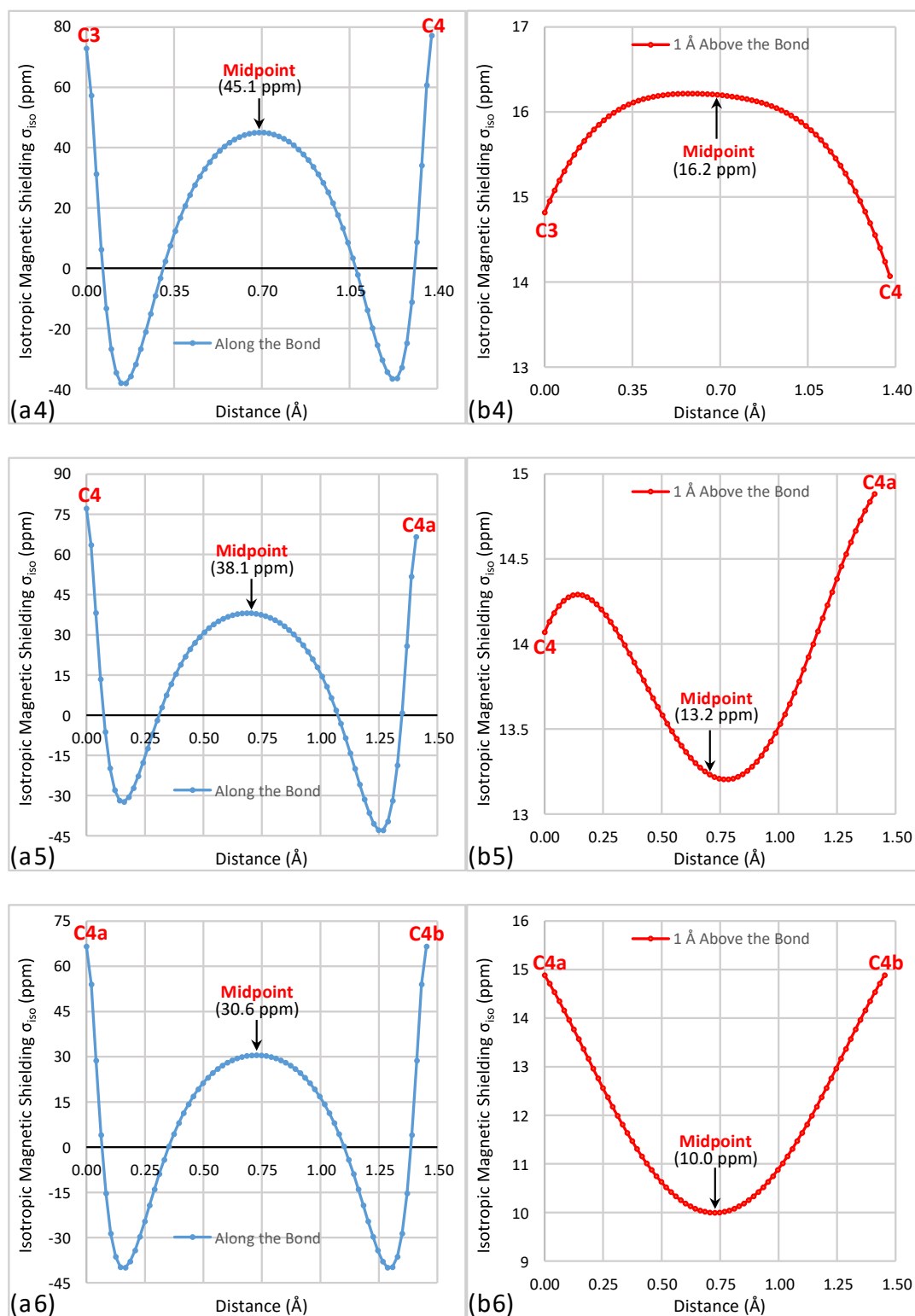


Figure 7-15: Continued.

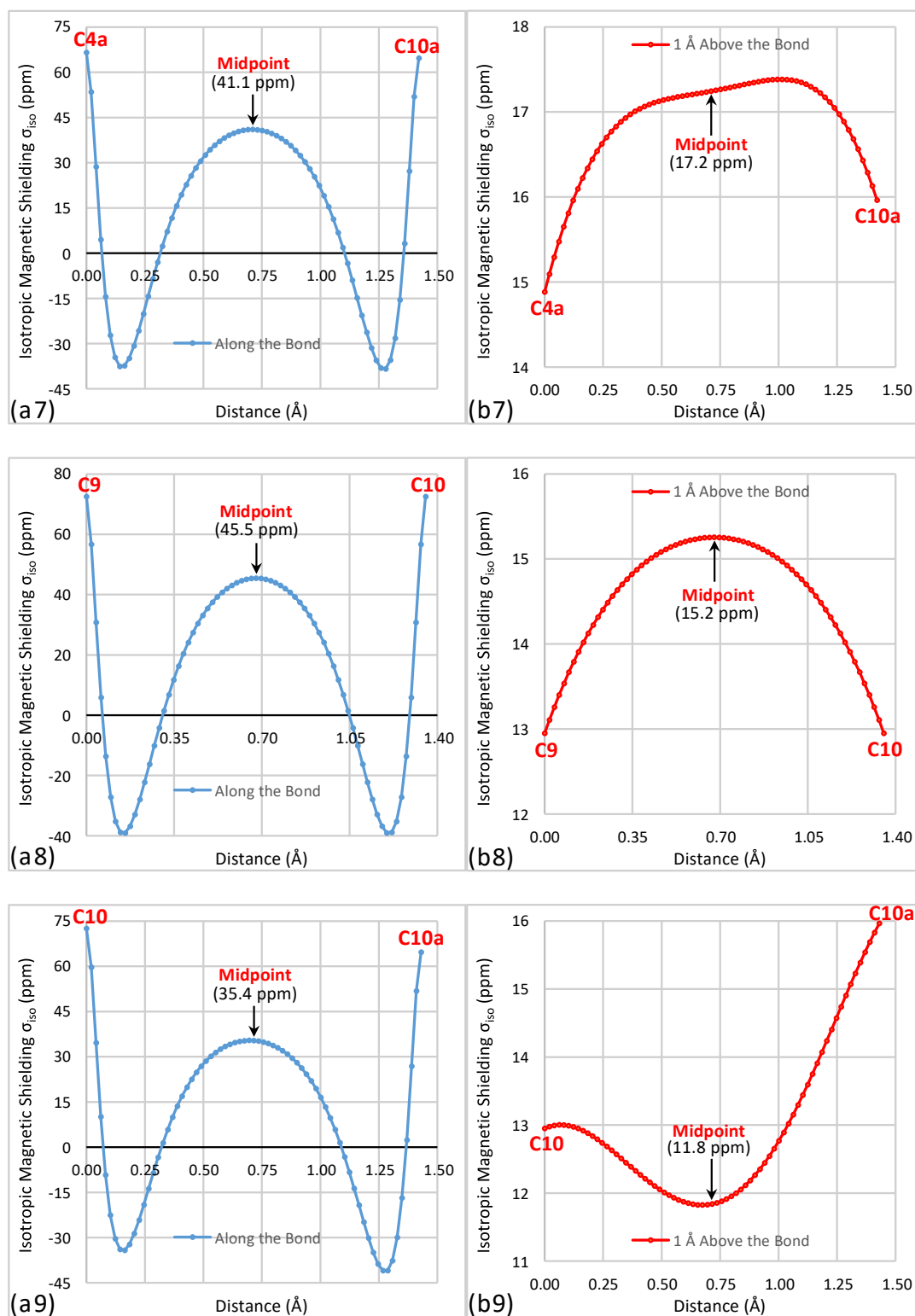


Figure 7-15: Continued.

Similar to the case of anthracene, the 3D shielding calculation for phenanthrene were performed using the new technique which reduces computational costs (see chapter two, section 2-2-3-2). As in other 3D visualisations, the shielding variations in phenanthrene are illustrated by two isosurfaces, see figure (7-16).

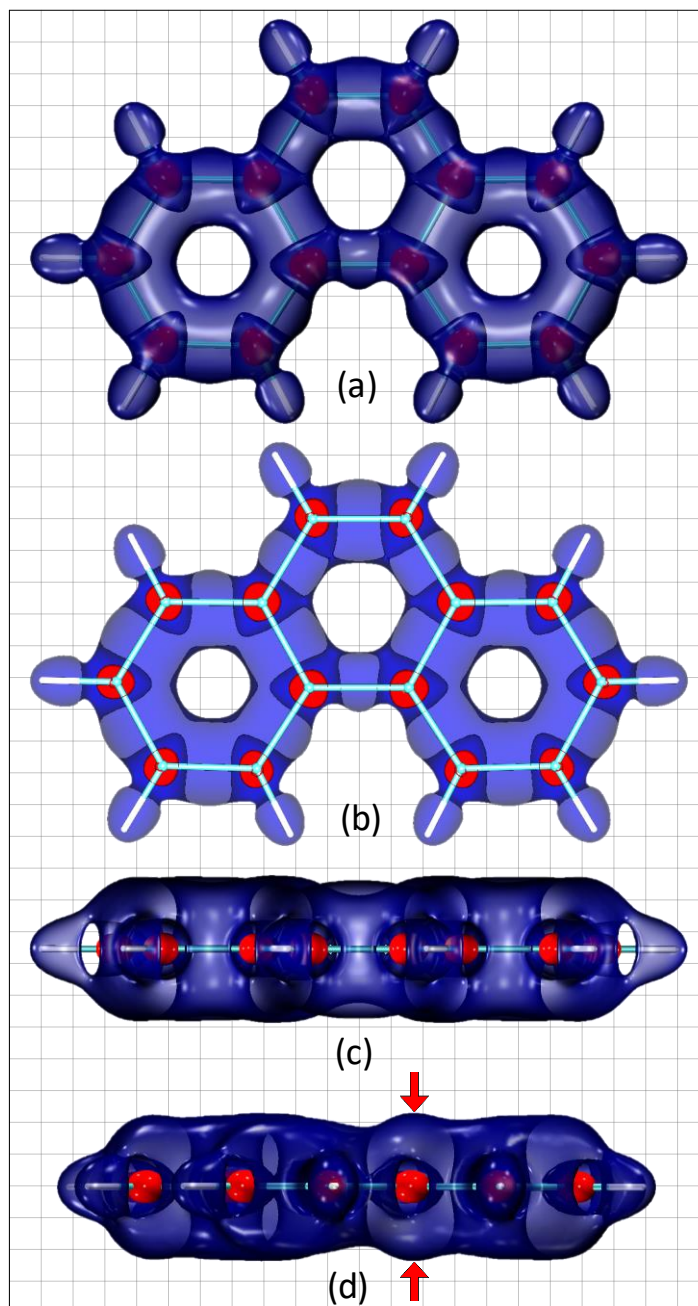


Figure 7-16: (a) Front; (b) horizontal cross-section; (c) axial; and (d) side-view of the isotropic shielding (σ_{iso}) isosurfaces for phenanthrene obtained from MP2-GIAO/6-311+G(d) calculations. The isosurfaces visualise the most common shielding values for aromatic molecules; +16(blue)/-16(red) (ppm).

The blue isosurface corresponds to the +16 (ppm) shielding value, whereas the red isosurface corresponds to the -16 (ppm) shielding value. As expected, phenanthrene molecular framework is enclosed within a well-shielded shape following the bonds. The only deshielded areas are around carbon nuclei. Also, the C-C bonds are clearly more shielded than the C-H bonds.

The (hole) created by the $\sigma_{\text{iso}} = 16$ (ppm) in the central ring centre is clearly much bigger than the corresponding (hole) in each of the terminal rings. Additionally, the shielding cloud above and below the C-C bond at the fused location, namely, C4a-C10, shows a higher vertical expansion than the other C-C bonds, see figure (7-16 (d)). This fully agrees with the preceding discussion of the shielding properties of the C-C bonds.

7-4 Conclusions

A general trend observed in the isotropic shielding calculations for anthracene and phenanthrene is that the nuclear shielding values obtained at the MP2 level are higher than those coming from HF calculations (by about 10 ppm). On the contrast, the shielding values at 1 Å above the nuclei are slightly higher at the HF in comparison to MP2 values (by around 1 (ppm)).

For both methods, the carbon nuclei at the fused locations show lower isotropic shielding than the other nuclei. However, the shielding values at 1 Å above these nuclei tend to be the largest in comparison to other points at that height. As a consequence, both the $|\Delta\sigma_{\text{iso}(C-C')}^{0\text{Å}}|$ and $|\Delta\sigma_{\text{iso}(C-C')}^{1\text{Å}}|$ parameters reach their maximum when one of the carbons of the C-C bond is a fused carbon. The lowest values of these parameters are found for bonds which have no fused nucleus.

The shielding contour maps show that the structural skeletons of both molecules are well-shielded. C-C bonds are better and more evenly shielded than C-H bonds. The carbon nuclei are surrounded by deshielded-spheres which are not observed around hydrogen nuclei.

At heights between 0.50-1.00 Å, the σ_{iso} and $\sigma_{\text{iso}(zz)}$ maps show the tendency of the shielding clouds of the C-C bonds to move towards the inner regions of the rings. We refer to this phenomenon as horizontal shift-in. The extent of

the shift-in is proportional to the shielding of the local ring which contains the C-C bonds.

The examination of the 2D shielding maps shows that the shielding clouds above and below the molecular plane have a tendency to merge above and below the ring centres of well-shielded rings. This is most probably caused by π -electron delocalisation and the ring currents in these regions. As a result, a (cavity) called the less-shielded core, LSC, is formed which is centred at the middle region of the rings.

According to the shielding variation at different vertical heights at the ring centres, the central ring of the anthracene showed higher isotropic shielding content than the terminal rings. The phenanthrene rings show the opposite shielding behaviour.

Comparing shielding variation vertically above each ring centre in both molecules indicates that with increasing the shielding strength, the maximum shielding value becomes much closer to the molecular plane. This can also be considered as a type of the shift-in but in a vertical rather than horizontal direction.

The maximum global average shielding values classify anthracene as having higher total shielding than phenanthrene, 11.14 and 10.08 (ppm), respectively.

To sum up, both molecules can be classified as showing high levels of aromaticity. However, anthracene has a slightly advantage in global shielding over phenanthrene.

CHAPTER EIGHT

CONCLUSIONS

8 Conclusions

Multidimensional isotropic shieldings under various levels of quantum chemical methods have been evaluated for a wide range of compounds. The panoramic representations of the results have succeeded in showing the shielding behaviours of the studied molecules. The five parallel layers of shielding maps help in showing the magnetic change from the σ -bonding region at a molecular plane to the π -bonding region at around 1 Å above the plane. Some shielding features of lone pairs and π -electron localisation/delocalisation can be understood via the fifth map and the $\sigma_{\text{iso}(zz)}$ map. The $\sigma_{\text{iso}(zz)}$ map additionally shows the contribution of the antiparallel shieldings in the fifth map. The vertical grids and 1D ghost-atom lines succeeded in probing the shielding of chemical bonds. Different shielding isosurfaces are capable to represent the total shielding/deshielding trends through molecular space. The magnetic shieldings obtained from the above tools highlight some chemical features of chemical bonding, aromaticity and antiaromaticity.

The magnetic evaluations have been performed at different levels of theory of HF, MP2 and CASSCF, whereas the DFT method was limited for optimisation purposes. Comparing the shielding values from the HF and MP2 methods shows that higher difference between the nuclear shielding values than the values of points far from the nuclear positions.

For borazine and borazanaphthalene, the shielding behaviour around the N-B bonds shows the presence of triangular shielding clouds at the nitrogen centres, whereas deshielded-spheres surround the shielded centres of the borons. This reflects a semi-localisation of lone pairs about nitrogens. At 1 Å above the plane of both molecules, the shieldings of π -electron delocalisation and lone pair localisation above the nitrogen nuclei can be seen without interference. In comparison, benzene and naphthalene show stronger shieldings at the ring centre and greater homogeneous shielding distribution along C-C than B-N bonds. For instance, the shieldings at the ring centre of naphthalene are around five-times higher than that above the borazanaphthalene ring centre, whereas the shieldings above the borazine ring centre are slightly higher than that above the borazanaphthalene ring centre. However, the presence of the shielding interactions without the counter-effects of deshielding interactions above both borazine and borazanaphthalene is considered as a sign of the presence of electron

delocalisation and diatropic current, which are both a feature of aromaticity. In addition, the deshielded spheres around the carbon nuclei of benzene and naphthalene are smaller in size and more evenly surround carbon nuclei than those around boron nuclei of borazine and borazanaphthalene. From this, both borazine and borazanaphthalene are shown to be moderately aromatic.

Each shielding cloud of the C=O bonds showed polarisation towards the oxygen atoms of the oxocarbon dianions and deshielded spheres surrounding each of the carbon centres. Several differences are found, deltate, for instance, displays high shieldings in comparison with other oxocarbon dianions and can be considered as aromatic. The deltate ring is fully shielded with no LSC - weaker shielding with LSC inside the ring is shown in squarate, which can be classified as moderately aromatic. The deshielded-spheres are connected to the deshielded-region at the ring centre in croconate and rhodizonate. Like cyclobutadiene, both croconate and rhodizonate are antiaromatic since the presence of strong deshielding activity as a consequence of the paratropic currents at their rings, with more deshielding activity inside the croconate ring.

Another noteworthy point, based on the shielding behaviour, is that unlike the deltate and squarate, croconate and rhodizonate have a tendency to become cross-conjugated dianions. Increasing the number (n) of $C_nO_n^{2-}$ manes increases the ring area. As a result, adding (-2e) charge to a larger ring causes lowering in value of (-2e/ring area). This is why the smallest three-membered ring of deltate gains the highest (-2e/ring area) ratio. Moreover, with increasing the number (n), the (-2) negative charge is constant, whereas the number of the C=O bonds and the associated electron withdrawing is increased. This can be obvious when comparing the charge distribution of $n=3$ to 6. Namely, with increasing the ring size, the carbon becomes more positively charged and the oxygen becomes more positively charged. Thus, the electron circulation, magnetic properties and aromaticity decrease with increase of the (n), as the electron density per volume unit of a ring is decreased.

The S_2N_2 ground state is considered moderately aromatic due to the overall shielding theme. Shielded/deshielded-spheres can be observed around sulfur/nitrogen atoms. The small size of S_2N_2 ring brings the S-N bonds closer,

which increases the σ -bonding interferences at the ring centre. This makes the LSC becomes deshielded. Based on the shielding behaviour, the main contributions of π -bonding and delocalisation come from the nitrogens. Both the S_1 and T_1 states show a magnetic profile similar to antiaromatic molecules. Most shielding features of the S_1 state can be observed in the T_1 state but with remarkably lower shieldings/deshieldings. The deshieldings at ring inner region of these states destroy the likeness with the S_0 shielding profile. Changes in locations and shapes of shielding/deshielding clouds are found in S_1 and T_1 which is caused to increase the convenience of the shielding/deshielding activities. for the S_0 , S_1 and T_1 states, no magnetic shielding evidence about the existence of S-S or N-N bonds.

According to the isotropic shielding evaluations, naphthalene can be considered as a good example for aromatic molecules. Among the S_0 , S_1 , S_2 and T_1 electronic states of naphthalene, the magnetic shielding findings show the S_2 state higher in isotropic shielding than that in the S_0 state. Deshieldings occupy the S_1 and T_1 naphthalene rings, but lower deshieldings are found for the latter. The four electronic states can be arranged in order of aromaticity degree as: $S_2 > S_0 \gg T_1 > S_1$. The vertical excitations not only lead to variation in aromaticity degree but also leads to variation in ordering of C-C bonds of the four states based on the shielding extent of the bonds.

No doubt that the shielding behaviours of the rings of these molecules agree with Clar structures of the molecules. Also, the general magnetic behaviour of both anthracene and phenanthrene corresponds to the magnetic behaviour of aromatic molecules. This includes, for instance, the shielding clouds surround the structural skeletons, the deshielded-clouds around carbons and the shielding behaviour at different vertical heights. However, some minor shielding differences between the two molecules are observed. The shielding variation at different vertical heights at the ring centres shows that higher isotropic shielding content in the central ring of the anthracene than in the terminal rings. The opposite shielding behaviour can be noticed in phenanthrene rings. Depending on the maximum global average shielding values besides global shieldings, anthracene has slightly more shielding content than the phenanthrene.

Several suggestions can be outlined depending on the isotropic shielding observations of this project:

- Shielding and deshielding activities show a tendency to avoid each other. For instance, when a shielded/deshielded-sphere is completely surrounded by a stronger opposite magnetic activity, the sphere is then shrunk or distorted. Another example, the shielding clouds are repelled to outside/farther regions of the ring when a deshielding activity is present at the inner region of an antiaromatic ring. However, when a shielding activity is strong enough, it can resist such shifts (the shielded-sphere of sulfur in S_2N_2 in S_0 , S_1 and T_1 is the best example for this case).
- The shielding behaviour in hetero-atom rings show a clear variation locally around bonds and globally around the ring. Such variations are caused by electronic charges and/or electronegativity difference between ring atoms.
- A magnetic shielding activity shows a tendency towards associating with magnetically-similar activities. An example that the carbon deshielded-spheres of croconate and rhodizonate associates with the deshieldings at the middle region of the rings. Also, the association of π -electron shielding clouds above and below aromatic molecules agrees with this observation.
- A less shielded core, LSC, is observed at the centre of the rings of aromatic molecules. σ -Bonding magnetic interferences at the middle region of a ring together with the π -electron shielding clouds and bonds shielding clouds lead to forming this core.
- The clouds of π -electron circulation can be found between 0.75 to 1.00 Å above a molecular plane.
- Strong magnetic shieldings can be seen around bonds of aromatic molecules, while lower shieldings with location displacement around bonds of antiaromatic molecules.

From the findings of this thesis, three signs of increasing aromaticity are observed. Firstly, increasing the shielding strength of a global shielding cloud around a molecule and its bonds. This increase is caused by the increase of the electron delocalisation and the diatropic currents of the molecule. Secondly, the maximum shielding value above the ring centre becomes much closer to the molecular plane. Thirdly, the global shielding cloud above and below the molecular plane becomes more vertically extended since the

increase of the induced magnetic field against the applied magnetic field. The three points above can be more obvious when comparing the different molecules or different electronic states such as borazine, borazanaphthalene, deltate, squarate, S_0 state of S_2N_2 , S_0 and S_2 states of naphthalene, anthracene and phenanthrene. Comparing the isotropic shielding behaviours of these molecules with benzene one can notice the similarity in the magnetic features.

On the other hand, increasing antiaromaticity is associated with increasing deshieldings at the ring centre, less shielding clouds of the ring bonds with displacement of the bond positions to outside the ring frame. This is obvious when looking at the isotropic shielding results of croconate, rhodizonate, S_1 and T_1 states of S_2N_2 and naphthalene and comparing them with cyclobutadiene.

Based on the findings of this thesis, a clear message is concluded from the magnetic isotropic shieldings. The message has pictorially and numerically told us that aromaticity, antiaromaticity and bonding of the studied molecules share/differ in the magnetic observations based on the likenesses/ differences in the nature of the molecules. What is more, qualitative and quantitative assessments are obtained to represent the aim of this project which allow making comparisons between different molecules as well as comparing the magnetic behaviours for different electronic states of a specific molecule.

In the end, we can say, the magnetic isotropic shielding evaluations, as a tool, can be implemented on different types of molecules to investigate aromaticity, antiaromaticity and bonding. This tool can be implemented not only by chemists of quantum chemistry field but also as a supportive technique by experimental chemists.

Abbreviations

ϵ_{xc}	Exchange Correlation Energy Per Particle of a Homogeneous Electron Gas
Λ	Magnetic Susceptibility Exaltation
ρ	Charge Density
σ_{iso}	Isotropic Magnetic Shielding
$\sigma_{iso(global)}$	Global Average Shielding
$\sigma_{iso(zz)}$	Vertical Component of Isotropic Shielding
AMBL	Active Middle Bonding Line
ASE	Aromatic Stabilisations Energy
B3LYP	Becke-3-parameters-Lee-Yang-Parr
CASSCF	Complete Active Space Self-Consistent Field
CPHF	Coupled Perturbed Hartree Fock
CSF	Configuration State Function
DFT	Density Functional Theory
E_{xc}	Exchange Correlation Energy
FORS	Full Optimized Reaction Space
GIAO	Gauge Including Atomic Orbital
HF-SCF	Hartree Fock Self Consistent Field Method
HMO	Hückel Molecular Orbital Theory
HOMA	Harmonic Oscillator Model of Aromaticity
LCAO	Linear Combination of Atomic Orbitals
LDA	Local Density Approximation
LPM	Local Polynomial Method
LSC	Less Shielded Core
MBPT	Many Body Perturbation Theory
MIS	Magnetically Important Space
MO	Molecular Orbital
MP2	Møller-Plesset Second Order Perturbation Theory
MUS	Magnetically Unimportant Space
NICS	Nucleus Independent Chemical Shift
PAH	Polycyclic Aromatic Hydrocarbon
PDI	Para Delocalisation Index
SCF	Self Consistent Field
SCI	Six Centre Index
TRE	Topological Resonance Energy
TSNMRs	Through Space NMR Shieldings

References

- [1] M. Faraday, *Phil. Trans. R. Soc.*, **1825**, 115, 440-466.
- [2] A. Kekulé, *Bulletin Mensuel de la Société Chimique de Paris*, **1865**, 3, 98-110.
- [3] G. M. Badger, ***Aromatic Character and Aromaticity***, Cambridge University Press, **1969**.
- [4] D. Lloyd, ***Non-Benzenoid Conjugated Carbocyclic Compounds***, ELSEVIER, **1984**.
- [5] D. Lloyd, *Journal of Chemical Information and Computer Sciences*, **1996**, 36, 442-447.
- [6] D. Lewis and D. Peters, ***Facts and theories of aromaticity***, Macmillan Press, **1975**.
- [7] J. A. Elvidge and L. M. Jackman, *Journal of the Chemical Society (Resumed)*, **1961**, 859-866.
- [8] P. J. Garratt, ***Aromaticity***, McGraw-Hill, **1971**.
- [9] J. W. Armit and R. Robinson, *Journal of the Chemical Society, Transactions*, **1925**, 127, 1604-1618.
- [10] E. Clar, ***Polycyclic Hydrocarbons***, Academic Press, **1964**, Vol. 1.
- [11] H. Jiao, P. v. R. Schleyer, Y. Mo, M. A. McAllister and T. T. Tidwell, *Journal of the American Chemical Society*, **1997**, 119, 7075-7083.
- [12] V. I. Minkin, M. N. Glukhovtsev and B. I. A. Simkin, ***Aromaticity and antiaromaticity: electronic and structural aspects***, J. Wiley & Sons, **1994**.
- [13] M. Solà, *Frontiers in Chemistry*, **2017**, 5, 22.
- [14] P. R. von Schleyer and H. Jiao, in *Pure and Applied Chemistry* (1996), Vol. 68, pp. 209.
- [15] G. Portella, J. Poater, J. M. Bofill, P. Alemany and M. Solà, *The Journal of Organic Chemistry*, **2005**, 70, 2509-2521.
- [16] T. M. Krygowski, M. K. Cyrański, Z. Czarnocki, G. Häfeliinger and A. R. Katritzky, *Tetrahedron*, **2000**, 56, 1783-1796.
- [17] H. Fallah-Bagher-Shaidaei, C. S. Wannere, C. Corminboeuf, R. Puchta and P. v. R. Schleyer, *Organic Letters*, **2006**, 8, 863-866.
- [18] P. v. R. Schleyer, C. Maerker, A. Dransfeld, H. Jiao and N. J. R. van Eikema Hommes, *Journal of the American Chemical Society*, **1996**, 118, 6317-6318.
- [19] G. Subramanian, P. v. R. Schleyer and H. Jiao, *Angewandte Chemie International Edition in English*, **1996**, 35, 2638-2641.

REFERENCES

- [20] R. Gershoni-Poranne and A. Stanger, *Chemical Society Reviews*, **2015**, *44*, 6597-6615.
- [21] P. v. R. Schleyer, H. Jiao, B. Goldfuss and P. K. Freeman, *Angewandte Chemie International Edition in English*, **1995**, *34*, 337-340.
- [22] L. Pauling, *The Journal of Chemical Physics*, **1936**, *4*, 673-677.
- [23] J. A. Pople, *The Journal of Chemical Physics*, **1956**, *24*, 1111-1111.
- [24] J. S. Waugh and R. W. Fessenden, *Journal of the American Chemical Society*, **1957**, *79*, 846-849.
- [25] C. E. Johnson and F. A. Bovey, *The Journal of Chemical Physics*, **1958**, *29*, 1012-1014.
- [26] L. Salem, ***The molecular orbital theory of conjugated systems***, W.A. Benjamin, **1966**.
- [27] B. P. Dailey, *The Journal of Chemical Physics*, **1964**, *41*, 2304-2310.
- [28] H. J. Dauben, J. D. Wilson and J. L. Laity, *Journal of the American Chemical Society*, **1968**, *90*, 811-813.
- [29] J. P. Snyder, ***Nonbenzenoid Aromatics***, Elsevier Science, **1971**.
- [30] P. v. R. Schleyer, H. Jiao, N. J. R. v. E. Hommes, V. G. Malkin and O. L. Malkina, *Journal of the American Chemical Society*, **1997**, *119*, 12669-12670.
- [31] Z. Chen, C. S. Wannere, C. Corminboeuf, R. Puchta and P. v. R. Schleyer, *Chemical Reviews*, **2005**, *105*, 3842-3888.
- [32] P. B. Karadakov and K. E. Horner, *The Journal of Physical Chemistry A*, **2013**, *117*, 518-523.
- [33] H. Jiao and P. v. R. Schleyer, *Angewandte Chemie International Edition in English*, **1993**, *32*, 1760-1763.
- [34] B. Goldfuss, P. v. R. Schleyer and F. Hampel, *Organometallics*, **1996**, *15*, 1755-1757.
- [35] A. Sekiguchi, K. Ebata, C. Kabuto and H. Sakurai, *Journal of the American Chemical Society*, **1991**, *113*, 7081-7082.
- [36] M. Balci, M. L. McKee and P. v. R. Schleyer, *The Journal of Physical Chemistry A*, **2000**, *104*, 1246-1255.
- [37] P. v. R. Schleyer, M. Manoharan, Z.-X. Wang, B. Kiran, H. Jiao, R. Puchta and N. J. R. van Eikema Hommes, *Organic Letters*, **2001**, *3*, 2465-2468.
- [38] C. Corminboeuf, T. Heine, G. Seifert, P. v. R. Schleyer and J. Weber, *Physical Chemistry Chemical Physics*, **2004**, *6*, 273-276.
- [39] R. Gershoni-Poranne and A. Stanger, *Chemistry - A European Journal*, **2014**, *20*, 5673-5688.
- [40] A. Stanger, *European Journal of Organic Chemistry*, **2019**, *2019*, 857-859.

REFERENCES

- [41] S. Klod and E. Kleinpeter, *Journal of the Chemical Society, Perkin Transactions 2*, **2001**, 1893-1898.
- [42] E. Kleinpeter, S. Klod and A. Koch, *Journal of Molecular Structure: THEOCHEM*, **2007**, 811, 45-60.
- [43] E. Kleinpeter and A. Koch, *The Journal of Physical Chemistry A*, **2012**, 116, 5674-5680.
- [44] E. Kleinpeter, A. Holzberger and P. Wacker, *The Journal of Organic Chemistry*, **2008**, 73, 56-65.
- [45] S. Klod, A. Koch and E. Kleinpeter, *J. Chem. Soc., Perkin Trans. 2*, **2002**, 1506-1509.
- [46] P. E. Hansen, A. Koch and E. Kleinpeter, *Tetrahedron Letters*, **2018**, 59, 2288-2292.
- [47] E. Kleinpeter and A. Koch, *The Journal of Physical Chemistry A*, **2019**, 123, 4443-4451.
- [48] K. E. Horner and P. B. Karadakov, *The Journal of Organic Chemistry*, **2013**, 78, 8037-8043.
- [49] K. E. Horner and P. B. Karadakov, *The Journal of Organic Chemistry*, **2015**, 80, 7150-7157.
- [50] P. B. Karadakov and K. E. Horner, *Journal of Chemical Theory and Computation*, **2016**, 12, 558-563.
- [51] P. B. Karadakov, P. Hearnshaw and K. E. Horner, *The Journal of Organic Chemistry*, **2016**, 81, 11346-11352.
- [52] P. B. Karadakov, M. A. H. Al-Yassiri and D. L. Cooper, *Chemistry – A European Journal*, **2018**, 24, 16791-16803.
- [53] D. R. Hartree, *Mathematical Proceedings of the Cambridge Philosophical Society*, **1928**, 24, 89-110.
- [54] V. Fock, *Zeitschrift für Physik*, **1930**, 61, 126-148.
- [55] A. Szabo and N. S. Ostlund, ***Modern Quantum Chemistry: Introduction to Advanced Electronic Structure Theory***, Dover Publications, **1996**.
- [56] C. J. Cramer, ***Essentials of Computational Chemistry: Theories and Models***, Wiley, **2005**.
- [57] C. C. J. Roothaan, *Reviews of Modern Physics*, **1951**, 23, 69-89.
- [58] G. G. Hall and E. Lennard-Jones John, *Proceedings of the Royal Society of London. Series A. Mathematical and Physical Sciences*, **1951**, 205, 541-552.
- [59] J. P. Doucet and J. Weber, ***Computer-Aided Molecular Design: Theory and Applications***, Elsevier Science, **1996**.
- [60] W. G. Richards and D. L. Cooper, ***Ab Initio Molecular Orbital Calculations for Chemists***, Clarendon Press, **1983**.

REFERENCES

- [61] M. J. S. Dewar, *The Molecular Orbital Theory of Organic Chemistry*, McGraw-Hill, 1969.
- [62] E. G. Lewars, *Computational Chemistry: Introduction to the Theory and Applications of Molecular and Quantum Mechanics*, Springer Netherlands, 2010.
- [63] D. Young, *Computational Chemistry: A Practical Guide for Applying Techniques to Real-World Problems*, Wiley, 2001.
- [64] C. Møller and M. S. Plesset, *Physical Review*, 1934, 46, 618-622.
- [65] M. P. Mueller, *Fundamentals of Quantum Chemistry: Molecular Spectroscopy and Modern Electronic Structure Computations*, Springer US, 2007.
- [66] B. O. Roos, P. R. Taylor and P. E. M. Siegbahn, *Chemical Physics*, 1980, 48, 157-173.
- [67] P. E. M. Siegbahn, J. Almlöf, A. Heiberg and B. O. Roos, *The Journal of Chemical Physics*, 1981, 74, 2384-2396.
- [68] B. O. Roos, *International Journal of Quantum Chemistry*, 1980, 18, 175-189.
- [69] P. Siegbahn, A. Heiberg, B. Roos and B. Levy, *Physica Scripta*, 1980, 21, 323-327.
- [70] F. Jensen, *Introduction to Computational Chemistry*, 3 ed., Wiley, 2017.
- [71] D. Sholl and J. A. Steckel, *Density Functional Theory: A Practical Introduction*, Wiley, 2009.
- [72] J. C. A. Boeyens, *Chemistry from First Principles*, Springer Netherlands, 2008.
- [73] C. Lee, W. Yang and R. G. Parr, *Physical Review B*, 1988, 37, 785-789.
- [74] A. D. Becke, *The Journal of Chemical Physics*, 1993, 98, 5648-5652.
- [75] P. J. Stephens, F. J. Devlin, C. F. Chabalowski and M. J. Frisch, *The Journal of Physical Chemistry*, 1994, 98, 11623-11627.
- [76] M. J. Frisch, G. W. Trucks, H. B. Schlegel, G. E. Scuseria, M. A. Robb, J. R. Cheeseman, G. Scalmani, V. Barone, G. A. Petersson, H. Nakatsuji, X. Li, M. Caricato, A. V. Marenich, J. Bloino, B. G. Janesko, R. Gomperts, B. Mennucci, H. P. Hratchian, J. V. Ortiz, A. F. Izmaylov, J. L. Sonnenberg, Williams, F. Ding, F. Lipparini, F. Egidi, J. Goings, B. Peng, A. Petrone, T. Henderson, D. Ranasinghe, V. G. Zakrzewski, J. Gao, N. Rega, G. Zheng, W. Liang, M. Hada, M. Ehara, K. Toyota, R. Fukuda, J. Hasegawa, M. Ishida, T. Nakajima, Y. Honda, O. Kitao, H. Nakai, T. Vreven, K. Throssell, J. A. Montgomery Jr, J. E. Peralta, F. Ogliaro, M. J. Bearpark, J. J. Heyd, E. N. Brothers, K. N. Kudin, V. N. Staroverov, T. A. Keith, R. Kobayashi, J. Normand, K. Raghavachari, A. P. Rendell, J. C. Burant, S. S. Iyengar, J. Tomasi, M. Cossi, J. M. Millam, M. Klene, C. Adamo, R. Cammi, J. W. Ochterski, R. L. Martin, K.

REFERENCES

- Morokuma, O. Farkas, J. B. Foresman and D. J. Fox, (Gaussian, Inc., Wallingford, CT, 2016).
- [77] K. Aidas, C. Angeli, K. L. Bak, V. Bakken, R. Bast, L. Boman, O. Christiansen, R. Cimiraglia, S. Coriani, P. Dahle, E. K. Dalskov, U. Ekström, T. Enevoldsen, J. J. Eriksen, P. Ettenhuber, B. Fernández, L. Ferrighi, H. Fliegl, L. Frediani, K. Hald, A. Halkier, C. Hättig, H. Heiberg, T. Helgaker, A. C. Hennum, H. Hettema, E. Hjertenæs, S. Høst, I.-M. Høyvik, M. F. Iozzi, B. Jansík, H. J. A. Jensen, D. Jonsson, P. Jørgensen, J. Kauczor, S. Kirpekar, T. Kjærgaard, W. Klopper, S. Knecht, R. Kobayashi, H. Koch, J. Kongsted, A. Krapp, K. Kristensen, A. Ligabue, O. B. Lutnæs, J. I. Melo, K. V. Mikkelsen, R. H. Myhre, C. Neiss, C. B. Nielsen, P. Norman, J. Olsen, J. M. H. Olsen, A. Osted, M. J. Packer, F. Pawłowski, T. B. Pedersen, P. F. Provasi, S. Reine, Z. Rinkevicius, T. A. Ruden, K. Ruud, V. V. Rybkin, P. Sałek, C. C. M. Samson, A. S. de Merás, T. Saue, S. P. A. Sauer, B. Schimmelpfennig, K. Snegov, A. H. Steindal, K. O. Sylvester-Hvid, P. R. Taylor, A. M. Teale, E. I. Tellgren, D. P. Tew, A. J. Thorvaldsen, L. Thøgersen, O. Vahtras, M. A. Watson, D. J. D. Wilson, M. Ziolkowski and H. Ågren, *Wiley Interdisciplinary Reviews: Computational Molecular Science*, **2014**, *4*, 269-284.
- [78] W. Humphrey, A. Dalke and K. Schulten, *Journal of Molecular Graphics*, **1996**, *14*, 33-38.
- [79] D. Roy, A. K. Todd and M. M. John, (Semichem Inc., Shawnee Mission KS, 2016).
- [80] S. Park, T. H. Seo, H. Cho, K. H. Min, D. S. Lee, D.-I. Won, S. O. Kang and M. J. Kim, *Scientific Reports*, **2017**, *7*, 40260.
- [81] P. J. Fazen, J. S. Beck, A. T. Lynch, E. E. Remsen and L. G. Sneddon, *Chemistry of Materials*, **1990**, *2*, 96-97.
- [82] L. G. Sneddon, M. G. L. Mirabelli, A. T. Lynch, P. J. Fazen, K. Su and J. S. Beck, in *Pure and Applied Chemistry* (1991), Vol. 63, pp. 407.
- [83] A. Stock and E. Pohland, *Berichte der deutschen chemischen Gesellschaft (A and B Series)*, **1926**, *59*, 2215-2223.
- [84] S. H. Bauer, *Journal of the American Chemical Society*, **1938**, *60*, 524-530.
- [85] A. W. Laubengayer, P. C. Moews and R. F. Porter, *Journal of the American Chemical Society*, **1961**, *83*, 1337-1342.
- [86] L. J. Turbini and R. F. Porter, *Inorganic Chemistry*, **1975**, *14*, 1252-1257.
- [87] M. A. Neiss and R. F. Porter, *Journal of the American Chemical Society*, **1972**, *94*, 1438-1443.
- [88] C. Gervais, J. Maquet, F. Babonneau, C. Duriez, E. Framery, M. Vaultier, P. Florian and D. Massiot, *Chemistry of Materials*, **2001**, *13*, 1700-1707.
- [89] D. Kim and J. Economy, *Chemistry of Materials*, **1994**, *6*, 395-400.

REFERENCES

- [90] G. Mamantov and J. L. Margrave, *Journal of Inorganic and Nuclear Chemistry*, **1961**, 20, 348-351.
- [91] P. J. Fazen, E. E. Remsen, J. S. Beck, P. J. Carroll, A. R. McGhie and L. G. Sneddon, *Chemistry of Materials*, **1995**, 7, 1942-1956.
- [92] T. Kar, D. E. Elmore and S. Scheiner, *Journal of Molecular Structure: THEOCHEM*, **1997**, 392, 65-74.
- [93] A. Stock, E. Wiberg and H. Martini, *Berichte der deutschen chemischen Gesellschaft (A and B Series)*, **1930**, 63, 2927-2937.
- [94] C. W. Rector, G. W. Schaeffer and J. R. Platt, *The Journal of Chemical Physics*, **1949**, 17, 460-465.
- [95] H. Watanabe, K. Ito and M. Kubo, *Journal of the American Chemical Society*, **1960**, 82, 3294-3297.
- [96] E. D. Jemmis and B. Kiran, *Inorganic Chemistry*, **1998**, 37, 2110-2116.
- [97] D. L. Cooper, S. C. Wright, J. Gerratt, P. A. Hyams and M. Raimondi, *Journal of the Chemical Society, Perkin Transactions 2*, **1989**, 719-724.
- [98] P. W. Fowler and E. Steiner, *The Journal of Physical Chemistry A*, **1997**, 101, 1409-1413.
- [99] E. Steiner, P. W. Fowler and R. W. A. Havenith, *The Journal of Physical Chemistry A*, **2002**, 106, 7048-7056.
- [100] R. Islas, E. Chamorro, J. Robles, T. Heine, J. C. Santos and G. Merino, *Structural Chemistry*, **2007**, 18, 833-839.
- [101] D. Benker, T. M. Klapötke, G. Kuhn, J. Li and C. Miller, *Heteroatom Chemistry*, **2005**, 16, 311-315.
- [102] P. Lazzeretti and J. A. Tossell, *Journal of Molecular Structure: THEOCHEM*, **1991**, 236, 403-410.
- [103] N. Matsunaga, T. R. Cundari, M. W. Schmidt and M. S. Gordon, *Theoretica chimica acta*, **1992**, 83, 57-68.
- [104] K. Jug, *The Journal of Organic Chemistry*, **1983**, 48, 1344-1348.
- [105] W. H. Fink and J. C. Richards, *Journal of the American Chemical Society*, **1991**, 113, 3393-3398.
- [106] R. C. Haddon, *Pure Appl. Chem.*, **1982**, 54, 1129-1142.
- [107] G. R. Dennis and G. L. D. Ritchie, *The Journal of Physical Chemistry*, **1993**, 97, 8403-8409.
- [108] B. Kiran, A. K. Phukan and E. D. Jemmis, *Inorganic Chemistry*, **2001**, 40, 3615-3618.
- [109] A. W. Laubengayer, O. T. Beachley and R. F. Porter, *Inorganic Chemistry*, **1965**, 4, 578-582.
- [110] B. Chiavarino, M. E. Crestoni and S. Fornarini, *Journal of the American Chemical Society*, **1999**, 121, 2619-2620.

REFERENCES

- [111] G. W. Schaeffer, R. Schaeffer and H. I. Schlesinger, *Journal of the American Chemical Society*, **1951**, 73, 1612-1614.
- [112] D. R. Armstrong and D. T. Clark, *Journal of the Chemical Society D: Chemical Communications*, **1970**, 99-100.
- [113] R. Hoffmann, *The Journal of Chemical Physics*, **1964**, 40, 2474-2480.
- [114] A. Kalemios, *International Journal of Quantum Chemistry*, **2018**, 118, e25650.
- [115] R. J. Boyd, S. Cheng Choi and C. C. Hale, *Chemical Physics Letters*, **1984**, 112, 136-141.
- [116] T.-K. Ha and C. Puebla, *Journal of Molecular Structure: THEOCHEM*, **1986**, 137, 183-189.
- [117] S. Cohen, J. R. Lacher and J. D. Park, *Journal of the American Chemical Society*, **1959**, 81, 3480-3480.
- [118] R. West, H.-Y. Niu, D. L. Powell and M. V. Evans, *Journal of the American Chemical Society*, **1960**, 82, 6204-6205.
- [119] R. West and H. Y. Niu, *Journal of the American Chemical Society*, **1962**, 84, 1324-1325.
- [120] D. Eggerding and R. West, *Journal of the American Chemical Society*, **1975**, 97, 207-208.
- [121] D. Eggerding and R. West, *Journal of the American Chemical Society*, **1976**, 98, 3641-3644.
- [122] F. Serratos, *Accounts of Chemical Research*, **1983**, 16, 170-176.
- [123] R. West, D. Eggerding, J. Perkins, D. Handy and E. C. Tuazon, *Journal of the American Chemical Society*, **1979**, 101, 1710-1714.
- [124] M. Ito and R. West, *Journal of the American Chemical Society*, **1963**, 85, 2580-2584.
- [125] R. T. Bailey, *Journal of the Chemical Society B: Physical Organic*, **1971**, 627-629.
- [126] P. v. R. Schleyer, K. Najafian, B. Kiran and H. Jiao, *The Journal of Organic Chemistry*, **2000**, 65, 426-431.
- [127] G. M. A. Junqueira, W. R. Rocha, W. B. De Almeida and H. F. Dos Santos, *Journal of Molecular Structure: THEOCHEM*, **2004**, 684, 141-147.
- [128] J. Aihara, *Journal of the American Chemical Society*, **1981**, 103, 1633-1635.
- [129] D. Quiñonero, A. Frontera, P. Ballester and P. M. Deyà, *Tetrahedron Letters*, **2000**, 41, 2001-2005.
- [130] D. Quiñonero, C. Garau, A. Frontera, P. Ballester, A. Costa and P. M. Deyà, *Chemistry – A European Journal*, **2002**, 8, 433-438.

REFERENCES

- [131] W. C. Herndon, *Journal of Molecular Structure: THEOCHEM*, **1983**, *103*, 219-234.
- [132] A. Moyano and F. Serratosa, *Journal of Molecular Structure: THEOCHEM*, **1982**, *90*, 131-136.
- [133] C. Domene, P. W. Fowler, L. W. Jenneskens and E. Steiner, *Chemistry – A European Journal*, **2007**, *13*, 269-276.
- [134] C. Puebla and T.-k. Ha, *Journal of Molecular Structure: THEOCHEM*, **1986**, *137*, 171-181.
- [135] C. Leibovici, *Journal of Molecular Structure*, **1972**, *13*, 185-189.
- [136] L. Farnell, L. Radom and M. A. Vincent, *Journal of Molecular Structure: THEOCHEM*, **1981**, *76*, 1-10.
- [137] F. P. Burt, *Journal of the Chemical Society, Transactions*, **1910**, *97*, 1171-1174.
- [138] N. N. Greenwood and A. Earnshaw, ***Chemistry of the Elements***, 2 ed., **1997**.
- [139] M. Goehring and D. Voigt, *Naturwissenschaften*, **1953**, *40*, 482-482.
- [140] M. M. Labes, P. Love and L. F. Nichols, *Chemical Reviews*, **1979**, *79*, 1-15.
- [141] R. L. Greene, G. B. Street and L. J. Suter, *Physical Review Letters*, **1975**, *34*, 577-579.
- [142] V. V. Walatka, M. M. Labes and J. H. Perlstein, *Physical Review Letters*, **1973**, *31*, 1139-1142.
- [143] Y. Jung, T. Heine, P. v. R. Schleyer and M. Head-Gordon, *Journal of the American Chemical Society*, **2004**, *126*, 3132-3138.
- [144] R. H. Findlay, M. H. Palmer, A. J. Downs, R. G. Egdell and R. Evans, *Inorganic Chemistry*, **1980**, *19*, 1307-1314.
- [145] J. Gerratt, S. J. McNicholas, P. B. Karadakov, M. Sironi, M. Raimondi and D. L. Cooper, *Journal of the American Chemical Society*, **1996**, *118*, 6472-6476.
- [146] S. Millefiori and A. Millefiori, *Inorganica Chimica Acta*, **1980**, *45*, L19-L22.
- [147] P. Brant, D. C. Weber, C. T. Ewing, F. L. Carter and J. A. Hashmall, *Inorganic Chemistry*, **1980**, *19*, 2829-2831.
- [148] R. R. Adkins and A. G. Turner, *Journal of the American Chemical Society*, **1978**, *100*, 1383-1387.
- [149] B. Braïda, A. Lo and P. C. Hiberty, *ChemPhysChem*, **2012**, *13*, 811-819.
- [150] G. Van Zandwijk, R. A. J. Janssen and H. M. Buck, *Journal of the American Chemical Society*, **1990**, *112*, 4155-4164.
- [151] A. Perrin, A. Flores Antognini, X. Zeng, H. Beckers, H. Willner and G. Rauhut, *Chemistry - A European Journal*, **2014**, *20*, 10323-10331.

REFERNCES

- [152] J. Kidd and H. Wollaston William, *Philosophical Transactions of the Royal Society of London*, **1821**, 111, 209-221.
- [153] L. Pauling, L. O. Brockway and J. Y. Beach, *Journal of the American Chemical Society*, **1935**, 57, 2705-2709.
- [154] M. Baba, Y. Kowaka, U. Nagashima, T. Ishimoto, H. Goto and N. Nakayama, *J Chem Phys*, **2011**, 135, 054305.
- [155] M. J. S. Dewar and C. De Llano, *Journal of the American Chemical Society*, **1969**, 91, 789-795.
- [156] B. A. Hess and L. J. Schaad, *Journal of the American Chemical Society*, **1971**, 93, 305-310.
- [157] B. A. Hess and L. J. Schaad, *Journal of the American Chemical Society*, **1971**, 93, 2413-2416.
- [158] N. Trinajstić, M. Milun and Z. Sobotka, *The Journal of Organic Chemistry*, **1972**, 37, 139-141.
- [159] J. Aihara, *Journal of the American Chemical Society*, **1977**, 99, 2048-2053.
- [160] J.-i. Aihara, *Journal of the Chemical Society, Perkin Transactions 2*, **1996**, 2185-2195.
- [161] K. B. Wiberg, *The Journal of Organic Chemistry*, **1997**, 62, 5720-5727.
- [162] S. Behrens, A. M. Koester and K. Jug, *The Journal of Organic Chemistry*, **1994**, 59, 2546-2551.
- [163] C. W. Bird, *Tetrahedron*, **1996**, 52, 9945-9952.
- [164] H. J. Dauben, J. D. Wilson and J. L. Laity, *Journal of the American Chemical Society*, **1969**, 91, 1991-1998.
- [165] F. Uçun and A. Tokatlı, *Chemical Physics Letters*, **2015**, 621, 5-11.
- [166] J. Dominikowska and M. Palusiak, *Structural Chemistry*, **2012**, 23, 1173-1183.
- [167] J.-i. Aihara, *The Journal of Physical Chemistry A*, **2003**, 107, 11553-11557.
- [168] E. Steiner and P. W. Fowler, *International Journal of Quantum Chemistry*, **1996**, 60, 609-616.
- [169] S. Li and Y. Jiang, *Journal of the American Chemical Society*, **1995**, 117, 8401-8406.
- [170] J.-i. Aihara, *The Journal of Physical Chemistry A*, **1999**, 103, 7487-7495.
- [171] R. C. Peck, J. M. Schulman and R. L. Disch, *The Journal of Physical Chemistry*, **1990**, 94, 6637-6641.
- [172] J. B. Pedley, R. D. Naylor and S. P. Kirby, *Thermochemical Data of Organic Compounds*, 2 ed., Chapman and Hall Ltd, **1986**, pp. 91,101.

REFERNCES

- [173] J. Aihara, *Journal of the American Chemical Society*, **1976**, *98*, 2750-2758.
- [174] Z. Zhou and R. G. Parr, *Journal of the American Chemical Society*, **1989**, *111*, 7371-7379.
- [175] J.-i. Aihara, *Bulletin of the Chemical Society of Japan*, **1977**, *50*, 2010-2012.
- [176] I. Gutman, M. Milun and N. Trinajstić, *Journal of the American Chemical Society*, **1977**, *99*, 1692-1704.
- [177] P. v. R. Schleyer, M. Manoharan, H. Jiao and F. Stahl, *Organic Letters*, **2001**, *3*, 3643-3646.
- [178] J. Poater, X. Fradera, M. Duran and M. Solà, *Chemistry – A European Journal*, **2003**, *9*, 400-406.
- [179] G. Portella, J. Poater and M. Solà, *Journal of Physical Organic Chemistry*, **2005**, *18*, 785-791.
- [180] M. K. Cyrański, B. T. Stępień and T. M. Krygowski, *Tetrahedron*, **2000**, *56*, 9663-9667.
- [181] A. Ligabue, U. Pincelli, P. Lazzeretti and R. Zanasi, *Journal of the American Chemical Society*, **1999**, *121*, 5513-5518.
- [182] M. Giambiagi, M. S. de Giambiagi, C. D. dos Santos Silva and A. P. de Figueiredo, *Physical Chemistry Chemical Physics*, **2000**, *2*, 3381-3392.
- [183] M. Mandado, M. J. González-Moa and R. A. Mosquera, *Journal of Computational Chemistry*, **2007**, *28*, 1625-1633.
- [184] S. Fias, S. V. Damme and P. Bultinck, *Journal of Computational Chemistry*, **2008**, *29*, 358-366.
- [185] P. Bultinck, S. Fias and R. Ponc, *Chemistry - A European Journal*, **2006**, *12*, 8813-8818.
- [186] J.-i. Aihara and H. Kanno, *The Journal of Physical Chemistry A*, **2005**, *109*, 3717-3721.
- [187] A. Stanger, *The Journal of Organic Chemistry*, **2006**, *71*, 883-893.
- [188] S. T. Howard and T. M. Krygowski, *Canadian Journal of Chemistry*, **1997**, *75*, 1174-1181.
- [189] S. Fias, P. W. Fowler, J. L. Delgado, U. Hahn and P. Bultinck, *Chemistry - A European Journal*, **2008**, *14*, 3093-3099.
- [190] J. Poater, J. M. Bofill, P. Alemany and M. Solà, *The Journal of Physical Chemistry A*, **2005**, *109*, 10629-10632.